論文 / 著書情報
Article / Book Information

題目(和文)	砂質土の内部浸食に関する実験的研究と微視的観察
Title(English)	Experimental investigation and microscopic observation on internal erosion of cohesionless soils
著者(和文)	Ouyang Mao
Author(English)	Mao Ouyang
出典(和文)	学位:博士（学術）, 学位授与機関:東京工業大学, 報告番号:甲第10359号, 授与年月日:2016年9月20日, 学位の種別:課程博士, 審査員:髙橋 章浩,北詰 昌樹,竹村 次朗,鼎 信次郎,千々和 伸浩
Citation(English)	Degree:Doctor (Academic), Conferring organization: Tokyo Institute of Technology, Report number:甲第10359号, Conferred date:2016/9/20, Degree Type:Course doctor, Examiner:,,,,
学位種別(和文)	博士論文
Type(English)	Doctoral Thesis

Experimental investigation and microscopic observation on internal erosion of cohesionless soils

Mao Ouyang

Dissertation

submitted in partial fulfillment of the requirements for the degree of

Doctor of Philosophy

at

Tokyo Institute of Technology

2016

Synopsis

Internal erosion is defined as the transport of detached finer particles through the soil matrix under seepage flow. The physical and mechanical responses of cohesionless soils subjected to internal erosion were investigated by laboratory experiments and microscopic observations.

A series of seepage tests and subsequent drained and undrained compression tests were conducted to investigate the mechanical responses of cohesionless soils subjected to internal erosion. Experimental results revealed that internal erosion not only led to dislodgement of fines, deformation of volume, and variation of hydraulic conductivity, but also caused an alternation of soils fabric and consequently a change of the mechanical behaviors. At small strain level, the eroded soils showed larger secant stiffness than uneroded soils containing the same initial fines contents under drained compression conditions. At medium strain level, the undrained peak strength of soils with erosion was larger than that of soils without erosion on the condition that their initial fines contents were the same, whereas, the drained strength of soils with erosion was smaller that of soils without erosion.

In order to interpret the mechanical behaviors of eroded soils from the microscopic observation, a plane strain erosion apparatus equipped with visible window was developed. The change of soil fabric during the seepage and compression tests was recorded by a digital microscope. Simultaneously, a image analysis approach was proposed and employed to describe the characteristics of internal erosion.

Through the developed apparatus and proposed method, the mechanical behaviors of eroded soils were qualitatively and quantitatively explained at both small strain level and medium strain level. It was demonstrated that at small strain level, a larger amount of fines was cumulated around the contacts points among coarse particles, which might be responsible for the larger secant stiffness of eroded soils comparing to that of uneroded soils. At medium strain level, for the soils with erosion, the fines were transported to the voids, leading to a smaller percentage of fines in the contact points among coarse particles, and further a smaller drained strength than that of soils without erosion.

Acknowledgments

I begin what could be an endless list with an expression of gratitude to Professor Akihiro Takahashi, my academic advisor during the study in Tokyo Institute of Technology. His constant encouragement and guidance, as well as the suggestions on what is research and how to tackle a problem, guided me toward the research goals. The role he played in this dissertation could never be overemphasized, and I must say that I could not have finished it without his help.

I am grateful to Professor Masaki Kitazume for his valuable comments and suggestions on my research. His advice on how to write academic papaers and the idea on how to friendly demonstrate the scientific illustrations greatly improved the quality of this dissertation.

I am also grateful to Associate Professor Jiro Takemura for his great care for my experimental work. Gratitude is also due to Professor Shinjiro Kanae, and Associate Professor Nobuhiro Chijiwa, who are my committee members, and broaden my view towards the academic research.

I would like to thank Associate Professor Tomihide Takeyama, Kobe University, who have motivated me to learn the constitutive models and numerical analysis during his stay in Tokyo Institute of Technology. I would thank Assistant Professor Kazuki Horikoshi as well. His constructive suggestions on the experimental apparatus and innovative ideas on the theoretical framework encouraged me during my study.

Mr. Sakea Seki, technician of the department, deserves credit for his help in maintaining and developing the experimental apparatus.

The Geotechnical Engineering Group at Tokyo institute of Technology is the kind of place where everyone helps everyone, so I say with confidence that all my colleagues have contributed in some measure to my efforts. Special gratitude goes to Dr. Lin Ke for teaching me to do laboratory tests, and Mr. Yang Li, Mr. Partha Saha, to name a few, for helping me on my research.

I acknowledge the Ministry of Education, Culture, Sports, Science and Technology, Japan (MEXT) for granting me a Monbukagakusho scholarship.

I come finally to my dear family, my parents – Mr. Guoyi Ouyang and Mrs. Fengping Hu, who continue to support, encourage, and love me, even when I meet with frustrations. The completion of this work dedicates to their most expressive and unconditional love.

Contents

1 Introduction **1**

1.1 Background . . . 1
1.2 Objectives . . . 2
1.3 Organization of the dissertation . . . 2

2 Literature review **5**

2.1 Introduction . . . 5
2.2 Influence of internal erosion on hydro-mechanical behaviors . . . 6
2.2.1 Assessment of internal instability . . . 6
2.2.2 Experimental investigations of internal erosion . . . 12
2.2.3 Theoretical and numerical modeling of internal erosion . . . 26
2.3 Experimental apparatus on internal erosion . . . 30
2.3.1 Internal stability tests . . . 30
2.3.2 Element test on internal erosion . . . 36
2.4 Image analysis on internal erosion . . . 42
2.5 Soil mechanics in triaxial and plane strain tests . . . 46
2.5.1 Stiffness of element test . . . 47
2.5.2 Soil strength of element test . . . 48
2.6 Summary . . . 52

3 Undrained behaviors of soils subjected to internal erosion by triaxial erosion tests **53**

3.1 Introduction . . . 53
3.2 Experimental program . . . 55
3.2.1 Tested materials . . . 55
3.2.2 Test apparatus . . . 55
3.2.3 Test procedures . . . 58
3.3 Test results . . . 59
3.3.1 Seepage test results . . . 59
3.3.2 Undrained compression test results . . . 66

3.4 Discussion . . . 68
3.4.1 Undrained peak state . . . 68
3.4.2 Quasi-steady state . . . 72
3.4.3 Phase transformation state . . . 76
3.4.4 Critical state . . . 77
3.4.5 Relation between key states . . . 78
3.5 Summary . . . 82

4 Optical quantification of internal erosion in plain strain physical models 83
4.1 Introduction . . . 83
4.2 Quantification of morphology of siliceous sand . . . 84
4.2.1 Aspect ratio . . . 87
4.2.2 Convexity . . . 88
4.2.3 Sphericity . . . 88
4.3 Experimental setup . . . 89
4.4 Test results and discussion . . . 92
4.4.1 Cumulative eroded soil mass . . . 92
4.4.2 Fines transportation at onset of internal erosion . . . 93
4.4.3 preferred coarse particle orientation . . . 95
4.5 Summary . . . 98

5 Plane strain erosion apparatus equipped with visible window 99
5.1 Introduction . . . 99
5.2 Plane strain erosion apparatus . . . 100
5.2.1 General description . . . 100
5.2.2 Plane strain cell . . . 101
5.2.3 Seepage control unit . . . 106
5.2.4 Pressure control unit . . . 109
5.2.5 Data acquisition . . . 109
5.2.6 Camera calibration . . . 110
5.3 Summary . . . 110

6 Interpretation on mechanical responses of eroded soils through microscopic observation 113
6.1 Introduction . . . 113
6.2 Tested materials . . . 114
6.2.1 Materials description . . . 114
6.2.2 Specimen preparation . . . 116

6.3 Experimental procedure . . . 116
6.3.1 Saturation . . . 119
6.3.2 Consolidation . . . 120
6.3.3 Seepage tests . . . 120
6.3.4 Drained compression test . . . 122
6.3.5 Post analysis . . . 122
6.3.6 Test conditions . . . 122
6.4 Test results . . . 123
6.4.1 Verification of the preparation method . . . 123
6.4.2 Seepage test results . . . 125
6.4.3 Drained compression test results . . . 127
6.5 Discussions . . . 128
6.5.1 Effects of flow rate . . . 129
6.5.2 Spatial distribution of fines . . . 131
6.5.3 Normalized secant stiffness . . . 133
6.5.4 Drained soil strength . . . 133
6.6 Qualitative assessment of internal erosion . . . 137
6.6.1 Effects of fines content on undrained behavior . . . 143
6.6.2 Effects of internal erosion on undrained behavior . . . 143
6.7 Quantitative evaluation of internal erosion . . . 144
6.7.1 Hypotheses . . . 145
6.7.2 Contact area . . . 150
6.7.3 Interpretation on internal erosion of plane strain erosion tests . . . 157
6.7.4 Interpretation on internal erosion of triaxial erosion tests . . . 157
6.8 Summary . . . 159

7 Conclusions and recommendations **163**
7.1 Conclusions . . . 163
7.2 Recommendations . . . 166

Appendices **183**

A Discussion on "Influence of initial fines content on fabric of soils subjected on internal erosion" **183**

B Reply to the discussion by Ahmad ALsakran et al. on "Influence of initial fines content on fabric of soils subjected to internal erosion" **186**

List of Figures

2.1 Drained responses of suffusional specimen and reconstituted specimen (after Ke and Takahashi (2015)) . . . 15
2.2 The schematic dynamic of the physical model tests (after Horikoshi and Takahashi (2015b)) . . . 21
2.3 Summary of hydromechanical boundaries in stress-gradient space (after Moffat and Fannin (2011)) . . . 22
2.4 Test apparatus with 245 mm diameter cell (after Kenney and Lau (1985)) . . . 31
2.5 Test apparatus with 580 mm diameter cell (after Kenney and Lau (1985)) . . . 32
2.6 Sketch of apparatus used for hydraulic filter tests (after Kenney et al. (1985)) . . . 34
2.7 Sketch of apparatus used for dry vibration tests (after Kenney et al. (1985)) . . . 34
2.8 Continuing erosion test apparatus (after Foster and Fell (2001)) . . . 35
2.9 Slot erosion test apparatus (after Wan and Fell (2004b)) . . . 36
2.10 Hole erosion test apparatus (after Wan and Fell (2004b)) . . . 37
2.11 The photography of the plane strain apparatus (after Alshibli et al. (2004)) . . . 41

3.1 Schematic diagram of the characteristics of typical undrained behaviors (after Alarcon Guzman et al. (1988); Muir Wood (1990); Tsukamoto et al. (2009)) . . . 54
3.2 Particle size distribution curves . . . 56
3.3 Revised triaxial apparatus for seepage test . . . 57
3.4 Flow rate in seepage tests . . . 60
3.5 Measured back pressure during seepage tests . . . 60
3.6 Onset of internal erosion in soil with 25% initial fines content (25_WE_N1) . . . 62
3.7 Evolution of hydraulic gradient during seepage tests . . . 62
3.8 Evolution of hydraulic conductivity during seepage tests . . . 63
3.9 Evolution of cumulative eroded soil mass during seepage test . . . 65
3.10 Evolution of volumetric strain during seepage test . . . 65
3.11 Stress strain curves of soils without erosion . . . 67
3.12 Effective stress paths of soils without erosion . . . 67
3.13 Stress strain curves of soils with erosion . . . 69

3.14 Effective stress paths of soils with erosion . . . 69
3.15 Normalized peak strength against fines content before compression . . . 71
3.16 Mean effective stress ratios against fines content before compression . . . 71
3.17 Relation between normalized tangent stiffness and axial strain of soils without erosion 73
3.18 Relation between normalized tangent stiffness and axial strain of soils with erosion 73
3.19 Shear stress ratios at quasi-steady state against fines content before compression . . 75
3.20 Normalized residual strength against fines content before compression . . . 75
3.21 Flow potential against fines content before compression . . . 76
3.22 Movement of particle grading curves . . . 79
3.23 Critical states of tested specimens in $e - \log p'$ plane . . . 79
3.24 Relation of normalized shear stress at undrained peak state and quasi-steady state . 81
3.25 Slope difference against fines content before compression . . . 81

4.1 (a) Original image taken by microscope VCR-800; the spectrum of fines is obtained from the dash blocks, and the spectrum of coarse particles is obtained from the solid blocks. According to the spectrum distinction between the fines and coarse particles, they can be segmented from the original image and is shown in (b) segmented image, where the black areas represent the fines; and the gray areas represent the coarse particles; (c) outline of the coarse particles by watershed algorithm; (d) illustration of preferred coarse particles orientation, and aspect ratio which is the ratio of the minimum distance to the maximum distance between two parallel tangential lines restricting the particle . . . 85
4.2 (a) Test apparatus equipped with the digital microscope VCR-800; (b) photos of tested sand with difference colors, including white, blue, black, red, green and yellow 86
4.3 Process of image analysis . . . 86
4.4 Definitions of considered particle morphologies . . . 87
4.5 Aspect ratio and its normalized value of silica no. 8 . . . 88
4.6 Convexity and its normalized value of silica no. 8 . . . 90
4.7 Sphericity and its normalized value of silica no. 8 . . . 90
4.8 Particle size distributions . . . 91
4.9 Schematic illustration of seepage test apparatus . . . 91
4.10 Cumulative eroded soil mass obtained from experiment and image segmentation . . 93
4.11 Deviation between cumulative eroded soil mass from image analysis and independent macroscopic observations against number of images used (15% initial fines content) . . . 94
4.12 Relationship between hydraulic gradient and average flow velocity (15% initial fines content) . . . 94

4.13 Mobile portion and hydraulic gradient during the onset of internal erosion 96
4.14 Rose diagram representation of preferred coarse particle orientation of soil before and after internal erosion 96
4.15 Two selected images of specimen with 15% initial fines content taken at hydraulic gradient of 0.65 and 0.70: the dashed line represents the outline of a coarse particle at a hydraulic gradient of 0.65, while the solid line represents that at around 0.70 . 97

5.1 Photograph of the main part of plane strain erosion apparatus 102
5.2 Schematic diagram of plane strain erosion apparatus 103
5.3 Layout of the plane strain cell (top view) 104
5.4 Revised pedestal in plane strain cell 104
5.5 Top cap in plane strain cell 105
5.6 The front transparent window in plane strain cell 105
5.7 The back plate in plane strain cell 107
5.8 Earth pressure transducer BED-A-500 (Kyowa Electronic Instrument Co. Ltd.) . . 107
5.9 Two water bladders in the plane strain cell 108
5.10 The transparent membrane employed in the plane strain cell 108
5.11 Procedure of camera calibration: (a) original image recorded by VCR-800; (b) illustration of distortions; (c) centroids of control points for camera calibration; (d) calibrated image 111

6.1 Microscopic images of silica no. 3 and colored silica no. 8 114
6.2 Comparison of size distribution data for silica no. 3 117
6.3 Comparison of size distribution data for original silica no. 8 117
6.4 Comparison of size distribution data for colored silica no. 8 118
6.5 Undercompaction criterion 118
6.6 Specimen preparation by non-linear undercompaction criterion 121
6.7 Flow rate in seepage test 121
6.8 Height of each layer in verification of the preparation method 124
6.9 Distribution of planar void ratio along the length of the specimen 124
6.10 Evolution of cumulative eroded soil mass during seepage test 126
6.11 Evolution of normal stress in direction of plane strain during seepage test 127
6.12 Relation of axial strain and volumetric strain 128
6.13 Relation of axial strain and deviator stress 129
6.14 Relationship between flow rate and normalized cumulative eroded soil mass 130
6.15 Relationship between flow rate and normalized normal stress in direction of plane strain 130
6.16 Particles sizes distribution curves of eroded soils 132

6.17 Illustration of the divided parts in the specimen . . . 134
6.18 Fines distributions in the top, middle and bottom layers . . . 135
6.19 Fins distribution in the divided parts with different boundary conditions . . . 135
6.20 Deviator stress at small strain level . . . 136
6.21 Demonstration of the derivation of secant stiffness . . . 136
6.22 Normalized secant stiffness at small strain level . . . 137
6.23 Normalized drained soil strength against fines content before compression test . . . 138
6.24 Apparatus for seepage tests . . . 139
6.25 Microstructure of soils before erosion; initial fines content: (a) 0%; (b) 15%; (c) 25%; (d) 35% . . . 141
6.26 Microstructure of soils after erosion; initial fines content: (a) 15%; (b) 25%; (c) 35% 142
6.27 Microscopic image taken before compression for soils without erosion . . . 146
6.28 Demonstration of the fines and coarse particles based on the microscopic observation 146
6.29 Brief review of the procedures in plane strain erosion tests . . . 147
6.30 The microstructure of soils with erosion in the key states . . . 148
6.31 The microstructure of soils without erosion in the key states . . . 148
6.32 The microstructure at small strain level for soils with and without erosion . . . 149
6.33 The microstructure at medium strain level for soils with and without erosion . . . 150
6.34 Definition of contact area at both densest and loosest states . . . 151
6.35 Influential factors of contact area . . . 151
6.36 Contact area distribution curves . . . 152
6.37 The 3D configuration of contact area in densest state . . . 154
6.38 The 3D configuration of contact area in loosest state . . . 154
6.39 Original image recorded by microscope VCR-800 . . . 155
6.40 Draw the contact area on the original image . . . 155
6.41 Calculate the fines percentage in the contact areas . . . 156
6.42 The relation between the contact points and the percentage of fines in contact area . 158
6.43 The normalized percentage of fines in contact area at both small strain and medium strain levels . . . 158
6.44 The stress strain curves of soils without erosion under undrained conditions . . . 160
6.45 The stress strain curves of soils with erosion under undrained conditions . . . 160

B.1 Particle size distributions and constriction size distributions . . . 188

List of Tables

2.1 Extended criterion for different types of soil 10

3.1 Properties of tested materials 56
3.2 Seepage test results 64
3.3 Undrained compression test results of soils without erosion 66
3.4 Undrained compression test results of soils with erosion 68
3.5 Information about reference data 72

4.1 Summary of test results 92

5.1 Calibration and regression characteristics of transducers 110

6.1 Shape of siliceous sands by Microscope and QICPIC 116
6.2 Properties of tested materials 119
6.3 Test conditions 123
6.4 Quantitative assessment of the specimen homogeneity 125
6.5 Seepage test results 126
6.6 Drained compression test results 127

Nomenclature

$\mathbf{n}$	unit vector
Δ	vector magnitude
γ'	submerged unit weight of the material
γ_w	unit weight of water
ϕ_k	inclination of unit vector
ϕ_s	angle of shearing resistance at quasi steady state
τ_c	critical erosive shear stress
ε_v	volumetric strain
b	fitting factor
C_c	curvature coefficient
C_u	coefficient of uniformity
CA_c	contact area for a given value of percent smaller P
CA_d	contact area in the densest state
CA_l	contact area in the loosest state
D	diameter of particle
d_0	average pore diameter of the coarse fraction
D_c^*	controlling constriction size
D_m	mean filter particle size
D_{15}	sieve size for the particles 15% pasing by weight in the coarse fraction

d_{15} sieve size for the particles 15% pasing by weight

D_{50} median grain size

d_{50} median particle size

d_{60} sieve size for the particles 60% pasing by weight

d_{85SA} the size of 85% passing by weight in fines fraction considering the surface area

d_{85} sieve size for the particles 85% pasing by weight in the fines fraction

d_{90} sieve size for the particles 90% pasing by weight

D_{c35} the size of 35% filter constriction size finer

D_{c95} the size of 95% filter constriction size finer

e void ratio

e_0 initial void ratio

e_c void ratio after consolidation

e_e void ratio after seepage test

e_l void ratio of loose finer particles

e_s skeleton void ratio

e_x void ratio of primary skeleton

e_{cs} intergranular void ratio after consolidation (before seepage test)

e_{es} intergranular void ratio after seepage test

$e_{max,HF}$ maximum void ratio of fine grains

e_{max} maximum void ratio

e_{min} minimum void ratio

F percentage of particles finer than D

F_{ce} fines content after seepage test

Fc fines content

FC_{max} maximum value of fines content

FC_{th} threshold boundary of fines content

G_r gap ratio

H percentage of particles between D and $4D$

i hydraulic gradient

i_{max} maximum hydraulic gradient

k hydraulic conductivity

K_d coefficient of erodibility

M_{qss} shear stress ratio at quasi steady state

N total number of particles

n porosity of specimen

P probability of internal instability

p chosen percentage of a contact area

p'_0 initial mean effective stress

p'_{pts} mean effective stress at the phase transformation state

p'_{qss} mean effective stress at the quasi steady state

PI plastic index

q unit flux

q_{15} deviator stress at 15% axial strain

q_{qss} deviator stress at quasi steady state

q_{ups} deviator stress at undrained peak state

R' hydrodynamic number

Rd relative density

s_d drained soil strength

s_p	undrained peak strength
s_{us}	residual strength
u_f	flow potential
v	kinematic viscosity of water
W_c	weight of the primary skeleton grains
$W_{l,max}$	maximum weight of fine soil grains
x_5	5% grain size of the tested materials
CSD	constriction size distribution
DEM	discrete element method
PIV	particle image velocimetry
PSD	particle size distribution

Chapter 1

Introduction

1.1 Background

Internal erosion is a versatile term in describing the phenomenon that the finer soil particles within the body of natural deposit or earth structure were detached and moved away by the seepage flow. Its influence could be interpreted from the view points of macro scale and micro scale. From the view of macro scale, internal erosion would cause the fines dislodgement away from the geotechnical structure, deformation of soils volume and alternation of hydraulic conductivity. From the view of micro scale, internal erosion might lead to the transportation and local accumulation of fines in the voids among coarse particles, the mobilization of the position of fines and coarse particles, and the alternation of shape and volume of voids.

Significant damages due to internal erosion were studied by Muir Wood (2007); Richards and Reddy (2007); Foster et al. (2000). Muir Wood (2007) reported that two large sinkholes were observed at the crest of the W.A.C Bennett Dam in British Columbia, Canada, where were assumed to be formed by internal erosion. The sinkholes were found to be huge threats for the dam safety. Foster et al. (2000); Richards and Reddy (2007) reviewed the dam failures in recent years, and concluded that nearly half of the world's earth dam failure was caused by internal erosion. It could be noted that the internal erosion could lead to the deterioration of geotechnical structures. However, whether the internal erosion could affect the mechanical behavior of soils, and how does the internal erosion affect the mechanical behavior of soils, are still not fully understood. A clear and explicit explanation on the soils fabric change caused by the internal erosion could be helpful for the practical geotechnical engineering projects.

1.2 Objectives

To answer the above mentioned two questions, the experimental investigation and microscopic observation on cohesionless soils subjected to internal erosion were carried out. The objectives of this research presented in this dissertation are:

1. To demonstrate the difference of mechanical behaviors of soil with and without internal erosion experimentally. The mechanical responses of eroded soils under undrained triaxial and drained plane strain conditions were assessed to reach this end.
   During the earthquake, the pore water cannot be drained during a relative short period, which caused an increase of pore water pressure at constant volume. This corresponds to the stress path under undrained conditions in geotechnical engineering. Therefore, the undrained compression tests were performed in triaxial apparatus to investigate the mechanical responses of eroded soil during earthquake.
   On the other hand, in order to microscopically observe the particles movements during the erosion and compression tests, a flat transparent window was fabricated in the equipment. It restricted the soils deformation to the direction of transparent window, thus, the seepage and subsequent compression tests were conducted in plane strain conditions. In addition, the embankments, dams, and levees, are usually assumed to be subjected to the plane strain conditions. The failure of these hydraulic structures maybe mainly because that the internal erosion occurred due to seepage flow lasted for a relatively long period, during which the pore water pressure could be dissipated. It corresponds to the stress path under drained condition in geotechnical engineering. The drained compression tests were then conducted on cohesionless soils under plane strain conditions.

2. To evaluate the change of physical and mechanical behaviors of cohesionless soils as a consequence of internal erosion quantitatively. The physical model tests were performed to optically quantify the characteristics of internal erosion so as to realize this target.

3. To understand the mechanisms for the different mechanical responses between soils with and without internal erosion. To achieve this objective, a plane strain erosion apparatus equipped with visible window was developed to examine the fabric change due to internal erosion. Moreover, macro scale consequence of internal erosion was interpreted from the micro scale observation.

1.3 Organization of the dissertation

This dissertation consists of seven chapters.

Chapter 1: *Introduction* – includes the background, objectives of this research, and an organization of the dissertation.

Chapter 2: *Literature review* – presents the current research related to this research. The review mainly focuses on fours parts: (1) the influence of internal erosion on hydro-mechanical behaviors; (2) experimental apparatus for internal erosion test; (3) image analysis on internal erosion; and (4) the soil mechanics in triaxial and plane strain tests.

Chapter 3: *Undrained behaviors of soils subjected to internal erosion by triaxial erosion tests* – a series of undrained compression tests were performed in a revised triaxial apparatus on specimens containing different initial fines contents. The influence of initial fines content and the internal erosion on soils undrained behaviors is examined. The test results are discussed in terms of undrained peak strength, normalized tangent stiffness at small strain level, residual strength and critical state lines. The relations between these key states are also presented in this chapter.

Chapter 4: *Optical quantification of internal erosion in plane strain physical models* – upward seepage tests were performed, and a series of images was recorded by a microscope during the testing. The approach for optical quantifying the characteristic of internal erosion is proposed. The applicability of the proposed method is demonstrated. Subsequently, the image analysis is employed to discuss the fines mobilization during the internal erosion and the fabric change caused by the internal erosion.

Chapter 5: *Development of plane strain erosion apparatus equipped with visible window* – describes the newly developed plane strain erosion apparatus equipped with visible window. The three components: plane strain cell, seepage flow unit and pressure control unit are elaborated in details. The data acquisition and camera calibration by using this apparatus are depicted in order as well.

Chapter 6: *Interpretation on mechanical responses of eroded soils through microscopic observation* – shows the results of the plane strain erosion tests. The influence of internal erosion on mechanical behavior of soils under plane strain conditions is examined. The normalized secant stiffness and drained soils strength are discussed. The effects of internal erosion are qualitatively assessed from the microscopic images taken in the upward seepage tests. Based on the images recorded in the plane strain erosion apparatus, the influence of internal erosion is quantitatively interpreted with respect to the mechanical behaviors at both small strain and medium strain levels.

Chapter 7: *Conclusions and recommendations* – includes a summary of the dissertation and its findings, together with the further recommendations.

Chapter 2

Literature review

2.1 Introduction

Internal erosion is defined as the subsequent transport of detached finer particles through the matrix under seepage flow. It is a common cause of accidents, but is not by itself likely to lead to failure, whereas, the alternation of fabric might count (Foster et al., 2000; Takahashi, 2016). Internal erosion could cause the migration of fines from the coarse skeleton, deformation of volume and change of permeability. The research of internal erosion starts from the study on the effectiveness of filters (Aberg, 1993). Subsequently, many investigations on the initiation hydraulic gradient, critical hydraulic gradient and instability criterion have been performed (Skempton and Brogan, 1994; Aydilek et al., 2005; Fannin, 2008; Fell et al., 2003; Sibille et al., 2015b). Some apparatus were also developed to examine the influence of internal erosion on soils hydraulic behaviors and mechanical responses (Chang and Zhang, 2011; Horikoshi and Takahashi, 2015b; Ke and Takahashi, 2014b). By employing the developed equipments, the drained, undrained and cyclic behaviors of soils subjected to internal erosion were elaborated. Considering that the soils vulnerable to internal erosion always contain a certain amount of fines, many triaxial and plane strain tests were performed on these soil mixtures in order to investigate the effects of fines on their mechanical consequences (Abedi and Yasrobi, 2010; Ishihara, 1993; Murthy et al., 2007; Ni et al., 2004; Yamamuro and Covert, 2001).

With the rapid development of computer vision technique, the image analysis techniques were improved and employed in the research on geotechnical engineering (Take, 2015; White et al., 2003; Arshad et al., 2014). The Particle Image Velocimetry (PIV) was proposed to study the deformation of geotechnical materials. Image subtraction method was utilized to investigate the transportation of fines induced by internal erosion (Rosenbrand and Dijkstra, 2012). Through the aid from the image analysis, the microscopic fabric change due to internal erosion could be presented.

This chapter consists of the literature reviews on four subsections: (1) influence of internal erosion on hydro-mechanical behaviors; (2) experimental apparatus on internal erosion; (3) image analysis on geotechnical engineering; and (4) soil mechanics in triaxial and plane strain tests.

2.2 Influence of internal erosion on hydro-mechanical behaviors

To investigate the effects of internal erosion on soils hydraulic and mechanical behaviors, the internal instability was firstly examined. The internal instability based on filtration design was evaluated by Foster and Fell (2001); Lafleur et al. (1989); Sherard et al. (1984); Sherard and Dunnigan (1989). Kenney et al. (1985) proposed the conception of constriction size, which is defined as the diameter of the largest sphere that will pass through a particular constriction. Then the research of internal instability was focused on the constriction size of specimens (Shire and O'Sullivan, 2013; Wan and Fell, 2008; Indraratna et al., 2007; Taylor et al., 2015). However, to justify the internal instability of soil materials cannot provide the information for the mechanical behaviors of soils subjected to internal erosion, a serious of experiments were performed on soils to examine the mechanical consequences (Ke and Takahashi, 2014a, 2015; Richards and Reddy, 2012; Moffat et al., 2011; Correia Dos Santos et al., 2015; Planés et al., 2016). As per the experiments results, some theoretical modeling and numerical simulation were proposed to interpret the conseqences of internal erosion with different parameters (Sibille et al., 2015a; Bonelli and Marot, 2011; Sterpi, 2003; Cividini et al., 2009; Hicher, 2013).

The review on the influence of internal erosion on hydro-mechanical behaviors consists of three parts: (i) assessment of internal instability; (ii) experimental investigations on internal erosion; and (iii) theoretical and numerical modeling of internal erosion.

2.2.1 Assessment of internal instability

According to Kenney and Lau (1985), the transportation of coarse particles can be characterized by means of a dimensionless hydrodynamic number, $R' = qx_5/nv$; where q is the unit flux (discharge rate divided by total cross sectional area), x_5 is the 5% grain size of the tested materials, n is the porosity of the material, and v is the kinematic viscosity of water. It was suggested that a minimum value of $R' = 10$ was required in order to obtain washout of the largest grains that could be washed out according to the geometric configuration.

Aberg (1993) performed seepage tests in a permeameter with the diameter of 190 mm. A 125mm thick layer of a test material, consisting of sand and gravel, was placed on top of a square mesh screen, the aperture of which varied between different tests. The tested materials was prepared by means of a procedure and compaction effort corresponding to the modified proctor method. The test material was then loaded by an about 400-mm-thick layer of 30-50 mm pebbles placed on a flexible metal cloth with 1.5 mm mesh size. The flow of water was directed downward. The total drop of head in the permeameter was 2.7 m (water head). The permeameter could be mildly vibrated by means of a vibrator, which was fastened to it. The test results confirmed that small hydrodynamic numbers reduced the amount of washout particles. There are two reasons for grading instability: scantiness of intermediate grain size, which interrupts the filter formation process during washout; and loose grains, which can move over large distances through the void space between fixed grains. The results revealed that for hydrodynamic numbers, $R' < 15$ or 20, the washout of grains was significantly small. Besides grain and pore geometry, the hydraulic conditions within the material then also had a deciding influence on the extent of the washout.

The controlling constriction size D_c^* was defined as a size characteristic of the void network in a granular filter and was equal to the diameter of largest particle that can possibly be transported through the filter by seepage flow (Kenney et al., 1985). It also describes the minimum size of particle that will be stopped by the filter under even the most severe hydraulic conditions, and therefore, the minimum size of particle required to initiate filtration. It was determined that D_c^* and filter performance were only slightly influenced by width of gradation and thickness of the filter. However, filter performance was found to be strongly influenced by hydrodynamic conditions within the filter. It was concluded that the concept of controlling constriction size is helpful in the design of geotechnical filters, particularly because it focuses on the sizes of base particles that must be brought to the filter in order to initiate filtration.

Vincens et al. (2015) presented a review on the approaches to determine the constriction size distribution for understanding filtration phenomena in granular materials. It was noted that the cumulative Constriction Size Distribution (CSD) was physically the key property that qualifies the soils retention capability as like a spatial acting sieve. The constrictions were defined as the narrowest sections of channels between larger volume (pores) within the pore network of granular materials, and they were the main obstacles for a small particle to overcome when flowing along pathways. Three approaches were used to determine the constrictions, i.e., experimental, numerical, and analytical models. It was noted that for uniformly graded soils with mainly rounded particles, the analytical approaches could be a promising method to calculate the CSD and combined the result with a quantitative assessment of filter capability. However, for naturally shaped grains, the analytical methods need to be qualified and further on adapted to consider the influence of

angularity and elongation. Finally, the challenging work was proposed to extend the procedures of calculating CSD to substantially non-uniform soils to consider the effects of heterogeneity in both grain skeleton and pore structure.

Shire and O'Sullivan (2013) presented microscale analysis of samples with various instability states by Discrete Element Method (DEM). Idealized samples with isotropic fabric and spherical particles were considered; these idealizations allowed the influence of the Particle Size Distributions (PSD) on the internal topology of the material to be isolated. Periodic boundaries were used to minimize boundary effects and achieve computational efficiency. The results confirmed that the internally unstable soils have a larger number of loose fines. The average connectivity or coordinate number reduced with reducing internal stability. The large numbers of loose, fine particles in highly internally unstable soils dominate the coordinate number values. The volume weighted coordination number, which accounts for the loose fines, also tended to increase in value with increasing stability. The materials considered were mainly gap-graded, and the results indicated that a reduction in gap ratio led to a more stable fabric. The conception of critical fines content, which is large enough to facilitate an internal stable fabric that fines participate in load transmission was proposed by Kenney and Lau (1985). This phenomenon was observed in the simulation, which supported the conception of critical fines content. The "coarse matrix, loose fines" fabric shown in the unstable gradings was a prerequisite for internal instability. It was concluded that for a soil that is internal unstable, should have constrictions that are large enough to allow fine particle to pass through.

Wan and Fell (2008) performed a series of laboratory seepage tests with constant water head on internally unstable soils. Improved procedures for predicting the internal instability of sand gravel soils with silty and clayey fines based on particle size distributions were proposed based on $d_{90}/d_{60}(h\prime)$ and $d_{90}/d_{15}(h\prime\prime)$ ratios where d_{90}, d_{60} and d_{15} are the sieve size for which 90%, 60% and 15% passing by weight. The probability of internal instability P was given by:

$$P = exp(Z)/[1 - exp(Z)] \tag{2.1}$$

$$Z = 2.378\log(h\prime\prime) - 3.648h\prime + 3.071 \tag{2.2}$$

$$Z = 3.875\log(h\prime\prime) - 3.591h\prime + 2.436 \tag{2.3}$$

It was concluded that the widely used methods to assess the internal instability were conservative, while the proposed method could give a better evaluation. However, for the gap-graded soils, it was not adequately to assess the internal instability by the proposed approach.

Li and Fannin (2008) compared the Kenney and Lau method with Kezdi criterion to assess the internal stability of cohesionless soils. These two methods are predicated on a similar approach

that involves quantifying the shape of particle size distribution curve over a defined interval, but differ in how that interval is determined. Kezdi (1979) proposed that $D_{15}/d_{85} > 4.0$ in PSD could be internal unstable, where D_{15} and d_{85} represent the diameter of 15% and 85% passing by weight in coarse and fines fraction, respectively. Kenney and Lau method for instability can be expressed as "the slope is flatter than $F\%$ per four times change in grain size" (Kenney and Lau, 1985), where F is the percentage of particles with diameter smaller than D; H represents the percent of fraction between D and $4D$. In the evaluation of gap-graded soils, the Kezdi method proves to be relatively more successful in distinguishing between stable and unstable gradations. In the evaluation of widely graded soils, the Kenney and Lau method proves to be relatively more successful. However, applying the Kezdi method to the point on the curve deemed most critical by the Kenney and Lau method causes it to be equally successful in distinguishing between stable and unstable gradations. Comparison indicates that the filter ratio (D_{15}/d_{85}) of Kezdi method is relatively more conservative for $F < 15\%$, and the stability index $(H/F)_{\min}$ of Kenney and Lau method is more conservative for $F > 15\%$.

A simplified Kovacs method was then proposed by Li and Fannin (2013) based on the Kovacs criterion. Kovacs (1981) noted a $d_0/d_{85} < 1$ to identify a soil that is not susceptible to internal instability, base on a characteristic grain size d_0 represents the average pore diameter of the coarse fraction and d_{85} represents the diameter of 85% pass by in the fines fraction. The threshold boundary for instability was established by the literatures as $d_0/d_{85} > 2.3$. The simplified Kovacs method was proposed by simply establishing the coarser fraction of a widely graded soil as that exceeding the stability index $(H/F)_{\min}$ of Kenney and Lau method.

Li and Fannin (2012) proposed a concept of a hydromechanical envelope to explain the onset of seepage induced instability in a cohesionless soil. The onset of instability was triggered by a critical value of hydraulic gradient that is found consistent with the observations of piping in uniform sand. The envelope takes the form of a linear relation that, for a particular soil, is governed by the proportion of effective stress in the finer fraction of soil particles.

Moffat and Herrera (2014) presented a theoretical model to determine the hydramechanical boundary of an internal unstable soils subjected to seepage flow. Based on the momentum balance equations, the materials were divided into three components: water, finer soil fraction and coarser soil fraction. The effective stress, porosity, friction angle between coarse and fines fraction and the proportion of effective stress transmitted by fines fraction were examined. It was reported that the effective stress and hydraulic gradient were the most important parameters to define the onset of internal instability. The model confirmed that the change of hydraulic gradient could result in a variation of mean vertical effective stress. The stress transmitted by fines fraction decreases as the value of

D_{15}/d_{85} increases. The reduction of stress transmitted by fines fraction followed the same trend as the critical hydraulic gradient reduction proposed by Skempton and Brogan (1994).

Chang and Zhang (2013b) summarized the criterion in estimating the soils internal instability. Based on the particles gradations, the soils were divided into well-graded soils and gap-graded soils. Gap ratio, G_r, is defined as the ratio of the maximum particle size, and the minimum particle size, of the severely under-represented portion in the particle size distribution. The extended internal stability criteria for soils under seepage flow was shown in Table. 2.1, as follows:

Table 2.1: Extended criterion for different types of soil

Gradation conditions	Fines content, $Fc(\%)$	Geometric criteria
Well-graded soils	$Fc < 5$	$(H/F)_{min} > 1.0$: internally stable
	$5 \leq Fc \leq 20$	$(H/F)_{min} > -(1/15)Fc + 4/3$: internally stable for low plasticity soils
	$Fc > 20$	Stable
Gap-graded soils	$Fc < 10$	$G_r < 3.0$: internally stable
	$10 \leq Fc \geq 35$	$G_r < 0.3Fc$: internally stable for medium plasticity soils
	$Fc > 35$	Stable

Indraratna and Vafai (1997) simulated the filtration process through a mathematical model, incorporating the hydraulic conditions and the relevant materials properties, such as porosity, density, friction angel, and shape and distribution of particles. The critical hydraulic gradient was employed to assume that the migration of particles was assumed to occur under applied hydraulic gradient exceeding the critical hydraulic gradient. The rate of erosion, and hence, the effectiveness of filter was quantified on the basis of the mass and momentum conservation theories. By dividing the base soil and filter domain into discrete elements, the evolution of the fines erosion and retention could be examined. The results from the mathematical model showed good agreements with the laboratory test results.

When the finer base particles penetrated to filters, the constrictions in filters could retain the base materials and form a self-filtration layer. Indraratna and Raut (2006) noted that the base particles larger than the constriction size D_{c95} do not influence the process of self-filtration because they do not penetrate the filter, where D_{c95} is denoted by the size of 95% filter constriction size finer. Therefore, it was proposed that the constriction size D_{c95} is a reasonable cutoff value, and the base soil particle size distribution modified accordingly could be more realistic in the analysis of

filtration.

Indraratna et al. (2007) presented a constriction based retention criterion for granular filter design. In filter materials, it is the constriction size rather than the particle size that influence the filtration process. It was reported that the controlling constriction size could be represented by D_{c35}, which means the size of 35% passing by in the constriction size distribution. Moreover, by surface area consideration of base soil, d_{85SA} was found to be a more appropriate representative parameter compared to the conventional d_{85} by mass. It was demonstrated that the proposed criterion, $D_{c35}/d_{85SA} < 1$, for identifying effective filters was more realistic, whereby the size of prescribed fines size d_{85SA} could be directly compared with the controlling constriction size of filters D_{c35}. Another advantages of employing the approach was that it considered the uniformity coefficient of particle size distribution, as well as the relative density. It could be also used to estimate the thickness of filter materials, the experiments results demonstrated that $225D_m$ (D_m is the mean filter particle size) could be regarded as a reasonable approximation.

Followed by the research on constriction size model, Indraratna et al. (2008) wrote a review article on the granular dam filter behaviors – from particle size to constriction based design criteria. It was pointed out that the constriction based analysis of filter behaviors could be employed in both uniform and well-graded base soils. The D_{c95} model provided a more rational and rigorous procedure for filter design by eliminating the obvious limitations of conventional particle size criteria based on the D_{15}/d_{85} ratio alone. Meanwhile, the D_{c35} model for identifying the effectiveness of filter is more realistic. However, the above models were proposed based on the cohesionless soils, for the models on cohesive soils is the future work. Based on the constriction size distribution, the hydraulic conductivity could also be estimated, and presented by Indraratna et al. (2012).

Later the constriction based design criteria was extended to assess the potential of internal erosion of granular soils by Indraratna et al. (2011). It was proposed that if $D_{c35}/d_{85} > 0.82$, the soils can be considered as potentially internal unstable. If $D_{c35}/d_{85} < 0.73$, the soils can be judged as internally stable. If the ratio of a given soil falls within the transition zone, further laboratory testing is required.

Indraratna et al. (2015) further performed more experiments and examined more previous data, accordingly, the assessment of internal instability based on constriction size was revised. Based on the particle size, the soil materials can be divided into coarse and fine fraction. The soil would be internally stable if

$$\frac{D_{c35}}{d_{85SA}} \leq 1 \tag{2.4}$$

It was demonstrated that this approach could give better evaluation of soils vulnerability to internal erosion.

There are many other researches related to the assessment of internal erosion. Taylor et al. (2015) proposed a new method in identifying the void constrictions based on the micro-CT images of sand. Lone et al. (2005) employed similar constriction size concept, and characterized the controlling size of filter materials. It was recommended to design the filter for graded cohesionless soils. The theoretical constriction size model was numerically modeled based on the probability of fines transportation model by To et al. (2016) to assess the internal instability. The numerical simulation revealed that the calculation based on constriction size was more realistic than the evaluation only based on the particle size distribution. Reboul et al. (2010) proposed a computational procedure in assessing the distribution of constriction size for granular materials. A two parameter model was proposed to obtain the constriction size distribution of gap-graded soils with certain relative density. A constriction size model, was also proposed, and evaluated by experimental results by Moraci et al. (2012). Later, Moraci et al. (2014) analyzed the internal stability of granular soil by different methods.

2.2.2 Experimental investigations of internal erosion

The flexible wall permeameter offers the potential for more complete control over stresses that act on soil specimen, and is better suited for minimizing side wall leakage. Bendahmane et al. (2008) developed a device to allow flows through the samples within the cells. So as to avoid all unwanted disturbances on the samples, saturation, consolidation, hydraulic and mechanical test stages were carried out inside the test cell without deconfining samples. The detection of erosion in the effluent was performed using optical aids and by weighting the amount of grains in the eroded fluid. In order to study the very beginning of internal erosion, to detect the possible initiation point, and to carry out real-time measurements of the eroded clay quantity, a photo sensor had been developed. The method had been validated through confirmation of the size distribution homogeneity achieved after mixing. By employing the developed apparatus, the mixtures of kaolinite content of 5%, 10%, 20% and 30% were performed under the hydraulic gradient ranging between 5 and 160 m/m, and isotropic confining pressure of 100 kPa, 150 kPa, 200 kPa and 250 kPa. The test results revealed that from the beginning of the test, the mass flow given by the optical sensor increased until reaching a maximum value. It then decreased sharply, to finally end with an asymptotic behavior toward zero. The tests showed that the higher the hydraulic gradient, the larger the mass of eroded clay. The tests showed that , depending on the hydraulic gradient, the erosion of the soils studied decreases as a function of the clay content. The erosion rate doubled when the clay content changes from 20 % to 10%. When

the kaolinite content increases, the initial permeability decreases, causing the global flow within the sample to be falling. When the velocity decreases, the hydraulic shear stress generated by the flow within the samples also decreases, and contributes to increase the internal erosion resistance. The maximum erosion rate decreased when the specimen was subjected to a larger confining pressure. The growth in the confining pressure and, therefore, in the material consolidation increases the interparticulate contact bonds and intensifies the internal erosion resistance. When the hydraulic gradient increases above a secondary threshold value, the erosion of sand grains is suddenly initiated and evolves very quickly as particle backward erosion, causing the whole sample to collapse.

Chang et al. (2011) investigated the erodibility of two landslide dams triggered by earthquake. It was noted that both the density and erosion resistance of soil increase with the depth of deposition. The coefficient of erodibility exponentially increases with the void ratio or decreases with the relative compaction. For the broadly graded landslide deposits, compaction plays a very import role in controlling soil erodibility. Increasing compaction efforts will increase the interlocking of soil particles, change the particles orientation, and enhance the formation of clusters. All these increase the shear strength of soils. Due to the increase of shear strength, the erosion resistance of the deposits will be enhanced. The prediction of the coefficient of erodibility and critical erosion shear stress were also proposed according to the empirical experimental data.

$$K_d = 20.075 e^{4.77} C_u^{-0.76} \tag{2.5}$$

where K_d is the coefficient of erodibility; e is the void ratio; and C_u is the coefficient of uniformity. It can be seen that the coefficient of erodibility increases with increasing void ratio and decreasing coefficient of uniformity.

$$\tau_c = 6.8(PI)^{1.68} Fc^{-1.73} e^{-0.97} \tag{2.6}$$

where τ_c is the critical erosive shear stress; PI is the plasticity index; Fc is the fines content and e is the void ratio. It can be seen that the critical erosive shear stress increases with increasing plasticity index, decreasing void ratio, and decreasing fines content.

Chang and Zhang (2011) developed a stress controlled erosion apparatus for studying internal erosion in soils. Subsequently, critical hydraulic gradients of internal erosion under complex stress states were investigated (Chang and Zhang, 2013a). It was suggested that the entire internal erosion process can be divided into four phases: stable, initiation, development, and failure. In the stable phase, there is no visible soil erosion and deformation. In the initiation phase, there is some loss of fine particles and a slight increase in permeability, but no significant soil deformation occurs. In the development phase, sudden increases in eroded mass, permeability, and deformation occur. In the failure phase, the soil experiences shear failure due to excessive loss of fine particles and seepage-induced stress changes. The soil permeability first increases suddenly and then decreases

gradually during the development phase. The increase of soil permeability is a result of the enlargement of the pores induced by the migration of fine particles. The subsequent decrease would be caused by the fact that some eroded fine particles are captured in the lower part, which induces clogging of the constrictions among coarse particles. Another reason for the subsequent decrease of soil permeability could be the local collapse of the soil skeleton. Corresponding to the four phases of internal erosion, there critical hydraulic gradients are defined: initiation, skeleton deformation, and failure hydraulic gradients. The initiation hydraulic gradient is mainly controlled by the pore structure of the soil. The skeleton-deformation hydraulic gradient is associated with buckling of the strong force chains within the soil due to lateral support by the fine particles. The failure hydraulic gradient depends on the initial stress state, the applied seepage forces, and the shear strength of the soil. Given the same porosity, the soil under triaxial extension stress conditions has higher initiation hydraulic gradients than those under triaxial compression stress conditions. It can be explained by that the vertically elongated pores were formed in the triaxial compression tests, whereas the horizontally elongated pores were developed in the triaxial extension tests. The skeleton-deformation hydraulic gradients under isotropic stress conditions are much larger than those under compression or extension stress conditions. This is because the buckling potential of the strong force chains in the soil is much lower for the tests under isotropic stress conditions. Stress dependent critical hydraulic gradients should be incorporated in engineering practice, because soils in the core and filters of zoned dams are typically under complex stress conditions.

The drained mechanical consequences of internal erosion on cohesionless soils were investigated by Ke and Takahashi (2015) as well. The soil mixtures containing silica no. 3 and silica no. 8 were used in their study. Silica no. 3 was regarded as coarse particles and form the skeleton of the specimen; silica no. 8 was treated as fines, which could be eroded away when subjected to certain seepage flow. Seepage tests were performed on those mixtures to create the internal erosion condition and drained compression tests were subsequently carried out to examine the mechanical behaviors. The test results of drained compression tests for the suffusional specimen and the reconstituted specimen are shown in Fig. 2.1. It was found that soil strength decreased after internal erosion, and the amount of drops became smaller when the soil was subjected to larger initial effective confining pressure. The volumetric strain for soils confined by a larger effective confining pressure was smaller than that for soils confined by a smaller effective confining pressure. Under the same initial effective confining pressure, the specimen with larger initial fines content indicated a larger amount of cumulative eroded soil mass in the seepage tests. At the subsequent compression test, is exhibited lower soil strength and secant stiffness. The tests suggested that internal erosion might create a distinct packing of soil particles, which might result from possible accumulation of fines at the spots where the constriction size – representing the size of pore channels in a soils – was smaller than that of fines. Those surviving fines after internal erosion might work as reinforcement

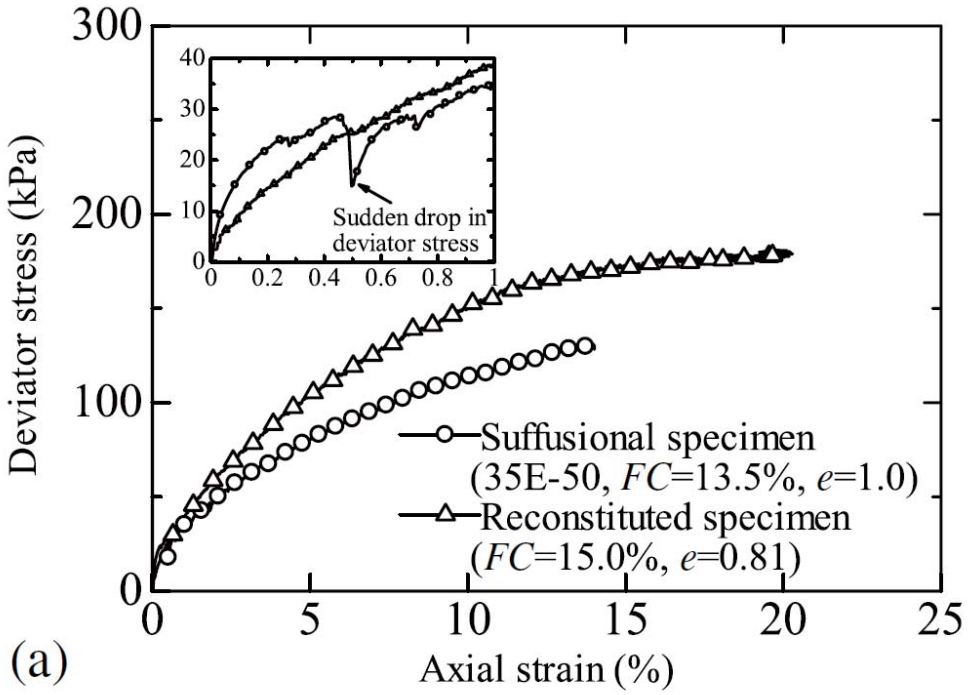

Figure 2.1: Drained responses of suffusional specimen and reconstituted specimen (after Ke and Takahashi (2015))

or jamming at the subsequent compression, resulting in a larger initial secant stiffness for the eroded soils.

Different from the particle size distributions, Chapuis et al. (1996) predicted the internal instability from the fines mobility criteria. It was proposed that even if filter criteria were met between adjacent soil layers, there may be a migration of fine particles of a soil within its own pore space. This problem was named as suffosion. The internal segregation of particles was evaluated by wet sieve analysis after dividing each sample into upper part, center part and lower part. The internal segregation was detected in the sample with slope of lower portion in particle size distribution equals 14%. It was demonstrated that segregation was severe when the sample was placed dry (vibratory table), but hardly detected when the sample was placed moist. Meanwhile, the moist compaction method was recommended for the internal instability tests because it gave negligible segregation and created less particle fragmentation than dry placed method. It was found that the permeability was changed for the sample prone to severe internal erosion. The vertical permeability increased in most of the samples, and fines started to accumulate at the bottom of sample when subjected to seepage flow. The influence of wet and dry placed condition on hydraulic conductivity was investigated. In the moist placed samples, the internal instability was less pronounced than in the dry placed samples.

In the dry placed base, all the head loss was concentrated between the last piezometer and the outer constant head water reservoir, taking place in the accumulated fines above the porous stone. Very small head losses occurred in the upper and central portions, and consequently the conductivities were high. The high values of hydraulic conductivity in the dry placed samples were related to the observed preferential seepage channels due to downward migration of fines.

The contact erosion at the interface between granular coarse soil and various base soils under tangential flow direction was investigated by Cyril et al. (2010). In their experiments, between the top of the coarse soil and the cell ceiling, there is a rubber bag connected to a pressurization system in order to apply a given vertical pressure aiming to reproduce the overburden pressure on size. The maximum pressure head difference between the upper water tank and the experiment outlet is about 3 m. Optical turbidity measurements are commonly used in studying particle transport. An infrared turbidimeter suing a four-beam pulsating technique was installed in the outlet to survey the variation in water turbidity and derive the solid transport rate, and a flow-meter to measure the water flow rate was installed. The test results revealed that the measured critical shear stress values were in the same order of magnitude as those measured from internal erosion test performed on various sand kaolinite mixtures. The erosion rate varies significantly with the fines type for a given coarse soil. It also proved that the erosion rate was not simply correlated to the critical shear stress. In order to better describe the effect of fines fraction, the effective critical velocity should be linked to the fines geometrical properties. Measured critical velocities were almost independent of the coarse fraction and it was highlighted that the velocity is a more convenient criteria than hydraulic gradient.

Fannin and Moffat (2006) observed the internal stability on cohesionless soils. The specimen was reconstituted by slurry mixing, under a vacuum, and deposited in the permeameter by hand placement using a spoon to yield a saturated homogeneous specimen, about 100 mm long. Accordingly, the fabric is believed more representative of a natural deposit than a compacted fill. Axial load was imposed to yield a vertical stress of 20 kPa on the top surface of the specimen by means of a perforated top plate. A conical trough directs particles that wash from the specimen to a flexible silicon hose; clamping the hose at intervals permits collection of a discrete sample and calculation of percentage loss of soil during reconstitution and each stage of test. Upon completion of testing, the specimen was excavated in three layers of equal thickness for grain size analysis of the top, middle and bottom portions respectively. Variables imposed in the program of testing were the opening size of the lower wire mesh screen and the duration of any imposed vibration. According to the results, it was found that a large amount of fines were eroded away prior to terminating the test, and was accompanied by a significant reduction in local hydraulic gradient, as preferential flow developed through a piped zone. The observations after the tests revealed that the loss occurred in a spatially preferential manner, with development of distinct zones through which flow was concentrated. The

particle size analysis after the seepage tests indicated that the more fines were transported from the top portion of the specimen than the middle and bottom. The results also suggested that the criterion provides for a conservative evaluation of the potential for instability of gap-graded soils, where unidirectional seepage occurs without vibration.

To clarify the distinction between suffusion and suffosion in internal erosion, Fannin and Slangen (2014) performed the review work on the definition of these two items. It was presented that experimental evidence suggests that the three variables of (i) a measured value of mass loss; (ii) a measured value of volume change; and (iii) a value of change in hydraulic conductivity, deduced from measurements of hydraulic gradient and flow rate, are sufficient to quantify, and hence distinguish between seepage-induced internal instability phenomena. Suffusion be characterised as seepage-induced mass loss without change in volume, accompanied by an increase of hydraulic conductivity. Suffosion be characterised as seepage-induced mass loss accompanied by a reduction in volume and a change in hydraulic conductivity. Fluidisation be characterised as seepage-induced volumetric expansion accompanied by an increase in hydraulic conductivity, without mass loss.

Later, the definition of suffusion and suffosion was revised as follows (Fannin et al., 2015): Suffusion should be characterized as seepage-induced mass loss without a change in volume and with or without any change in general hydraulic conductivity but with a change in local hydraulic conductivity. Suffosion should be characterized as seepage-induced mass loss accompanied by a change in volume and a change in hydraulic conductivity.

Fell et al. (2003) divided the process of internal erosion into four phases: initiation and continuation of erosion, progression to form a pipe, and formation of a breach. It was noted that the breach time is controlled largely by the ability of the downstream zone to handle increased seepage flows. This is controlled by the permeability and erodibility of the material forming the downstream zone. Monitoring of seepage, either by visual surveillance, or measurement, is the most common means of identifying that internal erosion and piping have occurred. Seepage monitoring system that set up to monitor different portions of the dam can be helpful. Also seepage monitoring system that can monitor for sediment transport can provide important information of the progression phase of the failure mode. It should, however, be recognized that there are many situations where it will be likely that seepage will be detected. It is not common to have sufficient change in the seepage, or in other factors such as pore pressure changes, or settlement, to identify conclusively that internal erosion has initiated and is continuing. It is more common to recognize when the erosion has progressed to the stage that a pipe has developed; or that there are changes in pore pressure, seepage, or settlement which may be related to internal erosion, but this is not conclusive and it may reflect other factors. These changes may be a precursor to a higher likelihood of internal erosion and piping, so it is

important they are observed, and when they are occur, investigated. Initiation of erosion by internal instability is likely to be a more slowly developing process, accompanied by more gradual increases in seepage, and changes in pore pressure with time. From the view of engineering, in vast majority of cases of piping through the embankment, the reservoir was either at a historic high level, or within 1 m of the historic high level, when progression of erosion to form a pipe occurred.

Fleshman and Rice (2014) performed a series of laboratory modeling to examine the initiation of internal erosion. The device imposes a uniform hydraulic gradient through a soil sample without converging or diverging flow conditions so that the hydraulic regime within the sample (pressures and gradients) can be easily assessed throughout the test, and the critical hydraulic conditions necessary to start the initiation piping process can be assessed. In stage of total heave (Stage 4), the variation in gradients for angular soils is decreased, but nearly all the gradients are significantly above the unit weight trend line for the other soils. It was believed that this trend is a result of the increase in angle of internal friction that increases the soil's bridging ability and also increases the inclination hat the heave mound can achieve before starting to slough. The downward progression of a zone of loosened soil (heave progression) is analyzed by finite-element seepage analysis. It was presented that very little head loss occurs in the loosened zone, where the hydraulic conductivity is approximately three times than than in the undisturbed sand. As a vertical hydraulic gradient is imposed on the sample, the forces acting on the grain include (1) the weight of the grain, (2) the buoyant force, (3) the seepage force, (4) normal and shear forces from the intergranular contacts and (5) the viscous shear force from the seeping water. The intergranular forces with vary as the other forces on the grain change, increasing or decreasing depending on the orientation of the grain contact. The magnitudes of the seepage forces are a function of the size of the interstitial voids and the velocity of the water seeping through the voids. According to Navier-Stokes theory, the magnitude of the viscous shear imposed on the grain increases not only as the average velocity through the void increases but also as the distance from the maximum velocity to the grain surface decreases. Thus, as the size of the void increases, not only does the velocity of the seeping water decrease but, given a larger void, the shear transfer from the water to the grain also decreases because of the greater distance to the maximum flow velocity. In the gap-graded soils, the pathway may be large enough to allow the smaller portion of the gradation to be removed from the soil matrix and deposited at the surface in the sand boil. The removal of the fine grains increases the hydraulic conductivity of the soil surrounding the preferential pathway, thus increasing the effective of the pathway in providing drainage to the interior of the sample. Sand boils were observed to collapse with increased hydraulic gradients. This collapse is likely the result of their drainage capacity being exceeded and he continuation of heave progression distributing the alignment of voids in the preferential pathway.

Skempton and Brogan (1994) performed a series of upward seepage tests on internally unstable sandy gravels. It was demonstrated that the hydraulic gradient when a significant proportion of soils was washouted out by internal erosion was far lower than the critical gradient given by the classical theory. Specifically, for the unstable sandy gravels, internal erosion can occur at hydraulic gradients one third to one fifth of the theoretical critical gradient for a homogeneous granular material of the same porosity. This was explained by the reason that a major part of the overburden load was carried on a framework of gravel particles, leaving the sand under relatively small pressures. By contrast, the heaven on sand from the stable sand gravels occurred at approximately the full theoretical gradient.

Up to now, internal eroison has been considered in hydraulic structures such as dikes, dams, embankments and canals, while the occuring of internal eroison in arid regions and non-hydraulic structures was observed Najafi and Eslami (2015). The statistic analysis was proposed to assessement the internal instability. It was developed and verified using a relatively large database of unstable soils. The results reveal that the soils in the investigated site were internal unstalbe, and could be classified as very vulnerable to internal erosion. Although the water table in the investigate site (Shahriyar, Iran) was very low, the damages there might be caused by intenral erosion.

Seghir et al. (2014) performed experiments in a laboratory column on different sand fines mixtures and subjected to controlled flow conditions to assess the effects of fines on the erodibility of mixtures. The soil samples in their study were mixtures made of Fontainebleau sand and fines – kaolinite or illite or silt. The results demonstrated that the initiation and rate of internal erosion were affected by the type of fines. The potential of instability was governed by the matrix porosity and the fines contents. Silt mixtures were the most vulnerable to internal erosion among the kaolinite mixtures and illlite mixtures. The hydraulic conductivity of the mixtures decreased with the increasing hydraulic gradient are erosion rate. This behavior indicated that the internal erosion not only involved particle detachment and subsequent transportation, but also caused particle clogging and likely clogging. It was suggested that the deposition and clogging processes could be taken into consideration when modeling the internal erosion.

The effects of internal erosion on soil drained strength was experimentally investigated by a series of one-dimensional upward seepage tests (Ke and Takahashi, 2012). The internal erosion was created by applying upward seepage flow through gap-graded siliceous soils. It was found that before internal erosion, the relation between average hydraulic gradient and flow velocity was basically linear. However, it became non-linear as soon as the internal erosion occurred, which indicated that the hydraulic conductivity was increased due to internal erosion. The initiation hydraulic gradient for the onset of internal erosion was around one-fifth to one-third of the theoretic hydraulic gradient,

which further proved the phenomenon observed by Skempton and Brogan (1994) that the initiation of internal erosion on internal unstable soils was far smaller than the theoretical value. It was also noted that the mixtures with larger relative density required a larger hydraulic gradient to initiate the internal erosion on the condition that their initial fines contents were the same. Moreover, the mechanical consequences of internal erosion were examined by cone penetration tests. The results showed that internal erosion could cause a reduction in cone tip resistance, and the extend of which might be related to the imposed hydraulic gradient. A larger imposed hydraulic gradient, suggesting a larger loss of fines, would lead to further reduction of cone resistance.

Ke and Takahashi (2014a) conducted many seepage tests in a revised triaxial erosion apparatus (Ke and Takahashi, 2014b) by constant flow rate control mode under isotropic confining pressure. The mechanism of internal erosion for saturated soils with different initial fines contents was examined. It was presented that the hydraulic gradient dramatically dropped with the progress of internal erosion, indicated by the erosion of large amount of fines. The erosion of fines resulted in an increase of contractive volumetric strain. The post erosion particle size distribution analysis indicated that the fines loss was larger in the upper layer than bottom layer. It was found that the specimens showed less increments in hydraulic conductivity under larger effective confining pressure within the test range. For the test performed in a larger confining pressure, the specimen indicated the least cumulative eroded soil mass and volumetric strain among the other cases within the test range. For the tests performed in soils with 15%, 25% and 35% initial fines content, the largest change in hydraulic gradient occurred in the soil with 35% initial fines content. Fines loss was larger for the soil with larger initial fines content and correspondingly, the internal erosion induced volumetric strain was larger. At the same small strain level, it was found that the deviator stress of soil with erosion was larger than that of the soil without erosion. When it comes to the same medium strain level, the soil with erosion showed smaller deviator stress compared to that of soil without erosion. In terms of stiffness, the internally eroded soils showed a larger initial secant stiffness at the same small strain level, whereas it became smaller at the same medium strain level.

A series of physical model tests on seepage induced internal erosion in a homogeneous embankment was performed by Horikoshi and Takahashi (2015b). The schematic diagram of the test apparatus is shown in Fig. 2.2. The seepage induced temporal and spatial variations of fines in the embankment was investigated through standard sieve analysis on subdivided areas. It was demonstrated that the laboratory physical model test could simulate the small scale loosely compacted embankment subjected to internal erosion. Under the transient seepage flow, a majority of fines was dislodged during the rising of phreatic surface. Both the disappearance of suction and transportation of fines resulted in a change of fines spatial distribution in the embankment. During the steady seepage flow, the fines not only moved horizontally by seepage flow, but also deposited vertically by gravitational

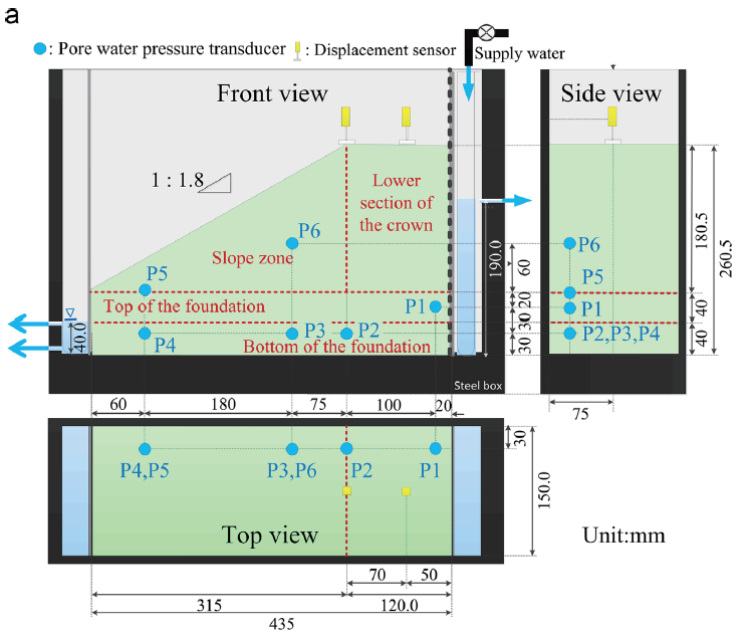

Figure 2.2: The schematic dynamic of the physical model tests (after Horikoshi and Takahashi (2015b))

force. The deposition of fines formed a fine-rich region in the foundation, and consequently caused a decrease of the permeability. The effects of repeated permeations were also examined, it was noted that fines was mainly deposited during the repeated permeations rather than transported horizontally.

Permeameter tests were performed on four widely graded cohesionless soils by Moffat et al. (2011), to study the susceptibility on internal erosion. The tested materials were reconstituted as a saturated slurry, consolidated, and then subjected to multi-stage seepage flow under increasing hydraulic gradient. The experiments revealed that the tested materials were internal unstable, internal erosion was observed in all test cases. Internal erosion appeared to be a time-dependent phenomenon, as evident from changes in local hydraulic gradient in soils with significant silt content. Fines migration yielded a relatively small and slow change in local hydraulic conductivity, but no change in specimen volume. The spatial and temporal progression of instability might be characterized by (i) localized erosion followed by reestablishment of a stable equilibrium, (ii) localized erosion followed by a period of unstable equilibrium within the specimen or (iii) localized erosion that triggers a particle migration within the whole specimen. The onset of instability, and its subsequent progression, was believed to be governed by a critical combination of hydraulic gradient and effective stress.

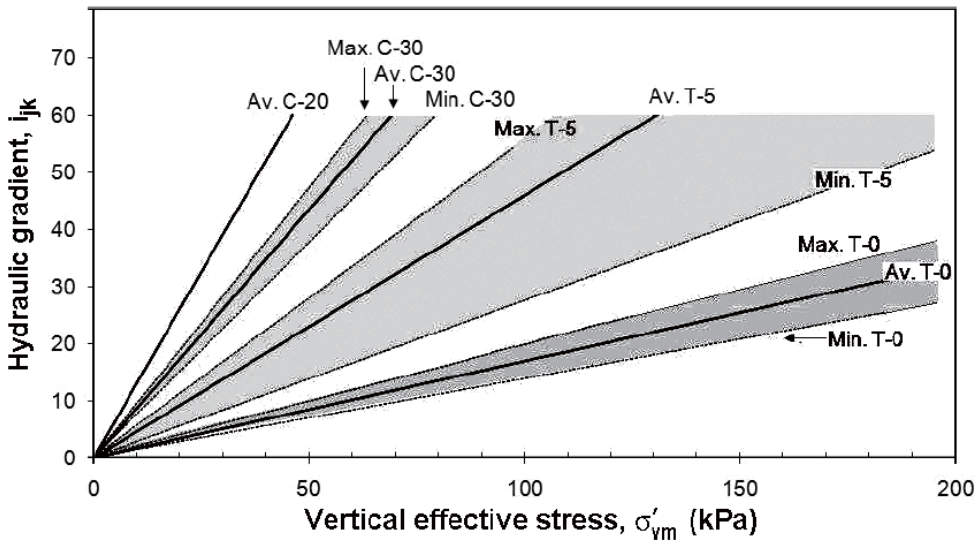

Figure 2.3: Summary of hydromechanical boundaries in stress-gradient space (after Moffat and Fannin (2011))

Moffat and Fannin (2011) presented the results of permeameter tests involving unidirectional seepage flow through reconstituted specimens of four widely graded cohesionless soils. The onset of instability was defined by a significant decrease in local hydraulic gradient over a relatively short period of time. It was found that the spatial variations of local hydraulic gradient and mean vertical effective stress governed the location where onset of particle migration occurred in a specimen. A trend of increasing critical hydraulic gradient with increasing mean vertical effective stress was found from the tests. The onset of internal instability was demonstrated to be triggered by either an increase in hydraulic gradient or by a decrease in effective stress. Each trigger yielded a similar response through the observation of particles migration. Meanwhile, the results suggested that the Kenney and Lau' s method might be applicable to evaluate the coarse-grained soils with a component of non-plastic silt. Figure 2.3 demonstrated the summary of the hydromechanical boundaries in stress-gradient space. It was noted that the critical hydraulic gradient was influenced by the vertical effective stress and the fines content. The critical hydraulic gradient increased with the increase of the vertical effective stress. At the same vertical stress, the critical hydraulic gradient for soils with larger fines content was larger comparing to that for soils with smaller fines content.

Several seepage tests on gap-graded glass bead specimens were performed by using a large oedo-permeameter device by Sibille et al. (2015b). The cylindrical specimens contained an initial percentage of fines from 20% to 40% and with an initial length comprised between 250 mm and 600 mm. The influence of hydraulic loading was investigated by increasing the controlled hydraulic

gradient with different amplitudes and stage durations. The test results revealed that the internal erosion was constituted of two phases: (i) slightly changes of hydraulic conductivity and specimen density depending on the initial percentage of fines; and (ii) large amount of fines washing out inducing both a large settlement of specimen and a relatively strong increase in the hydraulic conductivity. Therefore, it was indicated that internal erosion should be taken into consideration in order to prevent the damages related to strong deformation of hydraulic structures (dam or embankment), and strong increase in seepage flow rate through these structures. Meanwhile, it was noted that the key parameters affecting the development of internal erosion were the initial fines content and the evolution of applied hydraulic gradient.

Multichannel optical sensor was designed to measure the soil particles concentration during seepage test, further to quantify the soil stability under seepage flow (Marot et al., 2011a). This sensor was composed of four light-emitting diodes and four associated light-dependent resistor, allowing the measurement of fluid transparency. It can be installed close to the particles exit from the specimen due to its small size. The optical sensor could be able to measure a large range of clay, silt and sand concentrations in the effluent, without a significant influence of flow rate. The application of the sensor with a revised triaxial cell allowed a precise characterization of the initiation and development of internal erosion. The results demonstrated that the coarse grain shape could affect the development of internal erosion, the angularity of which may intensify the geometric blocking of eroded soils. The erosion of clay particles was observed with the filtration process, which induced a hydraulic conductivity decrease. The hydraulic conductivity decreased more with a higher concentration of eroded particles in the interstitial flow. Coarse particles distribution and morphology also influence the internal erosion process. Moreover, it was found that the clay erosion could be accompanied by sand erosion when subjected to a high hydraulic gradient.

To determine the soil erodibility classification, commonly Jet Erosion Tests (JET) and Hole Erosion Test (HET) are used. Based on the fluid energy dissipation and measured cumulative eroded soil mass, Marot et al. (2011b) proposed a new method to interpret the erodibility. It was shown that the erosion coefficient and the average critical shear stress obtained from JET and HET were not exactly the same for the same specimens. However, on the basis of energy method, the erosion resistance index were roughly the same for each soil, which allows one to choose a more suitable test between JET and HET.

Xiao and Shwiyhat (2012) performed a series of consolidated drained compression tests on the eroded specimens together with the companion specimens. It was found that the eroded particle gradations might depend on the grain size distribution and pore throat distribution of soils. Some fines were transported from the upstream portion to the downstream portion. The deposition of

fines in downstream portion led to clogging, further caused a decrease of the permeability. Due to the internal erosion, all the soils showed contractive volumetric strain, specifically, the gap-graded soils produced a larger volumetric strain than the poorly graded soils. For the undrained mechanical behaviors, the eroded specimens consistently showed the larger compressive strength than the companion specimens without erosion. The limitations of their research were also reported, which includes the modification of the test procedure to lengthen the duration of the seepage tests, identification of the critical hydraulic gradient, and the maintaining of high degree of saturation during the seepage tests.

Richards and Reddy (2012) conducted comprehensive laboratory seepage experiments using different soils types in a true triaxial piping test apparatus. Three general types of behaviors were examines: suffusion, concentrated leak erosion and backward erosion. It was shown that the seepage velocity was a better predictor of piping behavior for non-cohesive soils than the hydraulic gradient. The critical seepage velocity increased with an increase in the maximum principle stress, indicating a higher stabilizing effect against piping initiation. However, no systematic relationship was found between critical velocity and the minor or intermediate principle stress. The effects of seepage angle, degree of compaction and rate of seepage increase were also investigated. The results showed that the critical velocity was substantially lower when the seepage direction was at an angle below horizontal by as little as 10°C. Greater compaction increased the seepage velocity required to induce piping. No significant relationship was found with respect to the rate of increase in seepage during the tests. For the gap-graded mixtures containing low-plastic fines, suffusion was the primary mode of failure, and it occurred under significantly lower seepage velocity than required to induce backward erosion. Oncer suffusion initiated, it progressed to backward erosion at a much lower velocity than was required for backward erosion in the same soil without the low-plastic fines. For the internal unstable mixtures containing high-plastic fines, they required substantially higher differential pressures to induce piping, and at a very low seepage rate. Observations of the post eroded soils indicated that the samples failed by concentrated leak erosion rather than backward erosion or suffusion.

A comprehensive review on the piping phenomena was conducted by Richards and Reddy (2007). The piping was divided into three parts as: (i) heave, (ii) internal erosion, and (iii) backward erosion. It was noted that the current research on piping was limited, the deterioration of structure due to piping might be responsible for the design and construction standards. Most of the previous work focused on cohesive materials, in particular dispersive clays, the study of piping on non cohesive soils was limited. They concluded that even in spite of the number of advances in our understanding of piping phenomena, there are still a large number of incidents that occur due to concentrated leakage or formation of sinkholes in embankment dams. It reflects a need for increased attention to

prevent those potential failures.

Wan and Fell (2004a) developed the Slot Erosion Test (SET) and HET to study the erosion characteristics of soil in cracks in embankment dams. The erosion rate index, which represents the rate of erosion, and the critical shear stress, which suggests the minimum shear stress when erosion starts, were employed to describe the erosion characteristics. The results demonstrated that the erosion rate index spanned from 0 to 6, indicating the soils could differ in their rate of erosion by up to 10^6 times. It was noted that the rate of erosion was dependent on the fines content, plasticity, dispersivity, compacted water content, density and degree of saturation; and clay mineralogy, and possible the presence of cementing materials. Coarse grained, non cohesive soils, in general, erode more rapidly and have more critical shear stresses than fine grained soils. They also proved that knowledge of erosion characteristics of soils in the embankment core aids in the assessment of dam failure due to internal erosion.

Zhang et al. (2011) developed a robust probability based tool using Bayesian networks for the diagnosis of embankment dams distresses at the global level based on past dam distress data. 993 distressed in-service embankment dams in China was investigated, including general information on hte dams, distresses, and causes. It was concluded that for the distresses associated with overtopping of both homogeneous composite dams and clay core dams, the key dam distress factors identified are the primary spillway, gates and lifting devices, and flood design criteria. In contrast, seepage induced erosion and piping was found to be occurred at any part of a dam system. For seepage induced erosion and piping of homogeneous composite dams, the destresses are mostly associated with the embankment, followed by the foundation and embedded culverts. For seepage induced erosion and piping of clay core dams, the distresses are mostly associated with embedded culverts, followed by the foundation and embankment. The global level knowledge was then extended to the diagnosis of a specific distressed dam by Xu et al. (2011). The diagnosis was conducted by two sources of information, i.e., global level knowledge from the database and project specific evidence. Based on the results of the diagnosis, key distress factors for a specific dam was identified and suitable remedial measures were suggested. Further, the effectiveness of the adopted methods could be evaluated based on the proposed approaches.

To investigate the causes of dam failures, more than 1600 dam failure cases throughout the world excluding China were complied into a database by Zhang et al. (2009). The failure of earth dams, around 66% of the total dams failures, was mainly investigated. According to the dam zoning and corewalls, earth dams were divided into four typical categories: homogeneous earthfill dams, zoned earthfill dams, earthfill dams with corewalls, and concrete faced earthfill dams. It was concluded that the most common causes of earth dams failures were overtopping and piping, particularly

for homogeneous earthfill dams and zoned earthfill dams. Fore earfill dams with corewall, piping appears to be less likely because the corewall materials are less erodible and well designed filters are presented. At any part of the dam system, there are potential locations at risk for piping failure.

Zhang and Chen (2006) investigated the seepage failure mechanism of the Gouhou rockfill Dam, Chinea, during reservoir water filtration. Base on the geometrical criterion of Kenney and Lau (1985), the rockfill materials of Gouhou dam were assessed as susceptible to internal erosion if necessary hydraulic conditions were met. When the reservoir water infiltrated into the rockfill, the dam could be divided into two zones: a saturated zone inside the wetting front and an unsaturated zone outside the wetting front. The site investigated revealed that the wetting front was associated with a hydraulic gradient higher than the critical value initiating internal erosion. When the wetting front reached the downstream slope surface, embankment failure was triggered.

2.2.3 Theoretical and numerical modeling of internal erosion

To improve the understanding of mechanical consequence of soils subjected to internal erosion in hydraulic structures, Hicher (2013) performed numerical method based on the microstructural approach. The internal unstable materials were employed in the numerical simulation. Homogenization technique was applied to obtain an elasto-plastic stress strain relationship for granular materials. The local behavior of soils was assumed to follow a Hertz-Mindlin elastic law and a Mohr-Coulomb plastic law. The friction angle was made dependent on the actual void ratio, which could reflect the removal of certain particles. It was found that the progressive removal of solid fraction led to a decrease of sliding resistance of each interparticle contact, which created an disequilibrium between the external applied loading and internal contact forces. As a consequence, local sliding occurred, which led to macroscopic deformations of soil specimen. The amplitude of the deformation depended on the amount of removed particles, as well as the applied stress level. At large stress level, large deformation could develop when the removed fines fraction increased. It was demonstrated that the granular assemblies can develop instability at a shear stress level much lower than the critical state failure line, which is also termed as diffuse failure. The numerical simulation of constant-q loading, corresponding to a pore pressure increase within the soil mass, showed that the condition of instability, diffuse failure, could be reached when the removed fines fraction was high enough. The results elaborated that changes in the hydraulic conditions within the embankment dam can lead to a sudden collapse of the earth structure due to the existence of unstable states within the eroded soil mass.

The ground water table rising was detected in northern Italy, which caused serious problems: (i)

water flow into the oldest deep underground structures; and (ii) increase of pore pressure and consequent reduction of effective stress. Sterpi (2003) preformed some laboratory tests to investigate the erosion of fines from soils subjected to a controlled seepage flow. Then the phenomenon of erosion and transport was then modeled by combining the conservation of mass of moving fines with a suitable law of erosion in a single equation. This equation, coupled with the equation governing the seepage problem, made the evaluation of cumulative eroded soil mass possible. Finite Element Method (FEM) was then employed to investigate the influence of fines removal on the stress strain relations. Subsequently, the surface settlement induced by erosion was also assessed. It was found that the volume reduction and variation of mechanical responses were the possible direct consequences of internal erosion. The soil stiffness and strength were changed by internal erosion as well, in this particular case, the surface indicated settlement after fines removal. According to the experimental and numerical study, more experimental research on mechanical properties related to soils subjected to internal erosion was recommended to be performed.

To locally lower the ground water in northern Italy, a series of pumping wells was drilled in the urban city. This provision, could lead to possible erosion of fins fraction and consequently settlements of nearby buildings. Cividini and Gioda (2004) developed an approach to investigate the erosion and transportation of fines of soils subjected to seepage flow based on FEM. Firstly, the continuity equation and its discretization according to FEM were employed. Then, the erosion law governing the evolution of cumulative eroded soil mass was coupled to the FEM. Finally, the developed numerical analysis was proved by some test examples. The results demonstrated that the developed approach could be reasonably for analysis of erosion problems, although some possible improvements could be made, i.e., evolution of hydraulic conductivity and free surface problems.

To improve the method proposed by Cividini and Gioda (2004), Cividini et al. (2009) performed a series of laboratory erosion tests on reconstituted soil sample. An incremental erosion law was then proposed according to the experimental results, and was implemented in the finite element code for erosion transportation analysis. The improved estimation of seepage induced settlement was based on three independent simulations. (i) An unconfined seepage problem was modeled first to evaluate the water table lowering induced by the drilled wells. (ii) The incremental erosion law was employed to assess the local density of eroded soils. (iii) The local density was converted to volumetric strain, and it was applied in the FEM to calculate the induced settlements. The test results and numerical simulation pointed that the evolution of hydraulic conductivity and deposition of fines could be neglected. During the initial transient flow, the phreatic surface could be lowered, however, it was not accounted in the simulation approach. The seepage induced pore water pressure increase and effective stress decrease was not considered. The settlement of the surface was directly accounted by the loss of fines, or the volumetric strain. The further recommendations were the scale

of specimens in laboratory tests and the investigation of confining pressure on internal erosion.

The mechanical consequences of soils subjected to internal erosion was modeled by Muir Wood et al. (2010). It was elaborated that the internal erosion would change the grading of soils, and further affect its mechanical behaviors. The 2D Discrete Element Method (DEM) analysis provide an analogue of the real process of particle removal by internal seepage forces. The deformation and rearrangement induced by removal of particles were recorded and examined. The removal of soil particles increased the specific volume, but the external stresses remained unchanged, the volumetric strain also increased. A continuum model based on the asymptotic critical states and the state parameter was employed to examined the mechanical behaviors. The removal of fine particles narrows the grading and consequently raises the critical state line. However, the combined effect of material removal and skeleton compression is to leave an increase in specific volume and a consequent increase in state parameter. The results revealed that increase in state parameter reduces the available strength, increases the degree of mobilization of strength, and thus leads to the occurrence of distortional strains, which reproducing qualitatively and quantitatively the effects observed by DEM analysis.

Scholtès et al. (2010) proposed a multi-scale approach to evaluate internal erosion induced effects on mechanical consequences of granular materials. When the internal erosion occurs, fines would be eroded away from the specimen, leading to changes in the soil microstructure. Subsequently, these changes could affect the soils mechanical behaviors. The erosion of fines was simulated through the progressive removal of finest particles under isotropic and anisotropic stress states. A Discrete Element Method (DEM) and an analytical micromechanical model were used to investigate the change of deformation and property during the erosion process. It was found that the soil yielded from a stable state to an unstable state was related to mobilized friction near critical state. This suggested that failure or large strain could be locally developed in the internally eroded zones of hydraulic structures (dams or embankments) at critical state. The change of volumetric strain from dilative to contractive, seemed to be relative to the occurrence of failure, during the extraction of fines. The mobilized friction angle of the soil with fines removal was smaller than that of soils without fines extraction. It was suggested that the change of porosity due to internal erosion be one of the parameters to describe the effects of erosion on mechanical behaviors.

The internal erosion was characterized into two steps by Sibille et al. (2015a) as (i) detachment of solid particles from the granular skeleton under seepage flow; and (ii) the transportation of these detached particles by seepage flow. To directly simulate the process of internal erosion, the fully DEM coupled with Lattice Boltzmann Method (LBM) was proposed. Interpaticle interactions in the solid granular phase were described by DEM, whereas, the dynamics of water flow was solved by

the LBM. This numerical approach had the advantages to limit the hypotheses introduced to describe the fluid-solid interactions and to involve few mechanical parameters: one for the fluid phase, four for the solid phase and none for the fluid-solid interactions. The fluid flow was described at a scale smaller than the pore or the particle scale. The fluid flow was also regarded as low compressible material to satisfy a low Mach number; and the flow velocity was kept small to consider only laminar flows with a Reynolds number between 0.50 and 40.0 to simulate the first step of fines detachment. The simulation and experimental results showed that the erosion rate was linearly related to the hydraulic shear stress. The parametric study demonstrated that the erosion threshold depended on the cohesion of granular materials, whereas, the kinetics of erosion was independent. Furthermore, results from both direct numerical simulations and laboratory experiments suggested that the erosion rate could be interpreted as a function of flow power according to a power law. The exponent of the power law was about 0.5 for the two-dimensional simulations of HET, equal to 1.0 for the laboratory hole erosion test, and slightly higher than 1.5 for the suffusion tests. Finally, it was admitted that the direct numerical simulation considered only the detachment and transport of fines by seepage flow, the complementary analysis of filtration process might be necessary to consider.

Shimizu (2011) developed a microscopic numerical model of fluid flow through granular materials based on DEM. The compressibility of fluid during the particles movement was considered to calculate the fluid pressure in the void spaces, which is also the flow across void spaces in a one-dimensional form of Darcy's law. The calculated fluid pressure was then applied tot he particles involved in the void space as a body force proportional to the occupied area. This microscopic numerical coupling method permitted the analysis of the microscopic mechanical characteristics of granular materials associated with fluid, since many problems in geotechnical engineering involving such interaction between particles and fluid. The simulation performed by the microscopic numerical model showed good agreements with the analytical results. The localization of the fluid path and pore water pressure distribution could be calculated and observed, as well as their evolutions during the erosion process. Further improvement of the proposed approach was focused on the tracking of the water content in each void space to investigate the behaviors in unsaturated soils.

The erosion of fines was also modeled by Vardoulakis (2004) on matrix supported bimodal soils, which consists of fines and coarse particles. In the specific tested mixtures, the fines were regarded as “free” – experiencing no permanent intergranular stresses due to overburden. Erosion of fines was described by a three phase continuum model, consisting of stationary fines, transported fines and fluid. By the mass conservation equation and momentum balance relation, the erosion law could be obtained, accounting for the fact that only a fraction of fines could be eroded away. The results demonstrated that the erosion of fines was a relatively “slow” process. The observed increase

in hydraulic conductivity in gap-graded soils subjected to seepage flow (Skempton and Brogan, 1994) could be attributed to the fluidisation of fines fraction in soils.

2.3 Experimental apparatus on internal erosion

The experimental research on soil particles movement started from the filter design in Dam Engineering. Based on the empirical filter rule proposed by Terzaghi, many researcher found that some fines would be transported into the constrictions formed by filter materials, subsequently leading to the alternation of soils physical and mechanical characteristics. Therefore, the experimental studies focused on the internal stability were performed concerning the particle size distribution, constriction size distribution, relative density, and uniformity coefficient. After the acceptance that the suffusion would result in the change of soil mechanical behaviors, some new test equipments were devised to accommodate the suffusion into element mechanical tests, such as unconfined compression tests and drained and undrained triaxial compression tests. Following text will present the (i) internal stability tests and the (ii) element tests on internal erosion.

2.3.1 Internal stability tests

According to Fannin (2008), the first research related to internal stability started at the year around 1922 by Terzaghi, and it was described as follows. "In order to get the information concerning the mechanical effects of the seepage pressure on the subsoil, he filled a cylinder vessel with sand and let the water percolate through the sand in a vertical upward direction. The top surface of the sand supported a small weight. The hydraulic gradient i was steadily increased and the corresponding discharge was measured. As i increased the effective weight of the sand decreased, but the hydraulic conductivity k remained constant and the weight did not move, which indicated that the structure of the sand remained intact. However, at the instant when $i\gamma_w$ became equal to γ', the sand surface rose, k increased abruptly and the weight sank to the bottom of the vessel, as if the sand had suddenly disappeared. " Accordingly, Terzaghi concluded that the subsurface erosion can readily be prevented by covering the discharge points of water veins with a loaded inverted filter. Later, he proposed the classic filter criteria, which was defined as:

(a) Filter rule

$$d_x < 4d_1 \tag{2.7}$$

where $d_x = D_{15}$ and $d_1 = d_{85}$. The rule was based on an appreciation that the pore size of a broadly graded filter comprises at maximum 1/5th of the diameter of the biggest grain of the finest fraction of the filter material.

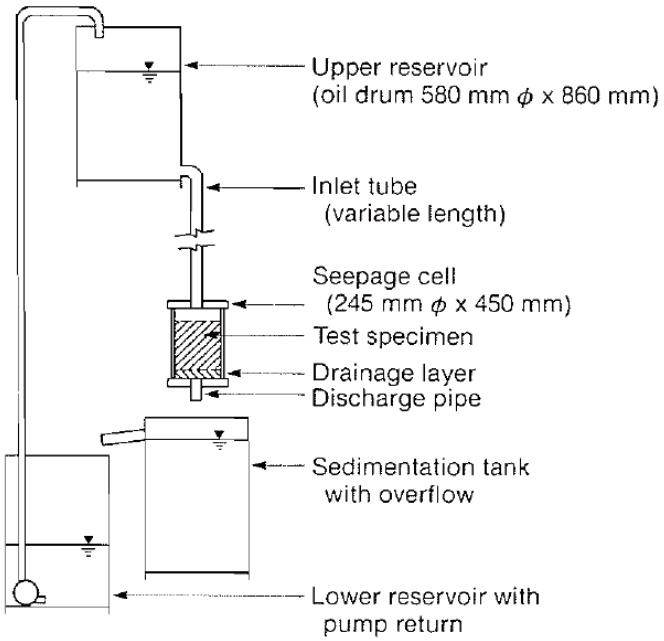

Figure 2.4: Test apparatus with 245 mm diameter cell (after Kenney and Lau (1985))

(b) Permeability expression

$$d_x > 4d_2 \tag{2.8}$$

where $d_2 = d_{15}$. The rule was based on the concept that permeability is proportional to the square of the finest grain size, 10 to 15% by mass and hence the filter is essentially more permeable than the soil.

To study the influence of particle size features on the internal stability, Aberg (1993) performed the washout tests in a permeameter with diameter of 190 mm. A 125 mm thick layer of tested material, consisting of sand and gravel, was placed on top of a square mesh screen, the aperture of which varied between different tests. The tested materials was prepared by means of a procedure and compaction effort corresponding to the modified proctor method. The tested material was then loaded by an about 400-mm-thick layer of 30-50 mm pebbles placed on a flexible metal cloth with 1.5 mm mesh size. The flow of water was directed downward. The total drop of water head in the permeameter was 2.7 m. The permeameter could be mildly vibrated by means of a vibrator, which was fastened to it.

To assess the internal stability of filter materials, Kenney and Lau (1985) performed a series of experiments. It basically consists of forming a compacted test specimen, applying seepage and vibrational forces to encourage loose particles to move towards the bottom of the sample, and deter-

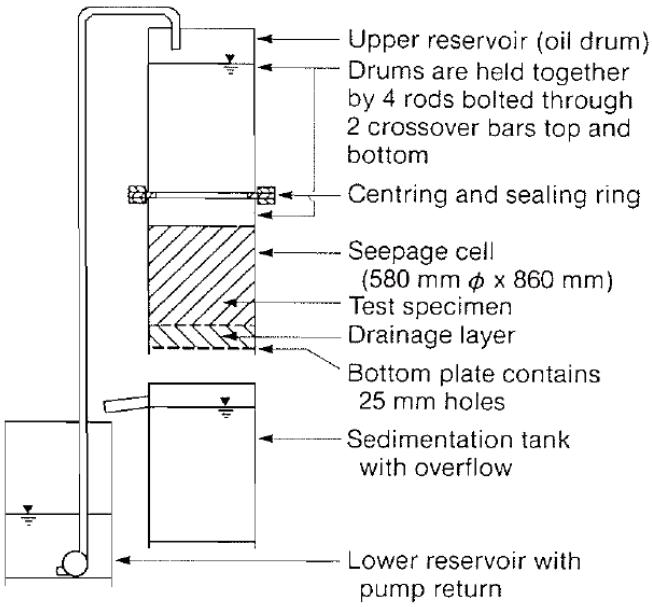

Figure 2.5: Test apparatus with 580 mm diameter cell (after Kenney and Lau (1985))

mining the changes of grain size distribution at various levels in the specimen. Most of their tests were performed in the seepage cells with 245 mm and 580 mm diameters, as shown in Figs. 2.4 and 2.5, respectively. Each cell was supported on two horizontal beams that spanned the sedimentation tank. Water from the upper reservoir flowed through the specimen, depositing particles in the sedimentation tank, and was returned by pump to the upper reservoir. A compressible rubber layer was used against the inside wall of each cell to prevent the formation of large seepage channels along the boundary. The specimens were vibrated lightly by manually tapping the horizontal beams with a rubber hammer. To top surface of each specimen was stressed by a spring loaded, perforated plate (10 kPa) which maintained positive effective stresses within the primary fabric. The conditions used in their experiments to cause the particles transportation were adjusted by the hydrnumber. It was set based on the finding that the particle transport through filters was maximized when vibration was used and the flow condition corresponded to a hydrodynamic number $R^{'} \geq 10$, where $R^{'} = qD_5/n\nu$, where q is unit flux, D_5 is 5% particle size, n is the porosity, and ν is the kinematic viscosity of water (1 $mm^2 \cdot s^{-1}$).

To further study the internal stability, Kenney et al. (1985) performed two general types of tests: hydraulic filter tests and dry vibration filter tests, to determine the controlling constriction size of granular materials. The experimental approach followed was to prepare a number of narrowly graded bases composed of nearly spherical particles, and to determine whether or no these base particles could be transported through the void networks of different filters. The sketch of apparatus

used for hydraulic filter tests is presented in Fig. 2.6. To ensure that large void channels were not formed between the tested materials and the wall of the cell, a thin lining of fine soils or a layer of soft rubber was placed along the cell wall. A large head loss across the filter was maintained in order to create the large seepage velocities within the filter. Flow was downward. For thick samples the hydraulic gradient across the filter was usually in excess of 3, and for thin samples of fine grained filters the gradient exceeded 50. The test procedure consists of testing a filter with progressively coarser bases. If base particles were transported through the filters, which suggests that the controlling constriction size of filter was larger than the size of base materials, then the next base in order of coarseness was used that test repeated. The experiment was ended when it was certain that no particle of the most recently used base came through the filter.

Figure 2.7 shows the sketch of cell used for dry vibration tests. The diameter of the cell is 135 mm. The principle of the test is that loose base particles at the surface of the filter and within the filter can be kept in motion by applying vibration forces. Base particles were acted upon by gravity and if they were smaller than the constrictions they move downward through the void network. If they were larger than the controlling constriction size, they became trapped within the void network. At the completion of tests, the filter was divided into horizontal layers, and grain size analysis were performed to trace the depth of penetration of base particles.

To examine the profile of hydraulic gradients during the piping, Skempton and Brogan (1994) carried out the tests in sandy gravels. The test apparatus consists essentially of a transparent permeameter with 139 mm diameter. The samples were moist tamped after though mixing to avoid segregation while they were placed in the cylinder. Four layers each about 40 mm thick were tipped in and packed by hand. An underlying gravel and coarse sand diffusing filter ensured reasonably uniform flow across the area of the sample. Under an initial small had, flow was allowed to continue until the sample became saturated and water began to trickle over the top edge of the cylinder into the lower basin, the discharge from which could be measured. Thereafter each increment of flow produced an almost instantaneous response in the three glass standpipe piezometers. Any changes in the sample were recorded before the next increment of flow was applied. Each test lasted about 1.5 h after the period of saturation. Fines washed out of the sample was collected, dried and weighted after the test had been completed. The test results revealed that a significant proportion of the sand content is washed out by piping at hydraulic gradient far lower than the critical gradient given by a classical theory.

To further investigate the continuing erosion boundaries, where the filter is too coarse to allow the eroded base materials to seal the filter resulting in unrestricted erosion of base soil, the laboratory experiments were performed in the University of New South Wales (Foster and Fell, 2001). The

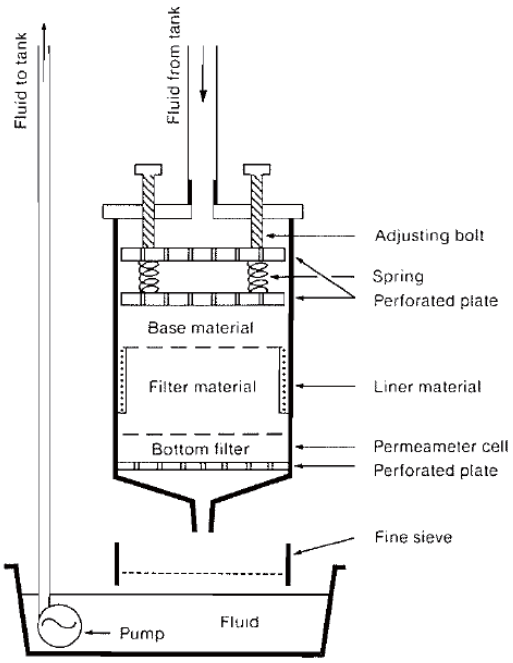

Figure 2.6: Sketch of apparatus used for hydraulic filter tests (after Kenney et al. (1985))

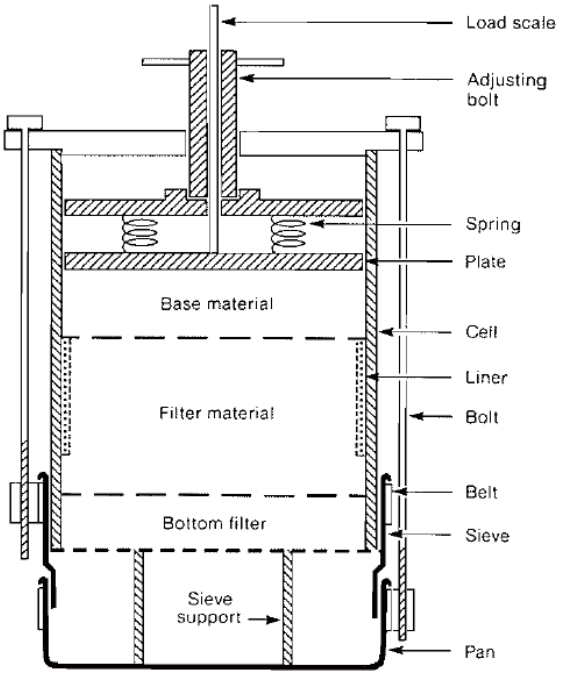

Figure 2.7: Sketch of apparatus used for dry vibration tests (after Kenney et al. (1985))

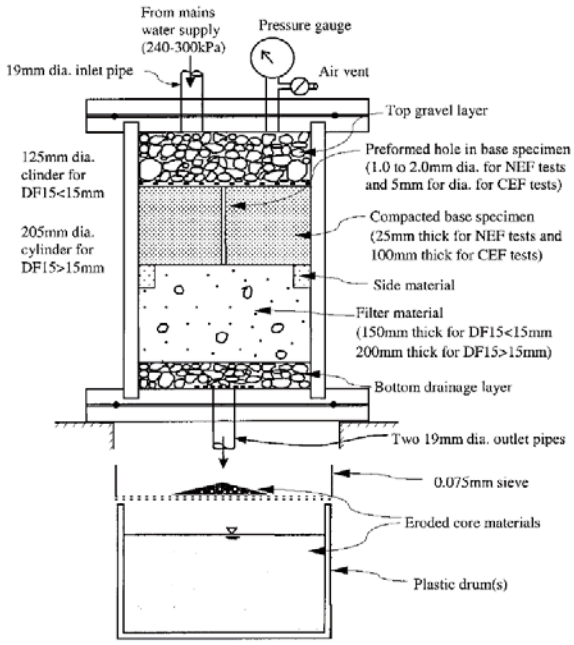

Figure 2.8: Continuing erosion test apparatus (after Foster and Fell (2001))

test apparatus is demonstrated in Fig. 2.8. The tested materials were obtained from the natural deposits or from the embankment of existing dams in Australia and New Zealand with fines content of 15-85%. In the continuing erosion tests, water passing through the filter during the tests was collected, and the eroded materials dried and weighted to determine the loss of base soil required to seal the filter. Meanwhile, progressively coarser filters were used until the filter was not sealed. Thicker base specimens were used to allow for greater erosion losses. From the test results, it was concluded that the broad grading, a low percentage of sand sizes and poor construction practices would tend to make the embankment dams susceptible to segregation.

Wan and Fell (2004b) conducted the laboratory slot erosion test and hole erosion test to examine the erosion characteristics of soil in embankment dams. The schematic diagram of slot erosion test apparatus is shown in Fig. 2.9. A 2.2 mm wide, 10 mm deep and 1 m long slot was formed along the surface of soil sample, which was compacted inside a 0.15 m wide, 0.1 m deep and 1 m long rigid sample box made of aluminum. The preformed slot was in contact with a transparent perspex cover plate of the sample box through which erosion of the slot can be observed during the tests. The tap water went through the soil sample horizontally to initiate erosion. The upstream and downstream pressure were set at 2.5 m and 0.3 m constantly. The flow rate was measured by a low meter, and double checked by measuring the volume of effluent water. Digital images of the specimen were taken at chosen time intervals during the tests so that the width of the performed slot

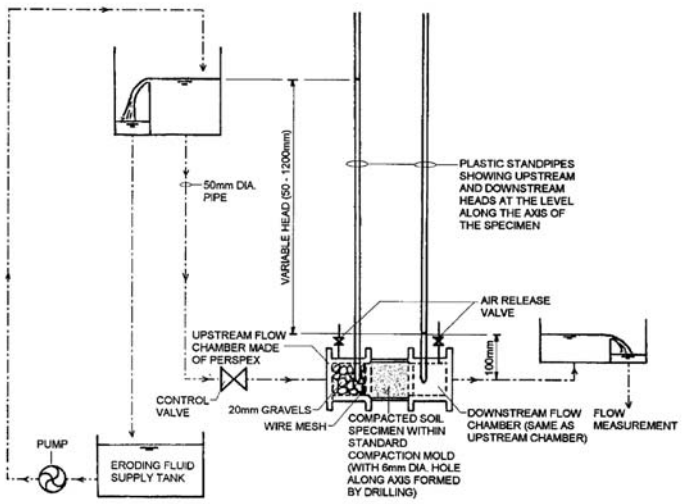

Figure 2.9: Slot erosion test apparatus (after Wan and Fell (2004b))

could be measured. The experiment was finished when the performed slot was widened to the edge of the sample box, or when the flow rate reached the maximum range of flow meter.

Figure 2.10 demonstrates the schematic diagram of hole erosion test assembly. A 6 mm diameter hole is drilled along the longitudinal axis of the soil sample to simulate a concentrated leak. The upstream water head was set 50 to 120 mm higher than the downstream water head. During the test, the actual hydraulic pressures were indicated by the heights of water columns inside the plastic standpipes. The flow rate, which was recorded by measuring the volume of effluent collected within a period of 10-20 s, was used as an indirect measurement of the diameter of the performed hole. The test was finished when the performed hole reached the edge of sample box, or when the flow rate exceeded the maximum range of flow meter. After the text, the specimen was extruded from the mold and sliced carefully to record the shape and size of the performed hole.

2.3.2 Element test on internal erosion

To investigate the seepage force and confining pressure effects on piping erosion, Tomlinson and Vaid (2000) developed a new permeameter capable of controlling some parameters. Artificial glass beads were prepared by water pluviation method to permit consistent repeatable uniform samples. By monitoring head, settlement, confining pressure, amount of eroded soils, and water outflow rate, the characteristics of piping erosion can be determined. It was noted that the grain size ratio is the most important parameter governing the erosion. The soils with $D_{15}/d_{85} < 8$ will not fail, whereas a $D_{15}/d_{85} > 12$ will not be able to retain base soils. For $8 < D_{15}/d_{85} < 12$, piping will only occur

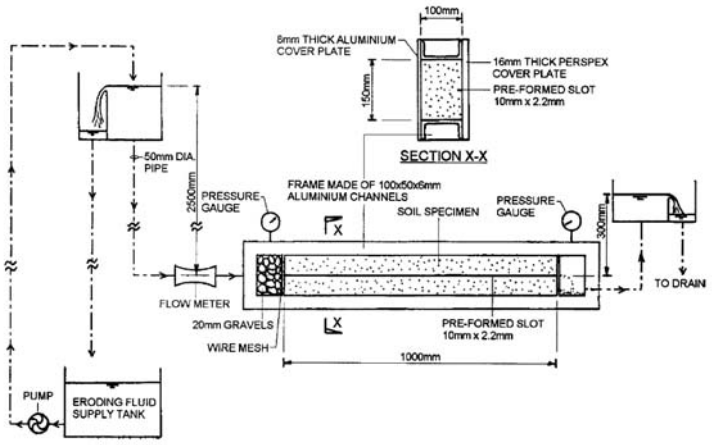

Figure 2.10: Hole erosion test apparatus (after Wan and Fell (2004b))

if the hydraulic gradient exceeds a critical state. It was also demonstrated that the critical hydraulic gradient was lower if the head was rapidly increased, as a filtration zone was inhibited from forming. The stability was inversely related to the confining pressure level for small size ratios.

Fleshman and Rice (2013) developed a laboratory apparatus for assessing the hydraulic conditions necessary for the initiation of piping erosion. That apparatus was designed to provide a constant hydraulic gradient throughout a sample with retaining the sample in a sample holder. Increasing differential head was applied across the sample while observations of soil behavior and measurement of pore pressure throughout the sample was made. The observations of the soil behavior during the tests showed there are four stages of the initiation of piping: 1) first visible movement, 2) heave progression, 3) boil formation, and 4) total heave. Tests were performed on sandy soils representing a variety of grain size, grain shape, gradation and specific gravity. The test results indicated that: 1) angular soils showed greater piping resistance, 2) graded soils showed greater piping resistance, and 3) soils with higher specific gravity showed greater piping resistance.

A device which could impose dynamic cyclic flow was developed by Hameiri and Fannin (2002). The flow conditions in the gradient ratio test, using head control, were similar to those in marine protection works. Each test included a stage of unidirectional flow, followed by stages of cyclic flow at a frequency of 0.2 Hz and 0.02 Hz. Flow reversal invokes an initial transient state of water head distribution in the sample, attributed to changes in hydraulic gradient to accommodate the new values of constant head at the inflow and outflow. The recommendation from the results was made that testing of filtration compatibility in dynamic cyclic flow include a stage of slow flow reversal to permit a quantification of water head distribution under steady flow.

Moffat and Fannin (2006) developed a large rigid wall permeameter that could examine the hydromechanical conditions prevailing at the onset of seepage-induced failure in soils with potential internal instability. The sully mixing and discrete deposition approach were employed to reconstitute a homogeneous, and saturated test specimen. Two arrays of pressure transducers, located on opposite sides of specimen, was installed to measure the variations of hydraulic gradient along the specimen. Two load cell with frictionless loading ram were fabricated in the top and bottom, to assess the influence of side wall friction and thereby establish the distribution of vertical effective stress along the length of the specimen. The results revealed that the developed apparatus allows a novel examination of the initiation of hydraulic gradient. The relationship between the effective stress and hydraulic gradient at the initiation of internal erosion could be further investigated.

To compared the internal erosion and surface erosion, a device for flow pump test was devised and presented by Reddi et al. (2000). Tested samples were 70% Ottawa sand and 30% Kaolinite mixtures with distilled water and NaCl solutions. A surface erosion test where the fluid was pumped through a cylindrical hole of 7 mm diameter, and an internal erosion test where the fluid was pumped through intact compacted samples, were performed. A simple capillary tube model was applied to estimate the critical shear stresses needed to cause erosion. It was found that the critical shear stress for surface erosion was larger than that for internal erosion. Erosion rates estimated using surface erosion parameters were significantly greater than those observed in internal erosion experiments. The results suggested that the fate of eroded particles, including particle deposition and pore clogging, may govern the internal erosion process far more than the surface erodibility of the soil.

A new apparatus, called true triaxial piping test apparatus or TTPTA, was developed for testing a wider variety of soils under a wider range of confining stresses, hydraulic gradients, and pore pressures by Richards and Reddy (2010). The TTPTA was capable of applying a range of confining stresses along three mutually perpendicular axes in a true triaxial test apparatus. Pore pressures were also controlled through regulated inlet and outlet pressures. The test determined the critical hydraulic gradient and, more importantly, the critical hydraulic velocity at which piping is initiated in non-cohesive soils. Three sets of initial tests were conducted using uniform sand to (1) assess the repeat ability of test results, (2) evaluate how the rate of change of inflow impacts the critical discharge rate at which piping is initiated, and (3) evaluate how the angle of seepage affects the critical velocity for piping initiation. It was found that the TTPTA was capable of yielding fairly consistent results. The seepage angle tests demonstrate that the angle between seepage flow direction and the direction of gravity is an important factor to consider when evaluating piping potential. Based on the results, the hydraulic gradient was found to be a less reliable indicator of piping potential than

the hydraulic velocity for non-cohesive soils.

A triaxial erosion apparatus was developed by Ke and Takahashi (2014b) to directly investigate the mechanical behaviors of eroded soils. By employing the newly developed apparatus, the back pressure in the specimen could be maintained so that the saturation degree during the erosion test could be relatively high. A consecutive monitoring system was installed to permit continuous recording of eroded soil mass. The mixtures of silica nos. 3 and 8, which are gap-graded non-cohesive soils and vulnerable to internal erosion, were used in the tests. The erosion tests were performed by constant flow rate control mode with measurement of induced pressure difference between the top and bottom of specimens under preferred stress states. The volumetric strain of the specimens was measured during the seepage and subsequent compression tests. The mechanical consequences of internal erosion, in terms of stress strain relationship, were evaluated by conducting monotonic compression and cyclic tests on the eroded soils. The results revealed that the hydraulic conductivity could increase due to internal erosion, so as to the volumetric strain. The drained compressive strength was also reduced by internal erosion. The undrained peak deviator stress of the soils with erosion was higher than that of soils without erosion. Undrained cyclic tests indicated that the eroded soil would fail after more cyclic loops compared to the original soil.

Chang and Zhang (2011) developed a stress-controlled erosion apparatus to investigate the initiation and development of internal erosion under complex stress states. The effects of internal erosion on soil stress strain behaviors was examined as well. The apparatus allowed independent control of hydraulic gradient and stress state. The hydraulic gradient was controlled using a water head control method. The eroded soils and the outflow rate were measured using a soil collection system and a water collection system, respectively. The erosion rate and variation in permeability could be measured during the seepage tests. A series of erosion tests were performed on cohesionless gap-graded soils under the same confining pressure but difference deviator stresses. The resulted indicated that the maximum erosion rate, the variations in soil permeability, and the total deformation of the specimen increased in the increase of deviator stress. The soils changed from dilative behavior to contractive behavior during the drained compression after loss a significant amount of fines.

Xiao and Shwiyhat (2012) modified a triaxial apparatus, made it permit the seepage through compacted specimens and allow collection of effluence and eroded soils. A poorly graded river sand with an addition of 10% kaolinite clay was used to create the gap-graded soils. The size of specimen was 5.1 cm in diameter and 10.2 cm in length, which was monitored for changes in volume and permeability during the seepage tests. After the seepage tests, the specimens were compressed by the consolidated undrained compression tests. The specimens were collected after the test, and the

particle size distribution was analyzed to determine the erosion rate. Companion control specimens were tested without erosion. The results showed that the internal erosion could affect the physical and mechanical properties of soils. The permeability of the specimens reduced after internal erosion, indicating fine particles migration and clogging within the specimen. The gap-graded soils exhibited a greater degree of erosion rate, permeability reduction, and volume change than the poorly graded soils.

The conventional triaxial compression test is the most common procedure used by geotechnical engineering researchers and practitioners to determine the strength and deformation properties of soils. It involves testing a cylindrical soil specimen under symmetric loading condition to present complex soil field conditions. However, most field cases such as behavior of earth dams, and stability analysis of slopes and levees are better presented if the soil is tested under plane strain conditions. Higher peak stress values followed by severe softening have been reported for specimens tested under plane strain loading compared to triaxial compression. Alshibli et al. (2004) developed a plane strain apparatus for soil testing, which is shown in Fig. 2.11. The design of the new apparatus took into consideration the flexibility in accommodating different specimen size, easy assembly procedure, and well-controlled boundary conditions. The apparatus was well instrumented with load, displacement, and pressure sensors and had the ability to capture localization and shear band development. A comparison between two experiments that were conducted on Ottawa sand was presented and the effects of inhibiting lateral movement of bottom end platen was discussed. The resulted demonstrated that the restraining lateral movement of bottom end platen would result in higher peak and residua load values.

Wanatowski and Chu (2006) presented a new plane strain apparatus. The main feature of than apparatus was that the intermediate principle stress could be measured by four submersible pressure transducers. Very loose to medium dense sand were tested by this apparatus. The resulted showed that the failure envelope obtained from the plane strain tests was lower than that from triaxial tests. In terms of friction angle, the value obtained from plane strain tests was higher than that from triaxial tests. The critical state line obtained under plane strain conditions was also different from that obtained under axisymmetric conditions. Under plane strain conditions, shear bands occurred for medium loose to dense specimens. However, no visible shear bands are observed for very loose specimens.

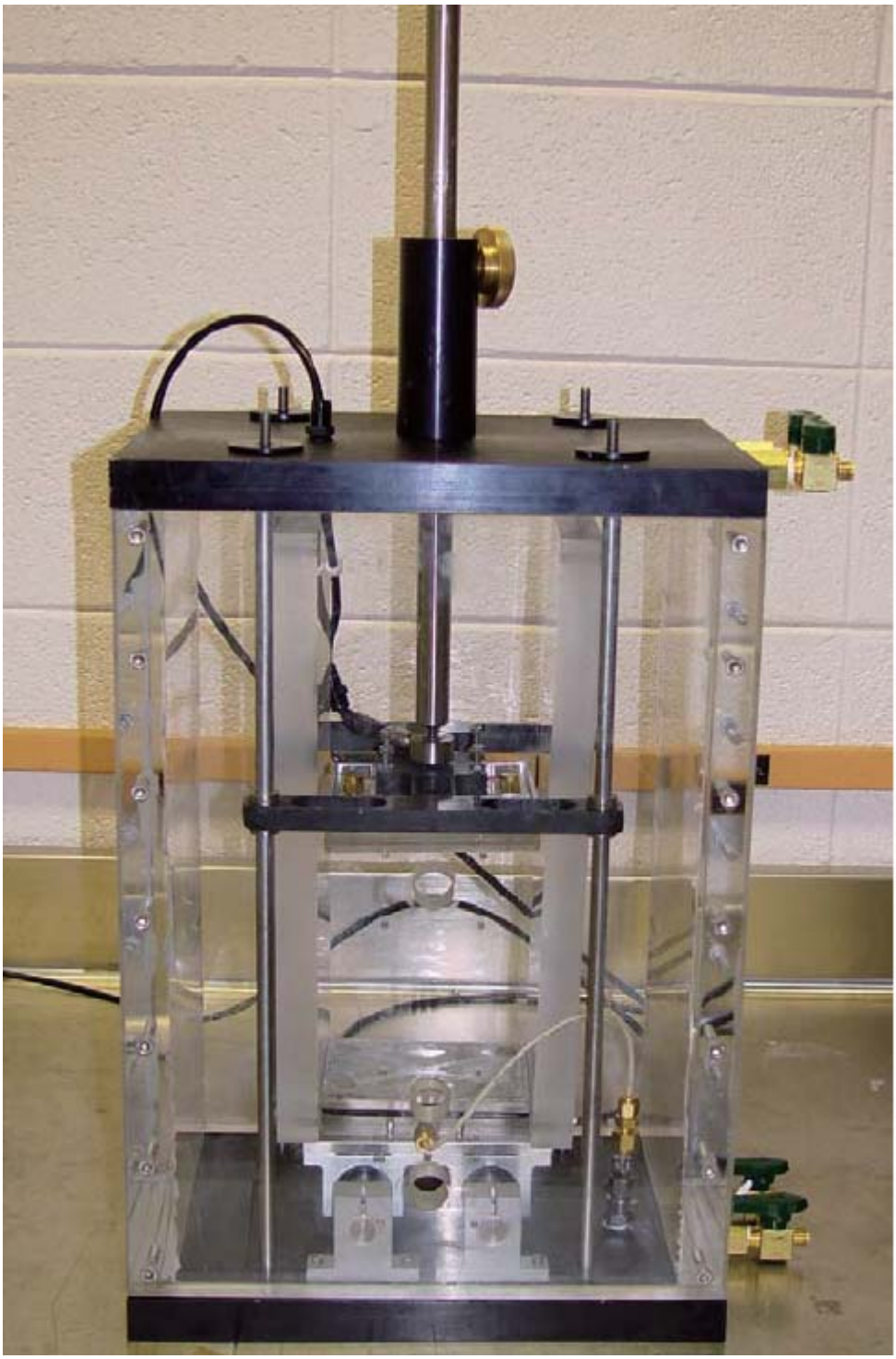

Figure 2.11: The photography of the plane strain apparatus (after Alshibli et al. (2004))

2.4 Image analysis on internal erosion

The characteristic of particle arrangement and composition directly contribute to the soils mechanical behaviors. To investigate the fabric of soils, many digital image analysis techniques were developed, including the experimental micro mechanics for geometerials. The quantification of geomaterials by image analysis is reviewed in this section, together with its application on the internal erosion.

Tovey et al. (1992) proposed several image processing and analysis techniques to study the mineralogy and microfabric of soils. The analysis began with a multi-spectral classification of SEM back-scattered electron images and X-ray maps, followed by particle size routines on the segregated mineral grains. Masking these large grains hen permitted intensity gradient techniques to be used to study the orientation patterns within the matrix. Finally, segmentation of the orientation image into domains of similar alignment showed how the orientation of matrix related to that of skeleton mineral grains. Two contrasting soil samples were used to illustrate the technique and the results indicated that the objective measurement was better than the qualitative interpretation. In one sample, the strong alignment of matrix orthogonal to the direction of alignment of most of the mineral grains was discovered.

Frost and Kuo (1996) noted that the frequency distribution of local void ratio is believed to be an important parameter, in addition to the void ratio, for describing the mechanical behaviors of granular materials. They proposed a fully automated implementation method, which used the high-level, image processing techniques. Oda (1972) investigated the initial fabric of granular materials, and proposed the method to quantify it. That method needed many subjective judgment and manual operation. The proposed method here eliminates operator judgment and manual work on obtaining the distribution of local void ratio, and makes the determination of that distribution more repeatable and efficient. The method was illustrated with measurement performed on synthetic and real images. The thickness of segmentation lines on correcting the images was discussed. Through the examination on the stability of proposed polygon network generation procedure, it was found that only polygons immediately adjacent to and contained part of moved particles affect the results.

Nonuniformity within specimens of granular materials is considered to be one of the major reasons for the dependence of the observed static and dynamic response during laboratory testing. To examine the uniformity of cohesionless specimens, Kuo and Frost (1996) proposed a resin-impregnation and digital image analysis method at microscopic, macroscopic and global scale. The proposed approach relies on the equivalence between volume fraction and the expected value of area fraction

where the area fraction of voids on two dimensional section is obtained using a computer based image analysis system. A sampling strategy which allows porosity variations in the vertical direction as well as in the radial direction of the specimen to be examined is proposed. The method was illustrated with the results of measurements performed on a typical specimen and allowed that a much large amount of uniformity exists when the soil was examined at a microscopic level. The results demonstrated that the proposed method could effectively and efficiently examine the uniformity of specimens.

Kuo et al. (1998) proposed an approach in determining the stereology based fabric tensors. Fabric tensors, which characterize the distribution of directional data from microscopic observations, are considered as a useful measure of the anisotropy for granular materials. Therefore, they proposed a method to measure the several stereology based fabric tensor, including surface area tensor, mean free path tensor and porosity tensor. The formulations of them in three dimensions could be obtained by making the observations in three mutually prependicular planes. The measurement techniques using image analysis and the implementation approach by mathematic algorithm were presented. It was demonstrated that the proposed method was not depended on the shape or size of particles and voids. Therefore, it could be generally applied to a wide range of granular materials.

Tovey and Dadey (2002) quantitatively studied the orientation patterns and microscopic porosity of marine sediment by digital image analysis. Orientation was specified by two separate parameters, an index of anisotropy and a direction of orientation. The results from the digital image analysis showed it was a promising method to quantify the marine sediment as well as other granular materials.

The effects of fabric anisotropy on granular soil response was presented by Yang et al. (2008). The image analysis based technique and an appropriate mathematical approach were used to quantitatively compare the mechanical behaviors of soils prepared at moist tamping method and dry deposition method, from the microscale level. It was found that the specimen prepared by the dry deposition method had a more anisotropic microstructure than the specimen prepared using the moist tamping method. It was considered directly associated with the experimental observation that different sample preparation methods produce samples with distinctive responses under otherwise identical conditions.

The image analysis technique is also employed in describing soil particles characteristics in a variety of aspects. The microstructure of soil sand samples extracted at a depth of 75 m from the Alberta, Canada, had been investigated by Doan et al. (2012). The high resolution three dimensional X-ray microtomography and cryo scanning electron microscopy were used to record the images. The

obtained images showed that some dense area composed of highly angular grain surrounded by fluids, which were separated by larger pores full of gas. In dense areas, 3D image analysis provided porosity values comparable with in situ log data and macroscopic laboratory determinations, indicating that they were representative of intact states. Hence, the image analysis could provide information on th morphology of the cracks and disturbance created by gas expansion. Bitumen was found to strongly adhere to the grains, with some grains being completely coated. The curved shape of some bitumen menisci suggested a bitumen wet behavior.

Reinson et al. (2005) studied the unsaturated flow in coarse porous media. The experimental measurements of seepage velocity and volumetric water content were obtained for a column of 12 mm galss beads using digital image analysis to capture the movement of a dye tracer front at several infiltration rate. The estimated curve for hydraulic conductivity versus matrix suction was compared to the theoretical value, the good agreements of which proved the proposed approach was reasonable and effective.

The image analysis was reported by Desrues et al. (1996) in studying of the strain localization in triaxial tests. The inception and development of strain localization were quantitatively and quantitatively described. Dense and loose Hostunn RF sand specimens were used in the testing under a confining pressure of 60 kPa. It was shown that the strain localization could occur in different localization patterns depending on the test conditions. The comparison of the local void ratio evolution in the shear zones with global void ratio measurement supported the fact that a limit void ratio was reached in the shear zone. Interestingly, this limit void ratio was significantly different from the final void ratio defined from the global measurements.

Digital Image Correlation (DIC) is an image processing technique that calculates fields of incremental displacement by comparing two digital images and locating numerous small regions in both images to high subpixel accuracy. This technique is particularly well suited to the visualization of geotechnical failure process such as plastic collapse of a shallow foundation or the evolution of failure within a physical model landslide as it can yield full-field displacements at high spatial and temporal resolution. Take (2015) provided an updated review of the factors that affect accuracy and precision of the technique and highlighted recent advances and emerging uses of DIC in geotechnical engineering applications. The DIC was reviewed with particular focus on subset texture and size, camera noise, choice of subpixel interpolation scheme, and the camera geometry errors associated with out-of-plane movement, self-heating, and the complexities of making observations through thick transparent windows. Example applications have been discussed where DIC measurements used to visualize failure process and make quantitative measurement of deformation within physical models, to measure surface heave in the field due to construction process, to use low-altitude

imaging to collect 3D point cloud data of ground movements, and to obtain field measurement of rail track stiffness under dynamic train loading. The other applications of DIC on geotechnical engineering were also mentioned, like the applications on transparent soils and digital volume correlations. Finally, the author concluded that it is expected that the number and breadth of DIC applications in geotechnical engineering will continue to grow due to the versatility of the technique. Encouragingly, as the accuracy and precision of DIC techniques are defined in terms of a fraction of a pixel, annual advances in the stability and spatial and temporal resolution of camera hardware will translate directly into annual improvements in the accuracy and precision of the technique, even in the absence of further improvements to DIC technologies.

A deformation measurement system based on Particle Image Velocimetry (PIV) and close-range photogrammetry was developed by White et al. (2003) for use in geotechnical testing. Digital photography was used to capture images of planar soil deformation. Using PIV, the movement of fines meshes of soil patches was measured to a high precision. Since PIV operates on the image texture, intrusive target markers need not be installed in the observed soils. The resulting displacement vectors were converted from image space to object space using a photogrammetric transformation (Heikkila and Silven, 1993). A series of validation experiments were presented. The results demonstrated that the precision, accuracy and resolution of the system were an order of magnitude higher than previous image-based deformation methods, and were comparable to local instrumentation used in element testing. It was concluded that the PIV could be a promising approach in geotechnical engineering.

In the experimental study of cone penetration in silica sand reported by Arshad et al. (2014), the DIC and PIV were utilized. During the cone penetration tests, the cone resistance was measured, and digital images of the cone penetrating into the sand samples were acquired simultaneously during the entire penetration process. The DIC technique was then used to process these images to obtain the soil displacement field resulting from cone penetration. The results from DIC analysis and measured cone resistance suggested that the soil displacement around an advancing cone depended on the density and crushability of the sand, as well as the depth of penetration.

Many soil mechanics at grain scale are also investigated based on digital image analysis. The experimental side of the micromechanics of soils, was a somewhat risky bet considering a still narrow field (Baudet and Pereira, 2013). Andrade et al. (2012) presented new computational and analytical tools to accurately measure the kinematics and inference of contact forces, directly from imaging tools. The grain sale data are then used to construct powerful multiscale models that can predict the emergent behaviors of granular materials, without resorting to phenomenology, but can rather directly unravel the micro-mechanical origin of macroscopic behaviors. The aim of these tools

is to furnish a “tomography to simulation” framework, where experimental techniques, imaging procedures, and computational models are seamlessly integrated. These integrated techniques will help define a new physical based approach for modeling and characterization of granular soil in the near future.

Andò et al. (2013) presented an combined X-ray tomography and three-dimensional image analysis to experimenally study the microscale geomechanics. It was reported that when the recorded images have a high spatial resolution, it could be able to get high quality measurements, i.e., displacement and rotation of individual particles. However, when it comes to the grain-to-grain contacts or production of fines by breakage, it could become challenging.

The size and shape of sand particles were quantified through the digital image analysis by Altuhafi et al. (2013). It introduced a programmatic approach for quantitative shape analysis that has the potential to be broadly adopted in geotechnical engineering research and practice. The approach generated three shape parameters: convexity, sphericity, and aspect ratio, which could be easily calculated from digital images. The database of 36 sands in terms of the shape parameters was quantified and presented in their paper.

The image subtraction was employed by Rosenbrand and Dijkstra (2012) to quantify the internal erosion. The observations were made for a gap-graded plane strain sample behind a transparent window. Image subtraction was used for analysis the transportation of finer particles. It was concluded that the transportation and removal of materials from the soil appear to be localized. This results in a localized depletion, which has implications for the mechanical and hydraulic stability of in situ construction.

2.5 Soil mechanics in triaxial and plane strain tests

One of the objectives of this search is to examine the mechanical consequences of soils subjected to internal erosion. To reach this end, a series of triaxial compression tests was performed in a revised triaxial apparatus. A plane strain erosion apparatus was developed, the mechanical responses of soils under plane strain conditions were also investigated. To compare the mechanics behaviors of soils with and without erosion, the soil mechanics in triaxial and plane strain tests are reviewed mainly in terms of soil (i) stiffness and (ii) strength.

2.5.1 Stiffness of element test

Research on the small strain (0.001% - 1%) characteristics of sedimentary soils and sand is important in engineering analysis and practical design. The effects of stress paths on the small strain stiffness of completely decomposed granite were reported by Wang and Ng (2005). A systematic laboratory investigation on the small strain characteristics of intact completely decomposed granite subjected to drained compression and extension stress paths was presented. Measurements from the bender elements illustrated that the elastic shear modulus of completely decomposed granite increases as the mean effective stress increases and the void ratio decreases. Significant nonlinear shear stiffness – shear strain, and bulk modulus - volumetric strain relationships were observed. At 0.01% shear strain, the measured average shear stiffness obtained from the extension tests was about 60% higher than that from the compression tests.

Many studied have been performed on the shear strength and stiffness of clean sands. However, natural sand generally contain significant amounts of silt or clay. The mechanical response of such soils was studied by Salgado et al. (2000), and it was noted that they behaviored differently from the clean sand. The tested materials were Ottawa sand with fines content in the range of 5% to 20% by weight. The effects of these non-plastic fines on small-strain stiffness and shear strength was discussed. It was noted that the small strain stiffness at a given relative density and confining stress level decreased dramatically with the addition of even small percentage of fines. It indicated that the geotechnical problems involving silty sand using stiffness properties of clean sand could cause serious problems.

It is known that clean soils behave nonlinearly from the very early loading stage. The nonlinearity could also change when the granular soils contain a certain amount of fines, since the stiffness and strength vary with fines content. A modified hyperbolic stress strain relation was proposed by Lee et al. (2004) to representing the degradation of elastic modulus of silty sands. The proposed model was based on two modulus degradation parameters that determine the magnitude and rate of modulus degradation as a function of stress level. A series of triaxial tests was performed, and the results were employed in demonstrating the feasibility of the proposed model. It was found that the small strain stiffness decreases with increasing fines content could be reasonably modeled by the new method. Regarding to the peak strength, the modified hyperbolic stress strain relation could give a better agreement with the experimental results than the conventional one.

A series of laboratory investigation on the static behaviors of silica sand containing various amount of either plastic or nonplastic fines was performed by Carraro et al. (2009). Specimens were reconstituted using the technique suitable for element testing of homogeneous specimens of sands

containing fines deposited in water. The fabric of sands containing fines was examined using the environmental scanning electron microscope. Static, monotonic, isotropically consolidated, drained triaxial compression tests were performed to evaluate the stress-strain-volumetric responses. Piezoceramic bender element instrumentation was developed and integrated into a conventional triaxial apparatus. Shear wave velocity measurements were made to evaluate the small strain stiffness of the sands tested at various state. It was observed that the small strain shear modulus was affected by both the amount of fines and their nature. Larger reduction was found for the mixtures of Ottawa sand with nonplastic silt than for Ottawa sand with Kaolin clay, on the condition that they were prepared with the same fines contents and relative densities. The more angular nonplastic silt particles tended to interact with irregularities on the surface of sand particles, increasing the "jamming" effect during shearing. Clay particles, in contrast, tended to "lubricate and smooth over" the defects on the sand particle surface. It was demonstrated that single geometrical models like intergranular void ratio or skeleton void ratio may not be suitable to explain the mechanical responses of sand containing different types and contents of fines. The effects of intrinsic microstructural characteristics and plasticity of the fines might be taken into consideration.

2.5.2 Soil strength of element test

It has been demonstrated that the secant angles of shearing are required in a rational approach of the strength and dilatancy of sands. The data of strength and dilatancy of 17 sands in axisymmetric or plane strain conditions at different densities and confining pressures were collated by Bolton (1986). It was noted that the critical state angle of shearing resistance of soil which is shearing at constant volume is principally a function of mineralogy and can readily be determined experimentally within a margin of about 1°C, being roughly 33°C for quartz and 40°C for feldspar. The extra angle of shearing of dense soil is correlated to its rate of dilation and thence to its relative density and mean effective stress, combined in a new relative dilatancy index. It was concluded that the relative proportions of friction and dilatant strength components are likely to be particularly important in investigations of the liquefaction potential.

Alarcon Guzman et al. (1988) carried out a series of undrained monotonic and cyclic shearing tests on sands. Following two interpretations were discussed: 1) the conditions leading to limited or steady-state flow deformation under monotonic loading; and 2) the state conditions marking the initiation of strain softening behavior under either monotonic or cyclic undrained loading. It was found that the effective stress path in monotonic undrained shear appears to constitute a state boundary that controls the initiation of strain softening under undrained cyclic shear loading. Evidence was presented in support the new concept of the collapse of soil fabric. The concept of

this state that the soil sustain unlimited volume deformation without increasing of deviator stress was defined as the critical state.

The state parameter was put forward by Been and Jefferies (1985). It was reported that a rational engineering approach to evaluate the performance of constructing structures was required. In particular, there was no single parameter which could measure the soil behaviors. The state parameter, which combines the void ratio and stress level with reference to the critical state, was proposed to describe the soil behavior. By employing the state parameter, the soils contractive and dilative behaviors could be reasonably estimated.

The effect of stress path on the steady state line of a liquefiable sand was investigated by Vaid et al. (1990). The results from undrained triaxial compression and extension tests on water deposited sands showed that the steady state line of a given sand though unique in the effective stress space, was not so in the void ratio – effective stress space. The quasi-steady state was defined as the state where the mean effective stress showed the local minimum value in the stress strain relations. The sand was contractive over a much larger range of void ratios in extension than in compression. It was concluded that the steady state strength was smaller in extension than in compression at a given void ratio, the difference increasing as the sand became looser.

A series of laboratory tests were performed in understanding the liquefaction potential of sand by Sladen et al. (1985). Analysis of undrained triaxial tests, undertaken to measure steady state parameters, suggested that there is a "collapse surface" in three dimensional void ratio – shear stress – normal stress space. A necessary condition for liquefaction was that the soil state lie on this surface. This collapse surface concept was fundamentally an extension of the steady state concepts, followed by the critical state soil mechanics. The collapse surface approach proposed that the use of residual strength parameters could be considered valid if there were some reasons that the soil strength might be reduced. It would give a larger safety for considering the stability of the structures.

Tsukamoto et al. (2009); Ishihara et al. (1975); Ishihara (1993) reported the liquefaction and flow failure ob sand under cyclic loading. The phase transformation state was proposed as the soil transfer from contractive behavior to dilative behavior. The vital engineering significance: 1) triggering condition, and 2) consequences of liquefaction was discussed. It was reported that the residual strength played a major role for the post seismic stability analysis. The examination of test results proposed a new way in examining the residual strength of different soils. The laboratory results based relation of normalized residual strength agreed well with that from the field parameters. It was considered as a consistent approach in investigating the soils undrained behaviors.

The flow potential of sand during liquefaction was examined by Yoshimine and Ishihara (1998). The flow potential was defined as the maximum value of excess pore water pressure ratio developed during undrained monotonic loading tests. A series of triaxial compression tests, triaxial extension tests and simple shear tests on Toyoura sand were conducted. The results revealed that the flow potential of sand was greatly affected by shearing mode. For sand at the same relative density, the flow potential in triaxial compression was lowest, which in triaxial extension, it was highest. It also noted that the flow potential was related to residual strength ratio. The instability of loose sand under undrained compression was examined by Leong and Chu (2002). The instability here was referred as the behavior where large plastic strain are generated rapidly due to the inability of a soil element to sustain a given load or stress.

In order to clarify the behaviors of sand containing an amount of finer fractions, many researches have been performed (Zlatovic and Ishihara, 1997; Ni et al., 2004; Thevanayagam et al., 2002; Yang and Wei, 2012; Thevanayagam and Mohan, 2000; Chang and Meidani, 2013; Yang et al., 2006a,b; Murthy et al., 2007; Yamamuro and Covert, 2001; Rahman et al., 2008; Yamamuro and Lade, 1998; Abedi and Yasrobi, 2010; Rahman et al., 2011; Bobei et al., 2009; Yang et al., 2015). The approach in investigating the behaviors of mixed sand could be mainly divided into three parts: 1) experimental observation under critical state soil mechanics; 2) intergranular void ratio to modify the state parameter; 3) microscale stress strain modeling.

Regarding to the experimental observations, Abedi and Yasrobi (2010) performed the tests with plastic fines content ranging from 0% to 30%. The results demonstrated that an increase in plastic fines led to an increase in instability, followed by a decrease with a further increase in fines content. The slope of steady state lines in effective stress path increased with increase of fines content, but after certain fines content, it began to decrease. Similar results on the plastic fines were also reported by Ni et al. (2004). Yamamuro and Lade (1998); Yamamuro and Covert (2001) performed a series of undrained monotonic and cyclic tests on silty sands. The tested materials were Nevada sand with up to 40% silt content. It was reported that the greater silt content appeared to provide a more volumetrically contractive responses throughout the entire stress strain curve. Unique steady state lines were not always exists for silty sands. Thus, a unique relation between void ratio and confining pressure, may not represent the behaviors of sand with non-plastic fines. Zlatovic and Ishihara (1997) presented that the normalization of the undrained stress strain curves and stress paths to the initial confining pressure, could provide a meaningful interpretation of soil behavior. Regarding to the effects of fabric on the undrained behavior, it was found that they are negligible up to the peak strength. However, once the shear straining reaches the state beyond the peak, the fabric becomes a very important factor governing the undrained response of non-plastic soil, which includes the

residual shear strength. When soil is largely sheared to reach the steady state, gradual remolding erases the initial fabric and ultimate stress state is, governed by the void ratio only, once again not affected by the initial fabric. A series of undrained compression tests on Ottawa sand containing 0%, 5%, 10%, and 15% non-plastic silt was performed by Murthy et al. (2007). The undrained mechanical responses were discussed at critical state, phase transformation state, quasi-steady state and state of undrained instability. The specimens were prepared by slurry deposition and moist tamping methods. It was observed that an increase in the non-plastic fines content leads to a downward shift of the critical state line in the void ratio - mean effective stress space and an increase of the critical state friction angle. The results revealed that the behavior in early stage of shearing was largely affected by the specimens initial fabric. The specimens prepared by moist tamping method demonstrated larger undrained peak strength than the slurry deposited specimens. The steady state lines for silty sand with various fines contents were investigated by Yang et al. (2006b). It was indicated that location of the steady state lines in the void ratio – mean effective stress space is different for each mixture, but parallel. Yang et al. (2006a) studied the instability line of the silty sand. It was reported that the slope of the instability lines increases with the increasing relative densities, and it approaches the slope of the failure line at a high relative density.

Thevanayagam and Mohan (2000); Thevanayagam et al. (2002) investigated the undrained behaviors of silty sand, and proposed to employ the intergranular void ratio to characterize the mechanical responses. Based on the intergranular void ratio and interfine void ration, the intergranular state parameters were introduced. These intergranular void ratios could be applied to describe the plastic compressibility at low and high fine contents. The stress strain behaviors of silty sand were compared with that of host sand by the proposed parameters. The results indicated that it was a promising approach in interpreting the behaviors of silty sand. Base on the intergranluar void ratio, the concept of threshold fines content was also proposed. The instability of the silty sand was then analyzed by the function of fines and coarse fractions with the division by threshold fines content. Rahman et al. (2008, 2011) modified the intergranular state parameter, and proposed the equivalent granular void ratio and equivalent granular state parameter. It was reported that at low fines content, an increase in fines content leads to a downward of critical state line in the void ratio – mean effective stress space; which at high fines content, the critical state line will move upward with increase in fines content. Therefore, the proposed a method to calculate the threshold fines content. Based on that, the equivalent granular state parameter was introduced and recommended in describing the soils undrained behaviors. Similar researches were carried out by Bobei et al. (2009); Yang et al. (2015). The global void ratio and skeleton void ratio, and the state parameters were examined and discussed based on the experimental results on silty sand.

The microscale modeling of the behaviors of sand mixing with fines was performed by Chang

and Meidani (2013). The proposed model was based on a micromechanical approach, which involves mean field assumptions. The dominant fraction changes according to the fines content. The applicability of the developed stress-strain model was shown to be promising in estimating the behaviors of soils containing full range of fines content. Yang and Wei (2012) investigated the collapse of silty sand by experiments and image analysis. The microscopic image of the particles demonstrated that fines work differently for soils with different fines contents.

2.6 Summary

It was demonstrated that the constriction size could be dominant rather than the particle size in assessing the internal instability. The experimental research, theoretical modeling and numerical simulation were performed in studying the controlling constriction size. The laboratory tests on investigating the hydro mechanical responses of soils subjected to internal erosion mainly focused on the initiation hydraulic gradient, flow velocity, cumulative eroded soil mass, and volumetric deformation. The simulation of internal erosion by various approaches demonstrated that the main feature could be reproduced, however, improvements were needed.

Permeameter was widely employed in examining the influence of internal erosion on hydraulic conductivity change and volume deformation. Some triaxial apparatus were revised to accommodate the seepage in the triaxial cell to investigate the internal erosion under stressed conditions. The mechanical consequences of cohesionless soils subjected to internal erosion were reported based on the developed apparatus.

Digital image analysis was a promising approach in the geotechnical engineering. The shape and fabric of the uniform particles could be identified based on the digital image analysis. However, recently, there was only limit research on the application of image analysis to internal erosion.

The soil mechanics in triaxial and plane strain conditions were reviewed in stiffness (small strain level) and strength (medium strain level). It was reported that the undrained responses of soils with fines were affected by the fabric. The mechanical behavior of soil containing amount of fines was examined, although few parameters were accepted to characterize its responses.

Chapter 3

Undrained behaviors of soils subjected to internal erosion by triaxial erosion tests

3.1 Introduction

Internal erosion is a subsequent transport of detached finer soil particles through the matrix under seepage flow. The initiation of internal erosion has been investigated in terms of the susceptibility of material, hydraulics and mechanics (Bonelli, 2012). This chapter investigates the mechanical consequences of soils subjected to internal erosion with different fines contents through the triaxial erosion tests.

Typical behaviors of granular soils in undrained compression test is introduced by Fig. 3.1. The deviator stress is defined as the difference between the axial and radial stresses. The undrained peak state (A and A' in Fig. 3.1) is a state where deviator stress reaches an initial local maximum value in the stress strain curve. Quasi-steady state (B and B' in Fig. 3.1) is where the deviator stress reaches a minimum value (Alarcon Guzman et al., 1988). Phase transformation state (C in Fig. 3.1) is an indication that soil behavior changes from contractive to dilative. The points D and D' stand for the critical state, which represents the ultimate condition where the plastic shearing could continue indefinitely without changes in volume or effective stress (Muir Wood, 1990). When the critical state coincides with the quasi-steady state, it indicates the occurrence of flow behavior (dash line in Fig. 3.1) (Tsukamoto et al., 2009). The limited flow behavior (solid line in Fig. 3.1) suggests that the deviator stress temporarily decreases after its initial peak, but reaches a larger value at critical state as shearing continues.

During the earthquake, the pore water cannot be drained during a relative short period, which caused an increase of pore water pressure at constant soil volume. This corresponds to the stress path

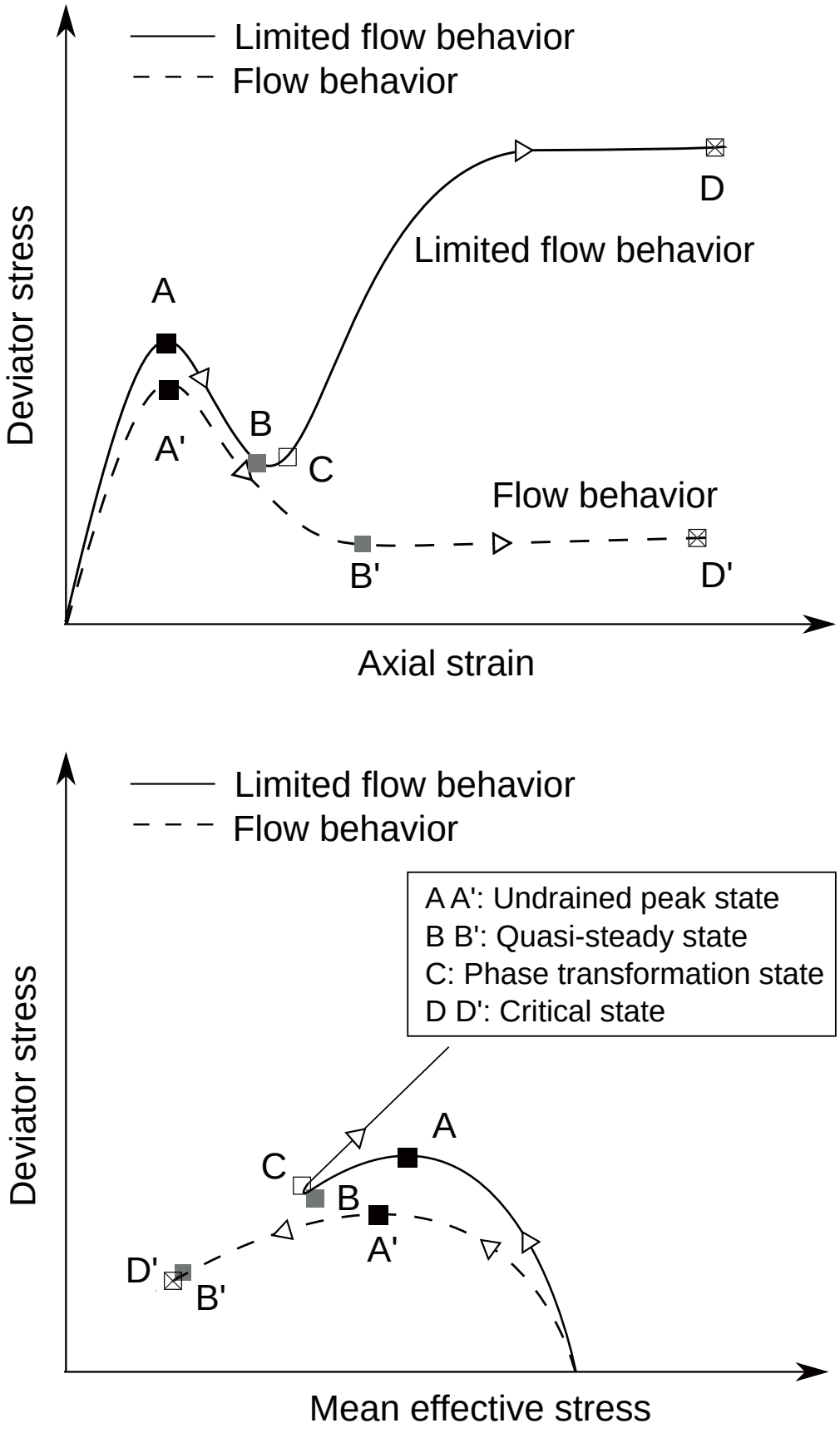

Figure 3.1: Schematic diagram of the characteristics of typical undrained behaviors (after Alarcon Guzman et al. (1988); Muir Wood (1990); Tsukamoto et al. (2009))

under undrained conditions in geotechnical engineering. Therefore, the undrained compression tests were performed in triaxial apparatus to investigate the mechanical responses of eroded soils during earthquake. The main objective of this chapter is to examine the difference of overall undrained behavior at both small strain level and large strain level of eroded soils and original soils. The undrained peak state is discussed in terms of peak strength and mean effective stress ratio. Besides, the tangent stiffness at small strain level is illustrated. Changes induced by internal erosion at quasi-steady state and phase transformation state are elaborated by interpreting the variance in residual strength and flow potential. The influence of internal erosion on critical state is investigated as well. Finally, the correlation between the undrained peak state and the quasi-steady state, together with that between undrained peak state and the phase transformation state, is demonstrated.

3.2 Experimental program

3.2.1 Tested materials

The materials in the experiments were mixtures of natural silica nos. 3 and no. 8. Individual particle is subround to subangular in shape, and predominant mineral is silica. Natural silica no. 3 is regarded as coarse particles, which forms the skeleton of the specimen. The natural silica no. 8 is treated as fines, which could be transported by seepage flow. Although the silica no. 8 is not strictly classified as fines (<0.075 mm), here in this study the fines is defined as the particle size less than 0.3 mm in standard sieve analysis due to the large size of the coarse particles (medium diameter of 1.76 mm). The density for the siliceous sand is 2.65 g/cm^3. The properties of the individual sand and the mixed sands with 15%, 25%, and 35% fines contents are shown in Table. 3.1. The particle size distribution curves are plotted in Fig. 3.2.

One group of tested specimens was prepared with initial fines contents of 0, 15%, 25% and 35% by weight. The undrained monotonic compression tests were performed on this group to examine the influence of initial fines content on the undrained mechanical behavior. Another group of tested specimens was prepared with 15%, 25%, and 35% initial fines contents, on which the seepage tests and subsequent undrained compression tests were performed to investigate the effects of internal erosion on soil behaviors. The seepage tests performed on this group of specimens were carried out in a revised triaxial cell developed by Ke and Takahashi (2014b), which is shown in Fig. 3.3.

3.2.2 Test apparatus

The main part of the revised triaxial erosion apparatus is summarized here. The vertical axial load is automatically applied by the load system with a motor-gear actuator, which could compress the

Table 3.1: Properties of tested materials

	Silica no. 3	15% mixtures	25% mixtures	35% mixtures	Silica no. 8
Fines content (%)	0	15.0	25.0	35.0	100
Maximum void ratio	0.94	0.79	0.77	0.74	1.33
Minimum void ratio	0.65	0.53	0.37	0.36	0.70
Median particle size (mm)	1.76	1.78	1.69	1.54	0.16
Curvature coefficient	0.96	8.69	8.54	0.074	0.99
Uniformity coefficient	1.31	13.0	16.4	19.3	1.05

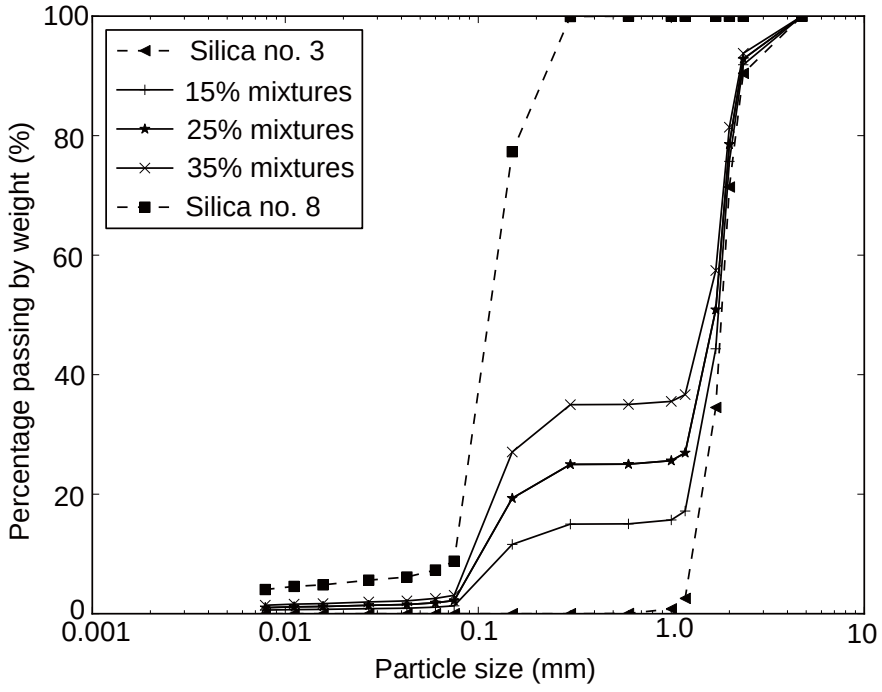

Figure 3.2: Particle size distribution curves

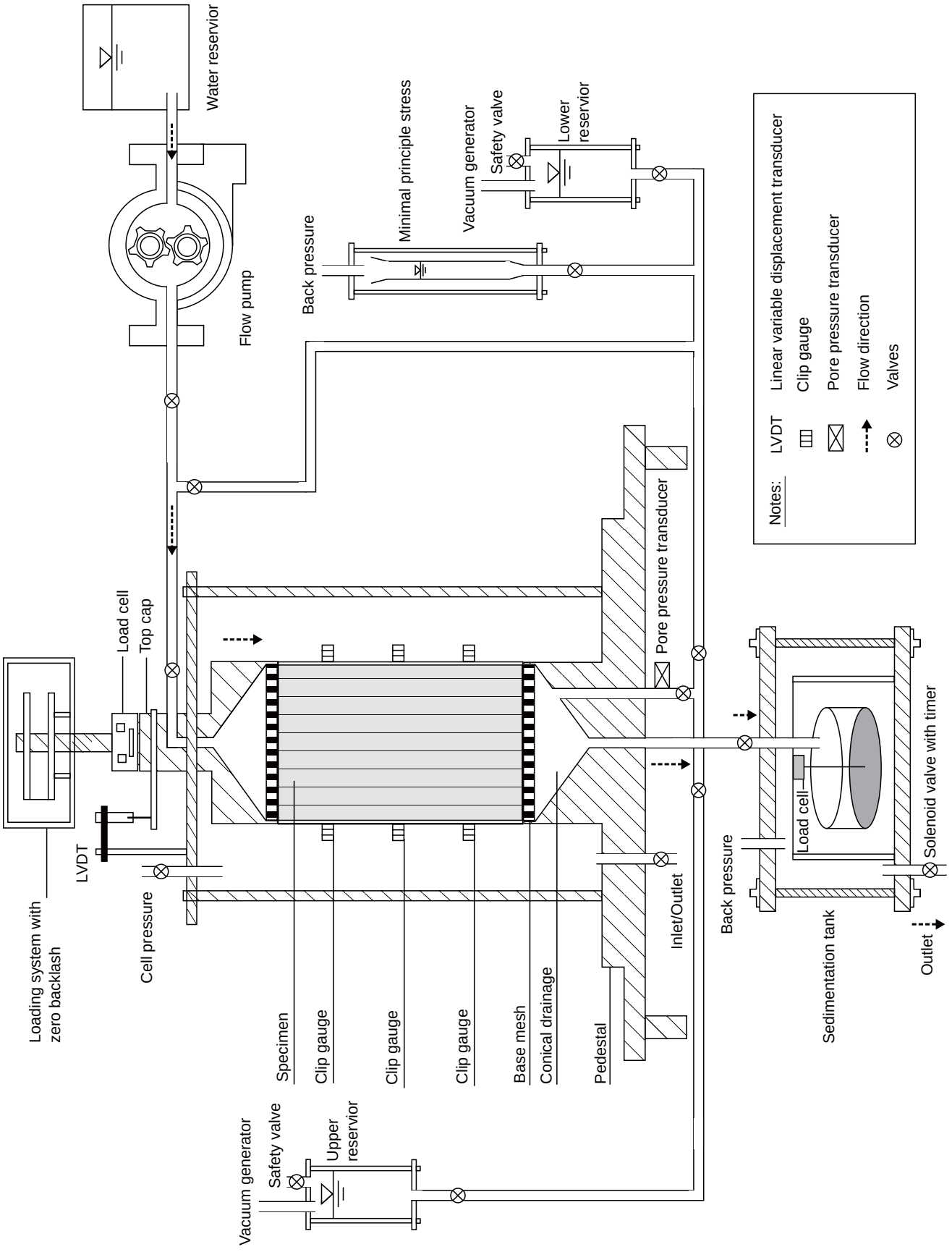

Figure 3.3: Revised triaxial apparatus for seepage test

tested specimen by a controlled strain rate. The cell pressure is applied by the regulated air pressure whose source is maintained constantly at 700 kPa through an automatic air compressor. A 5 mm thickness mesh with 1 mm openings, which follows the recommendation from the U.S. Department of Agriculture (USDA, 1994) to fully hold the coarse particles and allow the transportation of fines, is placed on the end-platen of the pedestal. The base pedestal is revised to accommodate the seepage tests. The drilled conical trough and the tube directly connecting the conical trough with the sedimentation tank are designed to allow the fully dislodgement of fines from the specimens. A miniature load cell in the sedimentation tank is installed to record the cumulative eroded soil mass during the seepage test.

3.2.3 Test procedures

All the specimens were prepared targeting the same initial relative density (Dr = 30%). The size of the soil specimens was approximately 70 mm in diameter and 150 mm in height. The moist tamping method was employed in this study, which was proposed by Ladd (1978) was employed to prevent the segregation of particles with different sizes. The undercompaction theory was recommended to avoid the effects that the lower portion of specimen would be densified by the succeeding compaction from the upper portion if each layer was compacted to the target density. Accordingly, when adopting the moist tamping method, other than the final layer, each layer could be compacted to a lower density than the target density of the whole specimen. Jiang et al. (2003) revised the undercompation criterion proposed by Ladd (1978), and evaluated the planar void ratios of very loose, loose, medium dense and dense specimens prepared with different undercompation criteria. It was demonstrated that the specimens prepared by the nonlinear average undercompaction criteria showed the most homogeneous distributions. Therefore, the nonlinear average undercompaction criterion was employed in this study. The soil specimen was prepared layer by layer with 10 layers in total. To validate that the target density was actually achieved, the after-test oven dry weight of the soil specimen was checked.

After the soil preparation, the top cap was attached and fixed on the top surface of the specimen. The vacuum saturation procedure (JGS, 2000; ASTM, 2012b) was adopted in the experiment. Vacuum was applied to the specimen through water reservoirs gradually until -80 kPa, keeping the pressure difference inside and outside of the specimen constant at 20 kPa. The de-aired water with a total volume of about 10 times of the pore volume was slowly injected into the specimens from the bottom. Generally, the B value of these specimens equaled or was greater than 0.95 in this test. After the saturation, all specimens were isotropically consolidated by an automatic control system to an initial mean effective stress of 50 kPa.

The undrained monotonic compression test was performed on one group of specimens containing 0, 15%, 25%, and 35% fines contents with an axial strain rate of 0.1%/min (JGS, 2000; ASTM, 2012b) upon the completion of the consolidation to examine the influence of fines content on the undrained behavior.

To study the influence of internal erosion of soil mechanical behaviors, seepage test was performed on the other group of specimens in the triaxial cell after the complete isotropic consolidation. The water in the seepage tests was supplied by the water reservoir shown in Fig. 3.3, and it was pumped into the specimens by the flow pump. It is known that the water head control mode could provide an easy calculation of hydraulic gradient, which could be directly employed to describe the hydraulic force induced by seepage flow. However, according to Richards and Reddy (2010), the critical flow (Q) when piping is initiated is the product of the hydraulic conductivity (k), the cross sectional area of seepage (A), and the hydraulic gradient (i) according to Darcy's law. The critical gradient and critical hydraulic conductivity were observed to change irregularly in these tests, while the cross sectional area of seepage was constant. The product of critical gradient and critical hydraulic conductivity was fairly constant from test to test; hence, the critical flow and critical velocity varied little. Therefore it was concluded that flow velocity might be the fundamental characteristic responsible for internal erosion in non-cohesive materials, which could yield more consistent results. Moreover, the flow rate control mode with a rotary pump could ensure continuous water supply for a relative long period. Thus the flow rate control mode was employed in the seepage tests.

The evolution of the applied flow rate was kept the same for all seepage tests, as shown in Fig. 3.4, which is the same as the tests conducted by Ke and Takahashi (2014b). At first, the seepage flow was assigned at a relatively lower flow rate. Then a constant large flow rate (5.2×10^{-6} m^3/s) was applied to the specimen. Upon the completion of the seepage test, the undrained monotonic compression test was performed on the eroded soils with an axial strain rate of 0.1%/min (JGS, 2000; ASTM, 2012b).

3.3 Test results

3.3.1 Seepage test results

According to Kenney and Lau (1985), the particles finer than grain size “d” would likely to be eroded from a soil matrix if there were fewer particles in the grain sizes from “d” to “4d”. In this study, the mixtures of silica nos. 3 and no. 8 were gap-graded soils. Therefore, part of fines would be transported by the assigned seepage flow and accumulated in the sedimentation tank (Fig. 3.3) according to Kenney and Lau's criterion. The results of seepage tests are summarized in Table. 3.2.

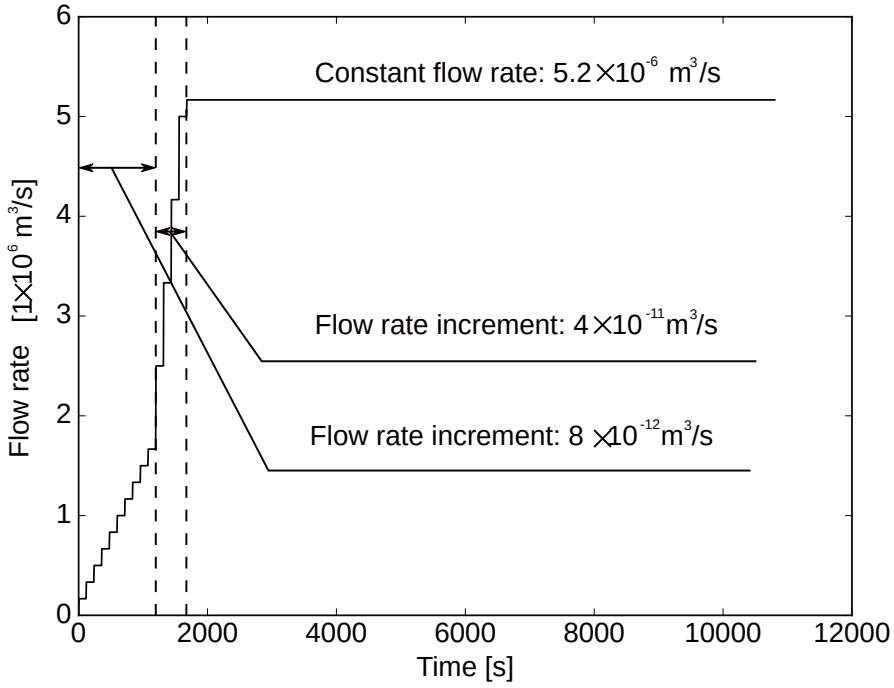

Figure 3.4: Flow rate in seepage tests

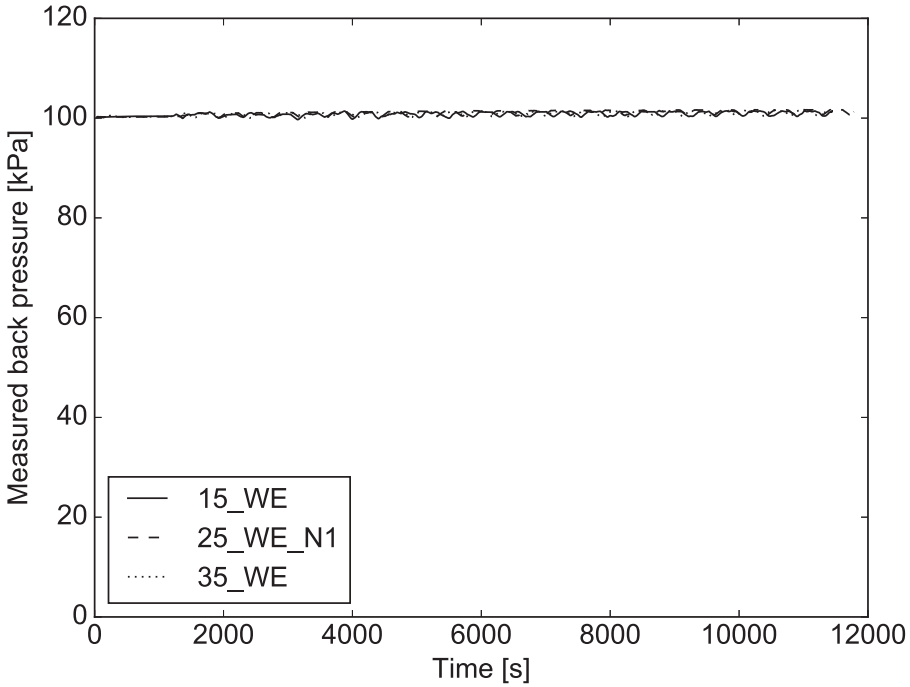

Figure 3.5: Measured back pressure during seepage tests

To show the repeatability of test results, seepage tests and subsequent undrained compression tests were carried out twice on the soils with 25% initial fines content, corresponding to the specimens 25_WE_N1 and 25_WE_N2 (where the first number in the specimen ID represents the percentage of initial fines content; the second entry is with or without erosion; and the third is the test number).

The saturation degree is greatly influenced by the inflow water. Due to the head loss and the corresponding drops in pore pressure during the seepage test, the dissolved air may probably be separated out in the tested specimens. Consequently, the saturation degree might decrease. Evancs and H.Y. (1988) found that the decrease of saturation degree would lead to an error of the hydraulic conductivity. In addition, it is well recognized that the quality of the compression tests on soils would be affected by the decrease of saturation degree. Therefore, a back pressure of 100 kPa was applied through the sedimentation tank (Fig. 3.3). Change of the back pressure during the seepage tests is shown in Fig. 3.5. Because the drainage valve connecting to the sedimentation tank was regularly opened and closed, the measured back pressure showed slight deviations around 100 kPa.

The hydraulic gradient at the initial 1000 s for the first case of soil with 20% initial fines content is plotted in Fig. 3.6. If the soil matrix kept constant during the seepage tests, the hydraulic gradient would be also kept the same with fixed applied flow rate. However, a moderate drop of hydraulic gradient could be observed at around 300 s, which can be regarded as a sign of the onset of internal erosion. According to Kovacs (1981), water flows through the pores would create a dynamic force on the particles of the specimens. The vector of this force is generally parallel to the direction of flow and hence to the vector of the hydraulic gradient. For the soils containing fines, when the force is greater than the forces holding the fines within the soil, the fines would probably start moving along a path determined by the internal structure of the soil matrix. The hydraulic gradient would change if the soil matrix changes. Therefore, the drop of hydraulic gradient during the seepage tests could be generally regarded as one of the indications of the onset of internal erosion.

Figure 3.7 shows the evolution of hydraulic gradient for cases 15_WE, 25_WE_N1 and 35_WE. It can be observed that the soil with 35% initial fines content showed the largest value of maximum hydraulic gradient. Sharp increases of the hydraulic gradient were detected at around 880 s, which might be responsible for the sudden increase of applied flow rate. Meanwhile, the increase of flow rate might lead to an increase of the hydraulic force on the fines. Large amount of fines were transported by the sudden applied hydraulic force. Temporary clogging probably occurred when these fines were stayed at the voids of coarse particles. This might be one of the possible reasons that the hydraulic gradient showed a sharp increase with a sudden increase of inflow rate. The reading from the cumulative eroded soil collection at this moment was basically zero. However, turbid flow with small amount of fines was observed in the effluent.

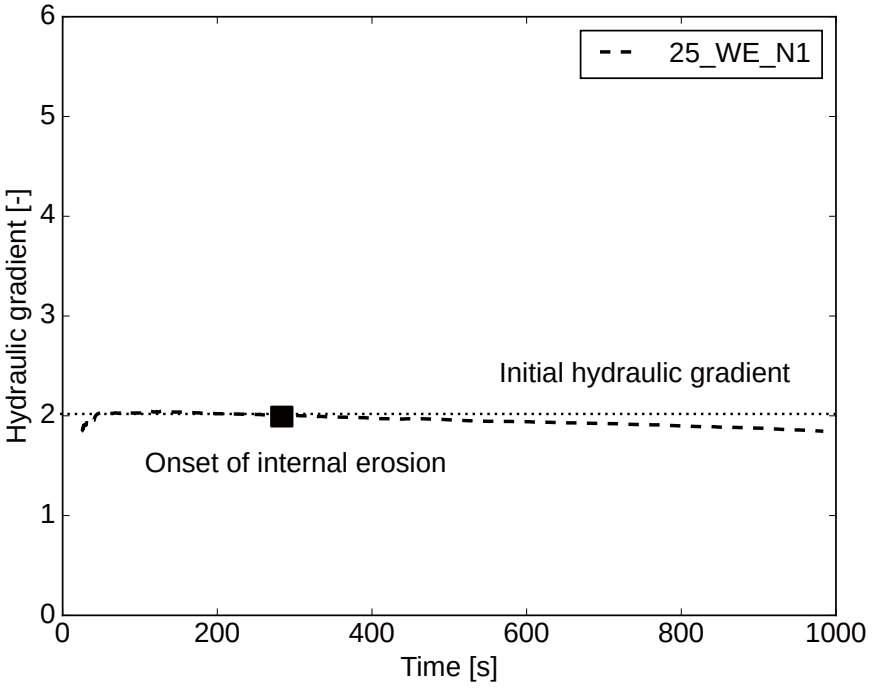

Figure 3.6: Onset of internal erosion in soil with 25% initial fines content (25_WE_N1)

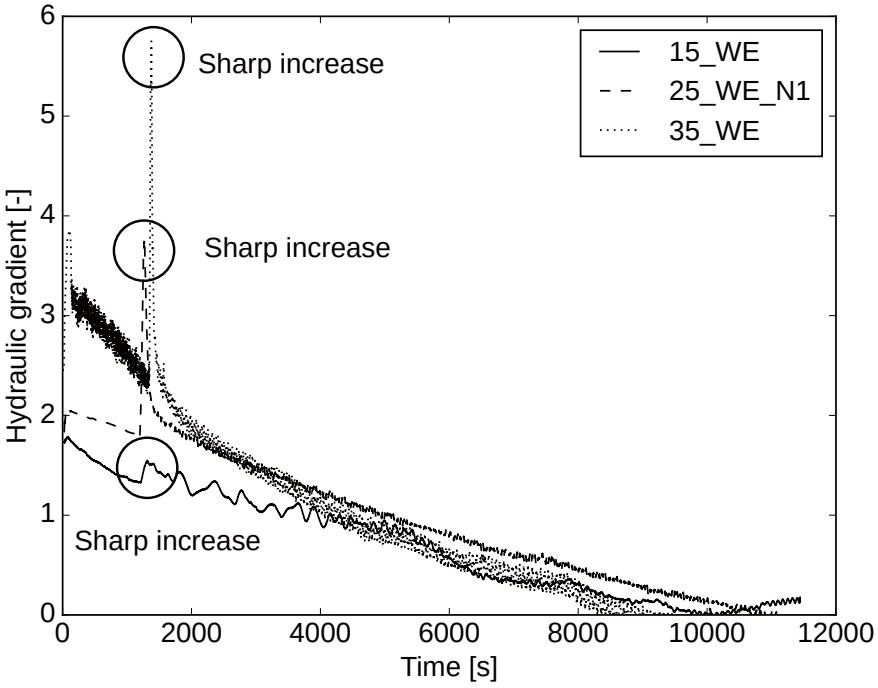

Figure 3.7: Evolution of hydraulic gradient during seepage tests

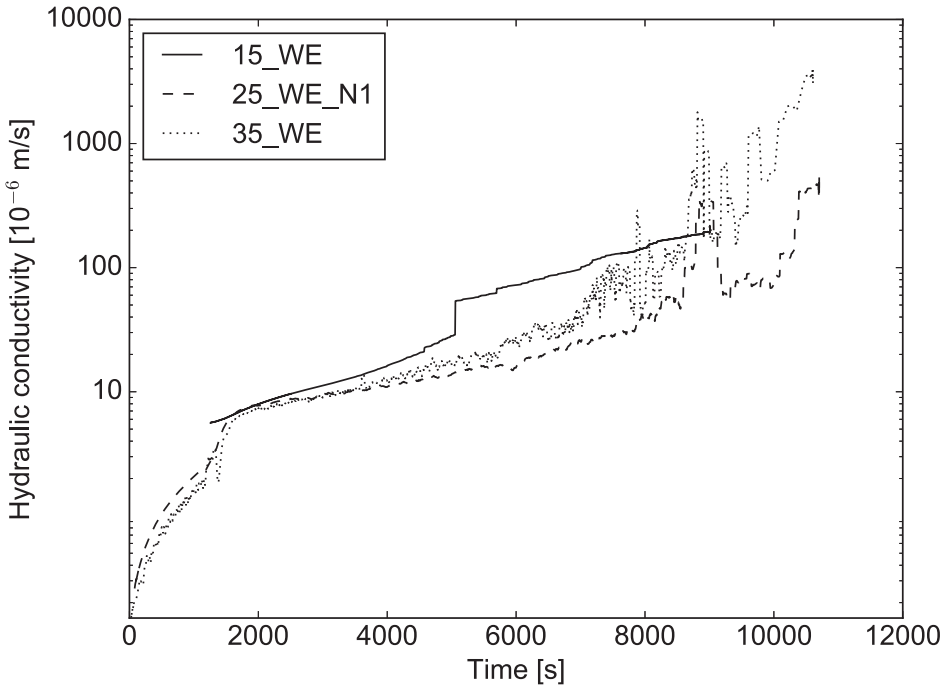

Figure 3.8: Evolution of hydraulic conductivity during seepage tests

The evolutions of hydraulic conductivities for cases 15_WE, 25_WE_N1 and 35_WE are shown in Fig. 3.8. Observation of the evolution of the hydraulic conductivity noted that the hydraulic conductivity varies test by test, and it was not kept constant during the seepage test. The variation of hydraulic conductivity indicated that the specimen might be inhomogeneous resulted from the preferred flow channels during the seepage tests.

After the initial peak, the hydraulic gradient gradually dropped with the progress of erosion of fines. It might because that the voids in the specimens increased due to the transportation of fines. Interestingly, the hydraulic gradients at the end of the seepage tests are similar for soils with 15%, 25% and 35% initial fines contents. One of the reasons might be the remaining fines content and post erosion void ratios for the eroded specimens were comparable, as indicated in Table 3.2.

The evolutions of the cumulative eroded soil mass are shown in Fig. 3.9. It is noted that the fines were eroded away from the specimen continuously at the constant flow rate. As the seepage tests were performed on gap-graded soils under isotropic stress state, it could be assumed that the effective stresses were mainly transferred by the coarse fractions. Therefore, the intergranular void

Table 3.2: Seepage test results

Specimen No.	Fc(%)[1]	e_0[2]	e_c[3]	e_{cs}[4]	Fce(%)[5]	e_e[6]	e_{es}[7]	ε_v(%)[8]
15_WE	15	0.68	0.67	0.96	8.75	0.80	0.98	0.11
25_WE_N1	25	0.61	0.56	1.08	12.0	0.81	1.06	1.62
25_WE_N2	25	0.61	0.54	1.05	13.1	0.81	1.06	2.21
35_WE	35	0.61	0.59	1.45	13.3	0.99	1.29	10.1

[1] Initial fines content;
[2] Initial void ratio;
[3] Void ratio after consolidation;
[4] Intergranular void ratio after consolidation (before seepage test) (=(e_c + Fc/100)/(1-Fc/100));
[5] Fines content after seepage test;
[6] Void ratio after seepage test;
[7] Intergranular void ratio after seepage test (=(e_e+Fce/100)/(1-Fce/100));
[8] Volumetric strain.

ratio, defined by regarding the fines as voids, is considered as one of the parameters in interpreting the relation between initial fines content and cumulative eroded soil mass. Observations of Table. 3.2 reveal that the intergranular void ratios were similar for specimens with 15% and 25% initial fines contents before and after seepage tests whilst the specimen with 35% initial fines content showed a reduction of intergranular void ratio after internal erosion. It suggests that the fines in these mixtures might not be involved in the stress transformation, which then resulted in an easier transportation of fines when subjected to certain seepage flow. Therefore, it could be concluded that the more the initial fines content, the larger the amount of cumulative eroded soil mass within the scope of this study.

The median particle size of coarse and fine particle is 1.76 and 0.16 mm (Table 3.1), respectively. If both are assumed as spheres, the diameter of the planar inscribed sphere in the minimum void space formed by coarse particles is much larger than the median diameter of fines. It suggests that the fines could be relatively easily transported through the matrix formed by coarse particles. Thus the increase in the initial fines content does not necessarily reduce the cumulative eroded soils for the tested materials.

After the erosion of fines from the specimens, the volume of specimen during the seepage tests could change correspondingly. Figure 3.10 shows the evolution of the volumetric strain during the seepage tests. There were many jumps in the volumetric strain change for the soil with 35% initial fines content, which might be attributed to the sudden erosion of the fines by seepage flow. It is

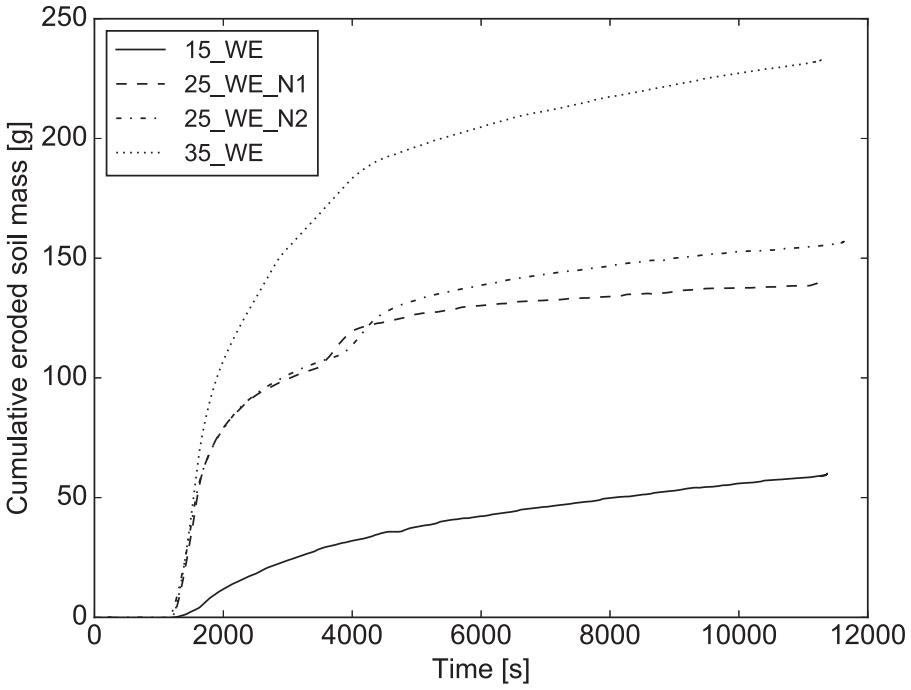

Figure 3.9: Evolution of cumulative eroded soil mass during seepage test

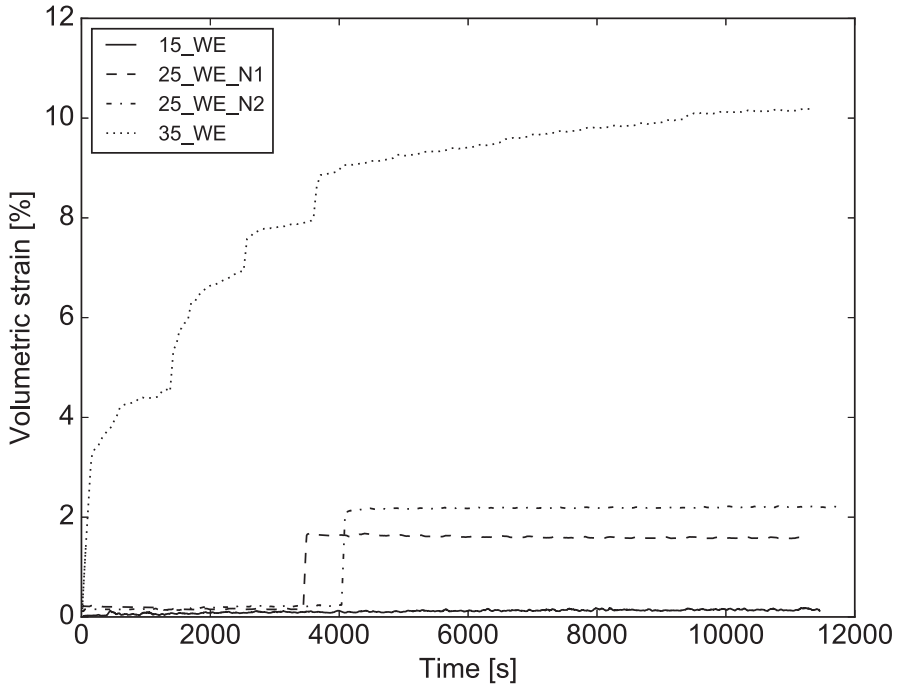

Figure 3.10: Evolution of volumetric strain during seepage test

Table 3.3: Undrained compression test results of soils without erosion

Specimen No.	Fc(%)	e_0	e_c	$\varepsilon_{au}(\%)^1$	$\varepsilon_{aq}(\%)^2$	$\varepsilon_{ap}(\%)^3$
00_WOE_N1[4]	0	0.84	0.84	–	–	–
00_WOE_N2[5]	0	0.82	0.82	–	–	–
15_WOE	15	0.68	0.67	0.99	3.92	4.58
25_WOE	25	0.61	0.56	2.27	2.34	3.60
35_WOE	35	0.60	0.56	0.58	8.11	8.59

[1] Axial strain at undrained peak state;
[2] Axial strain at quasi-steady state;
[3] Axial strain at phase transformation state;
[4] Test case for relative density 34%;
[5] Test case for relative density 41%.

indicated that the volumetric strain change was related to the initial fines content. For example, the volumetric strain of the soil with 35% initial fines content (35_WE) was approximately five times larger than the soil with 25% initial fines content (25_WE_N1) at the end of the seepage test.

3.3.2 Undrained compression test results

The undrained compression test results of soils without erosion is shown in Table 3.3. The relationships between the axial strain and the deviator stress for the undrained compression tests on soils without erosion are shown in Fig. 3.11 and the corresponding effective stress paths are plotted in Fig. 3.12.

It can be seen that the original soil with 35% initial fines content (35_WOE) showed the flow behavior, whereas those with 15% and 25% fines contents (15_WOE, 25_WOE) showed the limited flow behaviors. These indicate that the undrained mechanical behavior of the soil was influenced by the fines content and the soil becomed contractive with the increase of fines in this study.

Table 3.4 shows the undrained compression test results of eroded soils, including the maximum hydraulic gradient during the seepage tests. It can be observed that all the maximum hydraulic gradients were larger than 1.0, which was considered to remove the majority of fines from the specimen in these experiments. The hydraulic gradient of the specimen with 35% initial fines content (35_WE) showed the largest hydraulic gradient. It might be responsible for this mixture containing the largest amount of initial fines, which then led to the smallest hydraulic conductivity and largest hydraulic gradient.

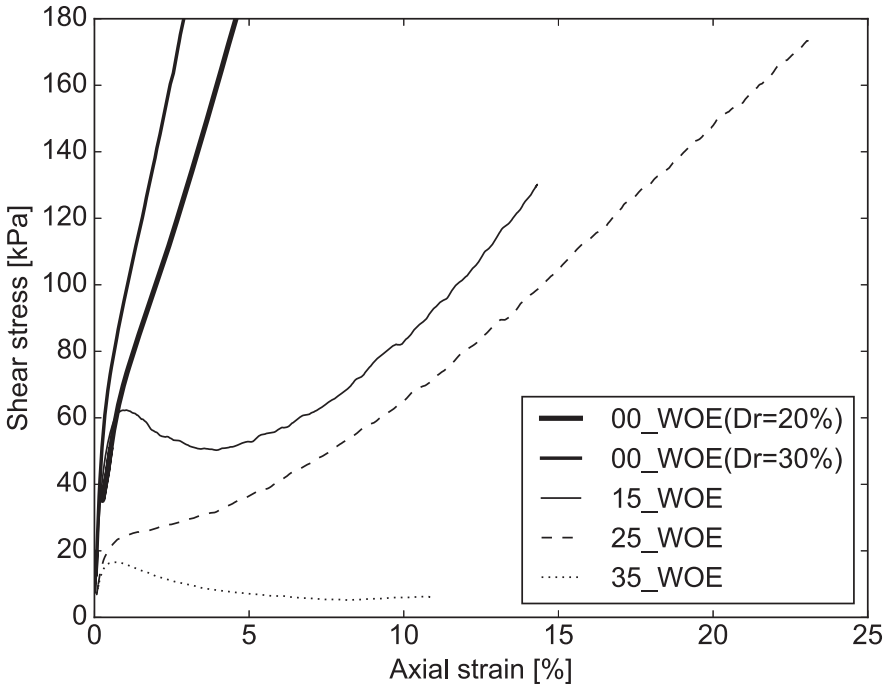

Figure 3.11: Stress strain curves of soils without erosion

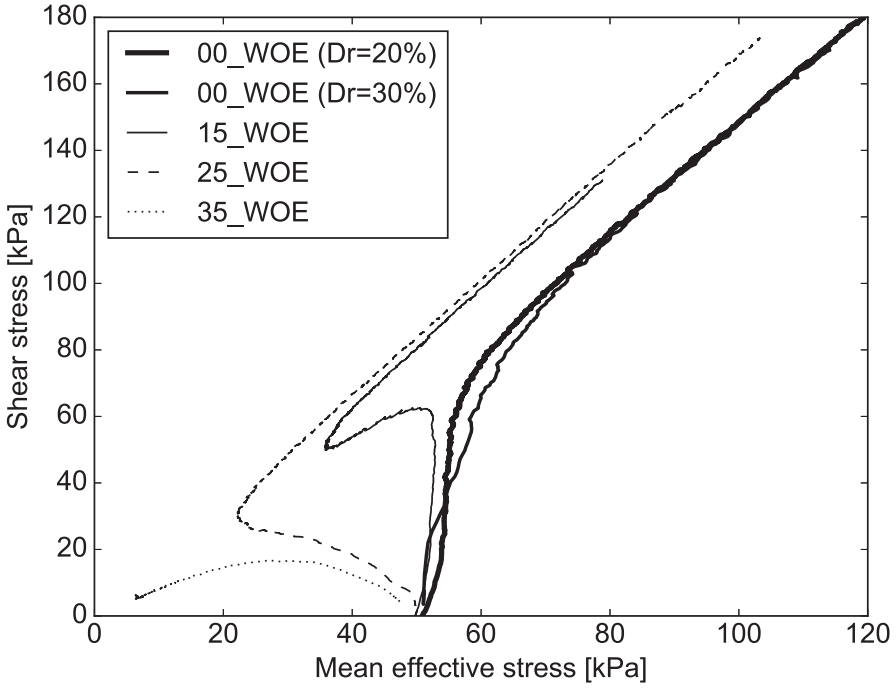

Figure 3.12: Effective stress paths of soils without erosion

Table 3.4: Undrained compression test results of soils with erosion

Specimen No.	Fce(%)	e_c	i_{max}[1]	e_c	$\varepsilon_{au}(\%)$	$\varepsilon_{aq}(\%)$	$\varepsilon_{ap}(\%)$
15_WE	8.75	0.67	2.07	0.80	1.00	3.77	4.92
25_WE_N1	12.0	0.56	5.05	0.81	1.93	3.93	6.59
25_WE_N2	13.1	0.54	5.39	0.81	2.20	4.64	4.70
35_WE	13.1	0.59	11.7	0.99	1.07	4.83	6.06

[1] Maximum hydraulic gradinet.

Figure 3.13 shows the stress-strain relationships of soils with erosion. All the specimens subjected to internal erosion showed limited flow behaviors. The effective stress paths of the soils with erosion are plotted in Fig. 3.14. It can be observed that all the eroded specimens show dilative tendency, i.e., the mean effective stress increases after passing through the phase transformation state.

The particle size analysis performed after compression tests revealed that the eroded specimens were not homogeneous, which might be responsible for the occurrence of erosion in some preferential flow paths. It was considered as the inherent consequences of seepage tests.

3.4 Discussion

Detailed examination of the undrained mechanical behavior can help to get a throughout understanding on the behaviors of soils with and without erosion containing different initial fines contents. The undrained characteristics of soil behavior at the undrained peak state, quasi-steady state, phase transformation state, and critical state are discussed in order. The relations between the key states are presented as well.

3.4.1 Undrained peak state

Undrained peak strength

The undrained peak state is the state where the deviator stress reaches the initial peak in the stress-strain curve under the undrained compression condition. It is associated with the onset of the flow failure (Yoshimine and Ishihara, 1998). One of the soil strength parameters related to the undrained peak state is the undrained peak strength (s_p) (Ishihara, 1993), which was customarily defined as

$$s_p = \frac{q_{ups}}{2} \tag{3.1}$$

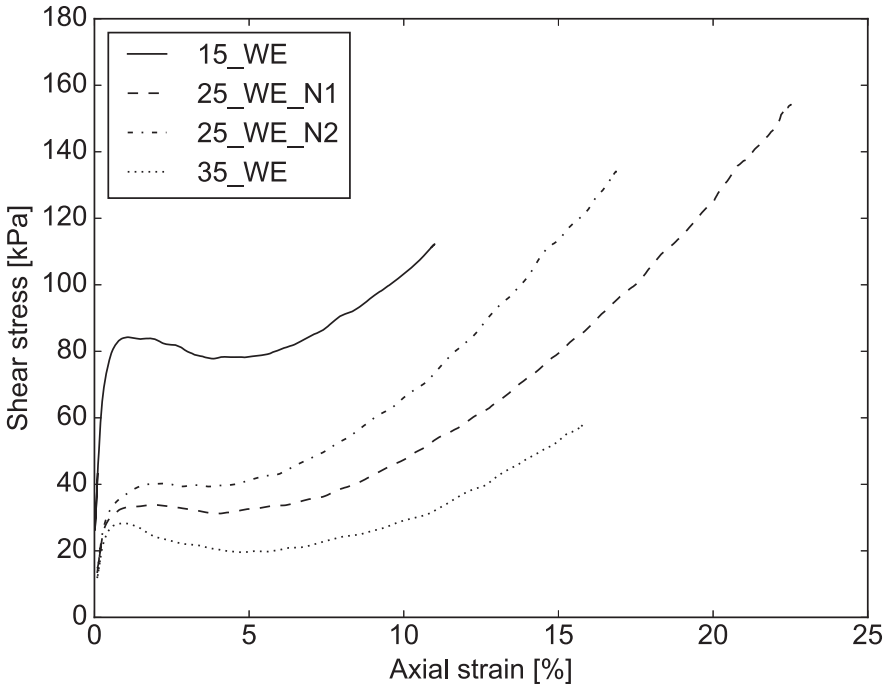

Figure 3.13: Stress strain curves of soils with erosion

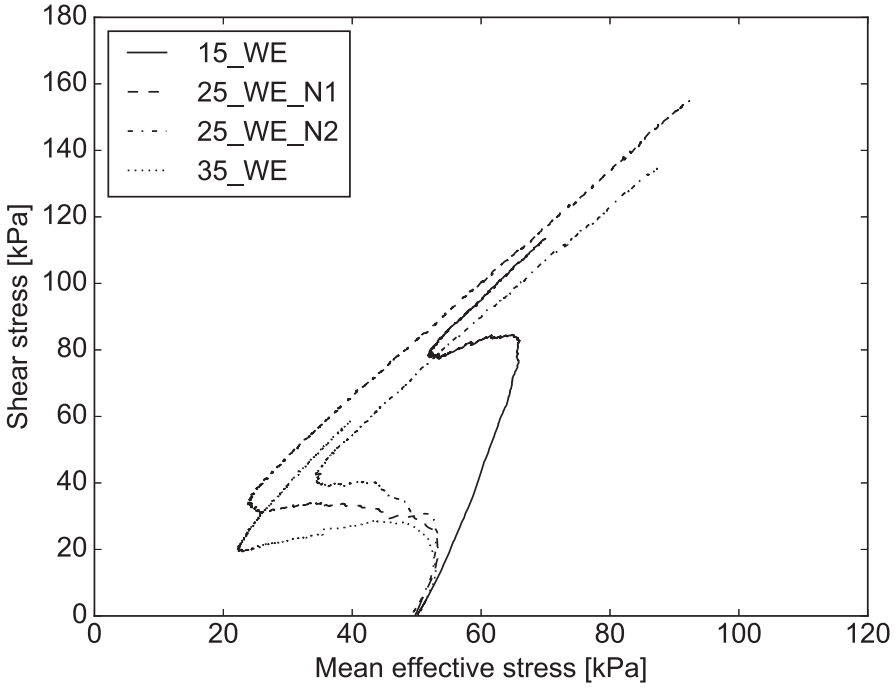

Figure 3.14: Effective stress paths of soils with erosion

where q_{ups} is the deviator stress at the undrained peak state. Figure 3.15 shows the relationship between the undrained peak strength normalized by initial mean effective stress and the fines content before compression. It is found that the original soil with 15% initial fines content (15_WOE) showed larger normalized peak strength than those with 25% and 35% initial fines contents (25_WOE, 35_WOE). Besides, it can be observed that the eroded soils showed the larger peak strength than those of the original soils with the same initial fines contents, although the void ratios of eroded soil became larger. Take the soils with 15% initial fines content for example, the original specimen (15_WOE) showed normalized peak strength of 0.63, whereas the eroded specimen (15_WE) showed normalized peak strength of 0.85. Moreover, it can be found that the normalized peak strength of the soils with erosion was not located in the same band compared with the soils without erosion. The normalized peak strength of soils with erosion seemsed to be sensitive to the fines content before compression. The normalized peak strength of the soils with erosion showed different values from 0.28 to 0.85, although they contained similar fines content around 10% (ranging between 9% to 13%).

Mean effective stress ratio

Another important parameter at the undrained peak state is the mean effective stress ratio, which is defined as the value of effective stress at undrained peak state (p'_{ups}) divided by initial mean effective stress (p'_0) (Ishihara, 1993). Figure 3.16 shows the mean effective stress ratio at the undrained peak state against fines content before compression.

Information about the reference data is shown in Table 3.5. These data are taken from the previous works on loose sands mixed with fines, prepared by the moist tamping method. It can be observed that the mean effective stress ratio was greatly influenced by the properties of tested materials. The reference data, soils with 35% initial fines content (35_WOE, 35_WE), and original soil with 25% initial fines content (25_WOE) were located in the same band (i.e., the mean effective stress ratio in between 0.5 and 0.7, irrespective to the fines content before compression). However, the mean effective stress ratios of the soils with 15% initial fines content (15_WOE, 15_WE) and the eroded soils with 25% initial fines contents (25_WE, 25_WOE) were located well above the band. Although the marked difference cannot be seen in the case of the eroded soil with 35% initial fines content, the mean effective stress ratios of soils with erosion were relatively larger than the soils without erosion.

Undrained tangent stiffness

It is generally accepted that soil behaves nonlinearly even at a relative small strain level. Undrained tangent stiffness at an axial strain in the range of 0.1% to 1.0% is important in interpreting the soil behavior at initial shearing stage. Figure 3.17 shows the undrained tangent stiffness of soils without

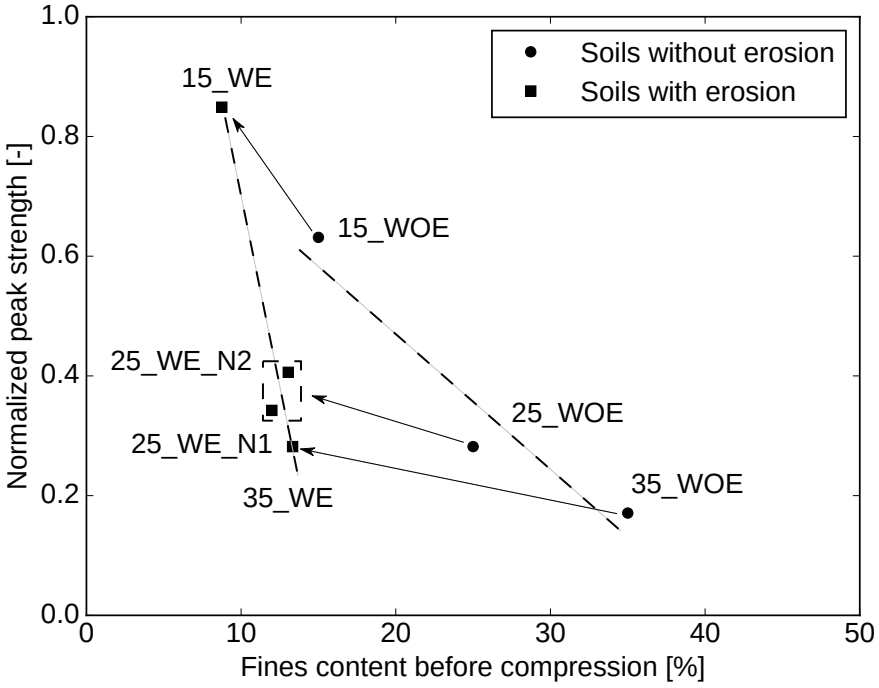

Figure 3.15: Normalized peak strength against fines content before compression

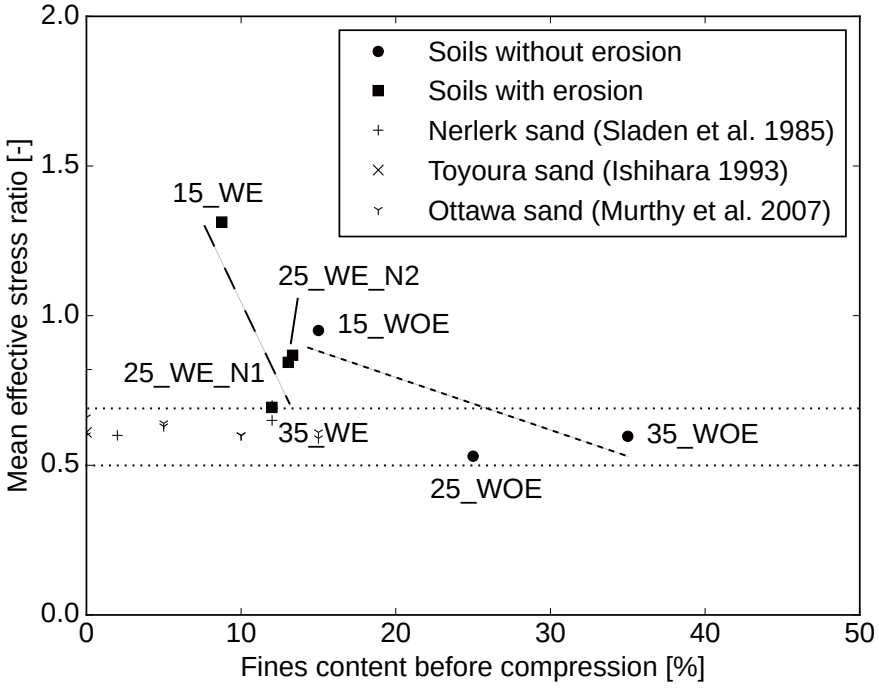

Figure 3.16: Mean effective stress ratios against fines content before compression

Table 3.5: Information about reference data

Tested materials	Fines content (%)	Relative density (%)	Preparation method	Reference
Leighton Buzzard sand, Nerlerk sand	0, 2.2, 12	10-30	Moist tamping	Sladen et al. 1985
Toyoura sand	0	7-65	Moist tamping	Ishihara 1993
Ottawa sand	0, 5, 10, 15	20-50	Moist tamping	Murthy et al. 2007

erosion. The undrained tangent stiffness here is normalized with initial mean effective stress and is plotted against the axial strain. The similar plots for the eroded soils are shown in Fig. 3.18. It can be noted that the uneroded soil with 15% initial fines content (15_WOE) showed larger normalized tangent stiffness than those with 25% and 35% initial fines content (25_WOE, 35_WOE) when the axial strain was less than 0.9%. That is to say, the soil with smaller initial fines content indicated the larger shear stiffness than those with larger initial fines content at a small strain level.

From Fig. 3.18, it can be observed that for the specimens with the same initial fines content, the post-erosion soil exhibited larger normalized tangent stiffness compared to that without erosion when its axial strain was less than 0.4%. Take the specimens with 15% initial fines content at 0.25% axial strain for instance, the eroded soil showed a normalized tangent stiffness of 200, whereas the eroded soil showed a normalized tangent stiffness of 230.

3.4.2 Quasi-steady state

Another key state of the undrained behavior is the quasi-steady state where the deviator stress shows a local minimum value in the stress strain curves. The quasi-steady state appears only when the metastable specimens exhibit the strain softening behavior during the undrained compression. The soil shows a minimum deviator stress at the quasi-steady state, which can be even smaller than that at critical state where the soil is sheared to a relatively larger strain. Residual strength, which is associated with the deviator stress at quasi-steady state, was recommended to use in stability analysis Sladen et al. (1985). They reported that the application of residual strength could be considered valid when the soil strength is believed to be affected by some factors. Thus, is would be safer if the residual strength is taken into consideration in analyzing the soil subjected to internal erosion.

The residual strength (s_{us}) at the quasi-steady state was customarily defined as (Ishihara, 1993)

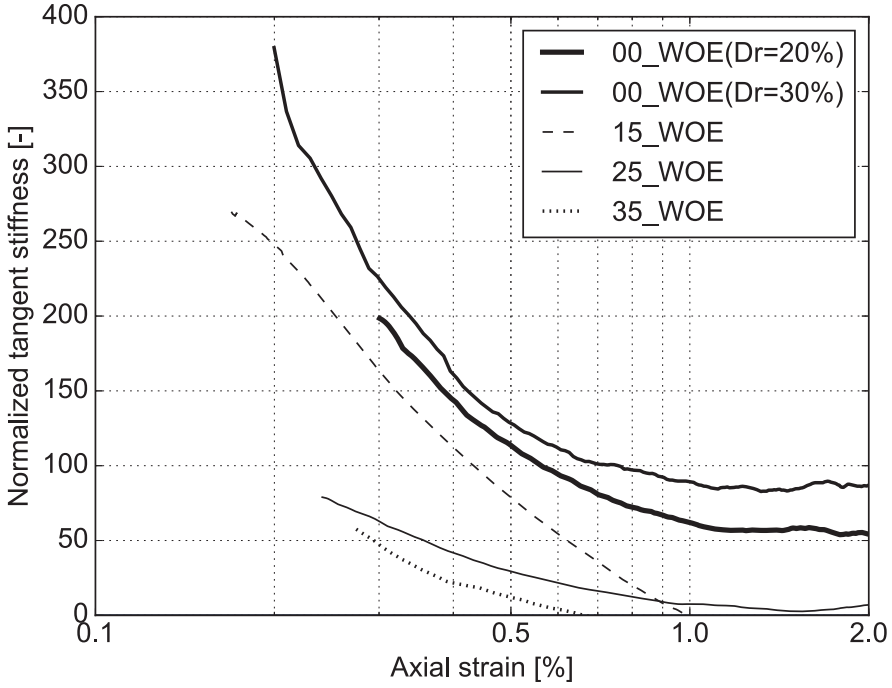

Figure 3.17: Relation between normalized tangent stiffness and axial strain of soils without erosion

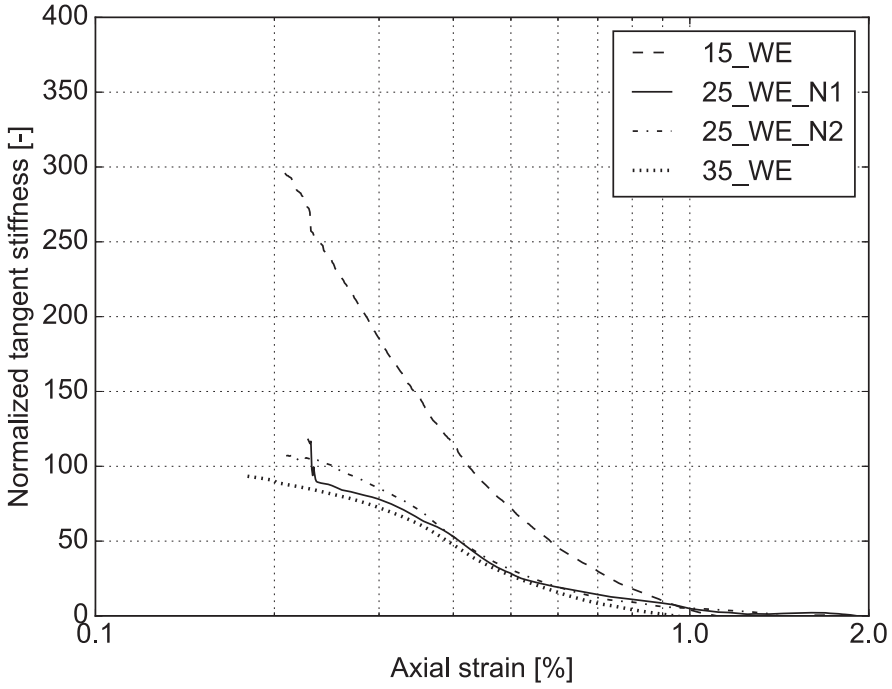

Figure 3.18: Relation between normalized tangent stiffness and axial strain of soils with erosion

$$s_{us} = \frac{q_{qss}}{2}\cos\phi_s = \frac{M_{qss}}{2}\cos\phi_s\left(p'_{qss}\right) \tag{3.2}$$

$$M_{qss} = \frac{6\sin\phi_s}{3-\sin\phi_s} \tag{3.3}$$

where q_{qss} is the shear stress at the quasi-steady state, ϕ_s is the angle of shearing resistance at the quasi-steady state, p'_{qss} is the mean effective stress at the quasi-steady state, and M_{qss} is the shear stress ratio at the quasi-steady state (q_{qss}/p'_{qss}). It can be observed from Figs. 3.11 and 3.13 that all of the mixtures with initial fines content of 15%, 25% and 35% showed strain softening behaviors after the initial peak in the stress strain curves. Therefore, it can be said that the quasi-steady state appeared for these specimens in this study.

Figure 3.19 shows the shear stress ratios at the quasi-steady state against fines content before compression on the soils with and without erosion. It is noted that the shear stress ratios of soils without erosion almost stayed in a narrow brand of 1.30, corresponding to an angle of shearing resistance of 32.2°at the quasi-steady state, irrespective of the fines content before compression. However, the shear stress ratio of soils with erosion did not show a constant value, and fluctuated around 1.30. This deviation from the band may suggest that the shear stress ratio at quasi-steady state was also influenced by the internal erosion.

The normalized residual strength with initial mean effective stress against fines content before compression is shown in Fig. 3.20. The normalized residual strengths of mixed Hokksund sand and Cehngbei silt from Yang et al. (2006b) are also plotted in this figure. These mixed soils were prepared by moist tamping method with fines contents of 0, 5%, 10%, 15%, 20%, 30% and 50%, targeting relative density ranging from 22% to 30%. It can be observed from Fig. 3.20 that the normalized residual strength was affected by fines content. For the siliceous sands in this study, the specimens with larger fines content before compression showed a smaller normalized residual strength. The normalized residual strength change with the fines content before compression in this study showed the similar tendency as the mixtures of Hokksund sand and Chengbei silt (Yang et al., 2006b).

Meanwhile, the soils with erosion showed a larger normalized residual strength than the soils without erosion at the same initial fines content in this study. For example, at the same initial fines content of 15%, the soil without erosion (15_WOE) showed a normalized residual strength of 0.41, but the soil with erosion (15_WE) showed a normalized residual strength of 0.63. It suggests that the soils became less contractive when they experienced internal erosion.

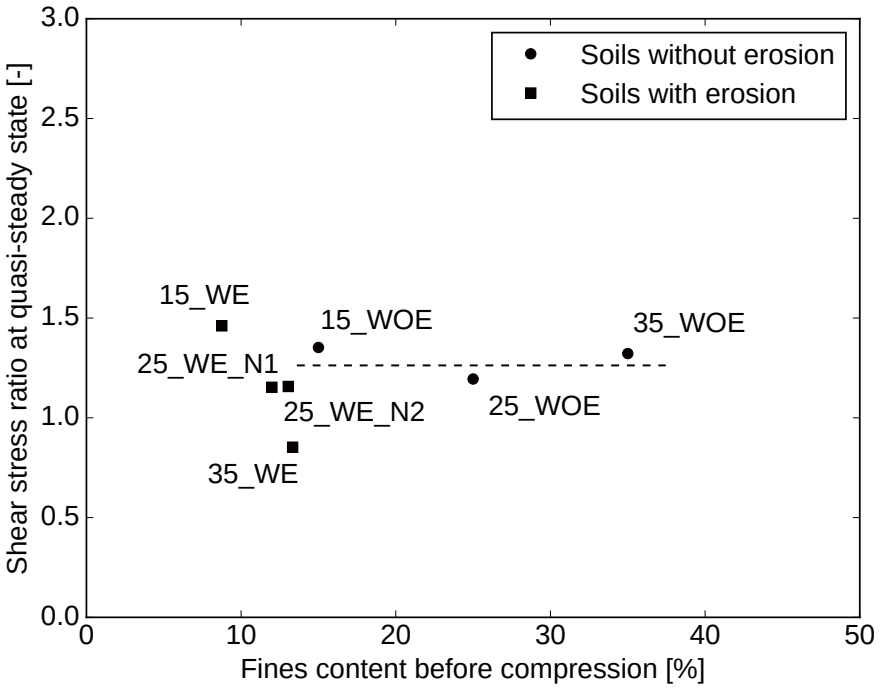

Figure 3.19: Shear stress ratios at quasi-steady state against fines content before compression

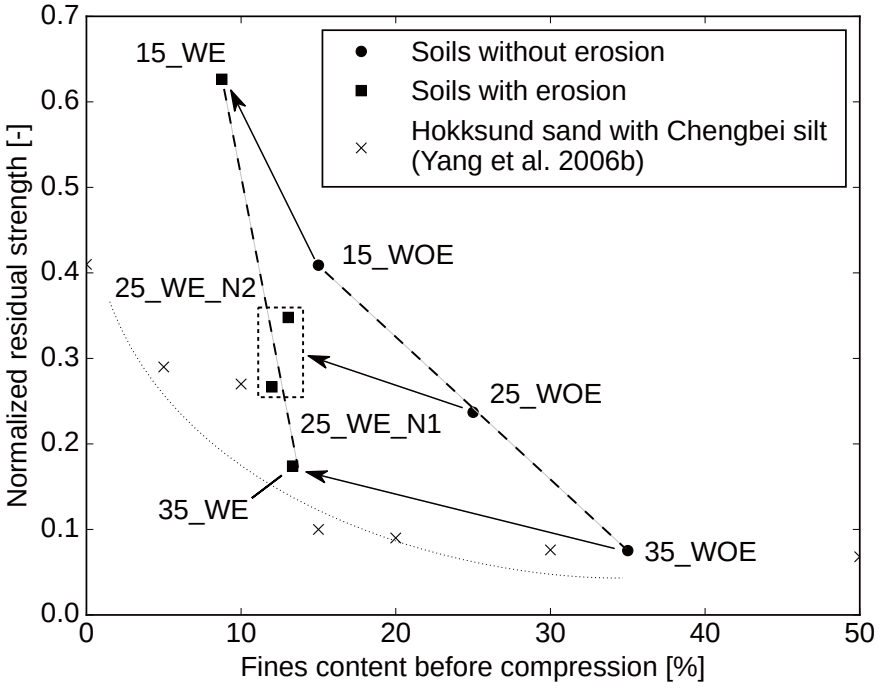

Figure 3.20: Normalized residual strength against fines content before compression

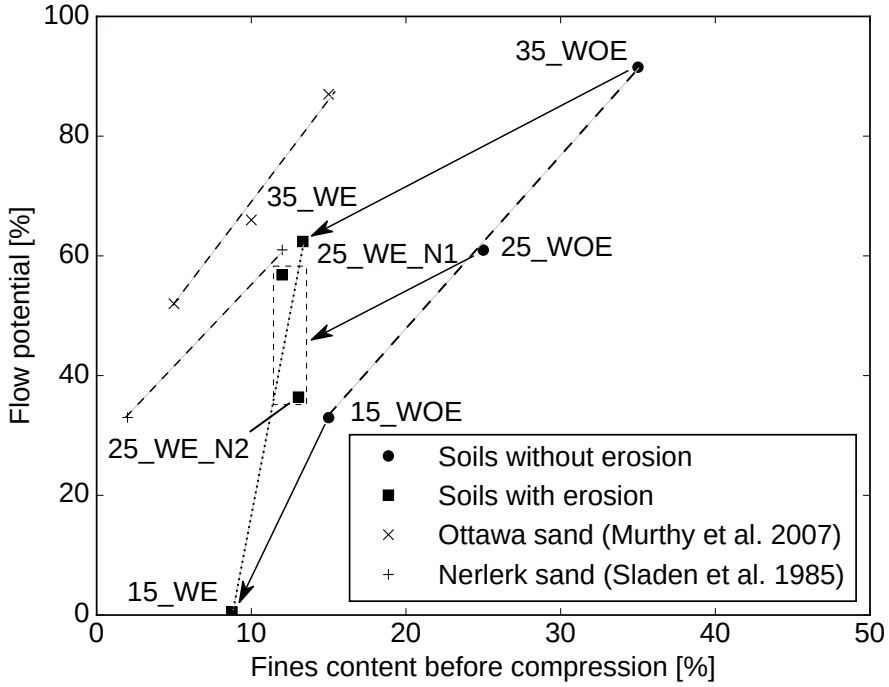

Figure 3.21: Flow potential against fines content before compression

3.4.3 Phase transformation state

Phase transformation state is the state where the soil shows a minimum mean effective stress in the effective stress path (Ishihara et al., 1975). It is also an indication that the soil changes from contractive behavior to dilative behavior. In many cases the phase transformation state is coincident with the quasi-steady state although the definitions of these two states are different, i.e., the former is defined by the minimum mean effective stress and the latter is defined by the minimum deviator stress. Typically, the quasi-steady state precedes the phase transformation state in the monotonic undrained compression.

The phase transformation state is one of the key states associated with the potential of flow failure because the value of excess pore water pressure during compression is the maximum in this state. The plow potential (u_f) proposed by Yoshimine and Ishihara (1998) represents the maximum excess pore water pressure ratio during the undrained monotonic compression test, and is expressed as

$$u_f = \left(1 - \frac{p'_{pts}}{p'_0}\right) \times 100\% \tag{3.4}$$

where p'_{pts} is the mean effective stress at the phase transformation state, and p'_0 is the initial mean

effective stress. The value of flow potential varies from 0 to 100%. The soil with a small value of u_f means that it generates a small amount of excess pore water pressure under the undrained compression.

The relationship between flow potential (u_f) and fines content before compression is shown in Fig. 3.21. Information about the reference data is shown in Table 3.5. It can be seen that the uneroded soils with 15%, 25%, and 35% initial fines contents indicated flow potential (u_f) ranging from 33% to 92% in this study. The flow potential was very sensitive to the fines content in the undrained compression test. In this study, the siliceous mixtures with a larger fines content before compression showed a larger flow potential than that with less fines content. The Nerlerk sand (Sladen et al., 1985) and Ottawa sand (Murthy et al., 2007) shown in Fig. 3.21 indicated the same tendency. That is to say, the potential of flow failure was considered higher for the soil containing a larger amount of fines.

One of the other observations from Fig. 3.21 is that the flow potential (u_f) of soils with erosion was smaller than that of soils without erosion at the same initial fines content. Taking the soils with 15% initial fines content for example, the flow potential (u_f) of soil without erosion (15_WOE) was 33%, whereas that of soil with erosion (15_WE) decreased to 0.5%. In addition, the slopes of the relationship between the fines content before compression and flow potential were more or less the same for the soils without erosion as indicated in the dash lines, while it was steeper for the eroded soil (dotted line in Fig. 3.21). This difference indicated that the compressibility of the eroded soil was more sensitive to the fines content compared to the uneroded soils.

3.4.4 Critical state

The concept of critical state can be employed to discuss the soil behaviors, which is defined as the state where the soils continue to deform without change of effective stress or migration of pore water (Roscoe et al., 1958). The pioneer study on the evolution of CSL with erosion is presented by Muir Wood (2007) through adopting the concept of "grading state index". In their approach, "grading state index" is defined as the ratio of the current grading to the limiting grading, which varies from 0 to 1 corresponding to the changes from single size grading to certain limiting grading. The direct consequences of internal erosion include the movement of particle grading curve due to amount the amounts of fines loss, which accordingly changes the grading state index. Figure 3.22 indicates the movement of particle grading curves of the tested specimens (25_WOE, 25_WE_N2) induced by internal erosion. Coincident with the studies of Muir Wood and Maeda (2008) and Muir Wood et al. (2010), the grading curve moves downward after internal erosion and the extent of that movement may represent the amounts of fines loss, suggesting a decline in grading state index.

Further, it may cause the upward movement of CSL in the $e - \log p'$ plane.

In this study, the undrained test results were interpreted to understand the corresponding evolution of CSL with internal erosion. For these cases without sufficient straining, a sigmoidal function fitting proposed by Murthy et al. (2007) was utilized to extrapolate the critical state, the details of which are explained in Appendix. Figure 3.23 shows the critical state of soils before and after erosion. The CSL of the original specimens with 35% initial fines content was derived from the results of the laboratory compression tests. Unfortunately, similar tests on the specimens with 15% and 25% fines contents have not been performed. Therefore, the CSLs of the soils with 15% and 25% initial fines contents, shown in Fig. 3.23, were postulated on the basis that soil with a smaller fines content shows a steeper CSL in the $e - \log p'$ plane (Murthy et al., 2007). Zlatovic and Ishihara (1997) concluded that critical state may erase the influence of initial fabric and in this circumstance the soil mechanical responses tend to become similar. It is noted from Table 3.4 that the fines contents of eroded specimens somehow locate on a similar CSL, which was above that of the uneroded specimens. The movement of CSL was in accordance with the theoretical prediction of Muir Wood and Maeda (2008) and Muir Wood et al. (2010): due to the decrease of grading state index induced by internal erosion, the CSL in $e - \log p'$ plane moves upwardly.

3.4.5 Relation between key states

The tested soils in this study showed a local maximum deviator stress at the undrained peak state and minimum deviator stress at the quasi-steady state. The local minimum mean effective stress appeared at the phase transformation state. The relationships between these states are compared below.

Undrained peak state and quasi-steady state

The tested specimens mostly exhibited peak strength followed by a local minimum in the stress strain curve, which corresponding to the residual strength at the quasi-steady state. The relationship of the deviator stress normalized by the initial mean effective stress between the undrained peak state and the quasi-steady state is shown in Fig. 3.24. According to the definition of the undrained peak state and quasi-steady state, the deviator stress at the former state would always be larger or equal to that at the latter state. To show the relationship clearly, a demarcation line where the deviator stress at undrained peak state equals to that at quasi-steady state is drawn as the solid line in Fig. 3.24. If the difference between the normalized peak strength and normalized residual strength is small, the state point is located around the demarcation line, suggesting a less contractive behavior. For example, the specimens 25_WOE and 25_WE_N2 showed a relatively less contractive behavior, so their states located very close to the demarcation line. It can be noted that, by comparing the

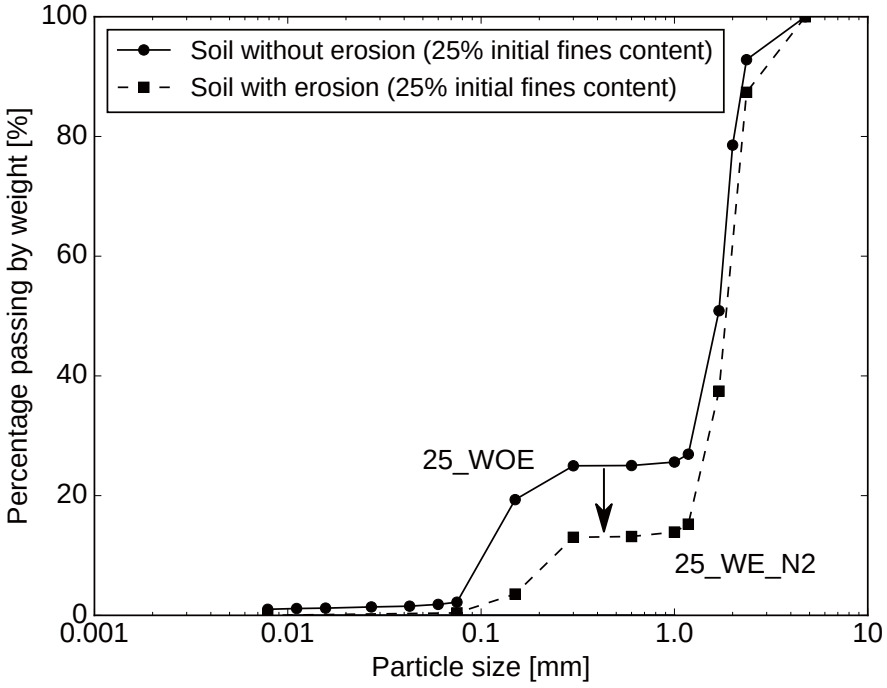

Figure 3.22: Movement of particle grading curves

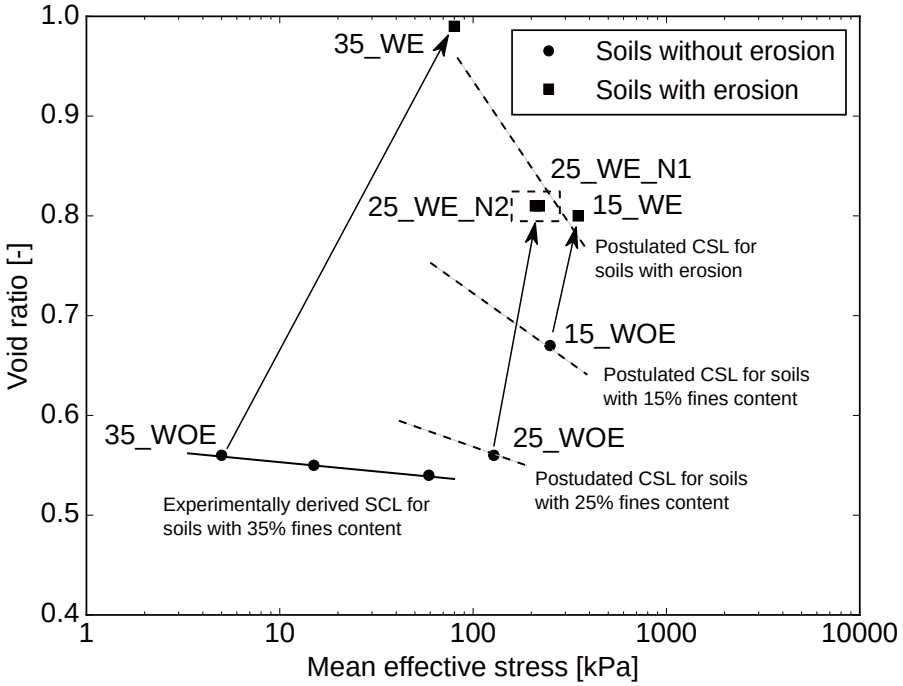

Figure 3.23: Critical states of tested specimens in $e - \log p'$ plane

relative positions of the points to the demarcation line, the points for the eroded soils were closer to the demarcation line, suggesting a less contractive response.

Undrained peak state and phase transformation state

The undrained peak state is associated with the onset of flow failure, and the phase transformation state is the state where soil behavior changes from contractive to dilative. Between these two states, a relatively small load might be sufficient to cause a large deformation of soil structure. That is to say, the soil would experience an instability state between the undrained peak state and phase transformation state (Leong and Chu, 2002).

The instability line is defined as the line connecting points of the deviator stress at the undrained peak state in the effective stress plane. Yang et al. (2006a) found that the instability line passes through the origin in the effective stress plane for the cohessionless soils. Therefore, the instability line here is described as the line connecting the origin to the point at the undrained peak state in the effective stress path. The instability zone is defined as the zone between the instability line and the line connecting the origin to the phase transformation state in the effective stress plane.

The normalized slope difference against fines content before compression are shown in Fig. 3.25. The normalized slope difference here is defined as the difference between the slope of the line connecting the origin to the phase transformation state and that of the instability line in the effective stress plane, normalized by the slope of the line connecting the origin to the phase transformation state. It enables an a quantitative evaluation of the instability zone: the soil with a larger slope difference indicates a wider instability zone. It is noted that the slope differences of soils with erosion were larger that those of soils without erosion at the same initial fines content, especially for the soil with 25% initial fines content, the slope difference of that without erosion (25_WOE) was 0.28, whereas the average slope difference of that with erosion (25_WE_N1, 25_WE_N2) was 0.48, suggesting that the instability zone was enlarged by the internal erosion.

The big change in the slope difference between the eroded soils and original soils might be resulted from the drastic change of its particles arrangements due to internal erosion. Intergranular void ratio assumes that fines function as voids and therefore the volume of fines is considered as voids. Accordingly, if the intergranular void ratios of soils before and after seepage tests are similar, the specimen losing larger volume of fines would have greater deformation to compensate the changes in volumes of voids, which might indicate greater changes of particles arrangements. Table 3.2 notes that the intergranular void ratios of specimens with 15% and 25% initial fines contents were similar before and after erosion, but more fines were eroded aways from the specimen with 25% initial fines content. Therefore, the matrix change of specimen with 25% initial fines content should

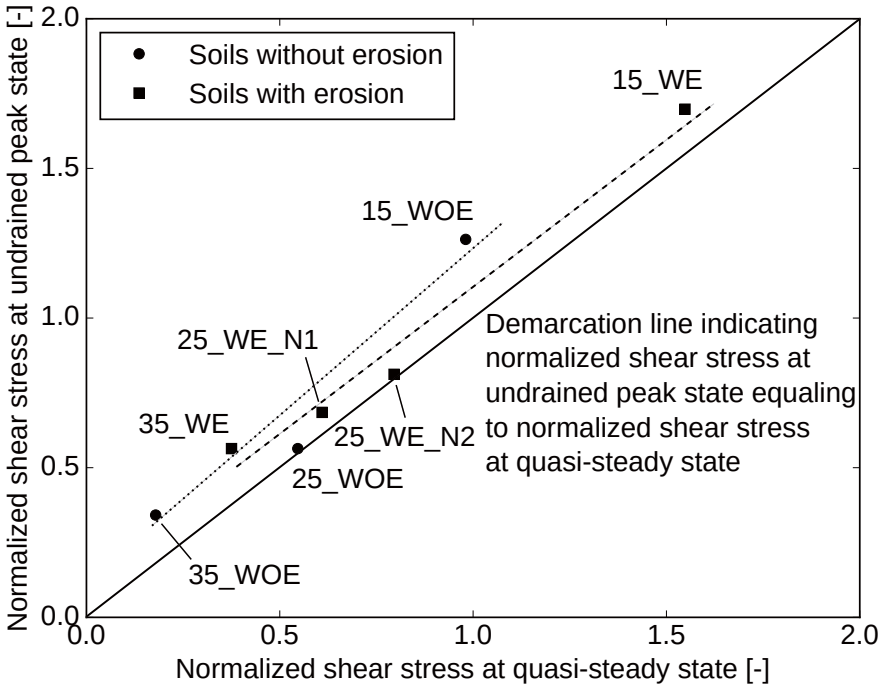

Figure 3.24: Relation of normalized shear stress at undrained peak state and quasi-steady state

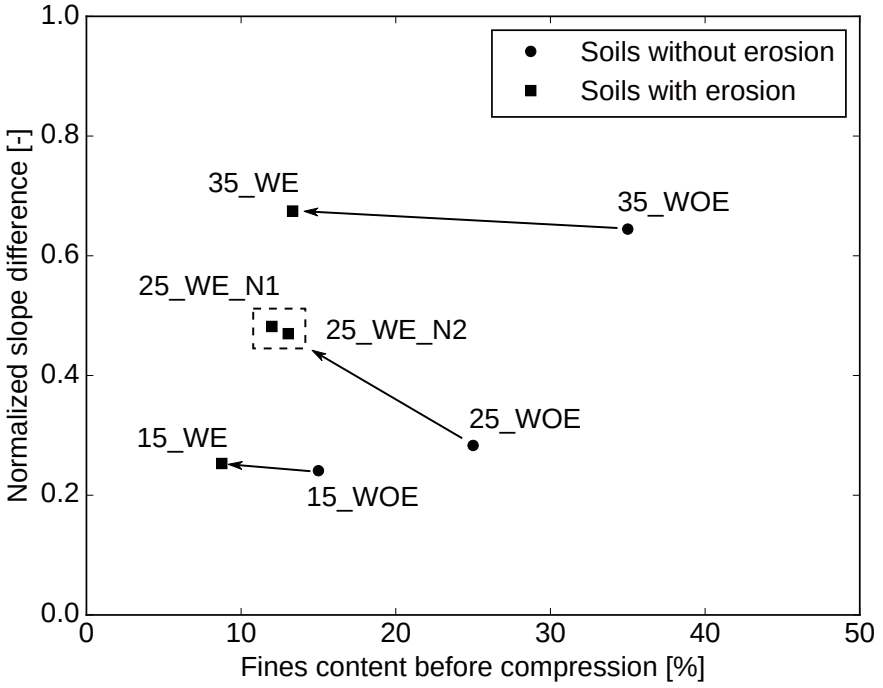

Figure 3.25: Slope difference against fines content before compression

be greater than that of specimen with 15% initial fines content. This tendency corresponded to a larger change of slope difference for specimen with 25% initial fines content (Fig. 3.25). In contrast, the intergranular void ratio of specimen with 35% initial fines content decreased after erosion, which suggests that the coarse fraction was further compacted after internal erosion. Although the specimen with 35% initial fines content showed the largest cumulative eroded soil mass, the balance between the amounts of fines erosion and compaction of coarse fraction led to less change of its slope difference than that of specimen with 25% initial fines content. Future study on the particle arrangements of soils subjected to internal erosion might be helpful in understanding its unstable behaviors in the instability zone.

3.5 Summary

Seepage tests and undrained monotonic compression tests were performed to examine the influence of initial fines content on the mechanical consequences of soils subjected to internal erosion. It is found that the seepage flow not only transports fines away from the specimen, but causes a drastic change of the undrained mechanical behaviors between soils with and without erosion. During the seepage tests, the soil with larger initial fines content shows a larger amount of cumulative eroded soil mass and a larger volumetric strain within the test range.

The amount of silica no. 8 in the tested mixtures would greatly affect their undrained behavior, resulting in the changes of peak strength and residual strength. Specifically, a smaller content of silica no. 8 would cause a larger peak, residual strength, and correspondingly a smaller flow potential.

The mean effective stress ratios (ratio of mean effective stress at peak to that at initial) of soils with erosion show different values from the soils without erosion. For the specimens with the same initial fines content, the post erosion soil exhibits larger undrained tangent stiffness compared to that without erosion at a relatively small axial strain level. The soils with erosion show larger residual strength than those without erosion if their initial fines content are the same. Meanwhile, the eroded soils generate a smaller amount of excess pore water pressure than the uneroded soils before reaching the phase transformation state. It is also noted that the slope difference between the line connecting the origin to the transformation state and the instability line in the effective stress plane is larger for the soils with erosion, indicating an enlarged instability zone after internal erosion.

Chapter 4

Optical quantification of internal erosion in plain strain physical models

4.1 Introduction

It is known that the behavior of soils is influenced by the particle morphology. The density and range of attainable voids vary with sand shape Mitechell and Soga (2005). Stiffness also depends on the size and shape of sand, so does the state parameter at critical state. It was found that the sand morphology affects the erosion potential as well. Horikoshi and Takahashi (2015a) employed the colored siliceous sand in the laboratory tests, which enables an easier identification and visualization of the spatial distribution of particular solid fraction in the whole soil specimens. However, in geotechnical research and practice, the sand size is quantitatively measured by standard sieve analysis, and the sand shape is qualitatively described. Distinct from that, the state-of-are image based techniques realize the quantification of the actual size and shape of sand with different colors.

Internal erosion could change the microstructure of soil Takahashi (2016). Rosenbrand and Dijkstra (2012) quantitatively investigated the spatial distribution of fines during internal erosion by image analysis. It was noted that internal erosion could cause localization of fines accumulation and erosion, which led to inhomogeneous of soils subjected to internal erosion. These non-uniformity in the soils might attribute to the instability of geotechnical structure when experiencing internal erosion. Correia Dos Santos et al. (2015) visually observed the transportation of fines in gap-graded soils during seepage tests, which threw lights on the design of embankment core materials.

The image processing technique is also applied in this research to quantitatively describe the characteristics of suffosional soil based on the images recorded by digital microscope, VCR-800 (see www.hirox.com). It is equipped with a compact 2.11-million-pixel Charge Coupled Device

(CCD) camera, which is capable of capturing high-quality color images consisting of 1600 and 1200 effective pixels in horizontal and vertical axis, respectively.

In this study, images are analyzed using the Open Source Computer Vision Library (OpenCV) (Bradski, 2000), by which the digital images can be viewed as two dimensional discrete components of spatial coordinates and the magnitude of feature value three color components R(red), G(green) and B(blue). The calibration of the microscope indicates that there is only 1.33% in the area distortion; therefore, the influence of lens distortion is neglected in the image processing. According to the distinct color of fines and coarse particles, their spectrum could be recognized from the original recorded image, and then are segmented in order to calculate the fines content. Figure 4.1 (a) and (b) show the typical original image and segmented image, respectively. The movement of fines at the onset of internal erosion is quantitatively obtained through comparing the locations of fines on two successively images which is termed as image subtraction. To detect the contours of coarse particles, the watershed algorithm is utilized. The change of preferred coarse particle orientation is identified through the outline of individual coarse particle in the images taken before and after internal erosion, as illustrated in Fig. 4.1 (c). Figure 4.1 (d) shows the illustrations of preferred coarse particles orientation and aspect ratio, which will be discussed in the following.

This chapter presents a systematic approach for quantitative analysis of size and shape of color siliceous sand particle, especially silica no. 8, in terms of several morphology parameters (i.e., aspect ratio, convexity and sphericity). Then the colored sand is regarded as fines fraction, and employed in the internal erosion tests. One dimensional upward seepage tests were performed on the gap-graded soils containing different initial fines contents. Subsequently, by analyzing the images recorded during the seepage tests, the characteristics of internal are quantitatively elaborated in respect of cumulative eroded soil mass, fines transportation at the onset of internal erosion and volume reduction accompanied with the alternation of preferred coarse particles orientation.

4.2 Quantification of morphology of siliceous sand

The apparatus equipped with microscope in quantifying the morphology of siliceous sand is shown in Fig. 4.2 (a). Figure 4.2 (b) presents the photos of tested sand with different colors, including white, blue, black, red, green and yellow. The white one is the original artificial sand, and commonly mentioned as silica no. 8. Thus, the other colored sands are interpreted and compared with the white one.

The process of image analysis is demonstrated in Fig. 4.3. Firstly, the images of siliceous sand are

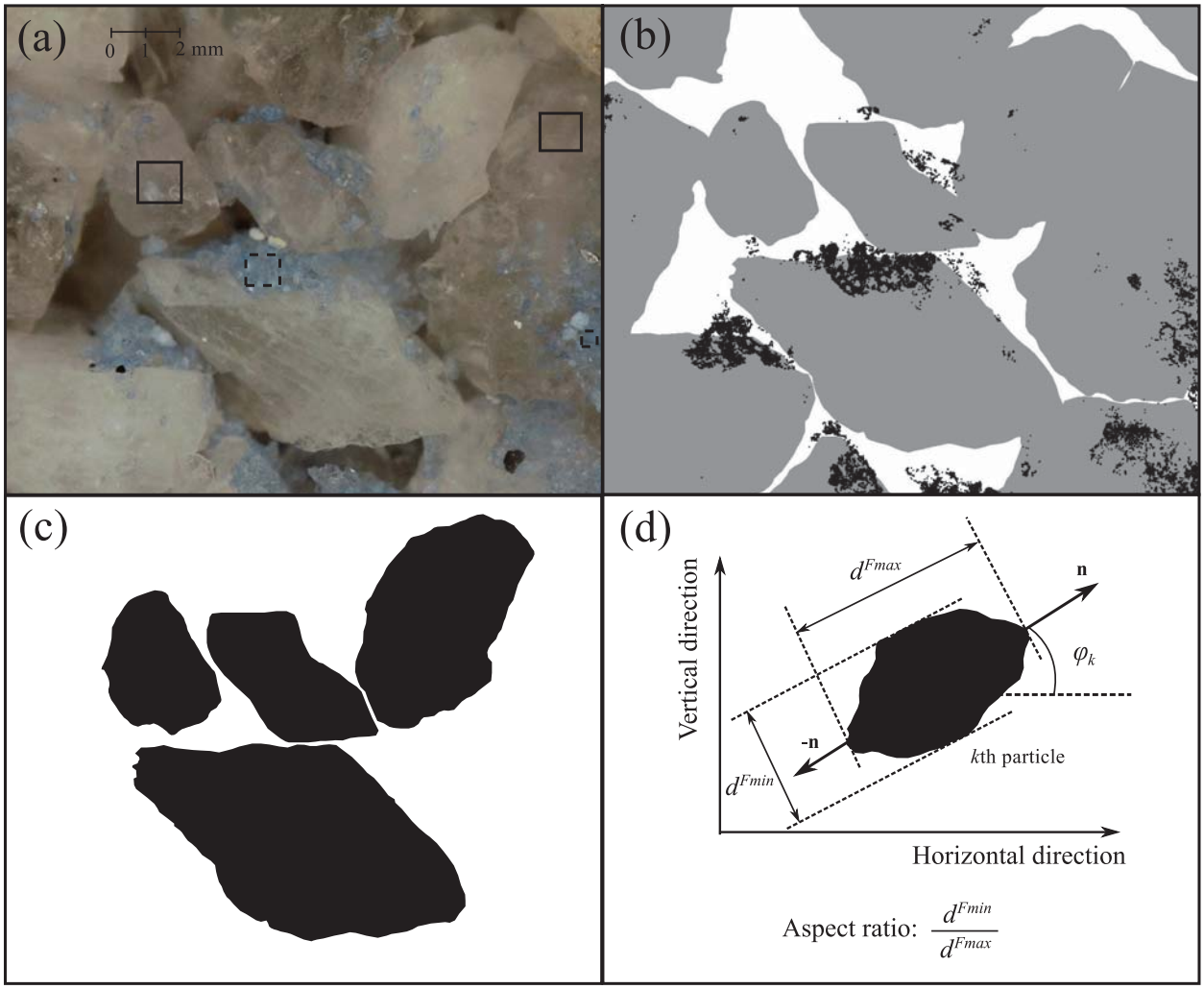

Figure 4.1: (a) Original image taken by microscope VCR-800; the spectrum of fines is obtained from the dash blocks, and the spectrum of coarse particles is obtained from the solid blocks. According to the spectrum distinction between the fines and coarse particles, they can be segmented from the original image and is shown in (b) segmented image, where the black areas represent the fines; and the gray areas represent the coarse particles; (c) outline of the coarse particles by watershed algorithm; (d) illustration of preferred coarse particles orientation, and aspect ratio which is the ratio of the minimum distance to the maximum distance between two parallel tangential lines restricting the particle

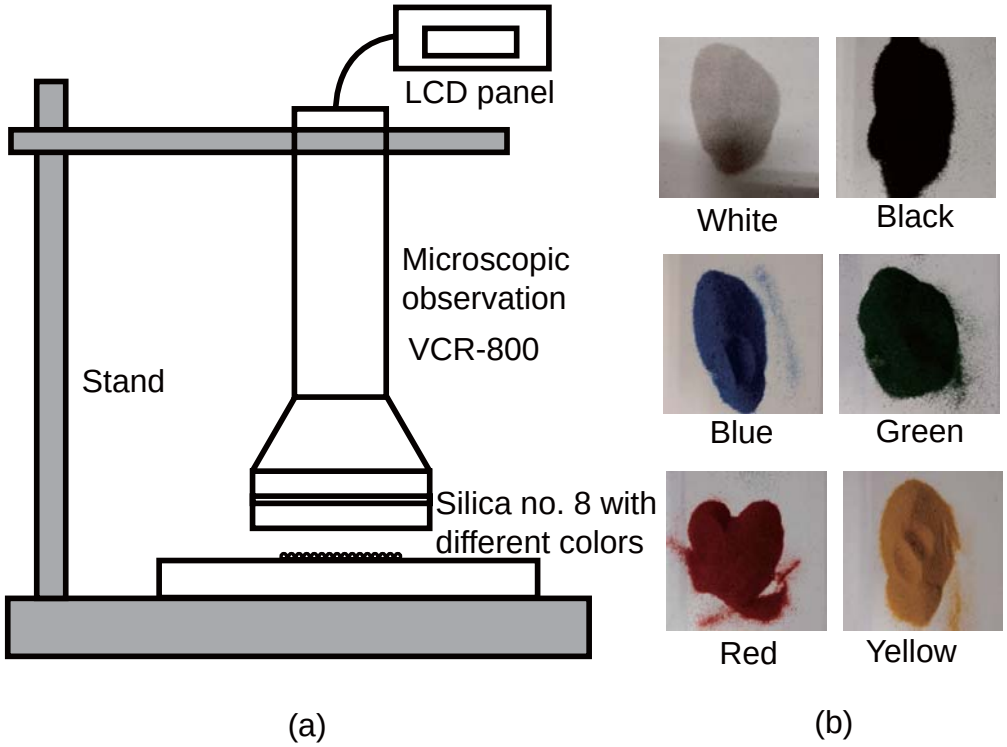

Figure 4.2: (a) Test apparatus equipped with the digital microscope VCR-800; (b) photos of tested sand with difference colors, including white, blue, black, red, green and yellow

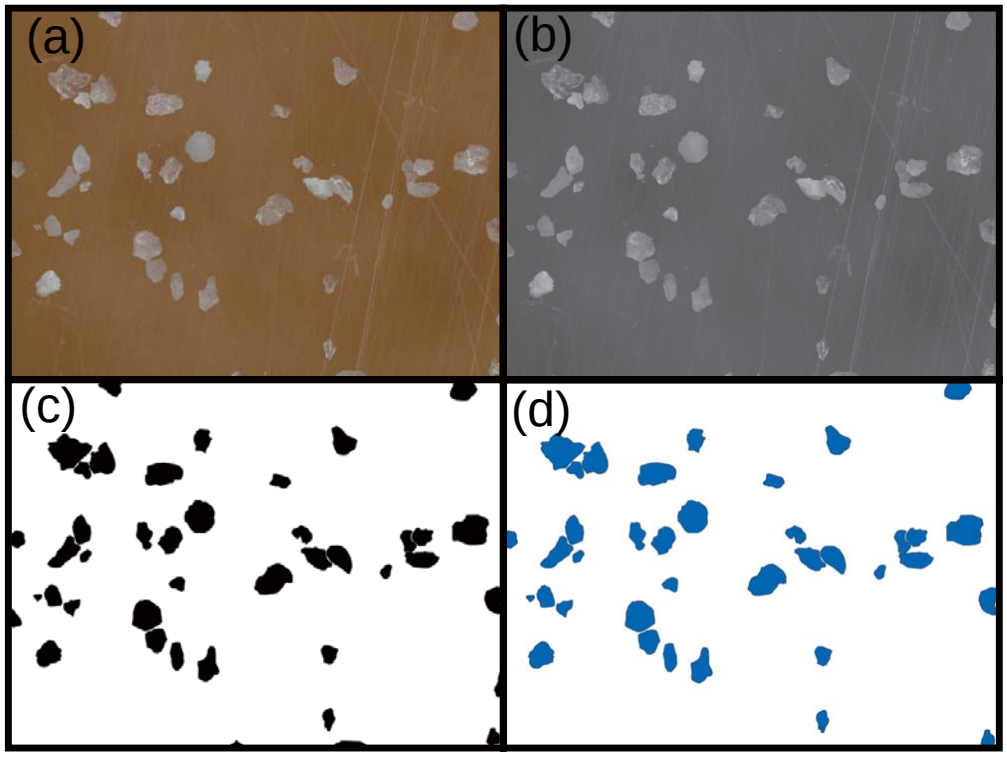

Figure 4.3: Process of image analysis

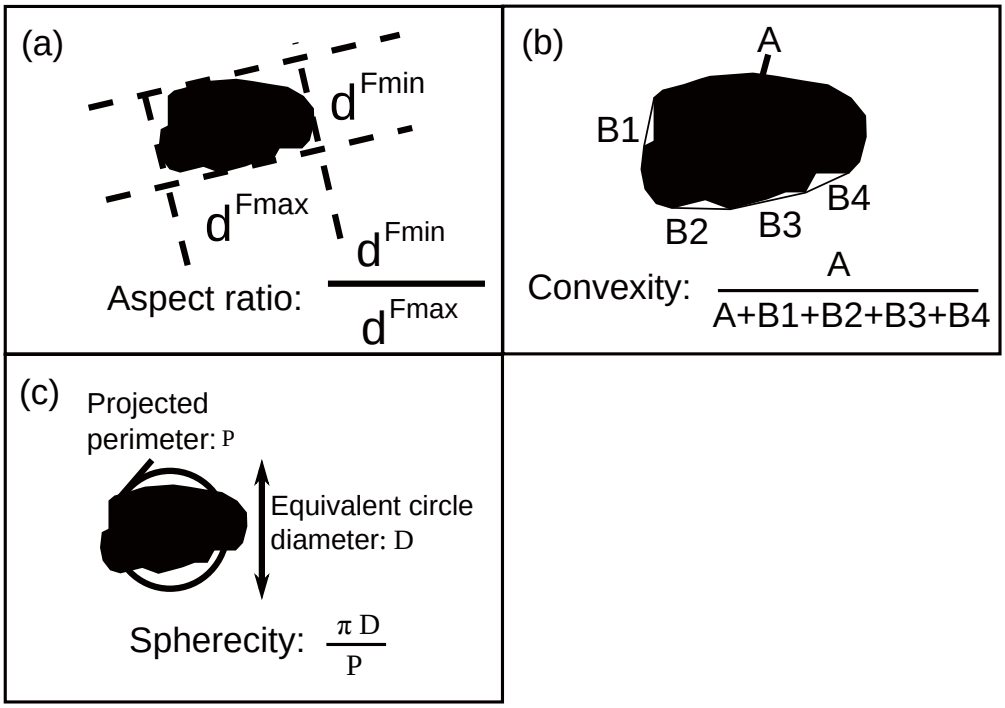

Figure 4.4: Definitions of considered particle morphologies

recorded by VCR-800 (Fig. 4.3 (a)), and then are converted to gray scale images, as shown in Fig. 4.3 (b). Watershed algorithm is utilized to obtain the contours of the sand particles from the gray scale image (Fig. 4.3 (c)). Finally, trim the contours in the edge and mark the left contours as region of interest (Fig. 4.3 (d)). After obtaining the configuration of the sand particles, the morphology in terms of aspect ratio, convexity and sphericity could be derived. Based on the processed images, the particles size and shape are quantitatively described in respect of aspect ratio, convexity and sphericity. The definitions and the measurement approaches are introduced in Fig. 4.4. Following text would discuss them in detail.

4.2.1 Aspect ratio

Feret's diameter is defined as the distance between two parallel tangential lines restricting the object perpendicular to that direction, as indicated in Fig. 4.4 (a). The maximum and minimum Feret's diameters are given as d^{Fmin} and d^{Fmax}, respectively. By using the Feret's diameters, the aspect ratio can be expressed as d^{Fmin}/d^{Fmax}.

Figure 4.5 shows the aspect ratio and its normalized value of different colored Silica no. 8. From the chart, it could be observed that aspect ratio of white sand is 0.71. Observations of the normalized

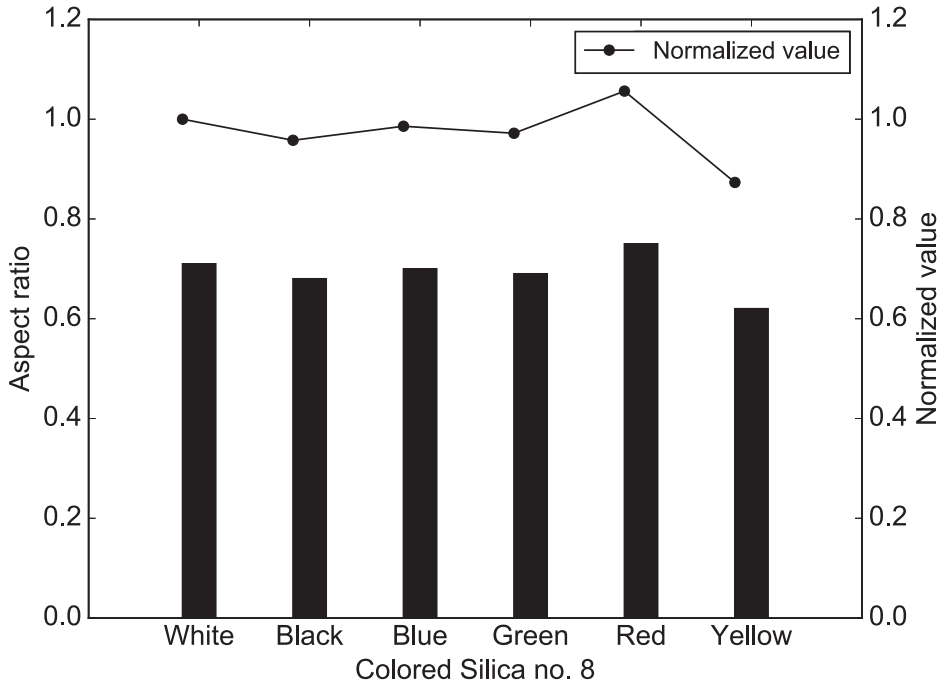

Figure 4.5: Aspect ratio and its normalized value of silica no. 8

value by white sand reveal that the aspect ratio of colored sand shows similar values with that of white sand.

4.2.2 Convexity

The convexity could reflect the compactness of particles, which is therefore defined as the ratio between the area of imaged particle (A) and that of convex hull ($A+B$), as shown in Fig. 4.4 (b), where B equals to $B1+B2+B3+B4$ in the figure. According to the quantitatively analysis of images, the values of convexity of difference colored Silica no. 8 are shown as the bars in Fig. 4.6. The white sand shows a convexity of 0.92. The average value of sand with six colors is 0.90, which is very close to the commonly used sand.

4.2.3 Sphericity

The definition of sphericity in this paper is shown in Fig. 4.4 (c), where D is the diameter of equivalent circle, which has the same area as that of the projected particle; P is the perimeter of

projected particle. The ratio of the perimeter of equivalent circle to that of the projected particle is defined as the sphericity. Accordingly, the measured sphericity and its normalized value are shown in Fig. 4.7. It could be noted that the colored Silica no. 8 show comparable values with that of white sand. The average value of sphericity obtained from the image analysis is 0.86.

Through the image-based techniques, the size and shape of colored Silica no. 8 are quantitatively described in terms of aspect ratio, convexity and sphericity. It notes that the image analysis allows an easy approach in depicting the particle configuration. Furthermore, the colored Silica no. 8 shows similar morphologies with that of commonly used white one, which makes the experiments employed colored sand and original sand comparable. Accordingly, the blue silica no. 8 was employed as the fines fraction in a gap-graded soils to examine its physical and mechanical responses during seepage tests. Image analysis technique was introduced and improved in quantifying the characteristics of internal erosion in varies aspects.

4.3 Experimental setup

The test material in this study was a mixture of silica no. 3 and colored silica no. 8. The original gray silica no. 3 was regarded as the coarse particles, which forms the soil skeleton. The silica no. 8 was artificially coated with blue pigment and then stabilized by baking; this was treated as fines, which could be eroded away by seepage flow. All specimens, with initial fines contents of 15, 25 and 35%, were prepared by the moist tamping method targeting 30% relative density to ensure the occurrence of internal erosion, with an initial water content of around 5%. Since the tested materials were almost the same as those used in Chapter 3, the properties of these siliceous sands and mixtures can be found in Table 3.1. The corresponding particle size distributions are shown by the solid lines in Fig. 4.8.

Upward seepage tests were performed on the gap-graded specimens. Figure 4.9 shows a schematic diagram of the test apparatus, which mainly comprised a rectangular seepage cell with a transparent window in the front and a water tank. The specimens were 100 mm wide, 35 mm deep and 60 mm high. Inlet flow was provided from the water tank, which could be raised or lowered to control the head difference assigned on the specimen. A 30 mm thick gravel diffusing filter was placed in the bottom of the specimen box to ensure a reasonably uniform flow across the soil and non-woven textile was placed below the specimen to prevent downward fines loss. A cylinder was installed at the outlet to measure the average flow velocity.

After completion of specimen preparation, water was allowed to continuously and gently flow

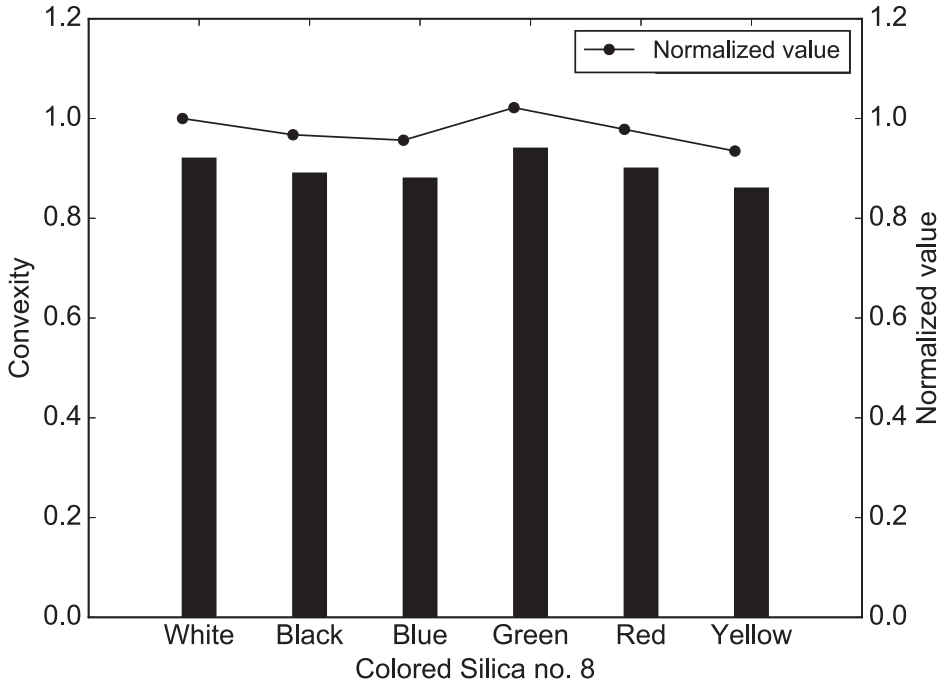

Figure 4.6: Convexity and its normalized value of silica no. 8

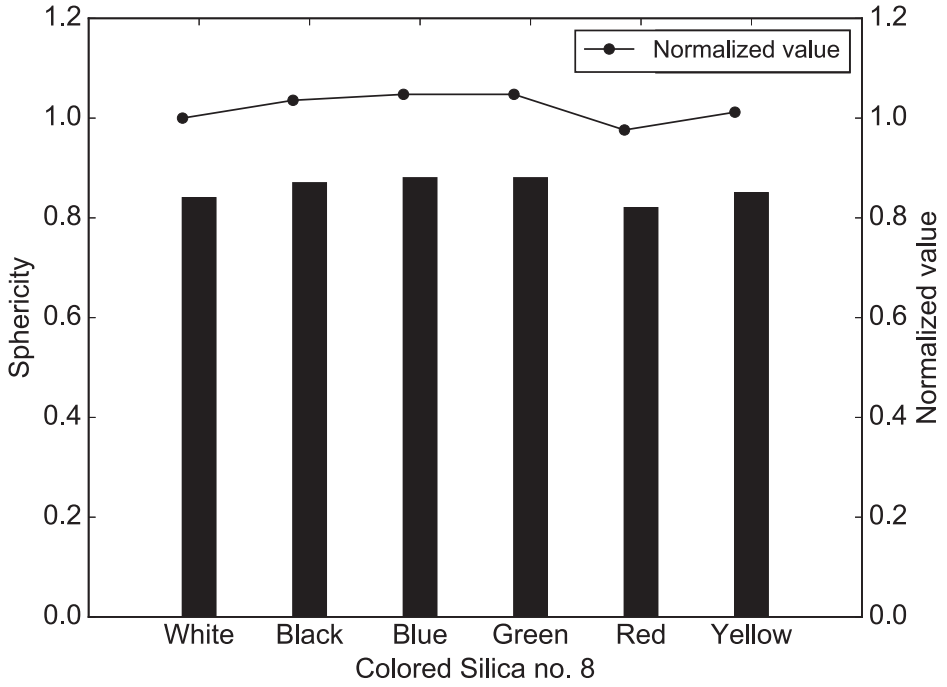

Figure 4.7: Sphericity and its normalized value of silica no. 8

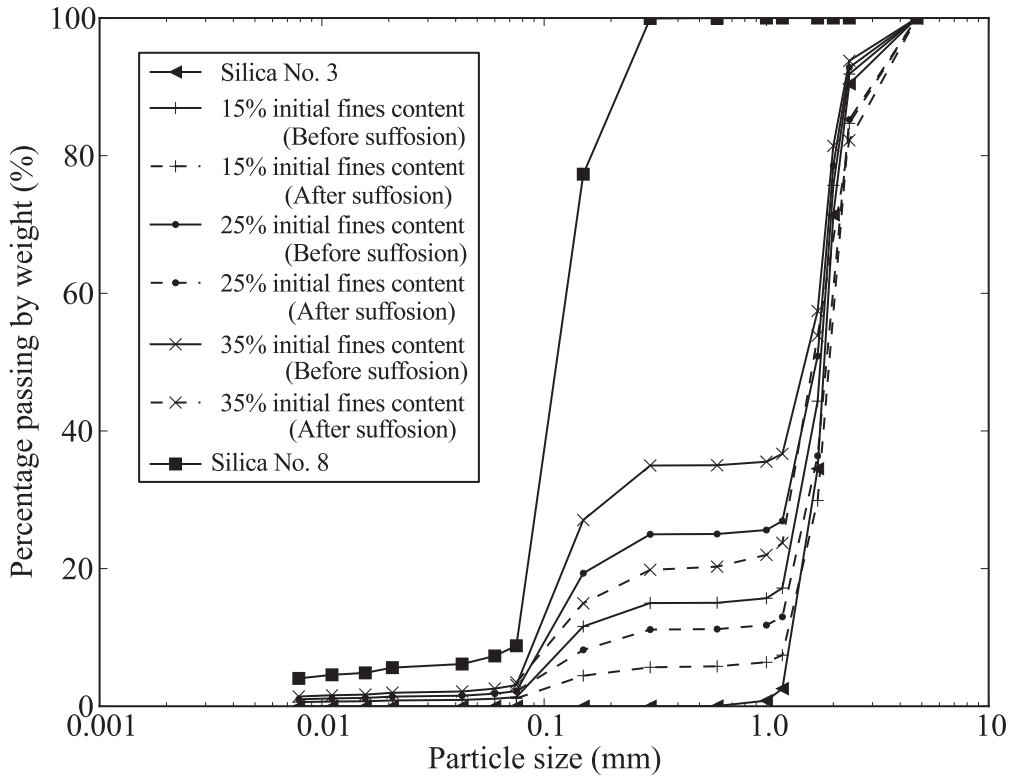

Figure 4.8: Particle size distributions

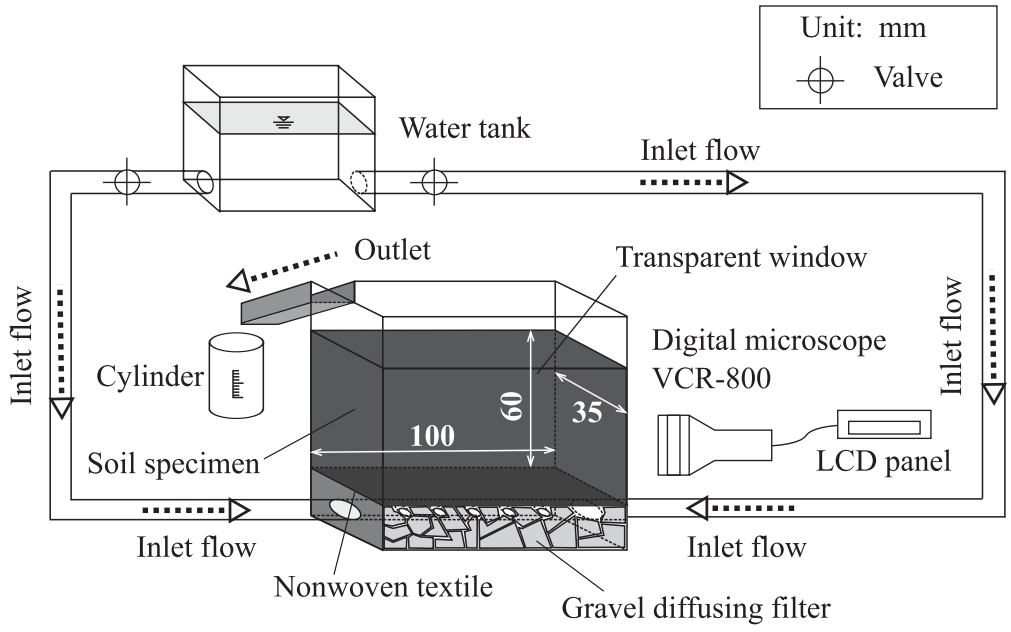

Figure 4.9: Schematic illustration of seepage test apparatus

Table 4.1: Summary of test results

Test	Initial fines content [%]	Initial void ratio [-]	Maximum assigned hydraulic gradient [-]	Cumulative eroded soil mass [g]	Volumetric strain [%]
1	15	0.71	1.1	34.54	2.5
2	25	0.65	1.2	44.34	4.2
3	35	0.63	1.0	61.45	5.8

through the soil until it became saturated. A series of images was recorded at different locations through the transparent window to analyse the soil structure after saturation. The microscope was then fixed on the middle of the specimen through the front transparent window in order to observe the micro-structural evolution of the soil subjected to internal erosion. The water tank was raised to increase the water head on the bottom of the specimen. For each increment, a time of 30 min was allowed to ensure completion of particle transportation. The increase in water head was repeated until no movements could be observed. The microscope was then moved to record images at various locations on the front transparent window, which were to be interpreted to acquire an understanding of the particle spatial distribution of eroded soil.

4.4 Test results and discussion

4.4.1 Cumulative eroded soil mass

A summary of the test results, including the maximum assigned hydraulic gradient, cumulative eroded soil mass and volumetric strain at the end of the test, is given in Table 4.1. After termination of the seepage test, the soil was collected and dried to obtain its particle size distribution. The particle size distributions of the soil after internal erosion are plotted as dashed lines in Fig. 4.8. The figure shows that the particle size distribution shifted downwards after the experiment, suggesting fines loss due to internal erosion. The percentages of cumulative eroded soil mass were calculated by employing the method proposed by Kenney and Lau (1985) who derived the percentage of fines loss by the amount of shift of the distribution curve. The results are shown in Fig. 4.10.

Based on color distinction, image segmentation was applied to the images of the eroded soils to obtain the spatial distributions of both fines and coarse particles. Repeatable and representative results of the derived cumulative eroded soil mass depend on the number of images applied in the analysis; therefore, 27 images taken from various locations on the transparent window were utilized.

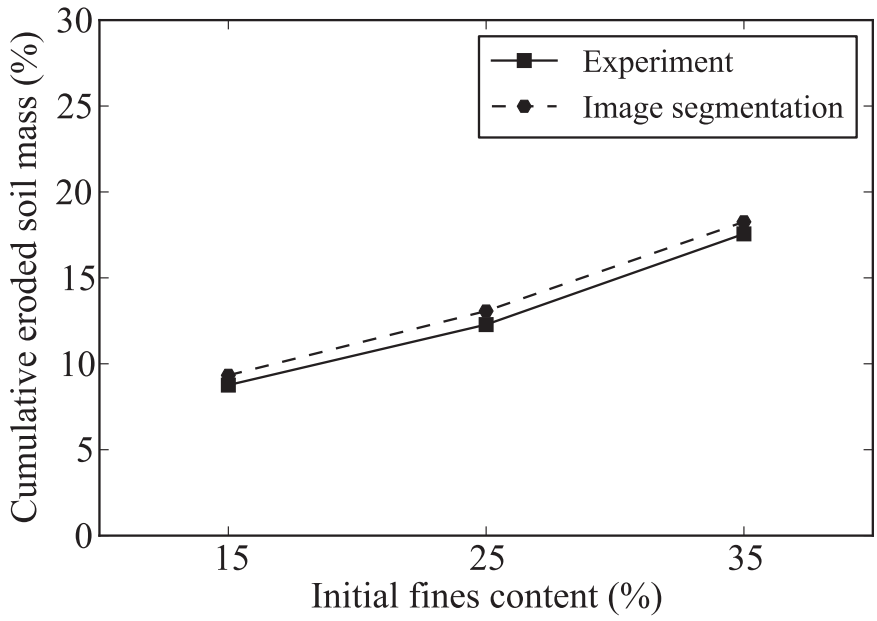

Figure 4.10: Cumulative eroded soil mass obtained from experiment and image segmentation

The deviation of cumulative eroded soil mass from the independent macroscopic observations against the number of images is shown in Fig. 4.11. The figure shows that one image (of size 8 mm 6 mm) is not sufficient to obtain a reasonable value, but 20 images, representing around 960 mm 2 (15% of the total front area), yields a reasonable result. The cumulative eroded soil masses estimated using image segmentation are plotted in Fig. 4.10, and there is good agreement between these values and the data from independent macroscopic observations. An average deviation of approximately 5% suggests that the image analysis technique is capable of describing the properties of internal erosion.

4.4.2 Fines transportation at onset of internal erosion

The hydraulic gradient at the onset of internal erosion was defined as the initiation hydraulic gradient by Chang and Zhang (2013a). That is, under the initiation hydraulic gradient, fines start to move (Skempton and Brogan, 1994). The relationship between hydraulic gradient and average flow velocity of the specimen with 15% initial fines content at the initial stage of internal erosion is shown in Fig. 4.12. It can be seen that the hydraulic conductivity started to change when the hydraulic gradient reached 022; this was regarded as the initiation hydraulic gradient in this test case. Five successive images over 30 s covering the period of the onset of internal erosion were then

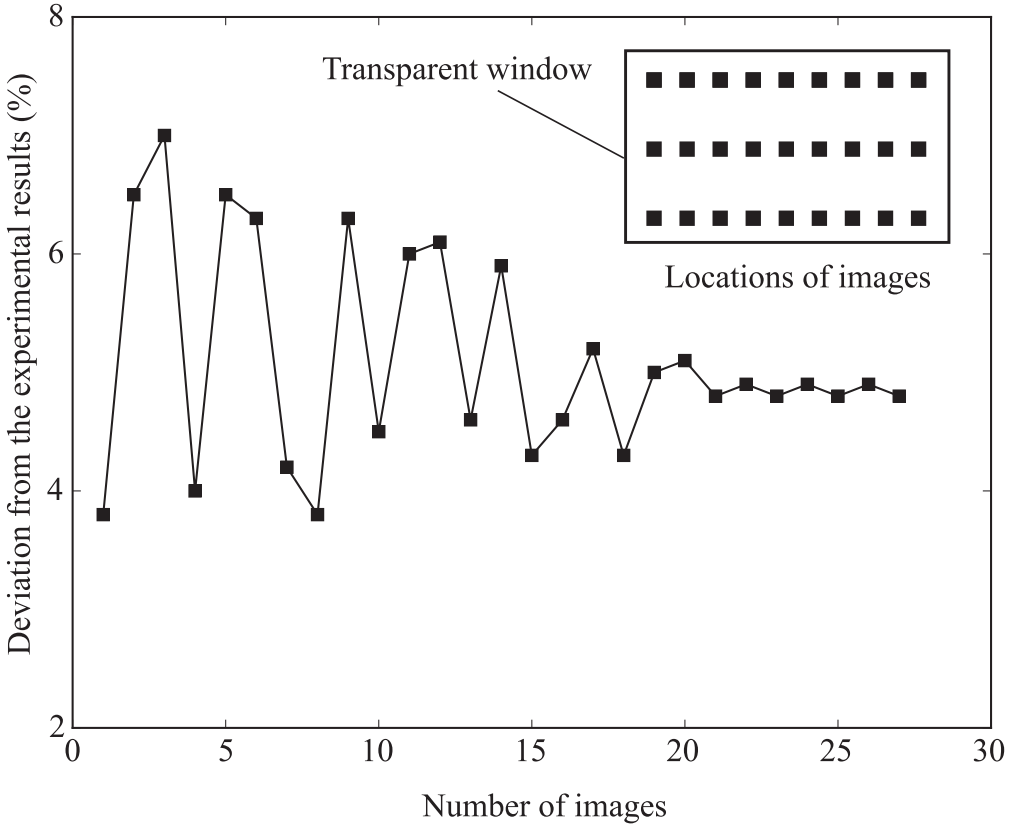

Figure 4.11: Deviation between cumulative eroded soil mass from image analysis and independent macroscopic observations against number of images used (15% initial fines content)

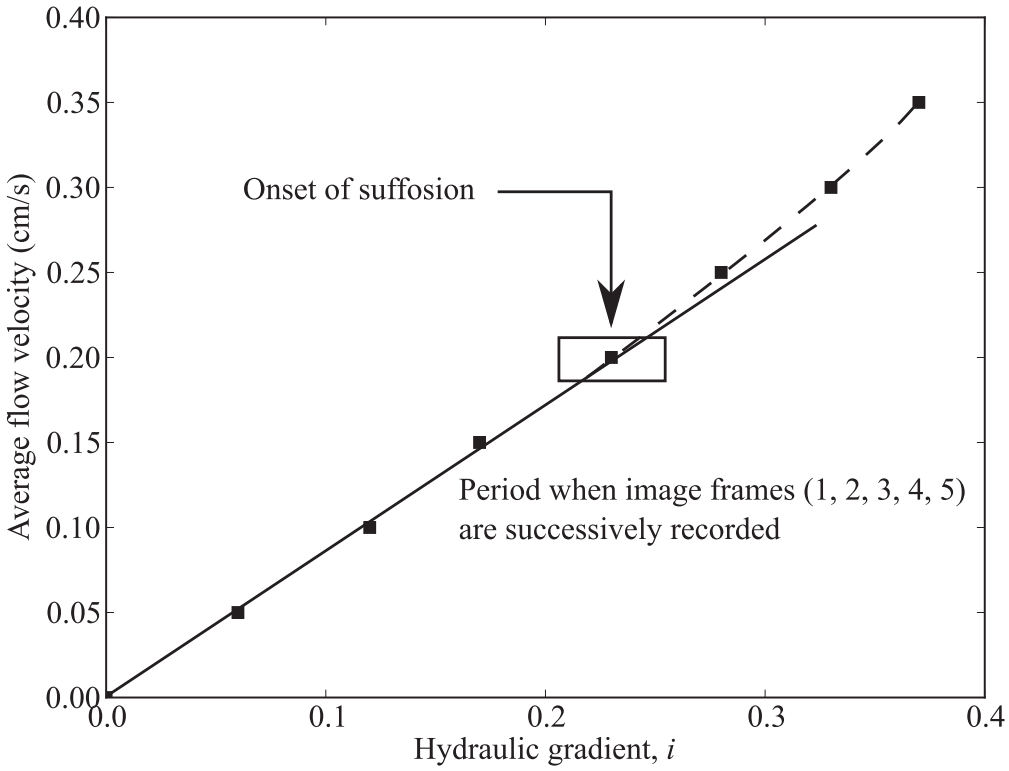

Figure 4.12: Relationship between hydraulic gradient and average flow velocity (15% initial fines content)

analyzed to assess fines transportation in microscale. Figure 4.13 demonstrates the mobile portions, consisting of the appearance and disappearance of fines, together with the hydraulic gradient. The mobile portion is defined as the fraction of area where fines move relative to the total image area with the underlying assumption that the disappearance of fines from the consequential image means they are transported by seepage flow. Major movements were found during the increase of hydraulic gradient, which might because that the sudden increase of hydraulic gradient led to increase of hydraulic force on the soil particles. These applied forces might disturb the internal equilibrium of the soils microstructure, and caused the transportation of fines consequently. However, during the constant hydraulic gradient, the disturbed microstructure probably recovered to the equilibrium state after the dislodgement of fines. Without change of the applied forces, or without change of the hydraulic gradient, the fines might be hardly moved, which then resulted in a small mobile portion during the constant hydraulic gradient. Similar phenomena were observed in the different increment steps during the seepage tests.

Regarding to the influence of the rate of hydraulic gradient increase on internal erosion, Tomlinson and Vaid (2000) found that the rapid increase of hydraulic gradient could prevent the formation of filtration zone, and thus trigging the internal erosion induced failure at small critical gradient. It was also noted that in the practical engineering, the application of gradual increment of hydraulic gradient was more realistic. However, the rate of hydraulic gradient increase could only affect the rate of the applied hydraulic forces. These applied forces would cause the particles movement. As long as the hydraulic gradient became constant, which means that there were not applied force in disturbing the equilibrium of soils microstructures, the particles could tend to be stationary.

It could be argued that the movement of fines observed through the transparent window might be different from that in the inside of the specimen and that the stress states in the physical model could be different from that in situ, and these points might be considered an inherent limitation of this analysis. However, the consistency of the above description with others in the literature (Moffat et al., 2011; Rosenbrand and Dijkstra, 2012; Horikoshi and Takahashi, 2015b; Ke and Takahashi, 2014a) may well demonstrate the applicability of the current method to detect the onset of internal erosion.

4.4.3 preferred coarse particle orientation

As indicated in Table 4.1, specimen volumes were reduced due to internal erosion, which might be due to loss of fines and the rearrangement of particles. Two images taken at hydraulic gradients of approximately 065 and 070 for the specimen with 15% initial fines content show the movements

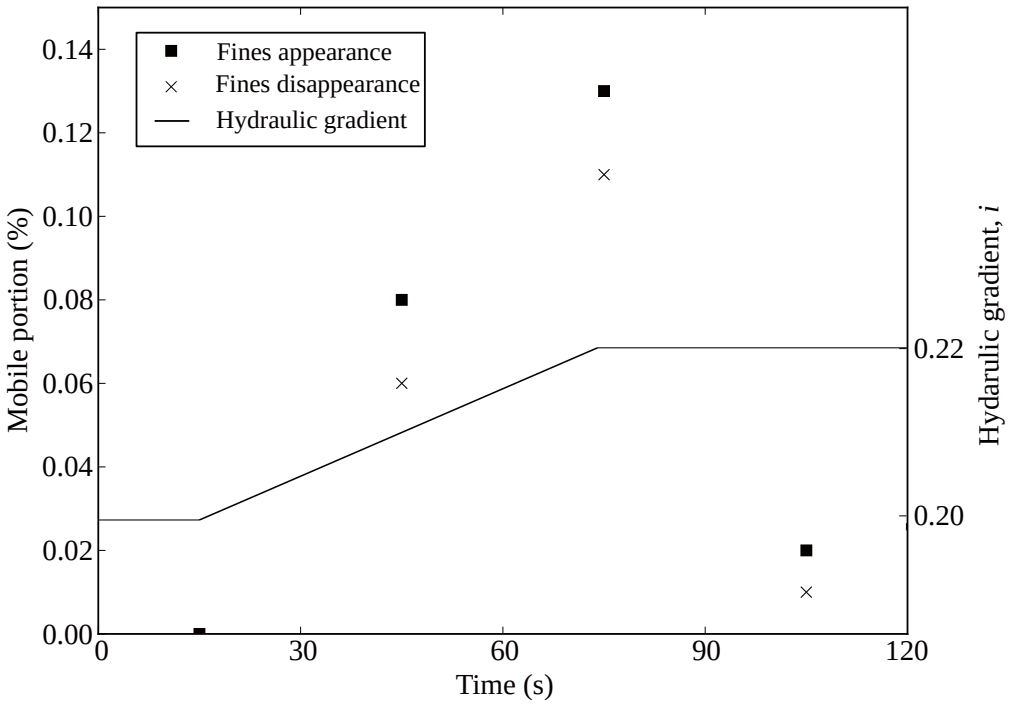

Figure 4.13: Mobile portion and hydraulic gradient during the onset of internal erosion

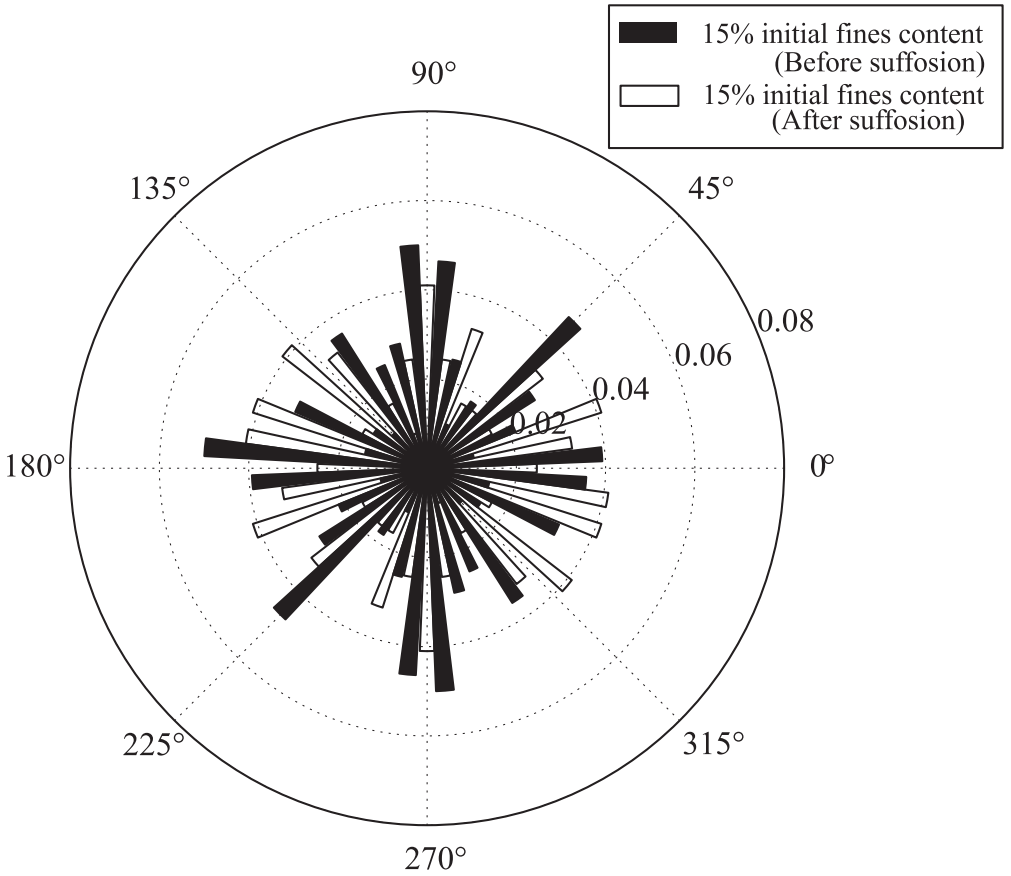

Figure 4.14: Rose diagram representation of preferred coarse particle orientation of soil before and after internal erosion

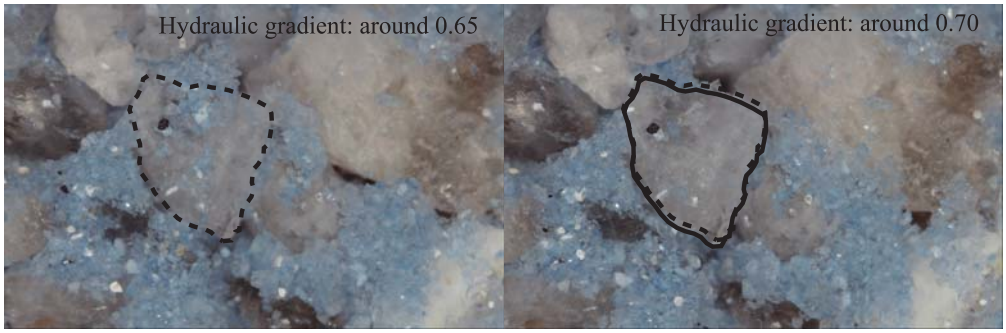

Figure 4.15: Two selected images of specimen with 15% initial fines content taken at hydraulic gradient of 0.65 and 0.70: the dashed line represents the outline of a coarse particle at a hydraulic gradient of 0.65, while the solid line represents that at around 0.70

of a coarse particle at the microlevel (Fig. 4.15). It can be seen that not only translation, but also rotation, of coarse particles occurred within the period of increasing hydraulic gradient.

To quantify the influence of internal erosion on the soil, the watershed algorithm was applied to obtain the outline of coarse particles and then to calculate the preferred particle orientation. The vector magnitude Δ proposed by Curray (1956) was employed to characterize the intensity of the preferred coarse particle orientation, expressed as

$$\Delta = \frac{1}{2N}\left[\left(\sum_{k=1}^{2N}\cos 2\phi_k\right)^2 + \left(\sum_{k=1}^{2N}\sin 2\phi_k\right)^2\right]^{1/2} \tag{4.1}$$

where N is the total number of particles and ϕ_k is the inclination of the kth unit vector n (see Fig. 4.1 (d)), which varies from zero for an isotropic particle arrangement to unity when all particle orientations are exactly the same. In the upward seepage test, it is expected that a change in the metastable structure might be trigged by the water flow, resulting in a horizontal distribution of preferred coarse particle orientation due to gravity acting on the particles.

Through image analysis, 200 coarse particles randomly selected from images taken before and after the seepage test for the specimen with 15% initial fines content were numbered and their orientations identified. The orientations with respect to the horizontal are shown in a rose diagram representation in Fig. 4.14. The value of Δ of the specimen before internal erosion was 0.091, which suggests that the specimen prepared by the moist tamping method tended to be isotropic (Yang et al., 2008), as expected. Regarding the soil after internal erosion, no particular preferred orientation was detected, and the Δ value was 0.052. However, since coarse particles could be categorized as subangular particles (with an average aspect ratio of 080 (Fig. 4.1 (d)) (Altuhafi et al., 2013),

the reduction of Δ by 42.9% might suggest that the force transformation along the coarse particles could be alternated due to internal erosion. Moreover, Fig. 4.14 indicates that many of the coarse particles were arranged horizontally after internal erosion.

4.5 Summary

In this chapter, the siliceous sand with difference colors was quantified by image analysis in terms of aspect ratio, convexity and sphericity. The results showed that the morphology parameters of colored silica no. 8 were similar with those of original artificial silica no. 8. It makes the experiments employed colored sand and original sand comparable.

The blue silica no. 8 was then employed in the study of internal erosion. One dimensional upward seepage flow was applied in the mixtures of silica no. 3 and blue silica no. 8, in order to investigate the features of internal erosion. Image analysis was applied to quantitatively describe the characteristics of soil subjected to internal erosion. The cumulative eroded soil masses calculated by means of image analysis were generally in accordance with those obtained from independent macroscopic observations, suggesting that image analysis is an effective tool for describing the features of internal erosion. With the respect to the observed area, for the gap-graded soil studied in this research, during an increase in hydraulic gradient, a large amount of fines tended to be transported, but were prone to be stationary under constant flow. The volume of the soil specimens decreased due to internal erosion and, as a result, the coarse particles were oriented horizontally.

Chapter 5

Plane strain erosion apparatus equipped with visible window

5.1 Introduction

From the heaven to internal erosion, many experimental devices had been developed for understanding the mechanism of these geotechnical phenomenon (Skempton and Brogan, 1994; Tomlinson and Vaid, 2000; Reddi et al., 2000). To assess the piping potential of embankment dams, Wan and Fell (2004b) performed the hole erosion test in the laboratory. Moffat and Fannin (2006) had developed a large permeameter to test the internal instability of cohesionless soils subjected to internal erosion, together with the spatial distribution of hydraulic gradient during the seepage tests. After the acceptance that the internal erosion could alter the physical and mechanical features of soil, some researchers had carried out the element tests to quantitatively verify the influence of internal erosion on the mechanical behaviors. Xiao and Shwiyhat (2012) had investigated the undrained behaviors of soils subjected to the internal erosion by triaxial apparatus through revising the pedestal to allow the dislodgement of fine fractions. To get a precise view of the hydraulic gradient change during the internal erosion, Chang and Zhang (2011) discussed the initiation hydraulic gradient and divided the internal erosion into four stages by providing the pressurized seepage flow in the revised triaixal device. Ke and Takahashi (2014b) further revised the triaxial apparatus by supplying the back pressure into the sedimentation tank, which is used for collecting the eroded soils, to make sure the tested specimens would have a high saturation degree even experienced internal erosion. Besides the laboratory tests conducted in the triaxial cell, Richards and Reddy (2010) developed a true triaxial piping test apparatus so as to evaluate the piping potential of small to middle embankment dams.

Although some apparatus have been developed for testing the characteristics of internal erosion

from the aspects of physics and mechanics, there is still some mechanisms on internal erosion need to be discovered. One of the main difficulties lies in observing the particles movement during the seepage test, which is also the definition of internal erosion that the fines be transported in the constrictions by seepage flow. Recently, the transportation of fines is indirectly measured by the cumulative eroded soil mass, the change of hydraulic gradient and conductivity, and the change of specimen volume, whereas, the microscopically description of fines dislodgement is not quantified. Moreover, internal erosion always occurs below the ground surface, subjected to certain earth pressure, it would be practical if the pressure would be applied on the specimens when subjected to seepage flow. Upon these difficulties, this chapter presents a developed plane strain erosion apparatus equipped with visible window, capable of microscopically observing the particles behaviors during the seepage and compression tests under plane strain conditions.

5.2 Plane strain erosion apparatus

5.2.1 General description

The plane strain erosion apparatus was developed based on the revised triaixal erosion apparatus (Ke and Takahashi, 2014b) to microscopically observe the internal erosion characteristics under the plane strain conditions. It mainly consists of a plane strain cell, a seepage control unit and a pressure control unit. To quantitatively describe the characteristics of internal erosion in particulate level, a transparent visible window was manufactured in the front of the plane strain cell. At the same time, the transparent membrane was applied in this research to provide a flexible boundary condition in both the seepage and compression tests. Additionally, colored siliceous sand was utilized as fine fraction in the mixtures for an easily identification of particles interface transportation. Regarding to the stress conditions, the vertical stress could be measured and controlled by the load cell; the normal stress perpendicular to the plane strain could be controlled by a E/P (Electronic to Pneumatic) transducer connecting to the water bladders through a water reservoir; and the normal stress in direction of plane strain could be measured by the installed earth pressure transducer in the back plate.

During the seepage tests, the evolution of cumulative eroded soil mass could be measured by the miniature load cell installed in the sedimentation tank. The volume deformation during the seepage test and the compression stage could be obtained either by the measurement of the water level in the reservoir connected to the water bladder or by the digital image correlation from the recorded videos. Besides the macro features of internal erosion, the micro characteristics, such as the contact area and fines accumulation could be quantified through the microscopic images recorded from the visible front window as well. The photography of the main components of the plane strain erosion

apparatus are shown in Fig. 5.1. The schematic digram of the plane strain erosion apparatus is demonstrated in Fig. 5.2.

5.2.2 Plane strain cell

The plane strain cell in this developed apparatus includes a revised pedestal and top cap, front and back plate, together with two water bladders in left and right hand sides. A photography indicates the relative positions of each component in the plane strain cell is illustrated in Fig. 5.3

The pedestal was modified with an inverted cone to allow the effluent water and eroded fine particles to exit the cell and accumulate in the sedimentation tank, as shown in Fig. 5.4. A 5 mm thick stainless mesh with 1 mm openings, which follows the recommendation from the U.S. Department of Agriculture (USDA, 1994) to fully hold the coarse particles and allow the erosion of fines, was placed on the end-platen of the pedestal. At the outlet of the trough, a plastic tube was fitted and connected to the sedimentation tank to collect the effluent and eroded fines.

Figure 5.5 shows the top cap in the plane strain cell, it was fabricated with a conical trough to accommodate the seepage test. A 5 mm thick stainless mesh perforated by 1 mm holes on a 2 mm center to center spacing was mounted in the top cap. This arrangement permits an unimpeded flow of water across the loading plate.

An 80 mm wide and 110 mm high acrylic window was made within the front plate to allow the observation of the specimen during both seepage and compression tests, as shown in Fig. 5.6. It could yield valuable insights to the spatial variation of individual particles movement during the seepage and compression tests. Moreover, it permits the recording of the specimens volume change during the whole experiments.

The back plate is a 200 mm wide and 170 mm high stainless steel plate. A hole with 30 mm diameter was made within the back plate to install the earth pressure transducer, as shown in Fig. 5.7. The type of earth pressure transducer is BED-A-500, and made by Kyowa Electronic Instrument Co. Ltd., as shown in Fig. 5.8. It has a capacity of 500 kPa and a resolution of 0.01 kPa. One argument with the earth pressure transducer was that the load measured by the cell under fluid pressure might be different from that measured under soil pressure. However, the calibration made by soil enclosed with membrane and that directly under fluid pressure did not show much difference, which was also proved by Wanatowski and Chu (2006). The arching effect seems does not affect much in the earth pressure transducer applied in this study. Therefore, it was employed to measure the normal stress in direction of plane strain during the seepage and compression tests.

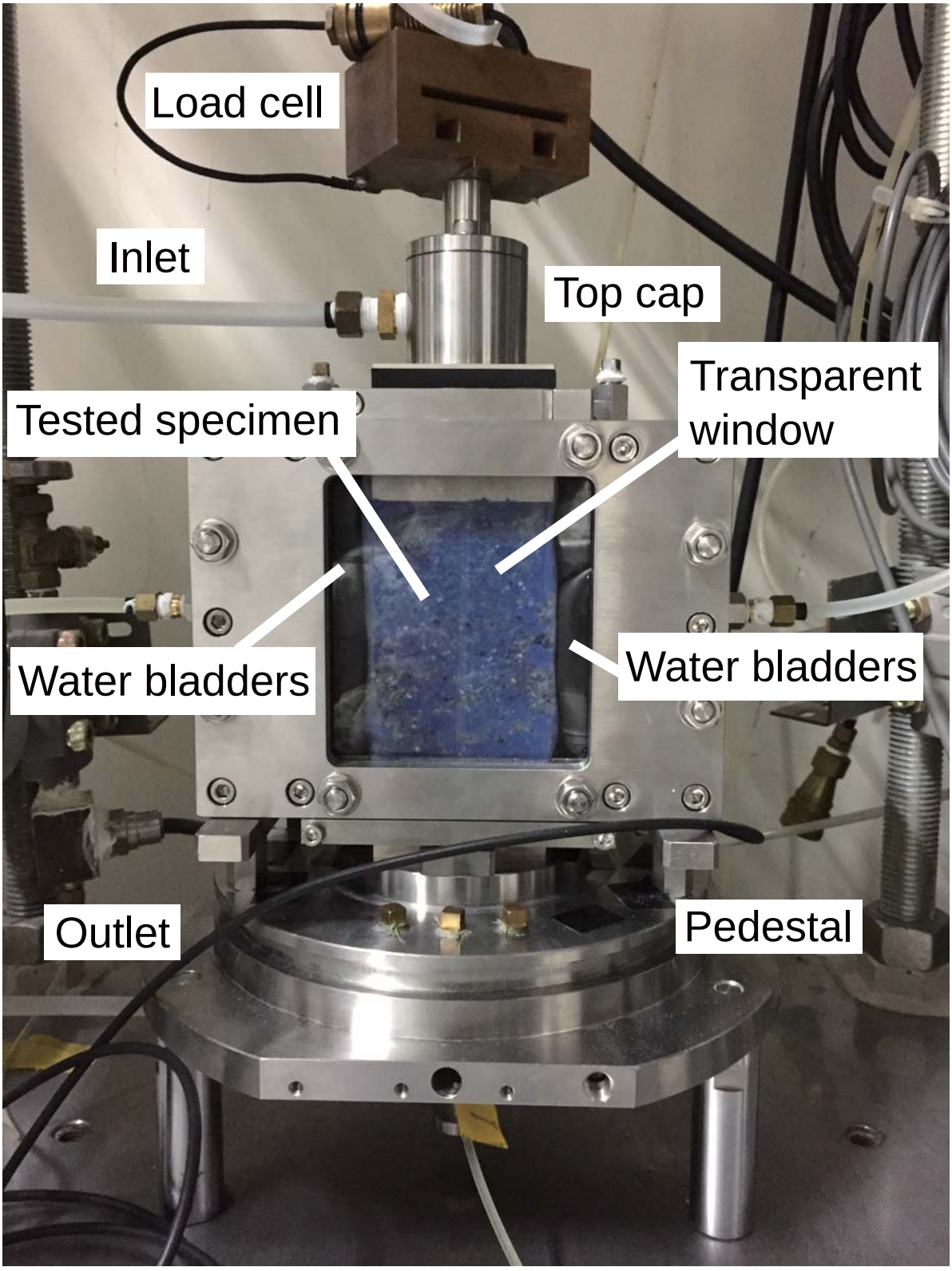

Figure 5.1: Photograph of the main part of plane strain erosion apparatus

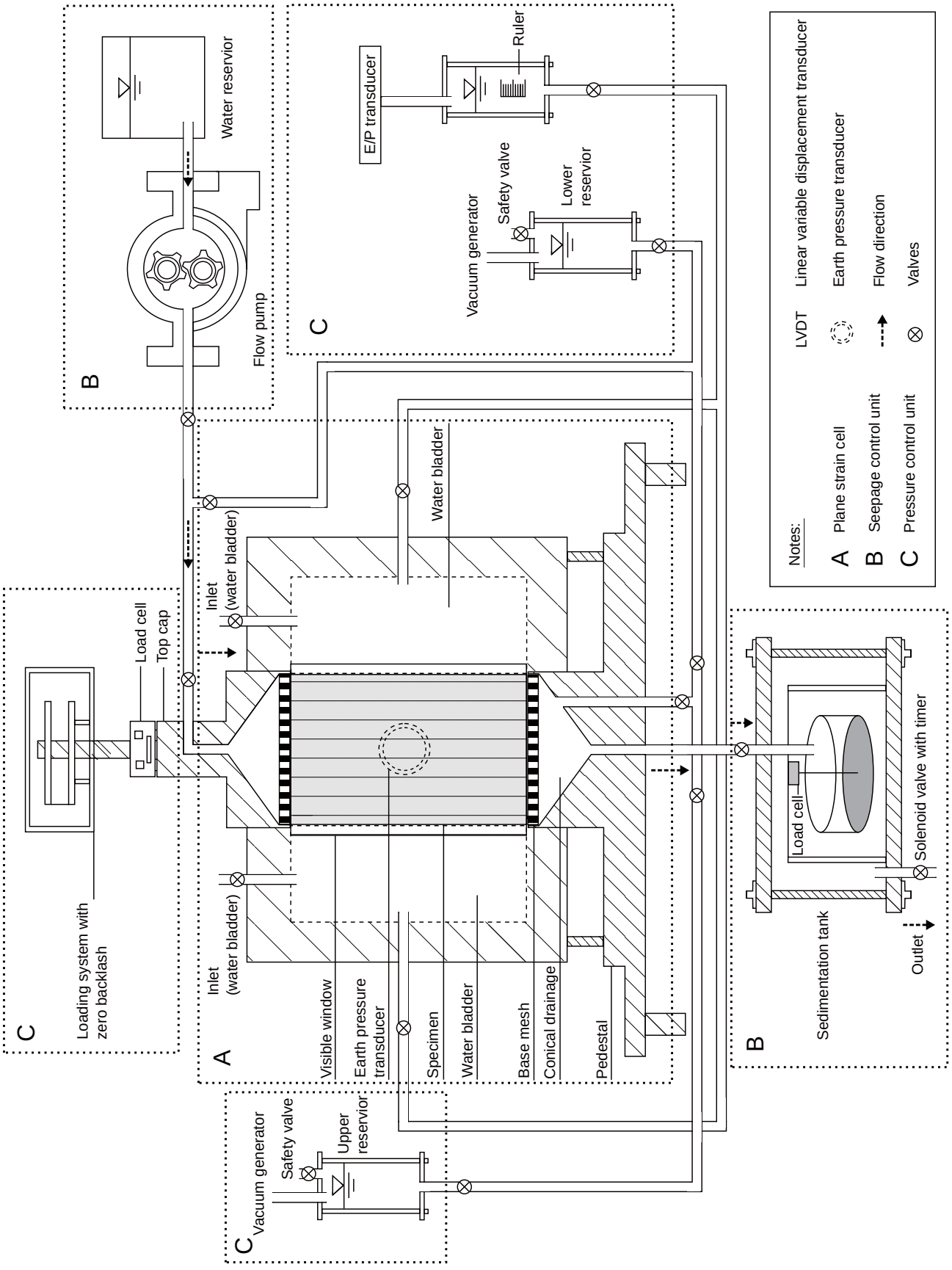

Figure 5.2: Schematic diagram of plane strain erosion apparatus

Figure 5.3: Layout of the plane strain cell (top view)

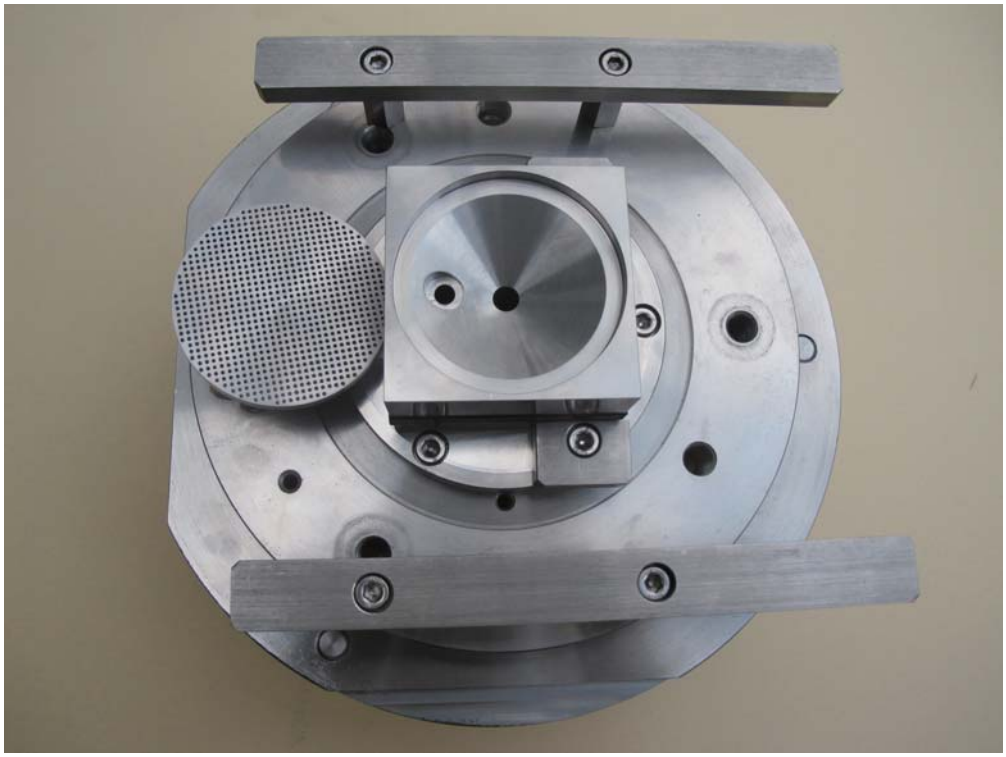

Figure 5.4: Revised pedestal in plane strain cell

Figure 5.5: Top cap in plane strain cell

Figure 5.6: The front transparent window in plane strain cell

Two water bladders were designed for this apparatus to provide the normal stress perpendicular to plane strain, as illustrated in Fig. 5.9. The bladders were made of rubber, and were guaranteed to a maximum pressure of 200 kPa, which was adequate to simulate the internal stresses within small embankments or dams. It also provided flexible boundary conditions, which would not only effectively avoid the side leakage during the seepage tests, but also allow precise observation of the deformation of specimen. The image based measurement of volume deformation could then be compared with the record of water level change in the reservoir connected to the water bladders, which provides double check for the investigation of volumetric strain during the testing.

To permit the observation of soil particles during the seepage tests and subsequent compression tests, the transparent membrane with 1 mm thickness was employed to enclose the specimens tested in the plane strain cell. Figure 5.10 shows the transparent membrane adopted by this developed plane strain erosion apparatus.

5.2.3 Seepage control unit

The seepage control unit consists of a water reservoir, a flow pump and a sedimentation tank. The water reservoir was used to provide the water for the seepage test. The water was prepared at least 24 hours before conducting the experiments, and was kept at room temperature. According to Richards and Reddy (2010), to examine the characteristics of cohesionless soils subjected to internal erosion, the application of flow rate as the control parameter might provide consistent results. Moreover, the tested materials in this study were cohesionless sands, the hydraulic conductivity of which was very large. Thus, the seepage tests controlled by hydraulic gradient might not be appropriate due to comparatively small hydraulic gradient to trigger and maintain the internal erosion. As per the above mentioned reasons, the seepage by performed in the plane strain erosion apparatus was controlled by flow rate. A rotary flow pump with maximum flow rate of $2.3 \times 10^{-5} mL/min$ was installed to pump the water into the specimen. To maintain the constant flow rate during seepage test, all the flow channels were designed to be the same size. The top cap was fabricated with a conical tough, and a perforated plat was mounted to be directly attached to the top surface of the specimen, and to minimize the possible water head loss (Fig. 5.5). The pedestal was symmetrically made with an inverted conical tough (Fig. 5.4), to maintain the constant flow rate and minimize the head loss as well. The eroded fine particles and the effluent water would be collected by the sedimentation tank (Fig. 5.2), which could be pressurized to simulate any reasonable downstream pressure or be open to atmosphere. In this research, the downstream pressure was maintained at atmospheric pressure. The cumulative eroded soil mass was gained by continuously weighing the

Figure 5.7: The back plate in plane strain cell

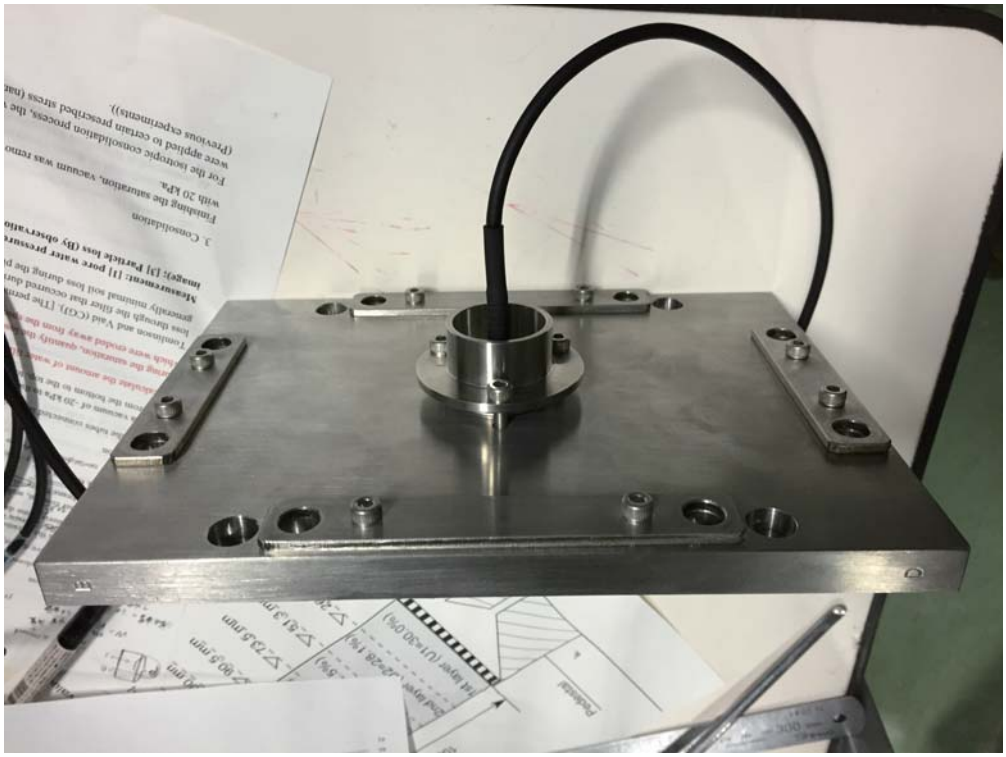

Figure 5.8: Earth pressure transducer BED-A-500 (Kyowa Electronic Instrument Co. Ltd.)

Figure 5.9: Two water bladders in the plane strain cell

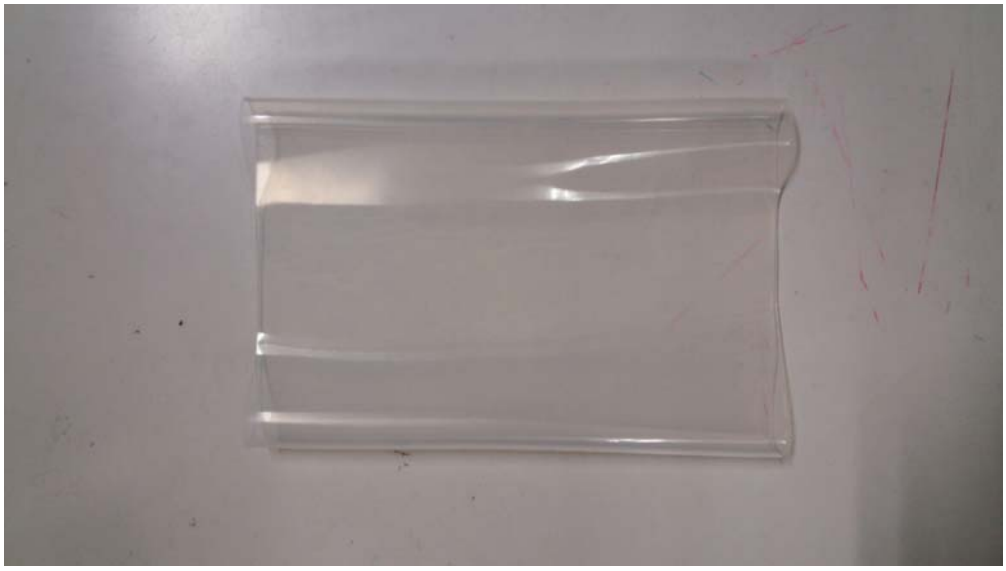

Figure 5.10: The transparent membrane employed in the plane strain cell

tray, which was fully submerged in the tank to collect the eroded fines. The miniature load cell installed in the sedimentation tank, which is waterproof and has a high sensitivity, could record the cumulative eroded soil mass within a continuous period. The theoretical resolution of the load cell is 0.00015 N (approximately 0.015 g).

5.2.4 Pressure control unit

The pressure control unit is composed of a loading system with zero backlash for controlling the vertical stress, and one reservoir connected to the E/P transducer for providing the normal stress perpendicular to plane strain.

The automated triaxial system, which could not only control but also measure the load and pressure by PC through 16-bit A/D and D/A converters, was employed in this study. The vertical load was automatically applied by a motor gear system, which could be controlled to operate at any rate. The maximum load it could apply is 50 kN. The vertical load could be measured by the load cell mounted above the top cap.

The normal stress perpendicular to the plane strain was applied by water pressure through the two water bladders (Fig. 5.9). The water bladder was connected with the water reservoir, which could be pressurized by the air pressure through an automatic air compressor. All the pressure lines were connected to a drying system to remove any condensed water. The control of normal stress perpendicular to plane strain was through E/P transducers, which were linked to a PC through a 16-bit D/A board.

5.2.5 Data acquisition

By the plane strain erosion apparatus, the vertical load could be measured by the submersible load cell attached at the top cap. The normal stress in direction of plane strain was measured by the Earth Pressure Transducer (EPT) (Fig. 5.8). An outer Linear Variable Differential Transformer (LVDT) was used to monitor the vertical displacement in the test. The cumulative eroded soil mass was gained by the submersible load cell with high sensitivity. The calibration and regression characteristics of the transducers are summarized in Table. 5.1.

Table 5.1: Calibration and regression characteristics of transducers

Transducer	Calibration against	Range	Type of regression	Coefficient of correlation	Accuracy[1] [%]
Load cell[2]	Dead weight	0-1500 [N]	Linear	0.99999	0.48
EPT[3]	Dead weight	0-500 [kPa]	Linear	0.99999	0.24
LVDT[4]	Micrometer	0-20 [mm]	Linear	1.00000	0.08
Load cell[5]	Dead weight	0-0.5 [kg]	Linear	1.00000	0.10

[1] Percentage of the maximum error in a calibrated range;
[2] Load cell for measuring vertical load [N];
[3] Earth Pressure Transducer for measuring the normal stress in direction of plane strain [kPa];
[4] Linear Variable Differential Transformer for measuring the vertical displacement [mm];
[5] Miniature load cell for measuring cumulative eroded soil mass [g].

5.2.6 Camera calibration

Other than the data obtained from the installed transducers, the images recorded by the microscope could also provide information on the interpretation of the mechanism of internal erosion. In order to obtain the correct and consistent information, the camera calibration was performed on all the microscopic images first to correct the camera distortions, and to convert the image pixels to object space. To calibrate the microscopic images, the method proposed by Heikkila and Silven (1993) was employed through the OpenCV package (Bradski, 2000). Figure 5.11 illustrates the procedure of camera calibration. The original image is shown in Fig. 5.11 (a); Fig. 5.11 (b) demonstrates that there are distortions in the recorded images, accordingly, the centroids of the control points are drawn in Fig. 5.11 (c); and the camera calibration toolbox in OpenCV was applied, the calibrated image is then shown in Fig. 5.11 (d). The calibration procedure was followed for all the image analysis in each tests to yield the consistent results.

5.3 Summary

A plane strain erosion apparatus was developed to evaluate the responses of soils under plane strain conditions. It is capable of directly investigate not only the marcoscale behaviors of soil subjected to internal erosion, but also the microscale features of particles during seepage and compression tests. The fabricated front visible window and the application of transparent membrane permitted the clearly observation of the particles movements. The earth pressure transducer attached at the back plate allowed the measurement of the normal strain in direction of plane strain. The

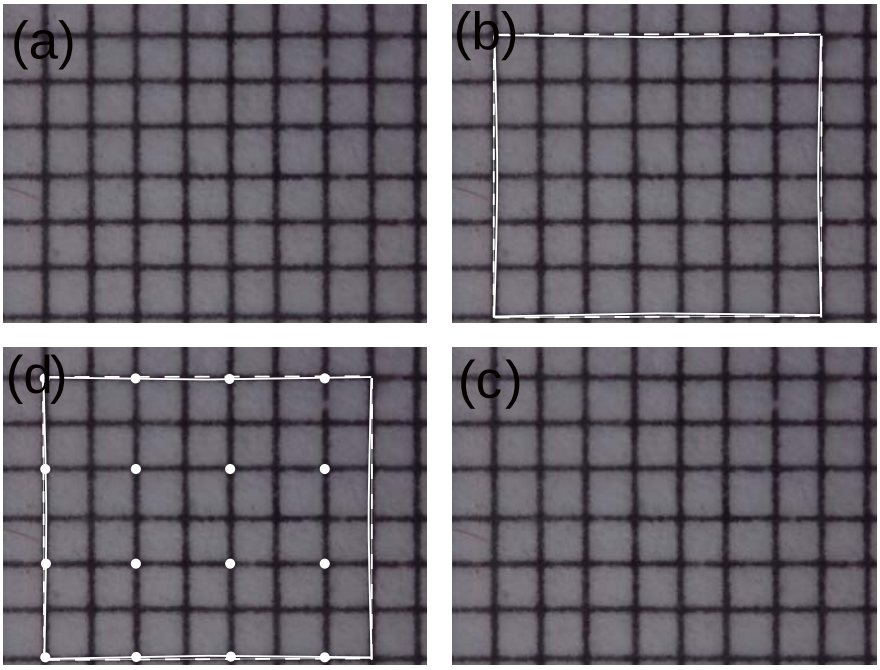

Figure 5.11: Procedure of camera calibration: (a) original image recorded by VCR-800; (b) illustration of distortions; (c) centroids of control points for camera calibration; (d) calibrated image

flexible boundaries provided by the water bladders could effectively avoid the leakage during the seepage tests. The mechanical responses of the eroded soils could be directly measured by the subsequent drained compression tests with strain rate control manner. The camera calibration was also performed on all the recorded images to convert the pixel value to the object value, and to minimize the lens distortion for the image analysis.

Chapter 6

Interpretation on mechanical responses of eroded soils through microscopic observation

6.1 Introduction

Several experiments have been performed in the laboratory by using the developed plane strain erosion apparatus. With controlled test conditions, the influence of internal erosion on soils physical and mechanical behaviors are elaborated in this chapter. The effects of flow rate, the spatial distribution of fines due to internal erosion, the normalized secant stiffness at small strain level and the drained soil strength are discussed in order.

To interpret the mechanical responses of eroded soils, a microscope was employed in this research, and the images recorded by which were analyzed and examined. In Chapter 3, it was reported that the soils prepared with different initial fines content showed different undrained characteristics. Although containing the same initial fines content, the soils with erosion showed different mechanical behaviors from the soils without erosion as well. It was assumed that the distinctions in the mechanical responses might be responsible for the change of soil fabric induced by internal erosion. Corresponding, upward seepage tests with microscopic observation were performed to qualitatively describe the influence of internal erosion on alternation of particles structure. By using the microscopic images taken during the seepage and drained compression stages in the plane strain erosion tests, the effects of internal erosion on mechanical responses are quantitatively evaluated. The detail examinations of the qualitative assessment and the quantitative evaluation are illustrated in this chapter.

Figure 6.1: Microscopic images of silica no. 3 and colored silica no. 8

6.2 Tested materials

6.2.1 Materials description

The tested materials were mixture of silica no. 3 and colored silica no. 8, which is mainly composed of quartz, and categorized as sub-round to sub-angular materials. The microscopic image of the mixtures recorded under the transparent window and transparent membrane is shown in Fig. 6.1. It can be seen that silica no. 3 and colored silica no. 8 showed totally two different dominant size. Silica no. 3 has a larger grain size, which forms the skeleton of the soil specimen, and was regarded as coarse particles. Silica no. 8 was artificially coated with blue pigment, and then stabilized by baking. It was regarded as fines, which could be eroded away by seepage flow. Meanwhile, observation of Fig. 6.1 revealed that both fines and coarse particles could clearly observed by the microscope put in the front of plane strain erosion apparatus.

To compare the morphology of the coarse particles, colored fines and the original fines, the siliceous sands were analyzed by the QICPIC imaging system in Imperial College London. By the QICPIC system, the particles could pass between a specially configured light source and a pair of imaging lenses was installed to minimize focusing problems (Altuhafi et al., 2013). A sequence of binary

images could then be recorded by the camera, and the particle size and morphology could be analyzed.

According to the analysis based on the images recorded by QICPIC system, the maximum Feret diameter and minimum Feret diameter could be calculated. Figure 6.2 shows the sieve size, maximum Feret diameter and minimum Feret diameter distributions of silica no. 3. Regarding to the silica no. 8, the particles were filtered by the 0.1 mm sieve so as to be adopted by the QICPIC system. Therefore, the standard sieve analysis, the maximum Feret diameter and minimum Feret diameter for particle diameters larger than 0.1 mm, together with the full standard sieve analysis for original silica no. 8 and colored silica no. 8 are illustrated in Figs. 6.3 and 6.4, respectively. The data presented in these figures indicated that the minimum Feret diameter is the size measured that most closely corresponded to the data of sieve size (Altuhafi et al., 2013).

The shape in terms of aspect ratio, convexity and sphericity for silica no. 3, original silica no. 8 and colored silica no. 8 were also investigated. The value of the morphology parameters obtained by both microscope and QICPIC for these sands is shown in Table. 6.1. It should be noted that these morphology parameters obtained by the QICPIC system shown in Table. 6.1 were obtained from the value associated with the median particle size. It can be observed that the colored silica no. 8 showed very similar value with the original silica no. 8 for all the measured items. Regarding to the convexity, the silica no. 3 showed a slightly larger value than the silica no. 8, which suggests that the silica no. 3 would be more hardly to be compacted. Silica no. 3 also showed smaller shpericity than the silica no. 8, which indicates the silica no. 3 is more round than silica no. 8. As for the aspect ratio, both silica no. 3 and silica no. 8 showed very similar value.

The comparison between the values obtained from microscope and QICPIC can note that the morphology parameters calculated from the images recorded by microscopeVCR-800 and those from the QICPIC system were comparable. The camera in QICPIC can record the 450 images per seconds, and allows a statistically representative number of particles to be considered in a short period. The combination of vibration, collisions, and use of vacuum could minimize the tendency of preferred alignment of particles so as to attain a relative realistic measure of the true 3D shape of the particles. Although the true 3D shape of particles is difficult to be recorded by the microscope VCR-800, the basic shape of the particles obtained through it was comparable to that obtained from QICPIC. Moreover, unlike the binary image recorded by QICPIC, the microscope VCR-800 permits the record of color image in RGB spaces. It makes the segmentation between particles with different colors possible, which permits the analysis of the interactions among colored particles. The digital microscope is cheaper than QICPIC as well, which allows a possible application to the practical engineering.

Table 6.1: Shape of siliceous sands by Microscope and QICPIC

	Approach	Aspect ratio [-]	Convexity [-]	Sphericity [-]
Silica no. 3	QICPIC	0.73	0.95	0.83
Original silica no. 8	QICPIC	0.72	0.91	0.88
Colored silica no. 8	QICPIC	0.71	0.91	0.86
Original silica no. 8	Microscope	0.71	0.92	0.84
Colored silica no. 8	Microscope	0.70	0.88	0.88

6.2.2 Specimen preparation

The tested specimens were 70 mm wide, 70 mm deep and 100 mm high. All the specimens in this research were prepared with 25% initial fines content. The properties of the tested materials are presented in Table 6.2.

The nonlinear undercompation theory was utilized, and the moist tamping method was applied in preparing the specimens. The targeting relative density for preparing the specimens was 42%. It was larger than that in the triaxial erosion tests. The hydraulic structures, such as dams and embankments, are assumed to be under plane strain condition, and might be suffered internal erosion. The fill materials in these hydraulic structures were probably compacted at relatively large relative density. Therefore, a relatively larger targeting relative density was chosen in the plane strain erosion tests than that in triaxial erosion tests. The undercompaction value of each layer against that of the first layer is plotted with the layer number, as shown in Fig. 6.5. In this research, the 100 mm high specimen was prepared targeting relative density of 42%, therefore, the recommended undercompaction of the first layer was chosen as 30%. The undercompaction value of each layer and the height of each layer after initial tamping are demonstrated in Fig. 6.6.

6.3 Experimental procedure

The experimental procedure in the plane strain erosion test includes the saturation, consolidation, seepage test, compression tests and post analysis. One of the objectives of this study is to investigate the characteristic of internal erosion under plane strain conditions, therefore, the seepage tests and subsequent drained compression tests were performed. The other objective is to explain the

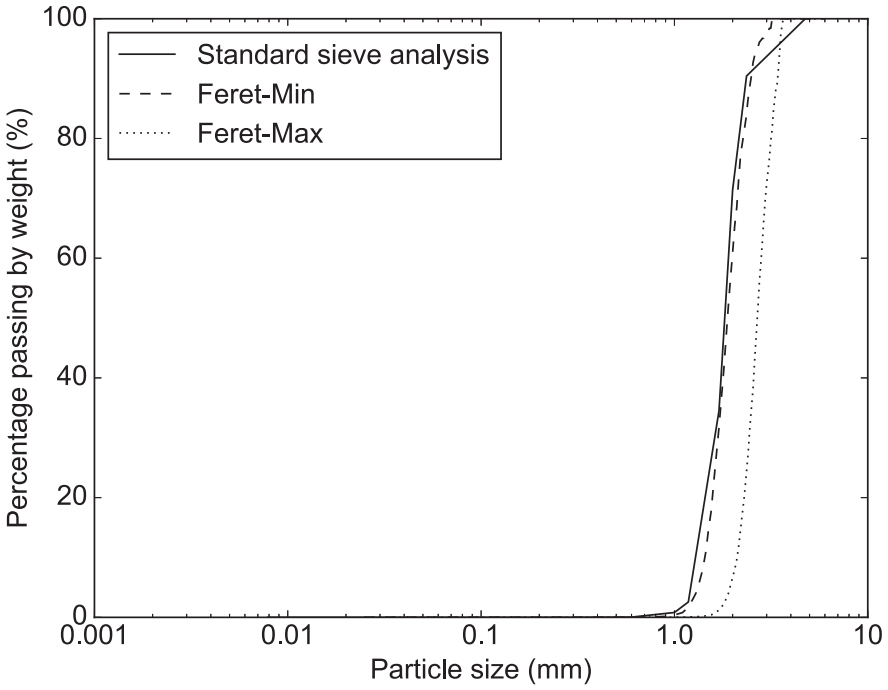

Figure 6.2: Comparison of size distribution data for silica no. 3

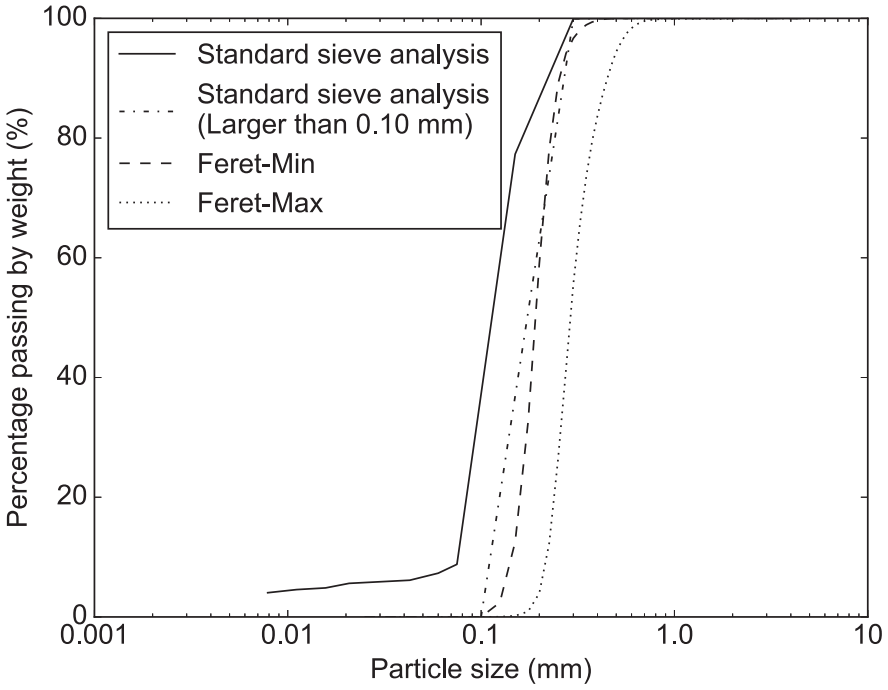

Figure 6.3: Comparison of size distribution data for original silica no. 8

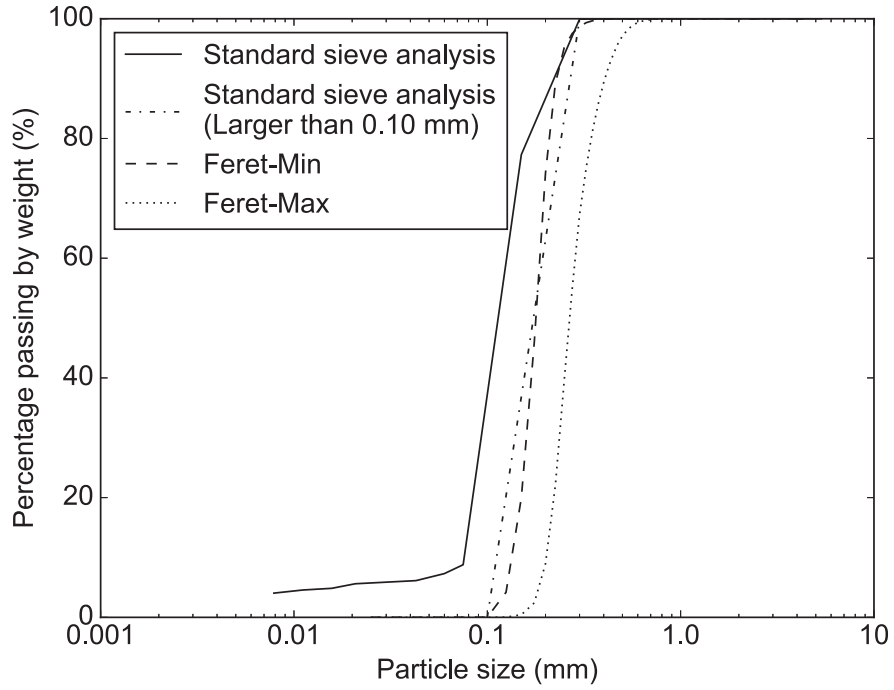

Figure 6.4: Comparison of size distribution data for colored silica no. 8

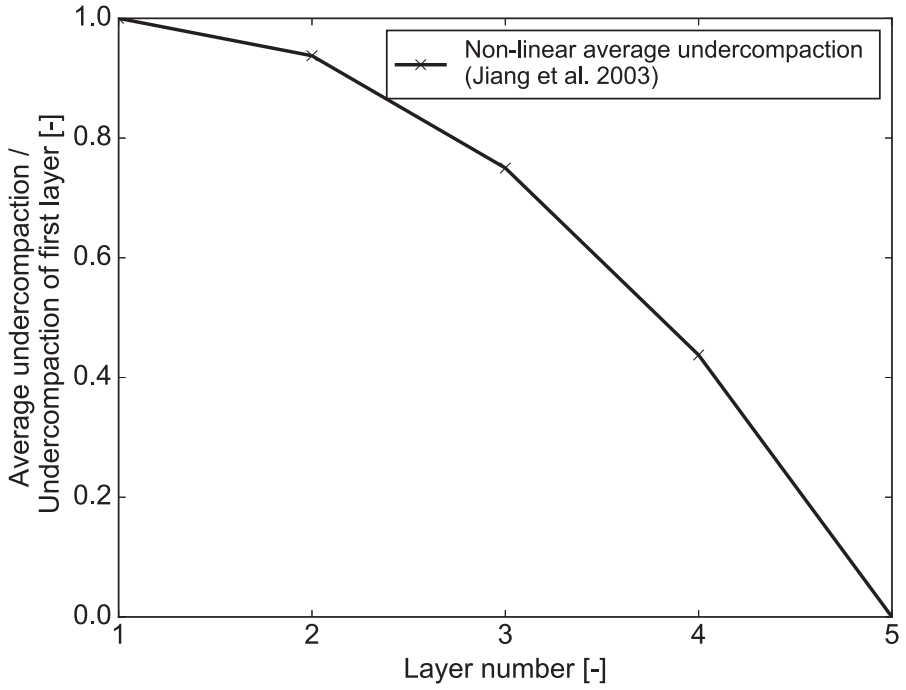

Figure 6.5: Undercompaction criterion

Table 6.2: Properties of tested materials

	Silica no. 3	25% mixtures	Colored silica no. 8
Fines content (%)	0	25.0	100
Maximum void ratio	0.94	0.77	1.33
Minimum void ratio	0.65	0.37	0.70
Median particle size (mm)	1.76	1.69	0.16
Curvature coefficient	0.96	8.54	0.99
Uniformity coefficient	1.31	16.4	1.05

mechanism of different mechanical behaviors of soils with and without erosion from the particulate level, thus the microscopic images during the whole testing were recorded my a digital microscope VCR-800. The post analysis, consisting the standard sieve analysis and the digital image analysis, were conducted to interpret the mechanism of internal erosion. The detailed description of each procedure is presented as following:

6.3.1 Saturation

Before the test, the deaired water was prepared by filling the reservoirs with tap water and constantly applying the possible maximum vacuum for at least 24 hours. The E/P transducers, earth pressure transducers and load cells were examined to adjust the zero point and span range. To guarantee that the specimen could achieve possible maximum saturate degree, all pipes were filled with deaired water, visual observation that no bubbles exist in the pipe lines was conducted.

The tested specimen was prepared according to the non-linear undercompaction theory as presented in Fig. 6.6. Firstly, the oven-dried weights of silica no. 3 and colored silica no. 8 were determined from the fines content and relative density. The initial water content was determined as around 5% according to the previous research (Ke and Takahashi, 2014b; Wanatowski and Chu, 2006). Then the wet soils were thoroughly mixed to ensure than the specimen could be uniform. Equally separated the specimen into 5 pieces, and kept them in a zipped bag to stabilize the moisture at least 16 hours before the tests. The scheme of moist tamping was then employed, and the specimen was prepared layer by layer with a scoop into the mold to a required height.

The vacuum saturate procedure was employed in this study. Two separated reservoirs were connected to the top and bottom of the specimens. After the preparation of specimen, vacuum was applied into the specimen through both water reservoirs gradually until it reached -20 kPa. Deaired

water was then allowed to be slowly injected into the specimen from the bottom to the top. The water flow was sufficiently slow enough to avoid the segregation of fines from the coarse particles. After a total volume of around 10 times of the void in the specimen was flowed through the soil, the saturate process was assumed to be finished.

6.3.2 Consolidation

After the saturation, close the vacuum, which means return the pressure of specimen to 0 kPa and increase the normal strain perpendicular to plane strain to 20 kPa. Simultaneously, the vertical stress was programmed to applied the vertical stress of 20 kPa to the soil. The saturation was then performed with a feedback control system. The normal stress was gradually increased up to the target value (50 kPa in this study) at a fairly low increment to avoid the particles migration. The vertical stress, controlled by a motor, increased to the determined stress ratio (vertical stress / normal stress perpendicular to plane strain) and kept this constant. In this research, the vertical stress was designed to be kept constant with the normal stress perpendicular to plane strain.

6.3.3 Seepage tests

After the consolidation, the specimens were ready for performing the seepage tests. The seepage tests in this study was controlled by flow rate based on its advantage of providing continuous flow within a relatively long period (Ke and Takahashi, 2014b). To investigate the influence of flow rate on the behaviors of cohesionless soils subjected to internal erosion, the inlet flow was applied by multi-stage approach. The flow rate for the seepage tests in shown in Fig. 6.7. Each stage lasted from around 5400 s, which was long enough to end the seepage test in one stage according to Ke and Takahashi (2014b). The maximum flow rate applied was $6.5 \times 10^{-6} m^3/s$, which was considered to be large enough to dislodge a amount of fines during the seepage tests. The seepage test was going to be ended until (1) there are no further eroded fines loss (i.e., $<$0.2 g per 600 s); (2) the effluent become clear and clean through visual observation; (3) on particles movement could be observed through the digital microscope; (4) there are no further increases in the vertical strain and horizontal strain of the tested specimen. Usually, the seepage tests lasted for around 5 hours by this apparatus. The seepage test was terminated by gradually decreasing the flow rate by the flow pump until it became 0.

During the seepage test, the vertical stress and the normal stress perpendicular to plane strain were kept constant. The cumulative eroded soil mass was recorded by the miniature load cell installed in the sedimentation tank. The microscopic images were recorded during each stage of the seepage

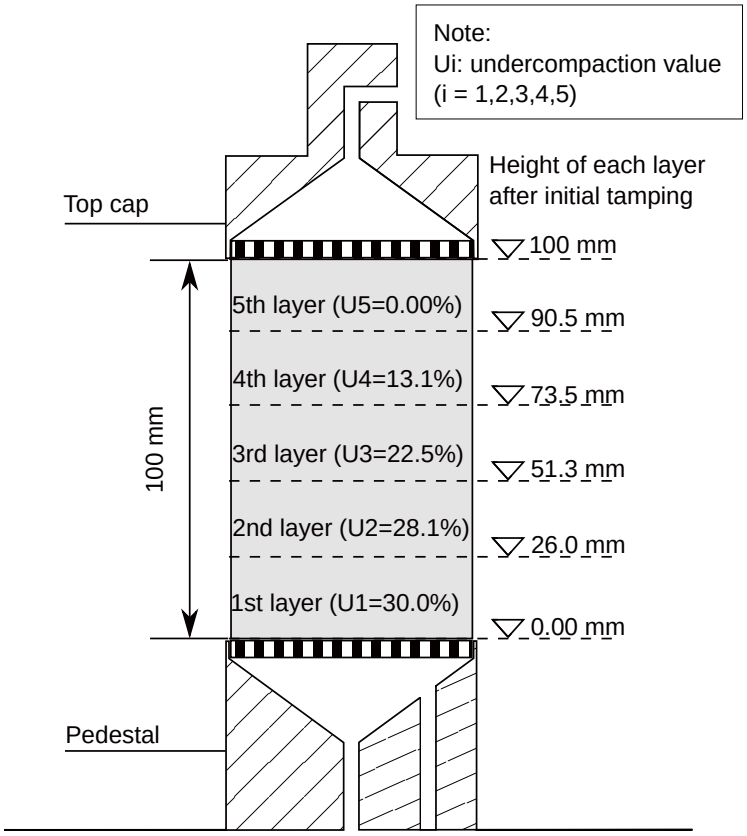

Figure 6.6: Specimen preparation by non-linear undercompaction criterion

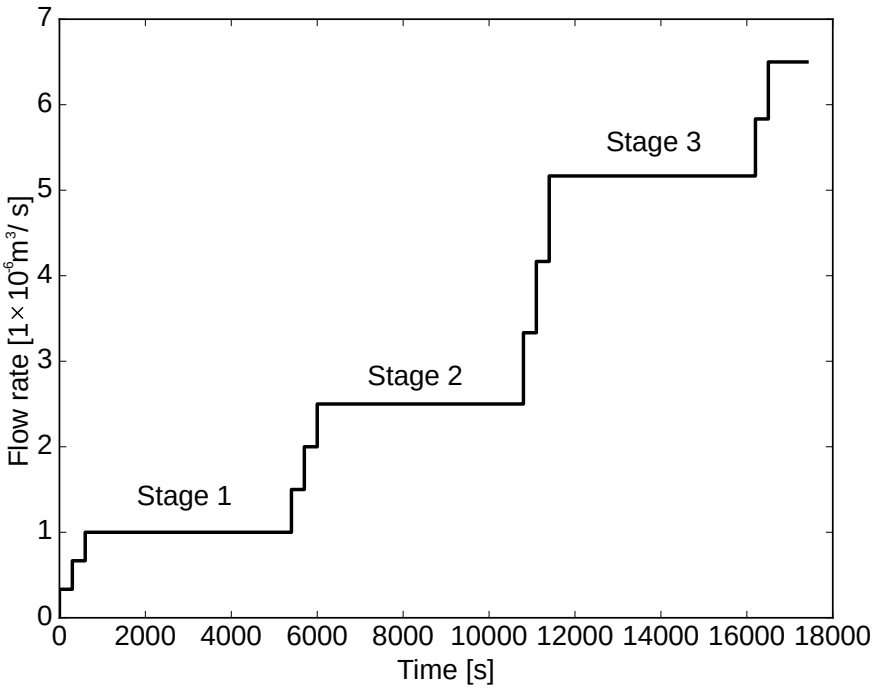

Figure 6.7: Flow rate in seepage test

tests at various designed height. The normal stress in direction of plane strain was measured to examine the change of stress within the specimen.

6.3.4 Drained compression test

Upon the completion of seepage tests, the drained compression test was performed. It is known that the embankments, dams, and levees, are usually assumed to be subjected to the plane strain conditions. The failure of these hydraulic structures maybe mainly because that the internal erosion occurred due to seepage flow for a relatively long period. Within this long period, the pore water pressure could be dissipated. It corresponds to the stress path under drained condition in geotechnical engineering. Thus, the drained compression tests were conducted on cohesionless soils under plane strain conditions by this developed apparatus. The drained compression test was displacement controlled with the axial strain rate of 0.1%/min, according to the standard criteria of triaxial compression tests. The normal stress perpendicular to the plane strain was kept constant, while vertical displacement increased at the designated strain rate. The stress strain relationship and the axial strain against deviator stress could be obtained through the drained compression tests.

6.3.5 Post analysis

After the drained compression test, the particle size distributions in different layers of the specimen were measured to identify the influence of internal erosion on spatial fines distribution. The specimen was manually divided into three or five layers. The soil in each layer was oven-dried to 110°C for 24 hours and the standard sieve analysis was performed to obtain the particle size distributions.

6.3.6 Test conditions

Table 6.3 shows the conducted tests and the controlled conditions. To examine the effectiveness of the preparation method, PS_CON (where the first entry means the plane strain erosion test and the second represents the consolidation) was ended after the consolidation. Seepage test and subsequent drained compression test were performed twice to show the repeatability, corresponding to the cases PS_WE_N1 and PS_WE_N2 (where the first entry means the plane strain erosion test, the second represents with or without erosion, and the third is test number). To compare the physical and mechanical responses of soils with erosion to that of soils without erosion, PS_WOE was performed with drained compression test just after the completion of consolidation.

Table 6.3: Test conditions

Case	Initial fines content	Consolidation	Seepage test	Compression test
PS_CON	25%	√	–	–
PS_WOE	25%	√	–	√
PS_WE_N1	25%	√	√	√
PS_WE_N2	25%	√	√	√

6.4 Test results

Through the experiments conducted by plane strain erosion apparatus, the test results are presented in this section. It mainly includes the verification of the preparation method in terms of the planar distribution of void ratio; and the summary of seepage test results and drained compression test results.

6.4.1 Verification of the preparation method

To verify the effectiveness of preparation in producing the soil specimen with reasonable uniformity, PS_CON was conducted. After the consolidation, the soil specimen was uniformly divided into five layers, and each layer was oven-dried at 110°C for 24 hours. The height of each layer is shown in Fig. 6.8. The void ratio in each layer was then measured, together with the target void ratio, is shown in Fig. 6.9.

To quantitative assessment of the homogeneity of the specimen, two indexes were employed in this study. The first one was the sample variance S, which is defined as

$$S^2 = \frac{1}{m-1}\sum_{i=1}^{m}(\overline{e}_i - \overline{e})^2 \tag{6.1}$$

where, $\overline{e}$ is the target void ratio, $\overline{e}_i$ is the mean void ratio in layer i, and m is the numbe of total divided layers.

The other one is the linear coefficient b, which is expressed as

$$b = \frac{m\sum y_i \times \overline{e}_i - (\sum y_i)(\sum \overline{e}_i)}{m\sum y_i^2 - (\sum y_i)^2} \tag{6.2}$$

where y_i is the coordinate in the vertical direction at the center of each layer i. The inclination of the regression line can be evaluated by the b value (Jiang et al., 2003). The greater is the b value is,

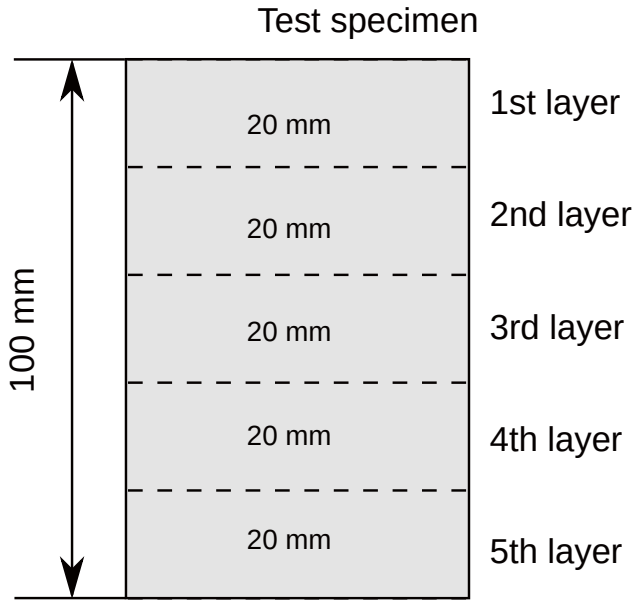

Figure 6.8: Height of each layer in verification of the preparation method

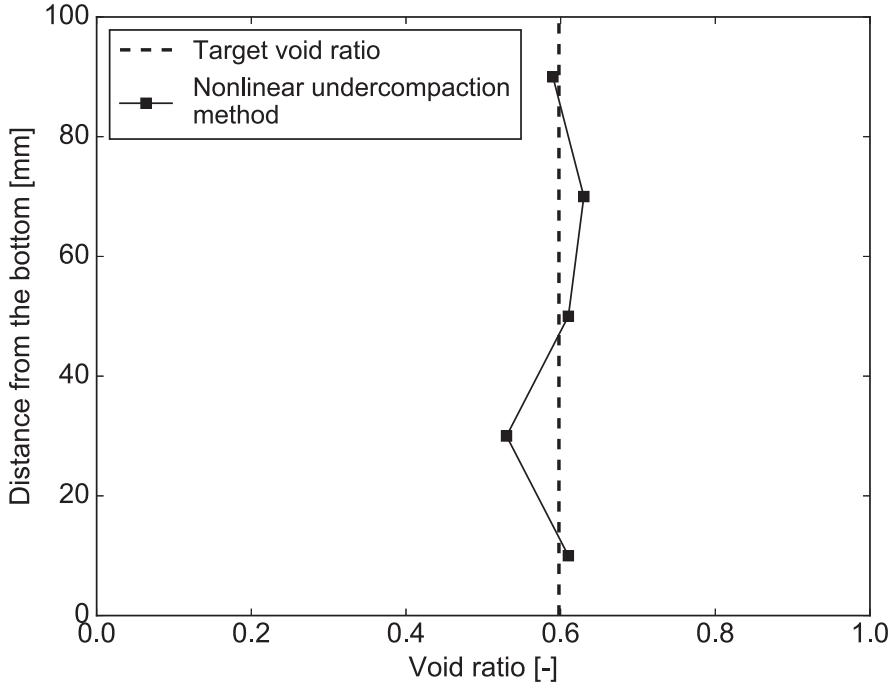

Figure 6.9: Distribution of planar void ratio along the length of the specimen

Table 6.4: Quantitative assessment of the specimen homogeneity

Case	Target void ratio	Sample variance, S	Linear coefficient, b [1/cm]
PS_CON	0.60	0.0371	0.0021

the greater is the difference between the planar void ratios at the top and bottom of the specimen. When the void ratios of each layer are the same, the regression line for the distribution of the planar void ratio would be a vertical line, and correspondingly b equals 0.

Table 6.4 presents the values of these two indexes for the specimens prepared in this study. It can be found that both the sample variance S and the linear coefficient b were close to 0, which means the void ratio in each layer was close to the target void ratio with little variance. Therefore, it could be said that the specimen prepared by moist tamping method with non-linear undercompaction theory could achieve reasonable homogeneity.

6.4.2 Seepage test results

A summary of the seepage test results is shown in Table 6.5. Observation of the table showed that the fines content after seepage test was smaller than that before seepage tests, which suggested that a certain amount of fines was dislodged by the seepage flow. The void ratios increased, corresponding to a decrease of relative density, due to internal erosion, which indicated the specimen became looser after seepage test. Moreover, there was a contractive volume deformation during the seepage test in this study.

The evolutions of the cumulative eroded soil mass are shown in Fig. 6.10. It was noted that the fines were eroded away by the applied seepage flow. The two cases PS_WE_N1 and PS_WE_N2 showed similar cumulative eroded soil mass at the end of the seepage tests. It suggested that the seepage tests performed by the developed plane strain erosion apparatus could yield consistent results.

Figure 6.11 demonstrates the evolution of normal stress in direction of plane strain during seepage tests. With the dislodgement of fines, it was found that the normal stress in direction of plane strain decreased correspondingly within this research scope. Observation of Fig. 6.11 also revealed that the two repeated casts showed similar tendency for the decrease of normal stress in direction of plane strain. It further indicated that the apparatus could be applied to get reliable results.

Table 6.5: Seepage test results

Case	Fc [%][1]	e_0[2]	Rd_0 [%][3]	e_c[4]	Fc_e [%][5]	e_e[6]	Rd_e [%][7]	ε_v [%][8]
PS_WE_N1	25	0.6013	42.18	0.5992	21.25	0.6477	30.57	1.92
PS_WE_N2	25	0.6008	42.30	0.5978	21.28	0.6472	30.70	1.91

[1] Initial fines content;
[2] Initial void ratio;
[3] Initial relative density;
[4] Void ratio after consolidation;
[5] Fines content after seepage test;
[6] Void ratio after seepage test;
[7] Relative density after seepage test;
[8] Volumetric strain.

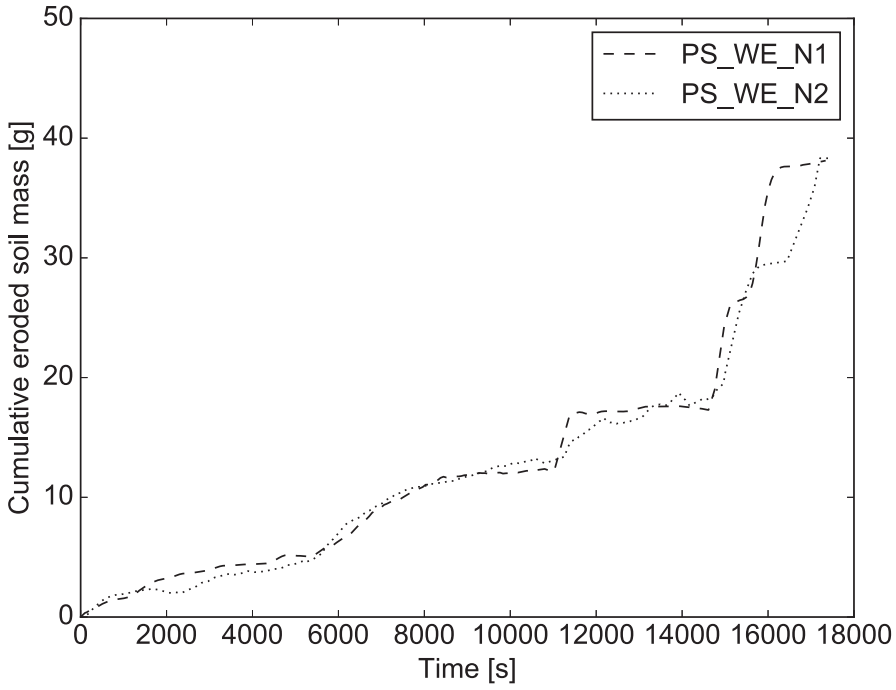

Figure 6.10: Evolution of cumulative eroded soil mass during seepage test

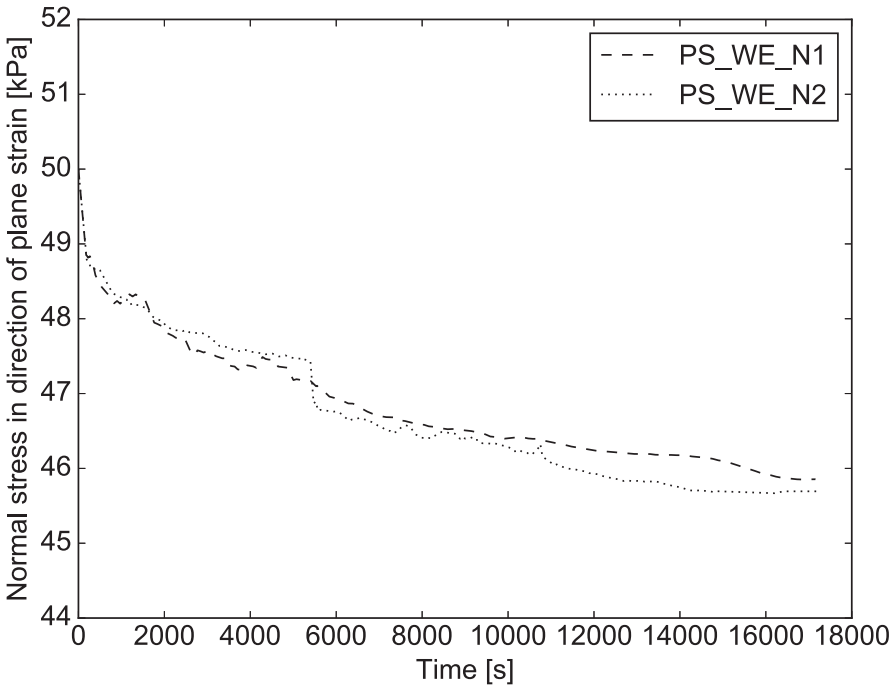

Figure 6.11: Evolution of normal stress in direction of plane strain during seepage test

6.4.3 Drained compression test results

Table 6.6 shows the drained compression test results of soils with and without erosion. The fines contents and void ratios before drained compression, together with the deviator stress at 15% axial strain, are presented in the table. It can be seen that the deviator stress at medium strain level (15% axial strain) for soil with erosion was different from that for soil without erosion.

The relation of axial strain and the volumetric strain is shown in Fig. 6.12. Figure 6.13 shows the corresponding relation between axial strain and deviator stress. It was noted that both soils with and

Table 6.6: Drained compression test results

Case	Fc_d [%][1]	e_d[2]	Deviator stress at ∼15% axial strain [kPa]
PS_WOE	25.0	0.59	265.9
PS_WE_N1	21.3	0.65	202.8
PS_WE_N2	21.3	0.65	204.9

[1] Fines content before drained compression test;

[2] Void ratio before drained compression test.

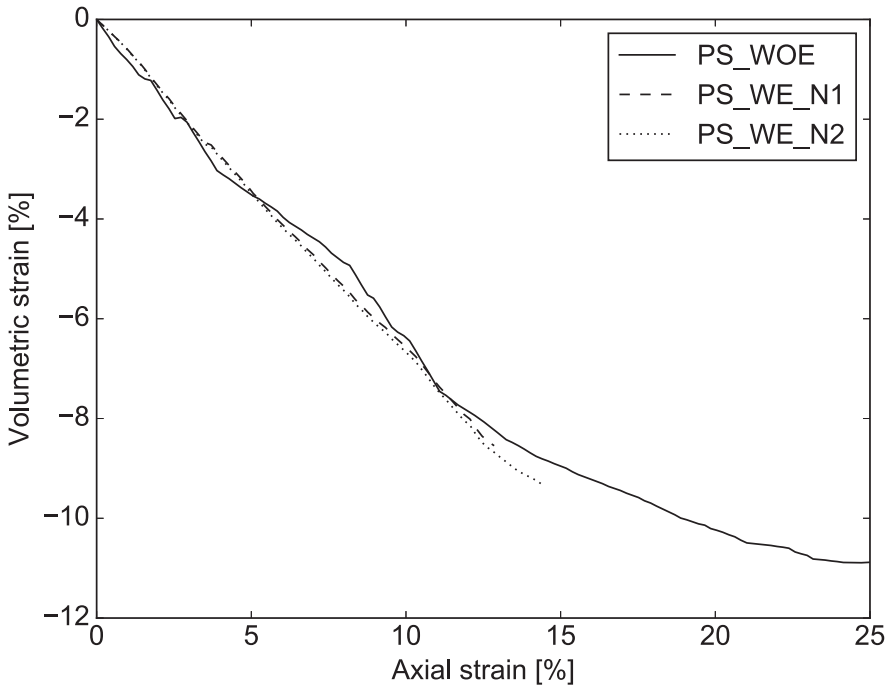

Figure 6.12: Relation of axial strain and volumetric strain

without erosion showed contractive volumetric deformation. At small strain level (axial strain $<$ 1%), the deviator stress of the soil with erosion was larger compared to that of soil without erosion at the same axial strain. Whereas, at medium strain level (1% $<$ axial strain $<$ 15%), the soil with erosion showed smaller deviator stress than the soil without erosion at the same axial strain. The interesting phenomena will be discussed in the next section.

6.5 Discussions

After getting the general impression on the results of seepage test and drained compression test, the detailed examination could help to throughly understanding the effects of internal erosion on soil behaviors. Specifically, the influence of flow rate on the cumulative eroded soil mass and the normal stress in direction of plane strain, and the spatial distribution of fines in the eroded specimens are discussed. Subsequently, the normalized secant stiffness and drained soil strength of soils with and without erosion are compared in this section.

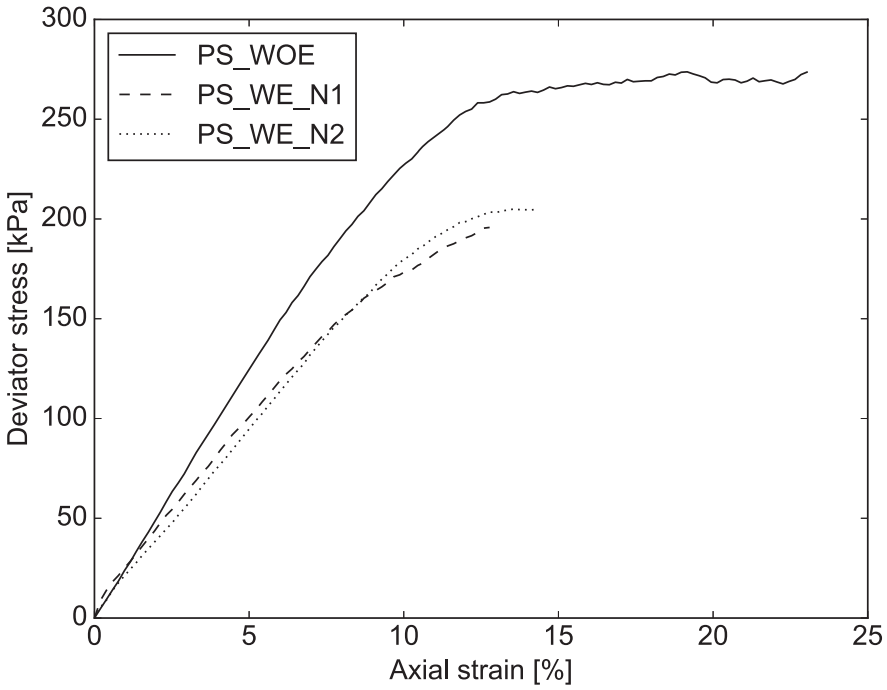

Figure 6.13: Relation of axial strain and deviator stress

6.5.1 Effects of flow rate

It was reported that the internal erosion could be affected by the hydraulic conditions, which is controlled by applied flow rate in this study (Tomlinson and Vaid, 2000; Richards and Reddy, 2010; Horikoshi and Takahashi, 2015b). The relationship between the flow rate and the normalized cumulative eroded soil mass is shown in Fig. 6.14. The normalized cumulative eroded soil mass is the cumulative eroded soil mass normalized by the total eroded soil mass. In Fig. 6.14, the flow rate of 1.0, 2.5 and 6.5 $\times 10^{-6} m/s^2$ represents the stage 1, 2 and 3 in seepage tests (Fig. 6.7), respectively. It can be observed that the cumulative eroded soil mass showed a larger value at a higher flow rate. For example, the normalized cumulative eroded soil mass of stage 2 was larger than that of stage 1. This maybe because that the hydraulic gradient would become large when the applied flow rate is large, with the assumption that the hydraulic conductivity does not change much, according to Darcy's law. Consequently, the hydraulic force acting on the fines become large, and more fines could be detached from the coarse particles and be eroded away from the specimen.

Figure 6.15 shows the relationship between the flow rate and normalized normal stress in direction of plane strain. The normalized normal stress in direction of plane strain is the normal stress in each stage normalized by the initial normal stress in direction of plane strain. It can be seen that the

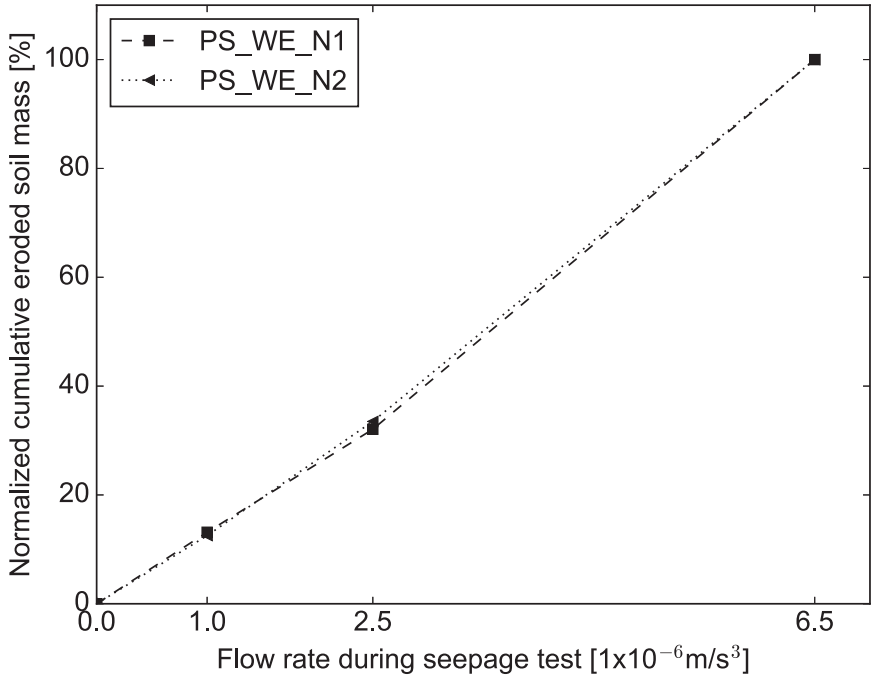

Figure 6.14: Relationship between flow rate and normalized cumulative eroded soil mass

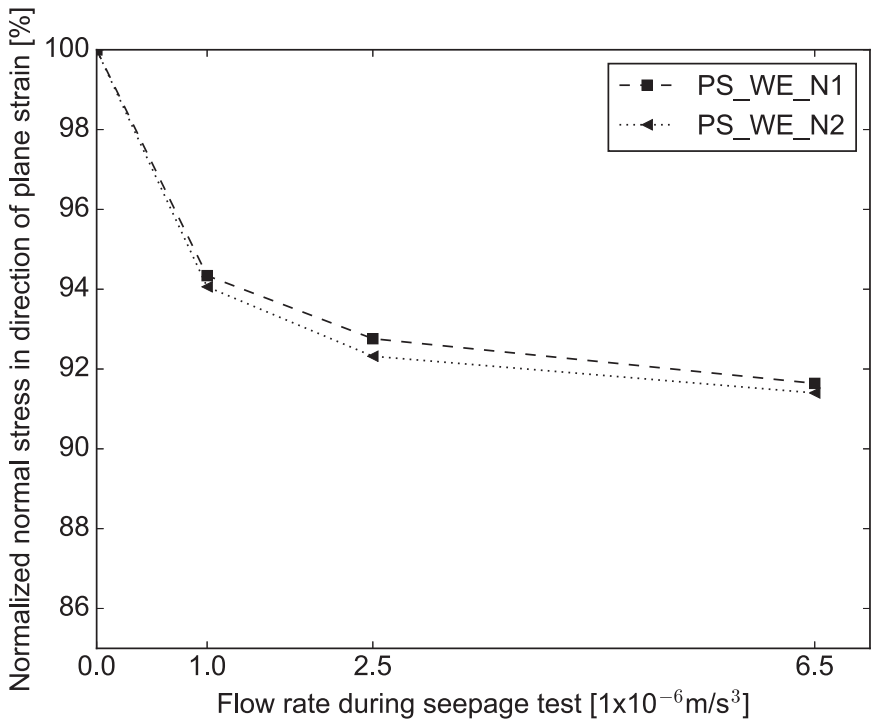

Figure 6.15: Relationship between flow rate and normalized normal stress in direction of plane strain

normal stress in direction of plane strain decreased with the increase of flow rate. The dislodgement of fines from the specimen, would make the specimen become lose. With the constant vertical stress and normal stress perpendicular to plane strain, the normal stress in direction of plane strain decreased consequently. It also can be found that the decrement of the normal stress in direction of plane strain in stage 1 was larger than that in stage 2 or in stage 3. This might be responsible for the metastable specimens prepared by moist tamping method. According to Takahashi (2016), some fines were stayed in contact with coarse particles when prepared by moist tamping method, which were assumed to be transferred the load under the plane strain conditions. As soon as the flow rate applied to the specimen, the fines that function as load transformation might be transported by the seepage flow (Horikoshi and Takahashi, 2015b; Tomlinson and Vaid, 2000), which resulted in a large decrease in the normal stress in direction of plane strain. On the other hand, after the seepage stage 1, the soil microstructure stabilized and fines were transported to the voids and would transfer less load under the stress states during seepage tests. Therefore, although the normalized cumulative eroded soil mass in stages 2 and 3 were larger than stage 1 (Fig. 6.14), the decreases of normalized normal stress in direction of plane strain were smaller than that in stage 1.

6.5.2 Spatial distribution of fines

For the cases conducted with seepage tests (PS_WE_N1 and PS_WE_N2), the soils were collected after the tests, and oven-dried at 100°C for 20 hours. Then the sieve analysis was performed. The particle size distribution curves of the eroded soils together with the initial size distribution are shown in Fig. 6.16. It can be observed that the particle size distributions curves for soils with erosion moved downward from the initial size distribution, which suggested that the fines were transported away from the specimen. The extend of shift down in the particle size distribution curves corresponded to the amount of eroded fines (Kenney and Lau, 1985). Figure 6.16 noted that around 4.8% of fines were eroded away, corresponding to cumulative eroded soil mass of around 38 g.

To examine the spatial distribution of fines induced by internal erosion, the specimen was divided by several parts. The illustration of the divided parts in the case PS_WE_N2 is shown in Fig. 6.17. The top, middle and bottom layers were divided equally to investigate the fines distribution along the length of the specimen. In each layer, two parts were divided, named as T1, T2 in top layer, M1, M2 in middle layer and B1, B2 in bottom layer, in order to examine the influence of the boundary conditions. T2, M2 and B2 were the portions near the water bladders, which means they were subjected to a flexible boundary conditions, however, T1, M1 and M1 were not subjected to flexible boundary conditions.

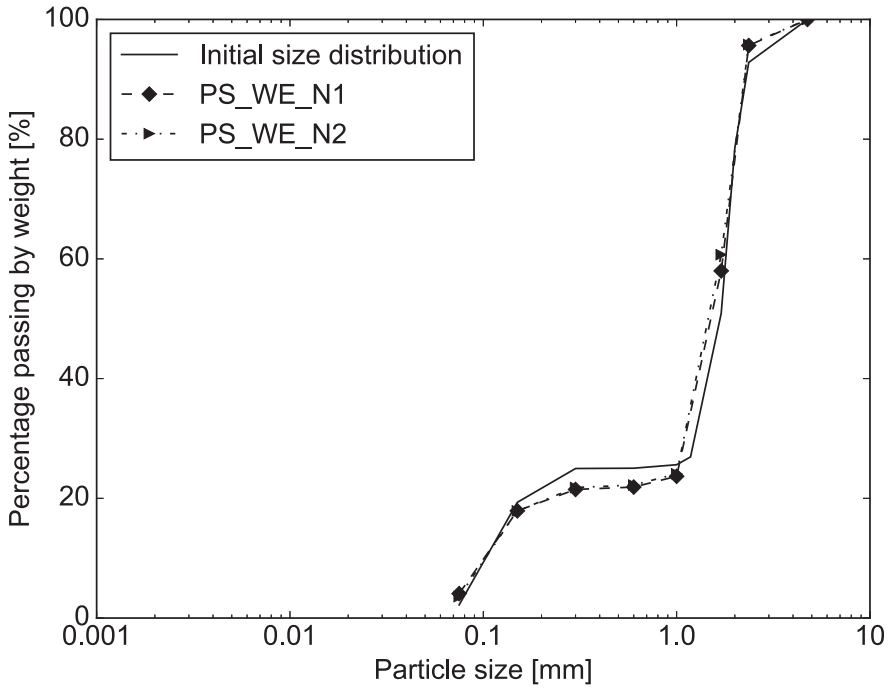

Figure 6.16: Particles sizes distribution curves of eroded soils

Figure 6.18 shows the particle size distribution curves in top, middle and bottom layers. It can be observed that the fines distributions in these three layers were not the same, which suggested that the internal erosion would cause an inhomogeneous specimens under the plane strain conditions. Similarly, such non-homogeneous of eroded specimen was also reported by Moffat et al. (2011); Rosenbrand and Dijkstra (2012); Horikoshi and Takahashi (2015b) under plane strain conditions, and Chang and Zhang (2011); Ke and Takahashi (2014b) under axisymmetric stress states.

For the bottom layer, the particle size distribution curves of B1 and B2 parts are plotted in Fig. 6.19. It was noted that although in the same layer, the fines spatial distributions were largely affected by the boundary conditions. Figure 6.19 noted that the B2 part showed larger fines loss than B1 part, which means that the part near the flexible boundary indicates larger fines loss than the other part. This might be one of the possible reasons that the total eroded soil mass under plane strain conditions was less than that under axisymmetric conditions, as presented in Chapter 3. Due to the larger flexible boundary in the triaxial erosion apparatus, more fines could be eroded away than the tests conducted by plane strain erosion apparatus.

The other two possible reasons that contribute to the different seepage tests results might be the low

saturation degree and denser state of the specimens in the plane strain erosion tests comparing to that in the triaxial erosion tests. Due to the difficulty in firmly sealing the membrane with the top cap and pedestal in the plane strain erosion apparatus, the back pressure was hardly to be applied to the specimen in the plane strain cell. It might lead to a relative low degree of saturation for the specimens performing the seepage tests. The low saturation degree could probably result in a low erodibility, which allowed less fines be eroded away from the specimen. Meanwhile, the specimens in plane strain erosion tests were prepared targeting around 42% relative density, which was larger than that in triaxial erosion tests (30% relative density). This means that the soils in plane strain erosion tests were denser than those in triaxial erosion tests, which might be also one of the reasons for the different total eroded soil mass between these two experiments.

6.5.3 Normalized secant stiffness

It is known that the secant stiffness at the small strain level could be very helpful in understanding the whole mechanical response. Figure 6.20 shows the deviator stress at the axial strain between 0 to 2% of soils with and without erosion. It can be observed that at axial strain less than 0.1%, the deviator stress for the soil with erosion was larger than that for the soil without erosion at the same strain.

To interpret the mechanical behavior with respect to secant stiffness, Fig. 6.21 demonstrates the definition of secant stiffness. Secant stiffness is the gradient of the stress strain curves, which reflects the relationship between changes of deviator stress with the changes of axial strain. Figure 6.22 shows the normalized secant stiffness against axial strain of soils with and without erosion. The normalized secant stiffness is the secant stiffness normalized by the normal stress perpendicular to plane strain (50kPa in this study). It can be noted that at small strain level (axial strain within 1%), the soil with erosion showed larger normalized secant stiffness than the soil without erosion. Taken the 0.1% axial strain for instance, the uneroded specimen showed normalized secant stiffness of 50, whereas the eroded soils showed normalized secant stiffness of 90 (PS_WE_N2) and 150 (PS_WE_N1).

6.5.4 Drained soil strength

According to ASTM (2012a), the drained soil strength can be defined according to the deviator stress at 15% axial strain. Therefore, the drained soil strength was defined as:

$$s_d = \frac{q_{15}}{2} \tag{6.3}$$

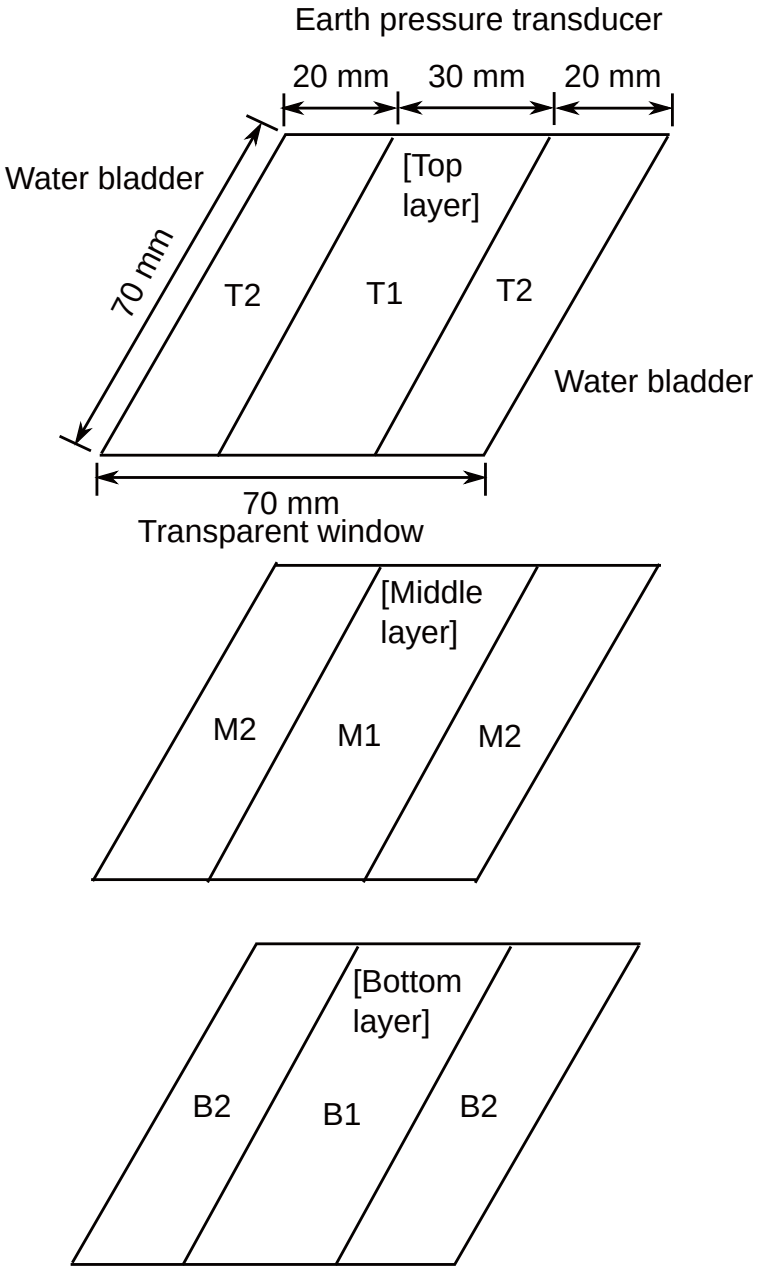

Figure 6.17: Illustration of the divided parts in the specimen

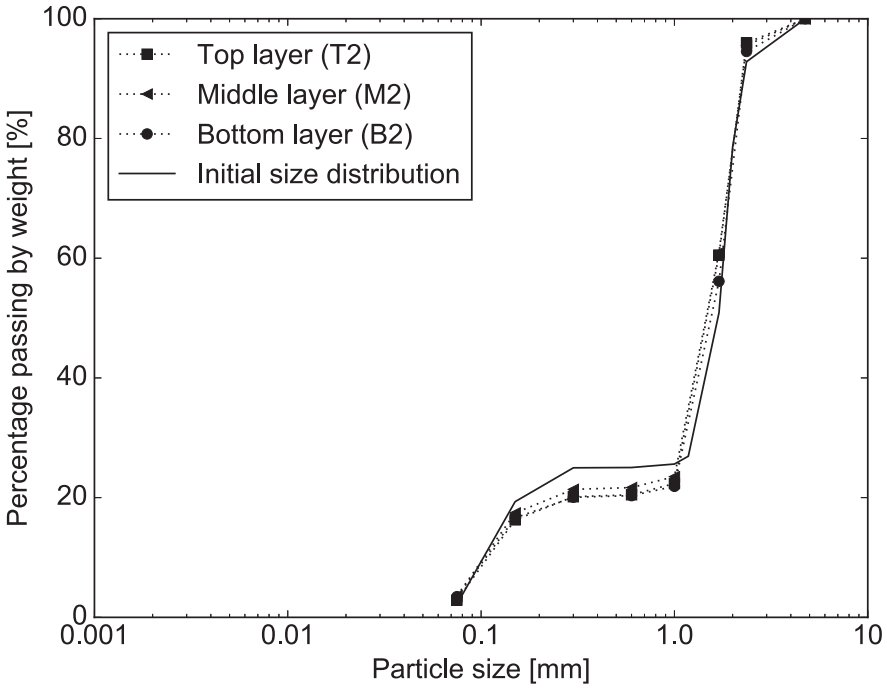

Figure 6.18: Fines distributions in the top, middle and bottom layers

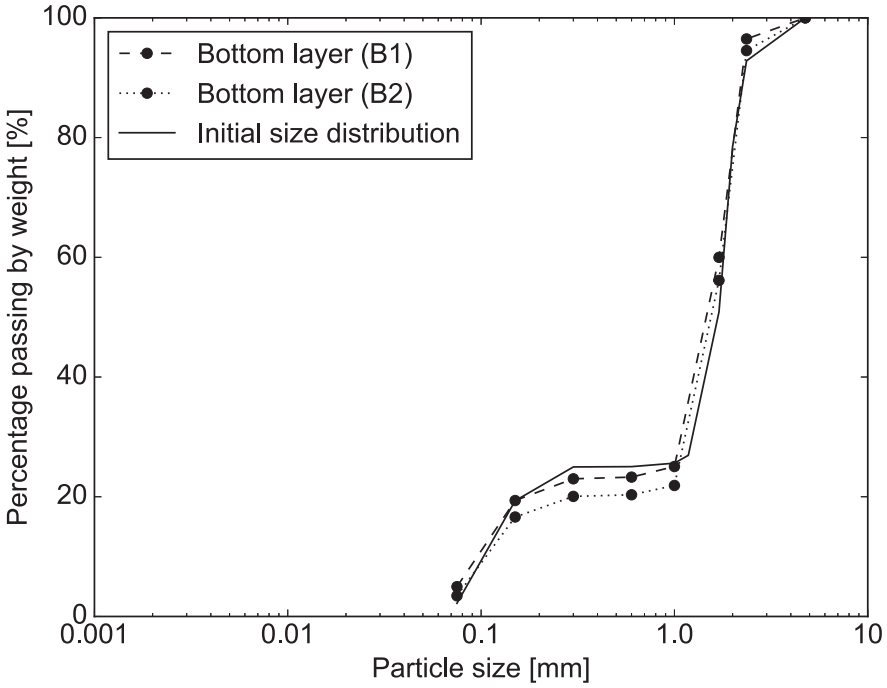

Figure 6.19: Fins distribution in the divided parts with different boundary conditions

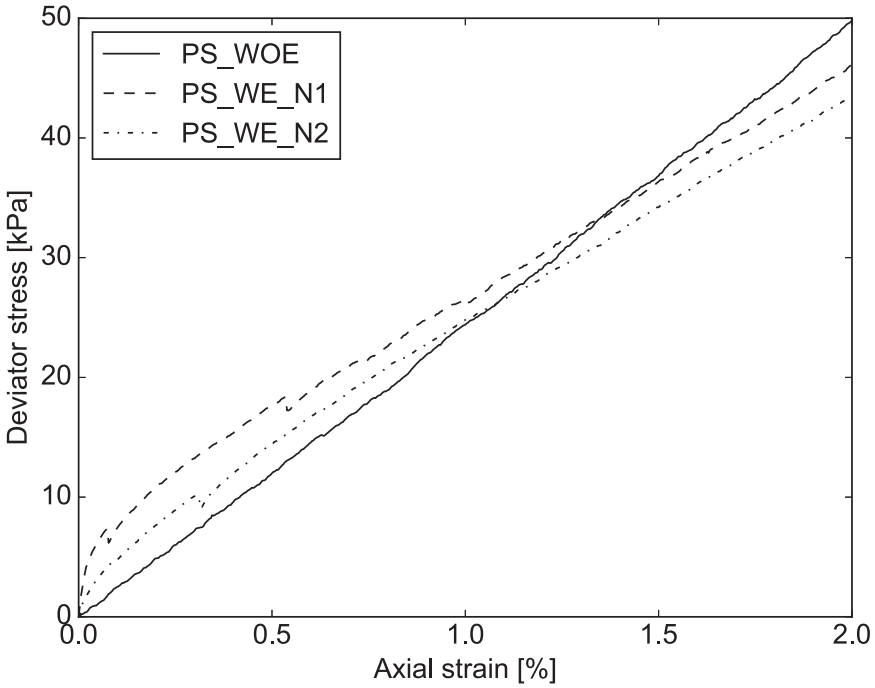

Figure 6.20: Deviator stress at small strain level

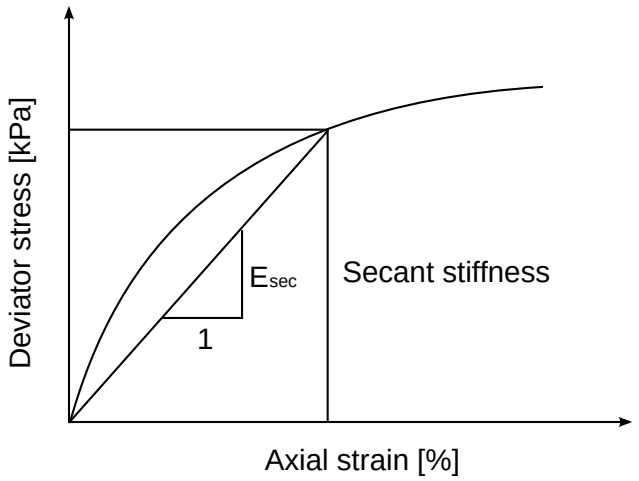

Figure 6.21: Demonstration of the derivation of secant stiffness

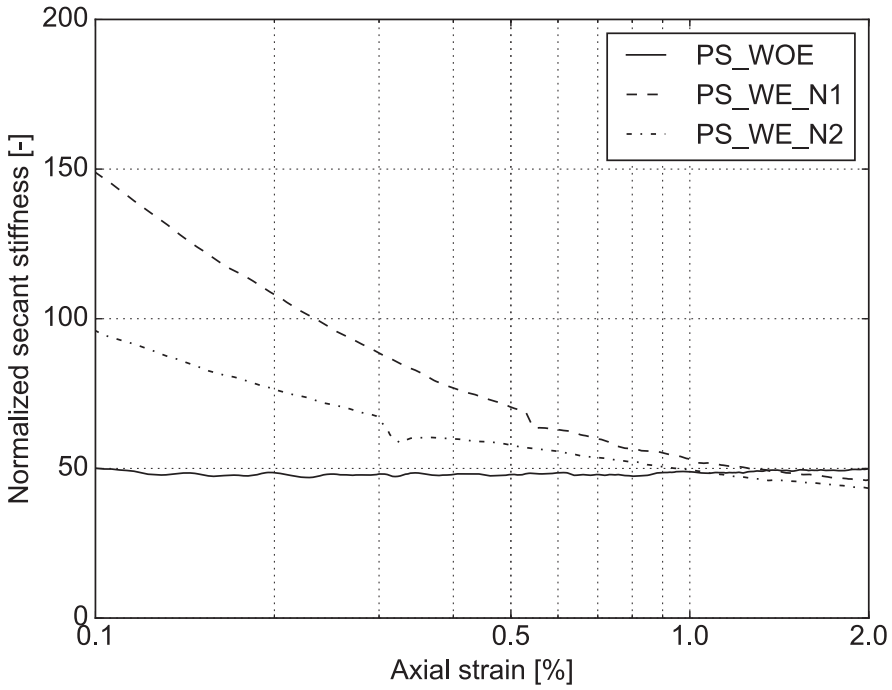

Figure 6.22: Normalized secant stiffness at small strain level

where s_d is the drained soil strength, and q_{15} is the deviator stress at 15% axial strain. Figure 6.23 shows the normalized soil drained strength against fines content before compression. The normalized soil drained strength was the drained soil strength normalized by the drained soil strength of soil prepared with the same fines content but without erosion (PS_WOE). It can be observed from the figure, that the drained soil strength decreased after internal erosion in this study. Moreover, comparing the strength of soils in plane strain erosion tests with the strength of soils in triaxial erosion tests for specimens containing 25% initial fines content, it was found that the strength for soils in plane strain erosion tests was larger than that in triaxial erosion tests. One of the reasons responsible for this might be that the specimens in plane strain erosion tests were prepared with larger relative density and smaller void ratio, which led to larger strength comparing to specimens in triaxial erosion tests.

6.6 Qualitative assessment of internal erosion

To qualitatively assess the influence of internal erosion on the soils mechanical behaviors presented in Chapter 3, upward seepage tests were performed to describe the changes of particles structure induced by internal erosion. The mixtures with 15%, 25%, and 35% initial fines content were

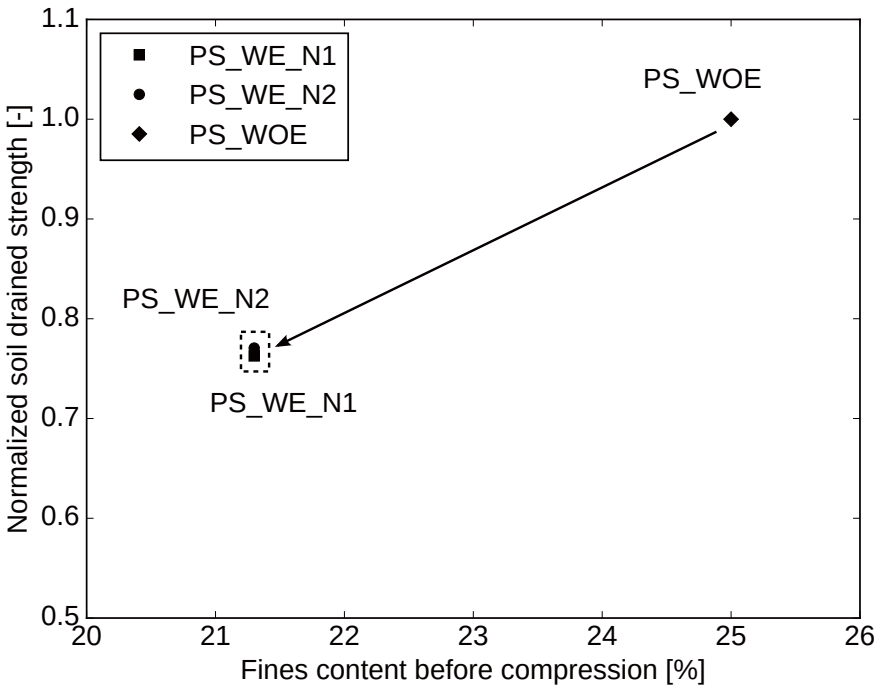

Figure 6.23: Normalized drained soil strength against fines content before compression test

prepared targeting a relative density of 30%. The moist tamping method was employed to create the similar soil fabric as that in the triaxial tests. Figure 6.24 shows the schematic diagram of the upward seepage test apparatus. The apparatus mainly consists of a rectangular seepage cell with a transparent glass window in front and a water reservoir. The internal dimensions of the rectangular seepage cell are 130 mm in height, 100 mm in length, and 30 mm in width. A 30 mm in thickness gravel diffusing filter was put to ensure a uniform flow across the specimens within a reasonable range. The size of the specimens is 60, 100, and 30 mm in height, length, and width, respectively.

After the preparation of specimens, a vertical stress of 50 kPa was applied to the soils to simulate the stress level in the triaxial cell under consolidation. The upward seepage flow was then applied from the bottom of the specimens after removing the vertical stress. The main objective of this test is to observe the change of soil microstructure, thus the influence of stress state is not considered at this point. The inlet flow was provided by the water reservoir, which can be raised or lowered to control its water head difference with the top of the specimens. The discharge rate was measured by the cylinder placed at the outlet from the basin. The applied maximum hydraulic gradient was large enough to dislodge most of the unstable fines aways from the specimens by the assigned upward flow. In this study, the maximum applied hydraulic gradient is over 1.0.

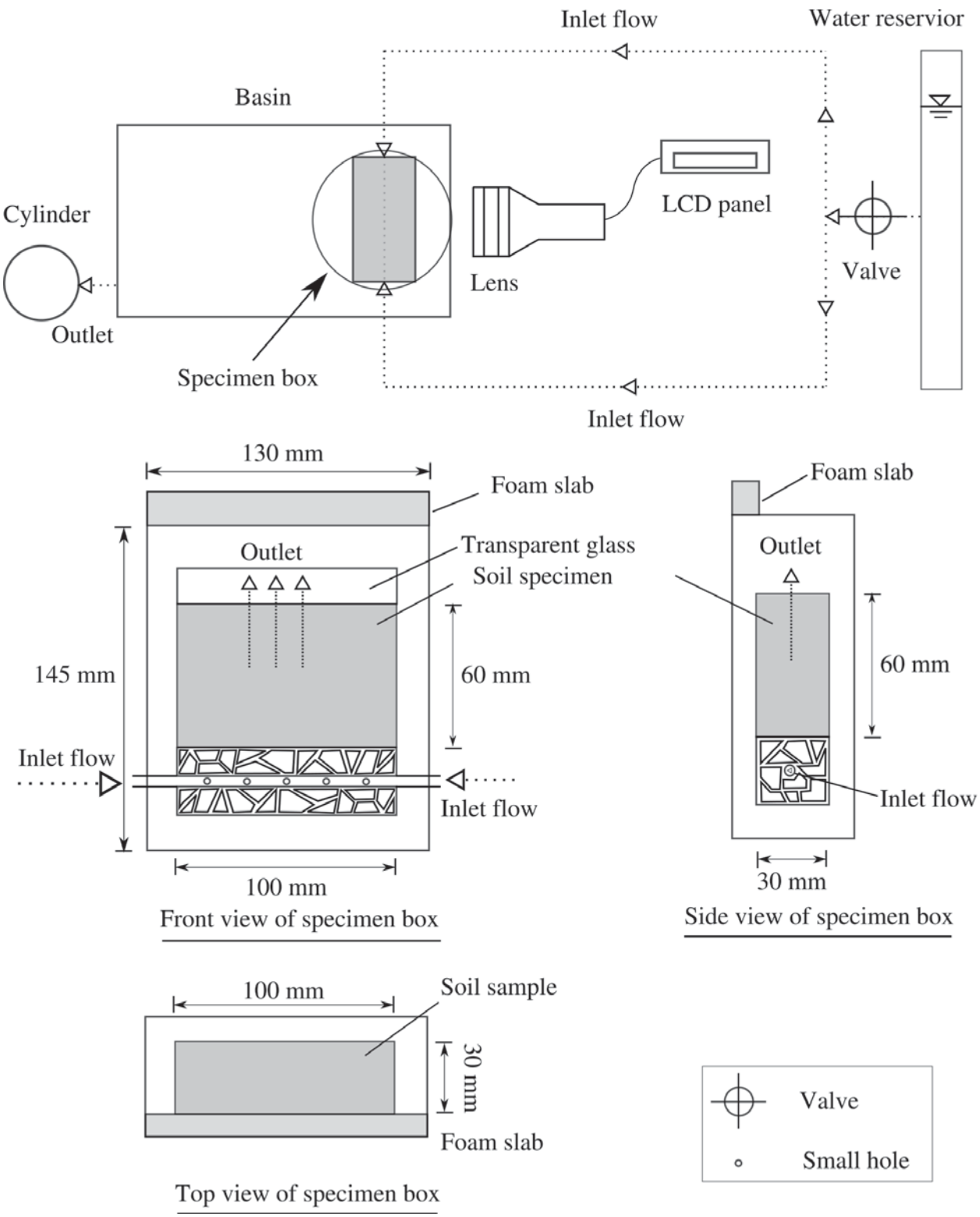

Figure 6.24: Apparatus for seepage tests

A digital microscope with a resolution of about 1000 units × 1000 units was used to observe the distributions of fines and coarse particles during the seepage tests. The lens of the microscope was placed in front of the transparent glass window, as shown in Fig. 6.24.

It is well recognized that if clean sand is mixed with fines, soil microstructure will change as a consequence and that change somehow corresponds to the amount of fines content (Yamamuro and Covert, 2001). An observation of the evolution of the microstructure of silica no. 3 with the increasing content of silica no. 8 (i.e., 0, 15%, 25%, and 35%), regarding as fines, is presented in Fig. 6.25. All those moist tamped specimens have the initial relative density of 30%. Initially, without the presence of fines, the contacts between coarse particles are well developed. With the introduction of small amount of fines (i.e., 15%), the coarse particles are coated by the fines and a fraction of fines fills the voids between coarse particles. In terms of the specimen with large amounts of fines (i.e., 25%), the dominant contact network of coarse particles might be partially destroyed, leading to more occurrence of separation coarse particles by fine fractions. When it comes to a larger fines content (i.e., 35%), the voids between coarse particles are almost occupied by fines.

Skempton and Brogan (1994) postulated that some fines that filling the voids would not take part in the load transfer, therefore, it is expected they would be dislodged by the upward seepage flow. The images collected upon the completion of internal erosion (Fig. 6.26) showed similar phenomenon that some fines occupying the voids formed by coarse particles were moved away by fluid flow. Although the results of upward seepage tests cannot be quantitatively compared to the downward seepage tests, they could be qualitatively correlated. For instance, fines were eroded away from specimens; hydraulic gradient and hydraulic conductivity changed; void ratios and volume of specimens were altered with the progress of internal erosion. Interestingly, at some spots, due to the small constriction size of voids, amounts of fines were impeded and consequently accumulated around the contact points of coarse particles, forming the jamming fines. Those fines would actively participate in the load transfer. Microscopically, these jammed fines may be involved in the load transfer and macroscopically they would result in different undrained responses from the soils without erosion, which will be discussed in detail later.

Albeit different, the flow direction is compared to triaxial erosion tests in Chapter 3, the inherent mechanism of internal erosion being the same, i.e., process of fines transportation. It is also argued that the fabric observed through the transparent window could be different from the inside of the specimen, which might be considered as an inherent limitation for the fixed wall seepage tests. Due to the formation of large void around the fixed wall, more fines would be eroded away near these fixed boundaries. Consequently, the images recorded in the front of the transparent window might

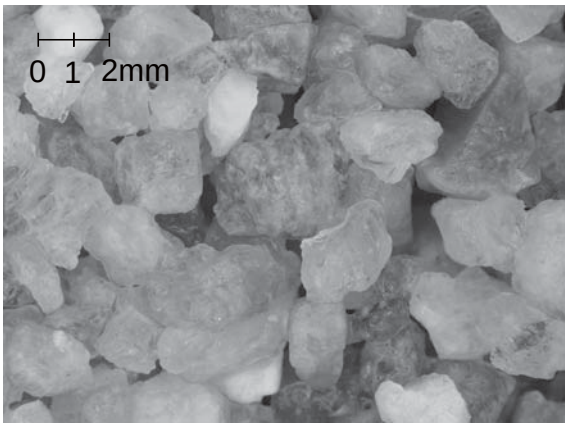

(a) Before erosion (0% initial fines content)

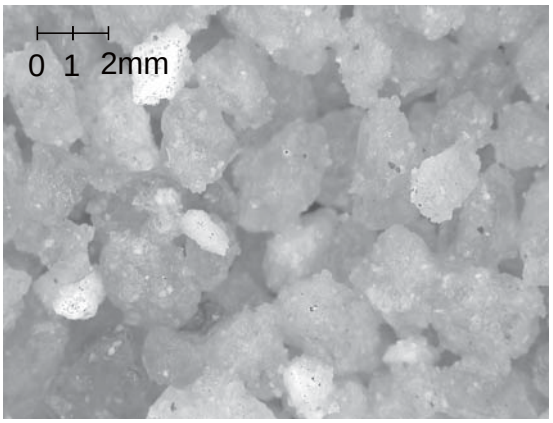

(b) Before erosion (15% initial fines content)

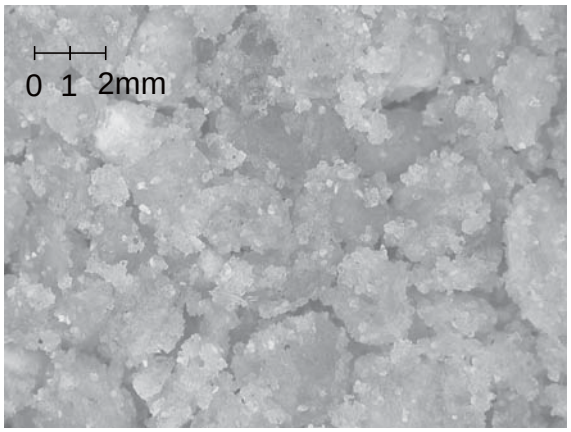

(c) Before erosion (25% initial fines content)

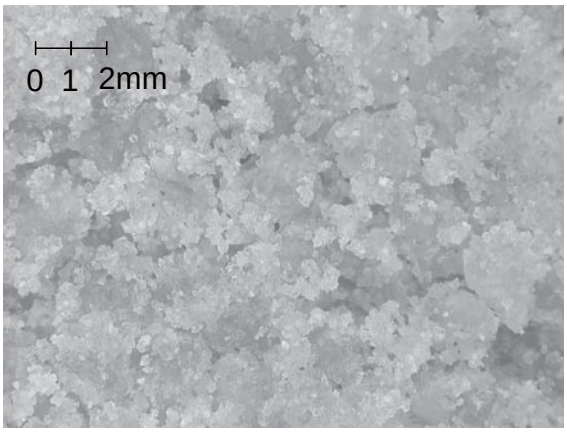

(d) Before erosion (35% initial fines content)

Figure 6.25: Microstructure of soils before erosion; initial fines content: (a) 0%; (b) 15%; (c) 25%; (d) 35%

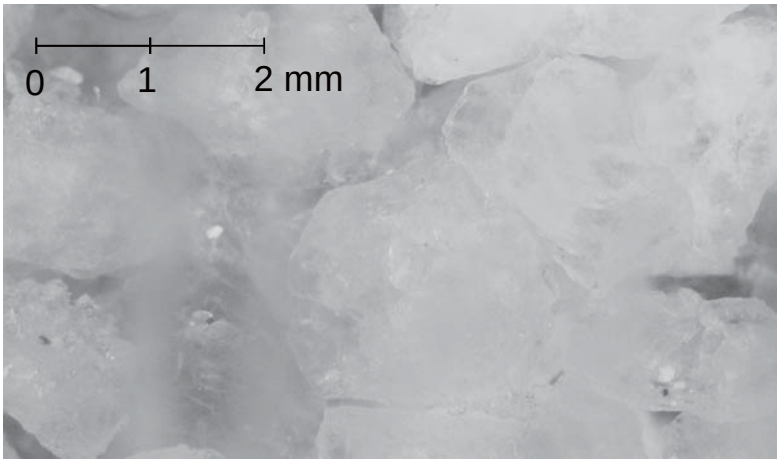

(a) After erosion (15% initial fines content)

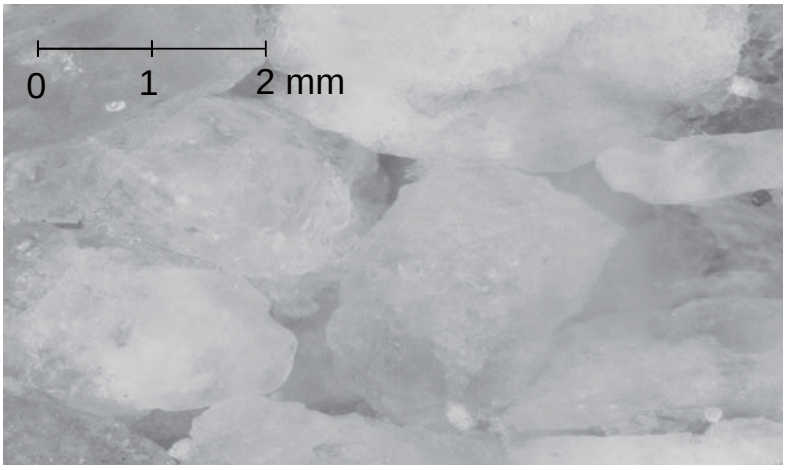

(b) After erosion (15% initial fines content)

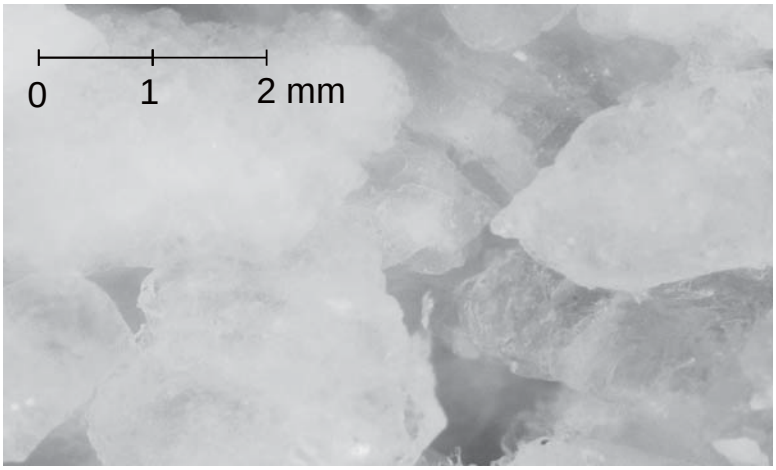

(c) After erosion (35% initial fines content)

Figure 6.26: Microstructure of soils after erosion; initial fines content: (a) 15%; (b) 25%; (c) 35%

exaggerate the phenomenon of internal erosion, whereas, the evolutions of soil microstructure could be presented, which is the very purpose of the upward seepage tests. Therefore, the images recorded from these tests were utilized as supplemental evidences in discussing soil mechanical behaviors in triaxial tests.

6.6.1 Effects of fines content on undrained behavior

As shown in Chapter 3, the uneroded specimens containing a smaller amount of fines show a larger value of peak strength, undrained tangent stiffness, and residual strength that that containing a larger amount of fines. These undrained behaviors on the soils without erosion may be affected by the soil fabric.

All the specimens in this study were prepared by moist tamping method. It is well known that the moist tamping method would create metastable structures among coarse particles. The images in Fig. 6.25 taken by a digital microscope reveal that the micro soil fabric to some extend in this study. The metastable structure can be clearly observed in the soil with 15% fines content because the voids between coarse particles are hardly filled with fines. However, in the soil with 25% fines content, the voids between coarse particles are partially filled with fines. In the soil with 35% fines content, these voids are largely filled with fines. Most of the coarse particles seem to be floating on the fines. Therefore, the metastable structure cannot be obviously observed in the soils with 25% and 35% fines contents.

Observation of the contacts in the binary soil mixtures are formed randomly by fines and coarse particles. The fines in between the coarse particles in the soil with 15% fines content are less than those in the soils with 25% and 35% fines contents. It might be possible to assume that the amount of the jamming fines is less in the soil with 15% fines content. According to Salgado et al. (2000), during compression, the coarse particles may be easily moved side away for the soil with less jamming fines (i.e., soil with 15% fines content), leading to greater direct contacts between coarse particles during shearing. The load may be more efficiently transferred through the coarse particles than through the fines. Therefore, it is possible to deduce that the uneroded soil with smaller fines content would show a relatively larger peak and residual strength than that with larger fines content within the test range.

6.6.2 Effects of internal erosion on undrained behavior

Through the comparison between the soils with and without erosion in Chapter 3, it is noted that the undrained behavior of the eroded soils is different from that of the uneroded soils. The soils with erosion show a larger peak and residual strength that those without erosion, which probably means

that the soils become less contractive after internal erosion. One of the reasons for the dilative behavior of soils with erosion might be the dilative characteristic of silica no. 3. As indicated in Figs. 3.11 and 3.12, the specimens made of silica no. 3 only show a fully dilative behavior in the undrained compression test even at a loose condition (initial relative density of 20% and 30%).

The soils with erosion have similar fines content before compression, but they showed different behavior during the undrained compression tests. For instance, the flow potential of eroded soils show a wide range of value within only a small range of fines content. Therefore, it could be said that the reason of the difference in the undrained behavior of soils with and without erosion is caused not only by the decrease of fines content because of internal erosion, but also by the change of the fabric. In this study, the soil fabric is observed by digital microscope and the collected images of soils subjected to internal erosion can be seen in Fig. 6.26.

The coarse particles of the soils soils with erosion were rearranged due to the internal erosion. The transportation of fines leads to an increase of void space. The hydraulic force induced by the seepage flow not only transports the fines, but also changes the position of the coarse particles, which may have resulted in a fabric that is different from the soils without erosion. This probably changes the way of load transformation in the soils with erosion compared with the soils without erosion.

The contacts between particles may also have been changed by the internal erosion. It can be observed in Fig. 6.26 that some fines still stay in between the coarse particles after the seepage test. During the progress of seepage flow, the fines were jammed in the slaps around the contact points between the coarse particles. Thus, the number of effective contact points increases due to internal erosion, resulting in a much more efficient transformation of the internal forces, consequently, a larger normalized peak and residual strength for the eroded soils than uneroded soils.

6.7 Quantitative evaluation of internal erosion

The results of plane strain erosion tests revealed that the responses of soils with erosion were different from those of soils without erosion. Specifically, at small strain level, the normalized secant stiffness of eroded soils was larger than that of uneroded soils; and at medium strain level, the drained strength of soils with erosion was smaller than that of soils without erosion.

For the sand mixtures with fines and coarse particles, it was reported that the mechanical behaviors were affected by the fines spatial distributions and the consequent contacts among particles (Yang

and Liu, 2016). Accordingly, the microscopic images taken from the front transparent window during the seepage and compression tests were examined and found that the fines spatial distributions of soils with erosion were different from those of soils without at both small strain and medium strain levels. Therefore, two hypotheses regarding to the evolutions of fines positions at both small strain and medium strain levels were proposed, in terms of soils with and without erosion respectively, in this section.

To prove the proposed hypotheses, on the basis of constriction size, the contact area between coarse particles was defined. Through the implementation of image analysis technique, the percentage of fines in the prescribed contact area could be obtained. Then the fines spatial distributions were employed to indicate the possible contacts between fines and coarse particles, which then suggested the effectiveness of load transfer during the compression tests. The influence of the internal erosion on the soils drained responses was quantitatively explained by using the percentage of fines in the contact areas at both small strain and medium strain levels.

Finally, the hypotheses were employed in discussing the undrained mechanical responses in triaxial erosion tests (Chapter 3), with respect to various states: undrained peak state, quasi-steady state, phase transformation state and critical state.

6.7.1 Hypotheses

It was recognized that the soils behaviors could be influenced by the preparation method (Takahashi, 2016; Yang et al., 2008). The specimens prepared by moist tamping method were assumed to be in a metastable state, as demonstrated by Sladen et al. (1985). One of the microscopic images of soils without erosion taken after the consolidation, or before compression, is shown in Fig. 6.27. Observation of this image noted that the fines were not simply to occupy the void space formed by the coarse particles but laid around the contacts between coarse particles. To elaborate the positions of particles during the experiments clearly, in the illustrations of the hypotheses, the coarse particles were represented as gray ellipses, and the fines were represented as black circles, as indicated in Fig.6.28. The sizes of gray ellipses were similar to those of the coarse particles, whereas, the fines were exaggerated for a better demonstration.

The procedures of the plane strain erosion tests for soils with and without erosion were briefly reviewed in Fig.6.29. The tested specimens were prepared by moist tamping method, and then saturated by deaired water and consolidated to targeting stress states. For soils with erosion, the seepage test was performed and the subsequent compression test was carried out on the eroded soils.

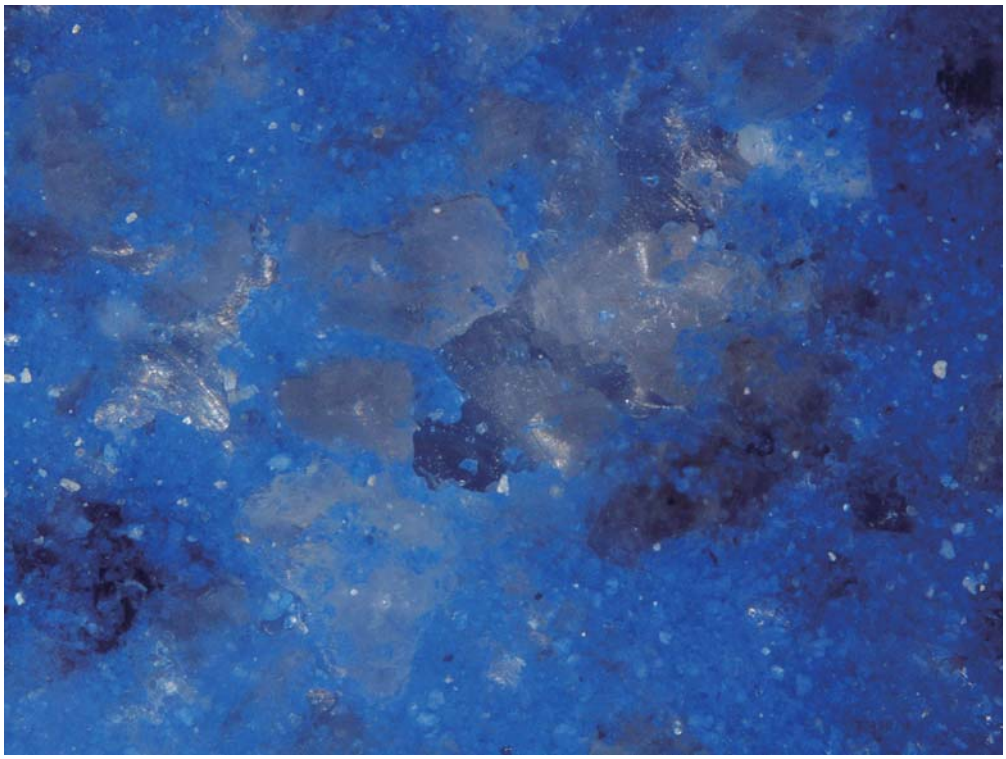

Figure 6.27: Microscopic image taken before compression for soils without erosion

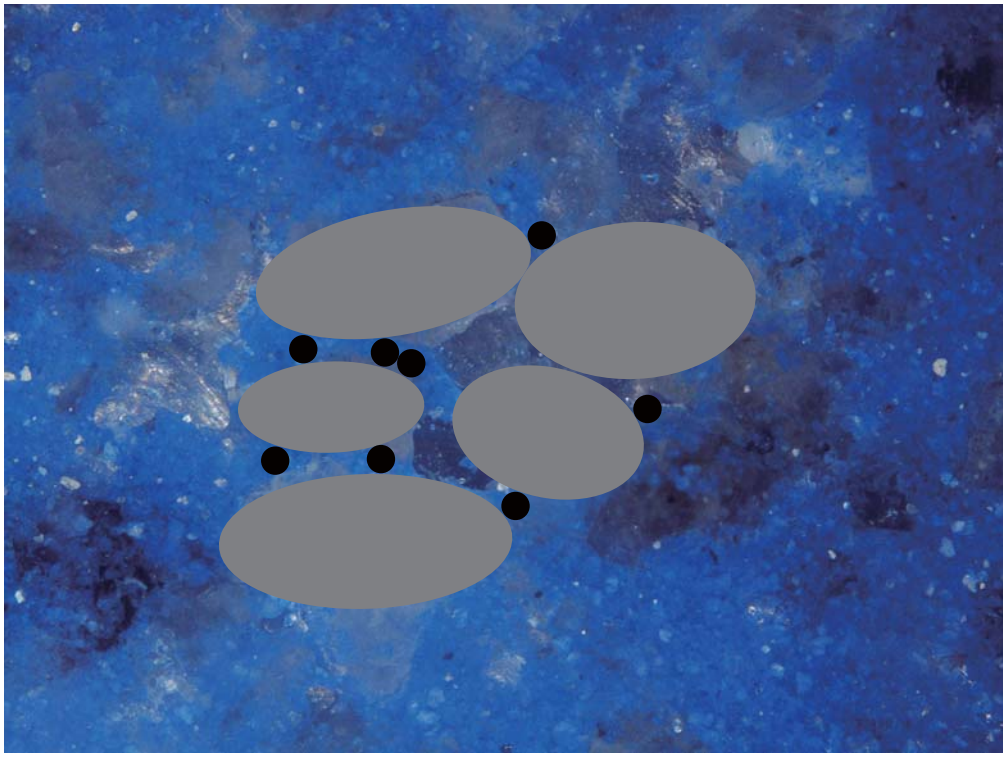

Figure 6.28: Demonstration of the fines and coarse particles based on the microscopic observation

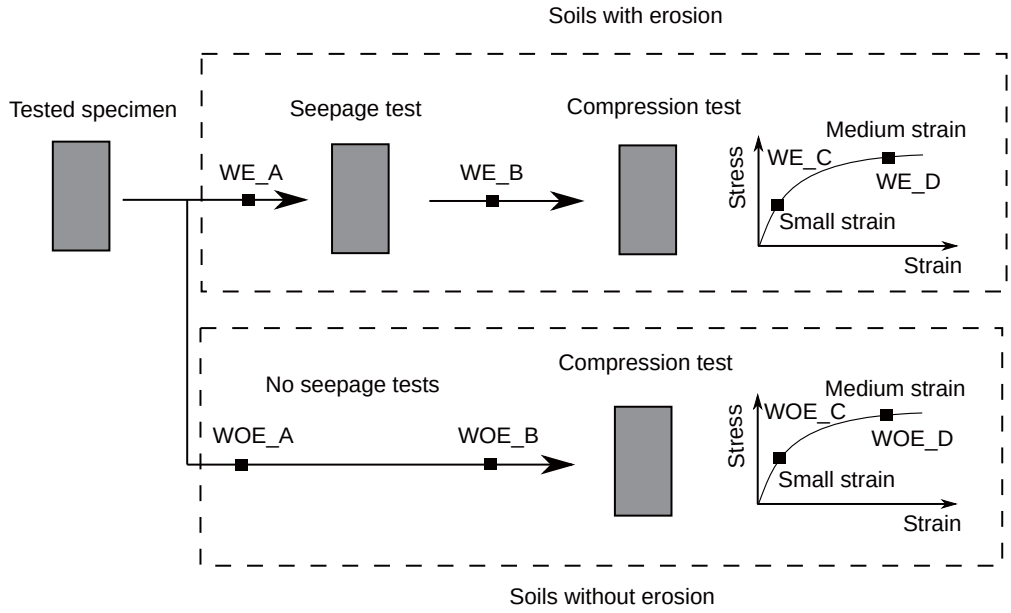

Figure 6.29: Brief review of the procedures in plane strain erosion tests

For soils without erosion, the seepage test was not performed, and the compression test was directly performed on the uneroded soils.

To investigate the fines spatial distributions during the whole testing, the microstructures of soils particles were examined in four key states. For soils with erosion, the four key states were WE_A, the state before seepage test; WE_B, after seepage test and before compression test; WE_C, at small strain level during the compression test and WE_D, at medium strain level during the compression test. Correspondingly, the key states for soils without erosion were named as WOE_A, WOE_B, WOE_C and WOE_D. Since the seepage test was not performed on soils without erosion, the soils microstructure at state WOE_A was the same as that at state WOE_B.

Two hypotheses were proposed on the relative positions of fines and coarse particles for soils with and without erosion, respectively.

One hypothesis for the soils with erosion is presented in Fig.6.30, with the soils microstructure in the four key states: WE_A, WE_B, WE_C and WE_D. In this figure, the short solid line represents the contacts between coarse particles, and the short dashed line represents the contacts with fines. The microstructure of soils before seepage tests was shown as WE_A in Fig. 6.30. After the seepage test, the microstructure was shown as WE_B in Fig. 6.30. It can be seen that some fines were eroded away during the seepage test, indicated as the dashed empty circle in Fig. 6.30. The fines were moved internally to the contacts between coarse particles as well, indicated as the checkboard

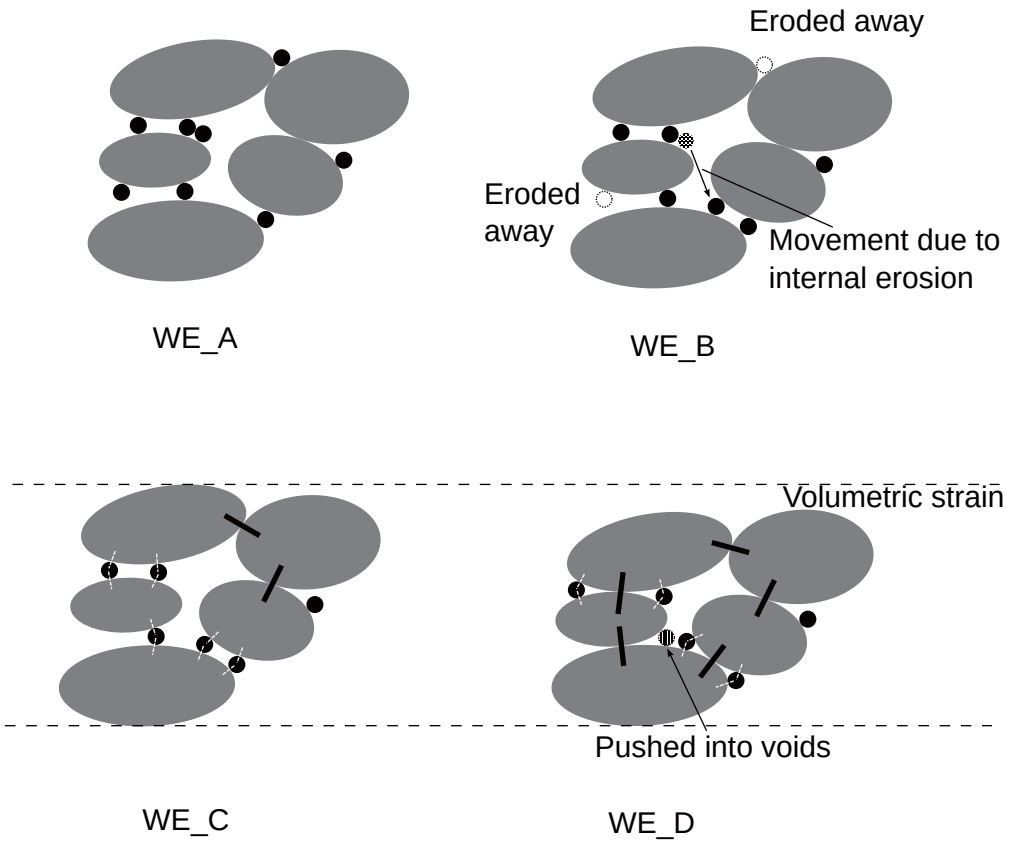

Figure 6.30: The microstructure of soils with erosion in the key states

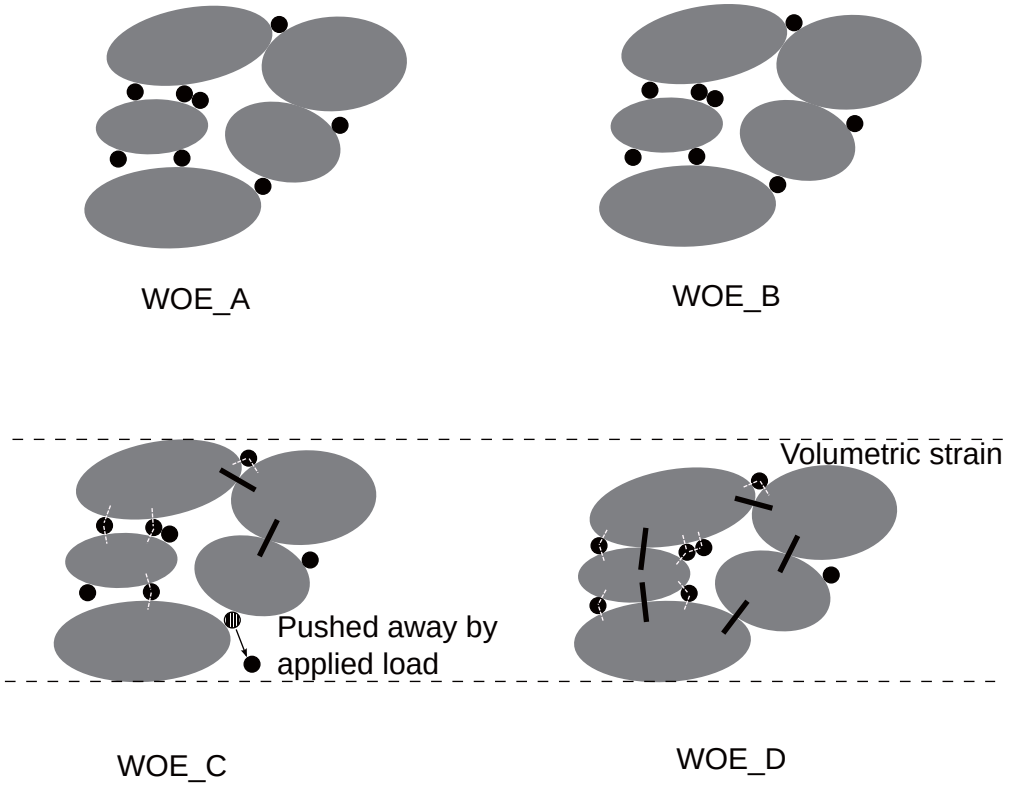

Figure 6.31: The microstructure of soils without erosion in the key states

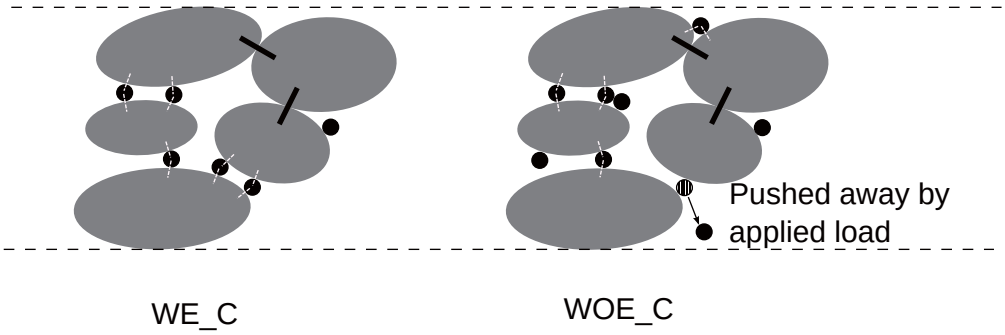

Figure 6.32: The microstructure at small strain level for soils with and without erosion

circle in Fig. 6.30. During the compression test, at small strain level (WE_C in Fig. 6.30), the fines, transported by seepage flow and then cumulated at the contacts between coarse particles, could transfer the load. At medium strain level (WE_D in Fig. 6.30), the specimens were compressed under drained condition, thus the volume of the specimens decreased, leading to a reduction of void ratio. The reduction of void ratio resulted in an increase of contacts between coarse particles, which reflected in the Fig. 6.30 was that there were more short solid lines in state WE_D comparing to those in state WE_C. It was responsible for the larger deviator stress of soils at medium strain level comparing to that at small strain level. But regarding to the influence of internal erosion, there were many voids created by the internal erosion, which allowed the fines to be pushed into, as pointed out in Fig. 6.30. The locations of these voids were not indicated in the illustrations, but will be discussed in the later quantitative examinations.

The other hypothesis for the soils without erosion is presented in Fig. 6.31, with the soils microstructure in the four key states: WOE_A, WOE_B, WOE_C and WOE_D. Similarly, the short solid line represents the contacts between coarse particles, and the short dashed line represented the contacts with fines. Since the seepage test was not performed on soils without erosion, the microstructure of soils in state WOE_B was the same as that in in state WOE_A. During the compression test, no fines were eroded away, whereas, the fines could be easily pushed away by the applied load due to the metastable structure of specimen prepared by moist tamping method at small strain level, as pointed out at state WOE_C in Fig. 6.31. At medium strain level, similar to the soils with erosion, the decrease of volume and the induced reduction of void ratio could lead to larger deviator stress comparing to that at small strain level.

According to Zlatovic and Ishihara (1997), the soils behaviors during the compression tests were affected by two factors: fabric and void ratio. As demonstrated in Figs. 6.30 and 6.31, for both soils with and without erosion, the void ratios at medium strain level were smaller than those at small strain level. Therefore, there were more contacts between coarse particles at medium strain level

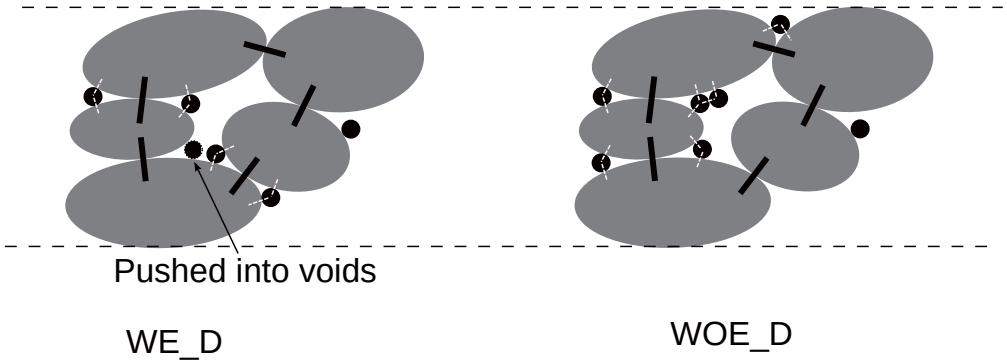

Figure 6.33: The microstructure at medium strain level for soils with and without erosion

than those at small strain level, which then resulted in larger deviator stress at medium strain level comparing to that at small strain level. To comparing the influence of internal erosion on the fabric, the microstructures at small strain level of soils with and without erosion are shown in Fig. 6.32. It can be noted that contacts between coarse particles were the same, whereas, the contacts with fines for soils with erosion were larger than those for soils without erosion. It suggested that more fines might be accumulated around the contacts between coarse particles, which could effectively transfer the load and then result in larger normalized secant stiffness for eroded soils comparing to that for uneroded soils. Figure 6.33 shows the comparison of the microstructure at medium strain level for both soils with and without erosion. The contacts between coarse particles were the same, but the contacts with fines for soils with erosion were smaller than those for soils without erosion. It indicated that the fines in the contacts between coarse particles were smaller for soils with erosion than that for soils without erosion, which further caused smaller soils strength (at medium strain level) for soils with erosion than that for soils without erosion.

6.7.2 Contact area

One of the possible approaches to prove the proposed hypotheses was to calculate the amount of fines in the contacts between coarse particles at different states, e.g. before compression test, at small strain level or at mediums train level. If the fines in the contacts between coarse particles were assumed to be able to effectively transfer the load, then the soils with a larger amount of fines in the contacts between coarse particles could probably indicate larger stress comparing to the soils with a smaller amount of fines in the contacts between coarse particles. Through the comparison of the amount of fines for soils with and without erosion at certain state, the influence of internal erosion on fines spatial distributions and the subsequent mechanical behaviors could be quantitatively interpreted. Then the questions go to how large is the area of contact between coarse particles, and how to quantify it through the laboratory tests.

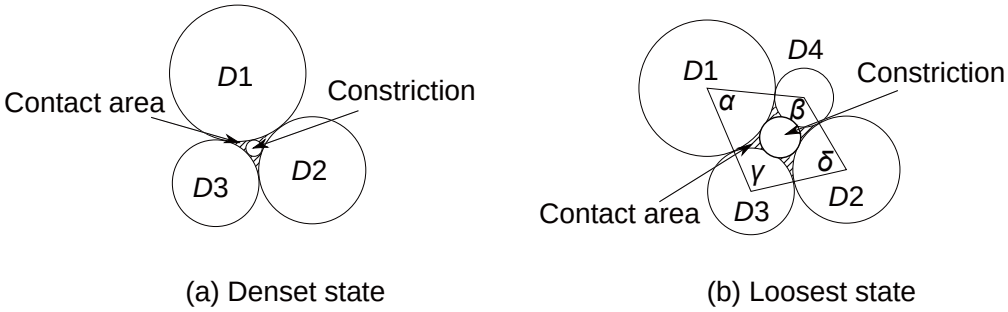

(a) Denset state (b) Loosest state

Figure 6.34: Definition of contact area at both densest and loosest states

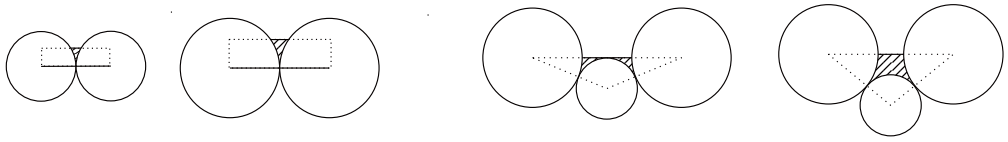

(1) particle size (2) relative density

Figure 6.35: Influential factors of contact area

Definition of contact area

To answer the questions, the conception of contact area is proposed and defined on the basis of constrict size. The tested materials in this research are cohesionless granular sands with median diameters of 0.16 mm and 1.76 mm for fines and coarse particles, respectively. With the large diameters, the elastostatic force might be neglected. Thus rather than the elastostatic force, the geometry configuration was primarily considered in the definition of contact area. According to Kenney et al. (1985), the constriction size was termed as the largest sphere that will pass through a particular void formed by coarse particles. For the gap-graded soils, the fines could pass through within the constriction size, and then the remaining fines might accumulate in the contacts between coarse particles. Therefore, the contact area was defined as the area of void confined by coarse particles subtracting the area of constriction size. The demonstration of constriction size is shown in Fig. 6.34, in terms of densest state and loosest state respectively. By employing the definition of contact area, the distributions of contact area at both densest and loosest state for the tested materials in this study could be obtained, which is shown in Fig. 6.36. It can be inferred that the soils showed the largest contact area at the densest state, whereas, it showed the smallest contact area at the loosest state under otherwise the same conditions.

Two factors would affect the contact area: particle size and relative density, as indicated in Fig. 6.35. It can be observed from the figure that the soil with larger particles showed larger contact areas; and

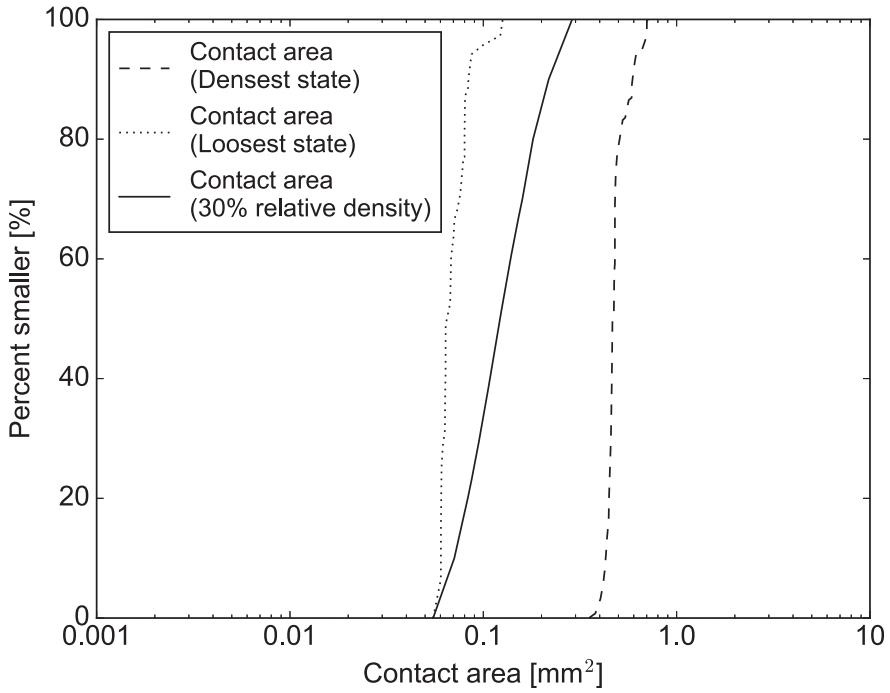

Figure 6.36: Contact area distribution curves

for soils with larger relative density showed larger contact areas. The effect of particle size on the contact area was already considered in the definition, whereas, the influence of relative density was not. By employing the similar implementation of relative density in constriction size, and assuming that when the relative density equals zero, the distribution of contact area is the same as that in the loosest state, the contact area at certain relative density could be expressed as:

$$CA_c = CA_l + p \times Rd \times (CA_d - CA_l) \tag{6.4}$$

where, p is the chosen percentage of a contact area, Rd is the relative density, CA_c is the contact area for a given value of the percent smaller p, CA_d and CA_d is the contact area in the densest and loosest states, respectively, for the same p. According to the Table 6.5, the relative density for the eroded specimen was 30%, therefore, the contact area of this specimen was plotted in Fig. 6.36. The controlling contact area is chosen as 0.085 mm^2 for 20% percent smaller in the contact area distribution. It was employed in the image analysis to quantitative interpret the effects of internal erosion.

It is recognized that the above definition of contact area was performed only in 2D plane, whereas, the soils are 3D solid spheres. To address it, Figs. 6.37 and 6.38 show the 3D configuration of sand particles from the observed front window, with respect to densest state and loosest state respectively.

It can be observed that the contact areas were obtained just from the geometry of the front view in Figs. 6.37 and 6.38. However, the volume confined by the particles could not be just represented by the 2D planar geometry configuration. For instance, if the radius of particle is 1, the confined planar area by three particles in the densest state is 0.16 and the confined 3D volume is 0.68; and regarding to the loosest state, the confined planar area is 0.86 and the confined 3D volume is 1.91. Specifically, in terms of value, the volume is 5.4 times larger than the area in the densest state and 2.2 times larger in the loosest state. It suggested that the definition of the contact area needed more studies.

Quantify the contact area through image analysis

Regarding to the other question of quantification of contact area through the laboratory tests, the analysis based on recorded microscopic images might be one of the possible solutions. During both the seepage and compression tests, the microscopic images were recorded by a high resolution digital image VCR-800. Through the calibration, it was noted that the outlines the coarse particles could be observed, which then permitted the pointing of the contact points between coarse particles.

The procedure for the quantification of contact area through image analysis is then briefly introduced here. Figure 6.39 shows one of the original images recorded by the VCR-800 during the plane strain erosion tests. Firstly, the original image was copied in order to compare with the later processed image. Then pick up the contact points between coarse particles manually according to the contours of coarse particles, the coordinates of which were then stored. After getting the coordinates of the contact points between coarse particles, the contact areas were drawn in the images as circles. The value of the contact area could be chosen from the contact area distribution curves, as indicated in Fig. 6.36. Here in the demonstration, the contact area was chosen as 0.085 mm2, and the processed image is shown in Fig. 6.40. Compare the Fig. 6.40 with Fig. 6.39, together with the implementation of the special pixel value of fines, the fines in the mapped contact area could be calculated, as shown in Fig. 6.41. The average percentage of fines in the contact area was obtained through the systematic analyzing a number of images.

In the process of image analysis, it was admitted that the circle might not be the best way to represent the contact areas of soils with irregular shape particles. However, if the particles were regarded as 3D solid spheres, as indicated in Figs. 6.37 and 6.38, the contacts between particles from the transparent window (front views) were not singles points, but were certain areas. The fines in these areas might transfer the load as well. Moreover, drawing the circle could be easily performed in the image analysis. Due to the isotropic features of circle, the analysis based on the fact that regarding the circle as contact area, could also get more robust results than the other

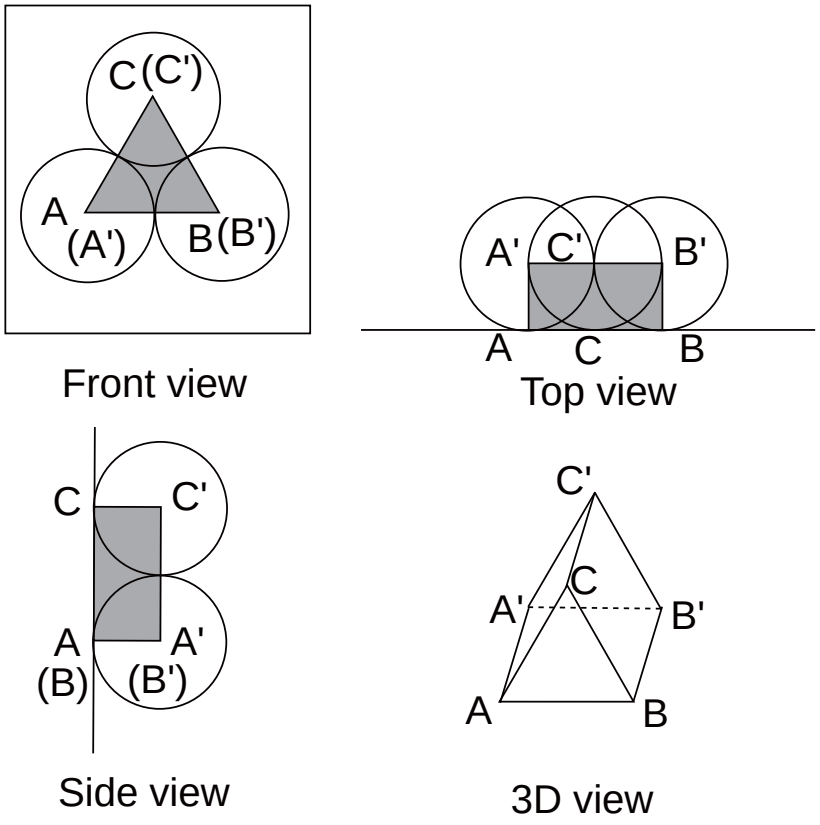

Figure 6.37: The 3D configuration of contact area in densest state

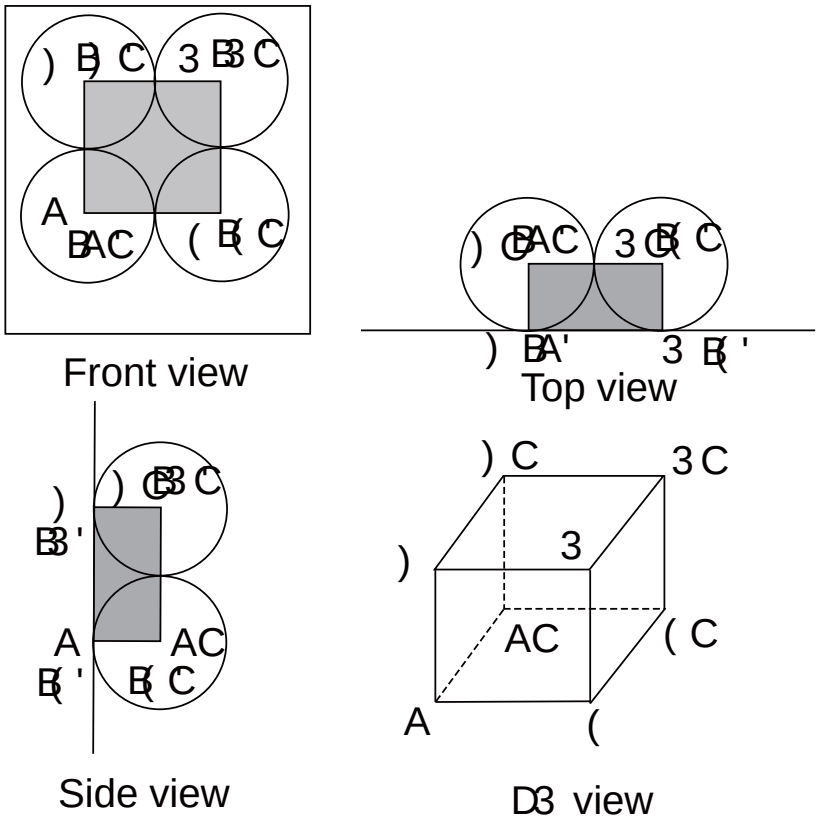

Figure 6.38: The 3D configuration of contact area in loosest state

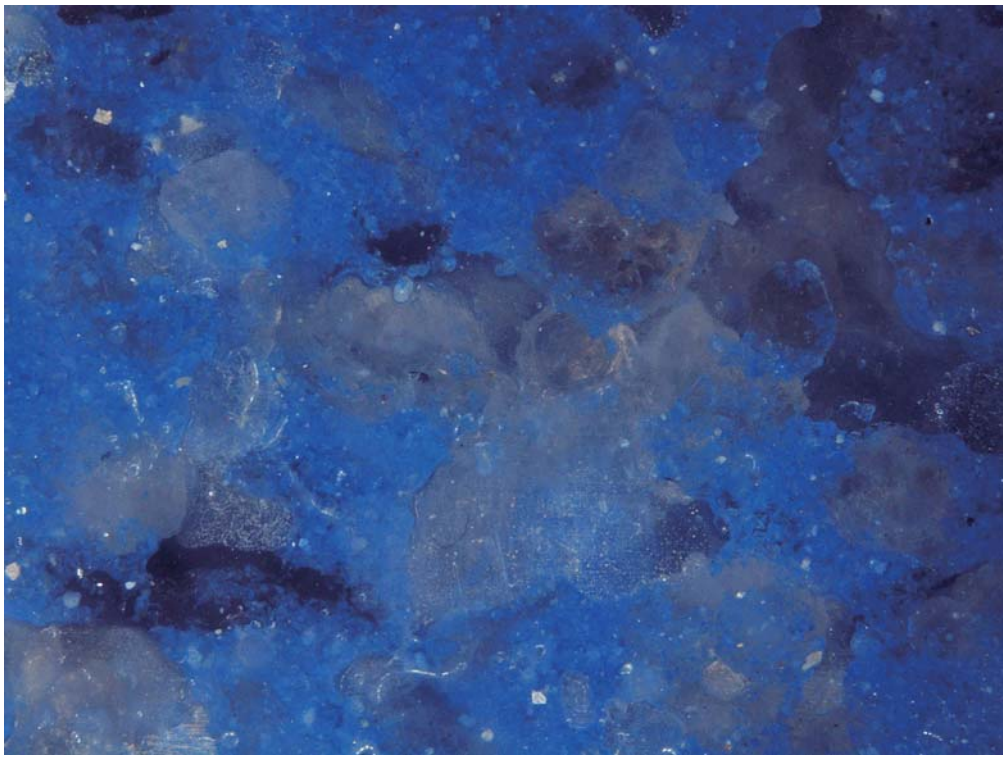

Figure 6.39: Original image recorded by microscope VCR-800

Figure 6.40: Draw the contact area on the original image

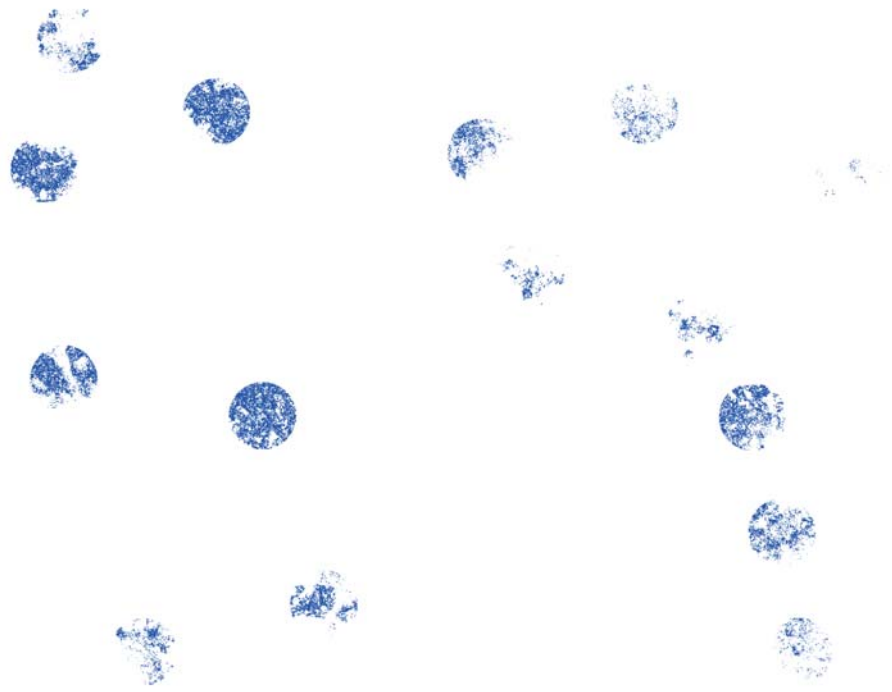

Figure 6.41: Calculate the fines percentage in the contact areas

anisotropic shapes. Taking the above mentioned reasons into consideration, the circle was treated as the contact area in this research.

As for the value of contact area, it was pointed out that the contact area would vary from the particle size. Therefore, the contact area in each microscopic image might not be the same due to the various sizes of the sands. However, since the natural sand was not sphere, it was difficult to identify its radii from the image analysis, and then the calculation of the contact area for each contact between coarse particles became very difficult. Thus, one of the controlling values for the contact area was chosen during the whole image process, which could benefit for not only the consistent results, but also the reduction of computation time.

Observation of the images revealed that some fines were moved perpendicular to the observed plane during the seepage and compression tests, which could not be quantitatively described through the image analysis. This was regarded as an inherent limitation of this research since the quantification by microscopic image can only represent the fines spatial distribution in the observed plane. The movement of fines perpendicular to the plane strain indicated that the soils specimens were not under perfect plane strain conditions. But it could infer that the fines might be pushed into the voids which were perpendicular to the plane strain at the medium strain level, as indicated in Fig. 6.30.

These fines were still in the observed area, but hidden behind the coarse particles, as shown in 3D configurations in Figs. 6.37 and 6.38.

6.7.3 Interpretation on internal erosion of plane strain erosion tests

To demonstrate the necessary number of contact points for obtaining the reliable results, the detailed examination of test case PS_WE_N1 was presented. Figure 6.42 plots the number of contact points against the percentage of fines in contact area before compression, at small strain level and at medium strain level. It could be observed that the data obtained from around 200 contact points could achieve a reasonable constant value. Then the average results obtained over 200 contact points were employed in quantitatively interpreting the influence of internal erosion on soils mechanical responses at different strain levels.

Figure 6.43 shows the normalized percentage of fines in contact area of soils with and without erosion. The normalized percentage of fines in contact area is the percentage of fines in contact area normalized by the percentage of fines in contact area before the compression. It can be found that the normalized percentage of fines at both small and medium strain level was different for soils with erosion comparing to that for soils without erosion. The examination on small strain level revealed that the normalized percentage of fines in contact area for soils with erosion was larger than that for soils without erosion. It suggested that more fines might be cumulated in the contacts between coarse particles, and resulted in larger normalized secant stiffness for the eroded soils than that for uneroded soils. At medium strain level, the normalized percentage of fines for soils with erosion was smaller than that for soils without erosion. This maybe because the fines were transported into the voids at medium strain level, leading to a smaller percentage of fines in contact area, and further a smaller drained strength than the soils without erosion.

6.7.4 Interpretation on internal erosion of triaxial erosion tests

Different from the drained conditions in the plane strain erosion tests, the triaxial erosion tests in Chapter 3 were performed under undrained conditions. The stress strain curves of soils with and without erosion in triaxial erosion tests under undrained conditions are shown in Figs. 6.44 and 6.45, respectively. The comparison between these two figures noted that for the soils containing the same initial fines contents, at the same axial strain, the deviator stress for soils with erosion was larger than that for soils without erosion until the undrained peak state. As demonstrated in the previous text, many fines were accumulated around the contacts between coarse particles due to internal erosion, which resulted in a larger amount of fines in the contact area for soils with

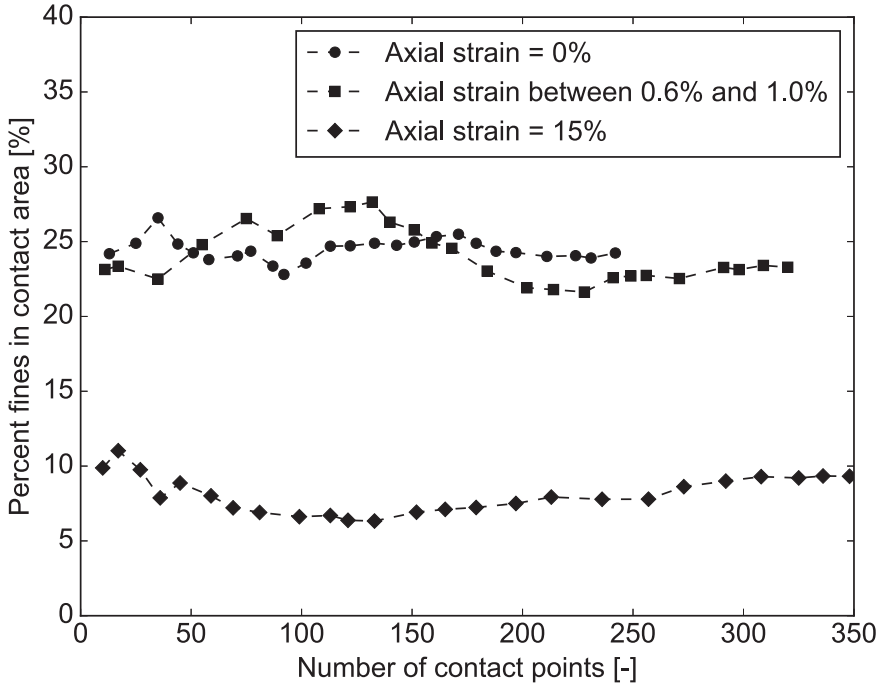

Figure 6.42: The relation between the contact points and the percentage of fines in contact area

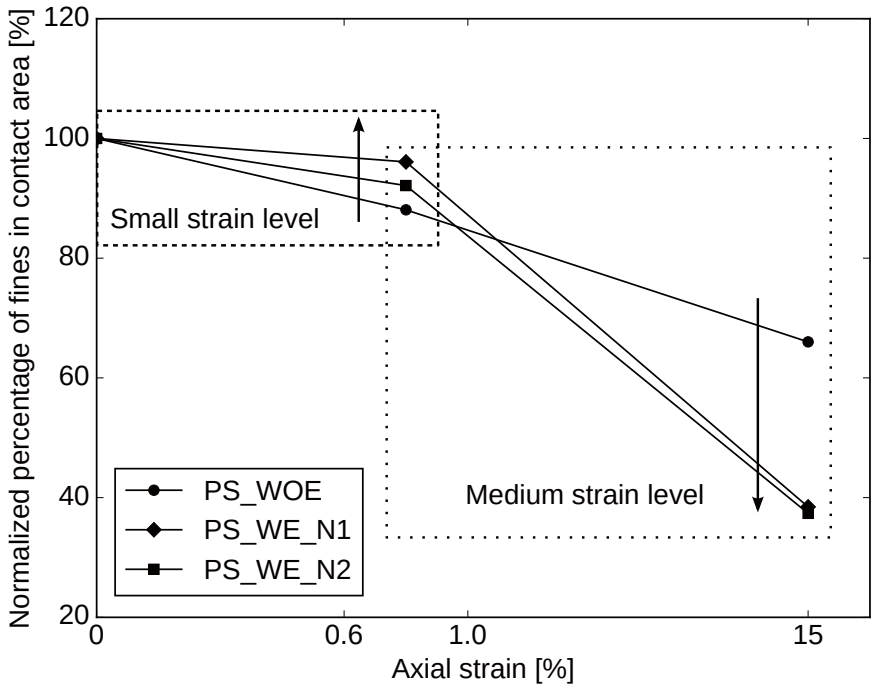

Figure 6.43: The normalized percentage of fines in contact area at both small strain and medium strain levels

erosion compared to that for soils without erosion. It then led to larger deviator stress or secant stiffness at small strain level for the eroded soils comparing to uneroded soils. Under the undrained compression conditions, the volume of the specimen would be kept constant, and then the fines reinforced structure created by internal erosion might be kept until undrained peak state, which caused larger undrained peak strength for soils with erosion than that for soils without erosion. However, due to the complicate change of pore water pressure under the undrained conditions, the proposed hypotheses need improvement to interpret the effects of internal erosion.

6.8 Summary

In this chapter, the results of plane strain erosion tests were presented. It demonstrated that the developed plane strain erosion apparatus was applicable to examine the influence of internal erosion on cohessionless soils under plane strain conditions. The drained mechanical responses of soils with erosion were different from that of soils without erosion. Moreover, the effects of internal erosion on both undrained and drained responses were interpreted from the particulate level.

The repeated cases showed similar results in the evolution of cumulative eroded soil mass and normal stress in direction of plane strain. It indicated that the developed plane strain erosion apparatus could yield consistent results. During the stage of larger flow rate, it showed large cumulative eroded soil mass. The normal strength in direction of plane strain decreased with the dislodgement of fines. The erosion of fines was affected by the boundary conditions. The soils near the flexible boundary showed large eroded fines than that the soils in the other parts. At small strain level, the normalized secant stiffness for soils with erosion was larger than that for soils without erosion at the same axial strain. Regarding to the medium strain level, the eroded soil showed smaller strength than the uneroded soil in this study.

Regarding to the interpretation of internal erosion from the micro scale, both the qualitative and quantitative evaluation were preformed. The images collected before and after internal erosion revealed that the soil fabric was altered by internal erosion. In the underoded soil with fines, the coarse particles were coated by the fines and the distribution of fines varied with the fines content. However, for the soils with erosion, most of the remaining fines were jammed around the contacts between coarse particles, which resulted in an increase of the number of effective contact points. By employing the conception of contact area, the percentage of fines in contact area can be examined through image analysis technique. It was found that the data obtained from around 200 contact points could achieve a reasonable constant value. At small strain level, the normalized percentage of fines at small strain level for soils with erosion was larger than that for soils without erosion. It

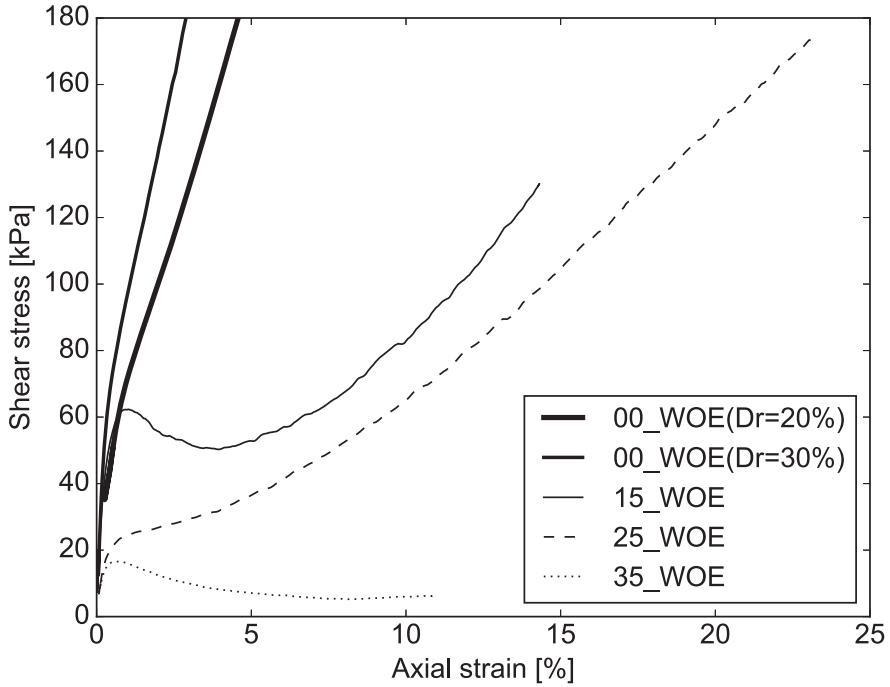

Figure 6.44: The stress strain curves of soils without erosion under undrained conditions

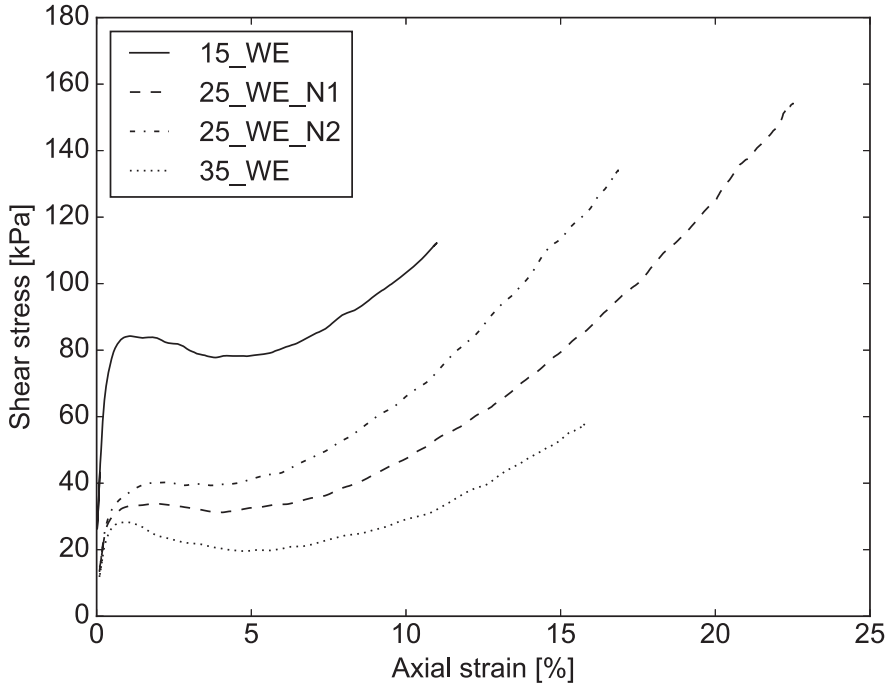

Figure 6.45: The stress strain curves of soils with erosion under undrained conditions

suggested that more fines might be cumulated in the contact points between coarse particles, and resulting in a larger normalized secant stiffness for the eroded soils. At medium strain level, the normalized percentage of fines for soils with erosion was smaller than that for soils without erosion. This maybe because that fines were transported into the voids at medium strain level, leading to a smaller percentage of fines in contact area, and further a smaller drained soil strength than the soils without erosion.

Chapter 7

Conclusions and recommendations

In this dissertation, the physical and mechanical responses of cohesionless soils subjected to internal erosion was investigated by laboratory experiments and microscopic observations. The undrained compression tests performed on soils with and without erosion demonstrated that the internal erosion would change the soil fabric, and consequently alter the mechanical behaviors. To examine the mechanism of the internal erosion, the soil fabric was quantitatively described through a proposed image analysis approach. To further interpret the effect of internal erosion induced fabric change on the change of mechanical response, a plane strain erosion apparatus equipped with visible window was developed. Through the proposed method and developed apparatus, the mechanical behaviors of eroded soils were quantitatively explained at both small strain level and medium strain level.

7.1 Conclusions

The conclusions obtained from the present study are as follows:

In **Chapter 3**, seepage tests and undrained monotonic compression tests were performed to examine the influence of initial fines content on the mechanical consequences of soils subjected to internal erosion. It is found that the seepage flow not only transports fines away from the specimen, but causes a drastic change of the undrained mechanical behaviors between soils with and without erosion. During the seepage tests, the soil with larger initial fines content showed a larger amount of cumulative eroded soil mass and a larger volumetric strain within the test range.

The amount of silica no. 8 in the tested mixtures would greatly affect their undrained behavior, resulting in the changes of peak strength and residual strength. Specifically, a smaller content of silica no. 8 would cause a larger peak, residual strength, and correspondingly a smaller flow

potential.

The mean effective stress ratios (ratio of mean effective stress at peak to that at initial) of soils with erosion showed different values from the soils without erosion. For the specimens with the same initial fines content, the post erosion soil exhibited larger undrained tangent stiffness compared to that without erosion at a relatively small axial strain level. The soils with erosion showed larger residual strength than those without erosion if their initial fines content are the same. Meanwhile, the eroded soils generated a smaller amount of excess pore water pressure than the uneroded soils before reaching the phase transformation state. It is also noted that the slope difference between the line connecting the origin to the transformation state and the instability line in the effective stress plane was larger for the soils with erosion, indicating an enlarged instability zone after internal erosion.

In **Chapter 4**, the siliceous sand with difference colors was quantified by image analysis in terms of aspect ratio, convexity and sphericity. The results showed that the morphology parameters of colored silica no. 8 were similar with those of original artificial silica no. 8. It makes the experiments employed colored sand and original sand comparable.

One dimensional upward seepage flow was applied in the mixtures of silica no. 3 and colored silica no. 8, in order to investigate the features of internal erosion. Image analysis was applied to quantitatively describe the characteristics of soil subjected to internal erosion. The cumulative eroded soil masses calculated by means of image analysis were generally in accordance with those obtained from independent macroscopic observations, suggesting that image analysis is an effective tool for describing the features of internal erosion. With respect to the observed area, for the gap-graded soil studied in this research, during an increase in hydraulic gradient, a large amount of fines tended to be transported, but were prone to be stationary under constant flow. The volume of the soil specimens decreased due to internal erosion and, as a result, the coarse particles were oriented horizontally.

In **Chapter 5**, a plane strain erosion apparatus was developed to evaluate the responses of soils under plane strain conditions. This apparatus is capable of directly investigate not only the marcoscale behaviors of soil subjected to internal erosion, but also the microscale features of particles during seepage and compression tests. The fabricated front visible window and the application of transparent membrane permitted the clearly observation of the particles behaviors. The earth pressure transducer attached at the back plate allowed the measurement of the normal strain in direction of plane strain. The flexible boundaries provided by the water bladders could effectively avoid the leakage during the seepage tests. The mechanical responses of the eroded soils could be

directly measured by the subsequent drained compression tests with strain rate control manner.

In **Chapter 6**, the results of plane strain erosion tests were presented. It demonstrated that the developed plane strain erosion apparatus was applicable to examine the influence of internal erosion on cohessionless soils under plane strain conditions. The repeated cases showed similar results in the evolution of cumulative eroded soil mass and normal stress in direction of plane strain, which indicated that the developed plane strain erosion apparatus could yield consistent results. During the stage of larger flow rate, it showed large cumulative eroded soil mass. The normal strength in direction of plane strain decreased with the dislodgement of fines. The erosion of fines was affected by the boundary conditions. The soils near the flexible boundary showed large eroded fines than that the soils in the other parts. At small strain level, the normalized secant stiffness for soils with erosion was larger than that for soils without erosion at the same axial strain. Regarding to the medium strain level, the eroded soil showed smaller strength than the uneroded soil in this study.

As for the interpretation of internal erosion from the micro scale, both the qualitative and quantitative evaluation were preformed. The images collected before and after internal erosion revealed that the soil fabric was altered by internal erosion. In the underoded soil with fines, the coarse particles were coated by the fines and the distribution of fines varied with the fines content. However, for the soils with erosion, most of the remaining fines were jammed around the contacts between coarse particles, which resulted in an increase of the number of effective contact points. By employing the conception of contact area, the percentage of fines in contact area can be examined through image analysis technique. It was found that the data obtained from around 200 contact points could achieve a reasonable constant value. At small strain level, the normalized percentage of fines at small strain level for soils with erosion was larger than that for soils without erosion. It suggested that more fines might be cumulated in the contact points between coarse particles, and resulted in a larger normalized secant stiffness for the eroded soils. Similar explanation could be given to explanation of the undrained triaxial erosion tests results, due to the constant volume during the compression tests under undrained conditions, the fines reinforced structure created by internal erosion could be kept until undrained peak state, which resulted in a larger undrained peak strength for eroded soils than uneroded soils. At medium strain level, the normalized percentage of fines for soils with erosion was smaller than that for soils without erosion. This maybe because that fines were transported into the voids at medium strain level, leading to a smaller percentage of fines in contact area, and further a smaller drained soil strength than the soils without erosion.

7.2 Recommendations

Due to the difficulties in sealing the membrane with the top cap during the load procedure, the undrained compression tests were hardly to be performed by the current apparatus. The improvements on the test apparatus were recommended for the future research. The proposed hypotheses were necessary to be improved for the interpretation on the undrained mechanical responses in terms of key states. The heterogeneity of soils during seepage tests and the compression tests needed more studies.

Bibliography

Abedi, M. and Yasrobi, S. 2010. Effects of plastic fines on the instability of sand. Soil Dynamics and Earthquake Engineering, **30**(3): 61–67. doi: 10.1016/j.soildyn.2009.09.001. (pages 5, 50).

Aberg, B. 1993. Washout of grains from filtered sand and gravel materials. Journal of Geotechnical Engineering, **119**(1): 36–53. doi: 10.1061/(ASCE)0733-9410(1993)119:1(36). (pages 5, 6, 31).

Alarcon Guzman, A., Leonards, G., and Chameau, J. 1988. Undrained monotonic and cyclic strength of sands. Jounral of Goetechnical Engineering, **114**(10): 1089–1109. doi: 10.1061/(ASCE)0733-9410(1988)114:10(1089). (pages ix, 48, 53, 54).

ALsakran, M., Zhu, J., and Dallo, Y. 2016. Discussion of "Influence of initial fines content on fabric of soils subjected to internal erosion". Canadian Geotechnical Journal, **53**(8): 1358–1359. doi: 10.1139/cgj-2016-0053. (pages 183, 186).

Alshibli, K., Godbold, D., and Hoffman, K. 2004. The louisiana plane strain apparatus for soil testing. Geotechnical Testing Journal, **27**(4): 1–10. doi: 10.1520/GTJ19103. (pages ix, 40, 41).

Altuhafi, F., OSullivan, C., and Cavarretta, I. 2013. Analysis of an image-based method to quantify the size and shape of sand particles. Journal of Geotechnical and Geoenvironmental Engineering, **139**(8): 1290–1307. doi: 10.1061/(ASCE)GT.1943-5606.0000855. (pages 46, 97, 114, 115).

Andò, E., Viggiani, G., Hall, S., and Desrues, J. 2013. Experimental micro-mechanics of granular media studied by x-ray tomography: recent results and challenges. Géotechnique Letters, **3**(3): 142–146. doi: 10.1680/geolett.13.00036. (page 46).

Andrade, J., Vlahinic, I., Lim, K., and Jerves, A. 2012. Multiscale tomography-to-simulation framework for granular matter: the road ahead. Géotechnique Letters, **2**(3): 135–139. doi: 10.1680/geolett.12.00023. (page 45).

Arshad, M., Tehrani, F., Prezzi, M., and Salgado, R. 2014. Experimental study of cone penetration in silica sand using digital image correlation. Géotechnique, **64**(7): 551–569. doi: 10.1680/geot.13.P.179. (pages 5, 45).

ASTM. 2012a. Method for consolidated drained triaxial compression test for soils. ASTM standard D7181-11. *In* Annual book of ASTM standards. Vol. 04.09. ASTM International, West Conshohocken, Pa. doi: 10.1520/D7181-11. (page 133).

ASTM. 2012b. Standard test method for consolidated undrained triaxial compression test for cohesive soils. ASTM standard D4767-11. *In* Annual book of ASTM standards. Vol. 04.08. ASTM International, West Conshohocken, Pa. doi: 10.1520/D4767-11. (pages 58, 59).

Aydilek, A., Oguz, S., and Edil, T. 2005. Constriction size of geotextile filters. Journal of Geotechnical and Geoenvironmental Engineering, **131**(1): 28–38. doi: 10.1061/(ASCE)1090-0241(2005)131:1(28). (page 5).

Baudet, B. and Pereira, J. 2013. Editorial: Experimental micro-mechanics for geomaterials. Géotechnique Letters, **3**(2): 42–43. doi: 10.1680/geolett.2013.3.2.42. (page 45).

Been, K. and Jefferies, M. 1985. A state parameter for sands. Géotechnique, **35**(2): 99–112. doi: 10.1680/geot.1985.35.2.99. (page 49).

Bendahmane, F., Marot, D., and Alexis, A. 2008. Experimental parametric study of suffusion and backward erosion. Journal of Geotechnical and Geoenvironmental Engineering, **134**(1): 57–67. doi: 10.1061/(ASCE)1090-0241(2008)134:1(57). (page 12).

Bobei, D., Lo, D., S.R.and Wanatowski, Gnanendran, C., and Rahman, M. 2009. Modified state parameter for characterizing static liquefaction of sand with fines. Canadian Geotechnical Journal, **46**(3): 281–295. doi: 10.1139/T08-122. (pages 50, 51).

Bolton, M. 1986. The strength and dilatancy of sands. Géotechnique, **36**(1): 65–78. doi: 10.1680/geot.1986.36.1.65. (page 48).

Bonelli, S. 2012. Erosion of geomaterials. John Wiley & Sons. (page 53).

Bonelli, S. and Marot, D. 2011. Micromechanical modeling of internal erosion. European Journal of Environmental and Civil Engineering, **15**(8): 1207–1224. doi: 10.1080/19648189.2011.9714849. (page 6).

Bradski, G. 2000. The opencv library. Doctor Dobb‘s Journal, **25**(11): 120–126. (pages 84, 110).

Carraro, J., Prezzi, M., and Salgado, R. 2009. Shear strength and stiffness of sands containing plastic or nonplastic fines. Journal of Geotechnical and Geoenvironmental Engineering, **135**(9): 1167–1178. doi: 10.1061/(ASCE)1090-0241(2009)135:9(1167). (page 47).

Chang, C. and Meidani, M. 2013. Dominant grains network and behavior of sandsilt mixtures: stressstrain modeling. International Journal for Numerical and Analytical Methods in Geomechanics, **37**(15): 2563–2589. doi: 10.1002/nag.2152. (pages 50, 51).

Chang, D. and Zhang, L. 2013a. Critical hydraulic gradients of internal erosion under complex stress states. Journal of Geotechnical and Geoenvironmental Engineering, **139**(9): 1454–1467. doi: 10.1061/(ASCE)GT.1943-5606.0000871. (pages 13, 93).

Chang, D. and Zhang, L. 2011. A stress-controlled erosion apparatus for studying internal erosion in soils. Geotechnical Testing Journal, **34**(6): 1–11. doi: 10.1520/GTJ103889. (pages 5, 13, 39, 99, 132).

Chang, D. and Zhang, L. 2013b. Extended internal stability criteria for soils under seepage. Soils and Foundations, **53**(4): 569–583. doi: 10.1016/j.sandf.2013.06.008. (page 10).

Chang, D., Zhang, L., Xu, Y., and Huang, R. 2011. Field testing of erodibility of two landslide dams triggered by the 12 May Wenchuan earthquake. Landslides, **8**(3): 321–332. doi: 10.1007/s10346-011-0256-x. (page 13).

Chapuis, R., Contant, A., and Baass, K. 1996. Migration of fines in 0-20 mm crushed base during placement, compaction, and seepage under laboratory conditions. Canadian Geotechnical Journal, **33**(1): 168–176. doi: 10.1139/t96-032. (page 15).

Cividini, A. and Gioda, G. 2004. Finite-Element approach to the erosion and transport of fine particles in granular soils. International Journal of Geomechanics, **4**(3): 191–198. doi: 10.1061/(ASCE)1532-3641(2004)4:3(191). (page 27).

Cividini, A., Bonomi, S., Vignati, G., and Gioda, G. 2009. Seepage induced erosion in granular soil and consequent settlements. International Journal of Geomechanics, **9**(4): 187–194. doi: 10.1061/(ASCE)1532-3641(2009)9:4(187). (pages 6, 27).

Correia Dos Santos, R., Caldeira, L., and Maranha Das Neves, E. 2015. Experimental study on crack filling by upstream fills in dams. Géotechnique, **65**(3): 218–230. doi: 10.1680/geot.14.P.198. (pages 6, 83).

Curray, J. 1956. The analysis of two-dimensional orientation data. Journal of Geology, **64**(2): 117–131. (page 97).

Cyril, G., Yves-Henri, F., Rémi, B., and Chia-Chun, H. 2010. Contact erosion at the interface between granular coarse soil and various base soils under tangential flow condition. Journal of Geotechnical and Geoenvironmental Engineering, **136**(5): 741–750. doi: 10.1061/(ASCE)GT.1943-5606.0000268. (page 16).

Dallo, Y., Wang, Y., and Ahmed, O. 2013. Assessment of the internal instability of granular soils against suffusion. European Journal of Environmental and Civil Engineering, **17**(4): 219–230. (page 185).

Desrues, J., Chambon, R., Mokni, M., and Mazerolle, F. 1996. Void ratio evolution inside shear bands in triaxial sand specimens studied by computed tomography. Géotechnique, **46**(3): 529–546. doi: 10.1680/geot.1996.46.3.529. (page 44).

Doan, D., Delage, P., Nauroy, J., Tang, A., and Youssef, S. 2012. Microstructural characterization of a canadian oil sand. Canadian Geotechnical Journal, **49**(10): 1212–1220. doi: 10.1139/t2012-072. (page 43).

Evancs, J. and H.Y., F. 1988. Triaxial permeability and strength testing of contaminated soils. In Donaghe, R.T., Chaney, R.C. and Silver, M.L., (eds). Advanced triaxial testing of soil and rock, ASTM STP 977: 387-404. American Society for Testing and Materials, Philadelphia. (page 61).

Fannin, J. 2008. Karl Terzaghi: From theory to practice in geotechnical filter design. Journal of Geotechnical and Geoenvironmental Engineering, **134**(3): 267–276. doi: 10.1061/(ASCE) 1090-0241(2008)134:3(267). (pages 5, 30).

Fannin, R. and Moffat, R. 2006. Observations on internal stability of cohesionless soils. Géotechnique, **56**(7): 497–500. doi: 10.1680/geot.2006.56.7.497. (page 16).

Fannin, R. and Slangen, P. 2014. On the distinct phenomena of suffusion and suffosion. Géotechnique Letters, **4**(4): 289–294. doi: 10.1680/geolett.14.00051. (page 17).

Fannin, R., Slangen, P., Mehdizadeh, A., Disfani, M., Arulrajah, A., and Evans, R. 2015. Discussion: On the distinct phenomena of suffusion and suffosion. Géotechnique Letters, **5**(3): 129–130. doi: 10.1680/jgele.15.00017. (page 17).

Fell, R., Wan, C., Cyganiewicz, J., and Foster, M. 2003. Time for development of internal erosion and piping in embankment dams. Journal of Geotechnical and Geoenvironmental Engineering, **129**(4): 307–314. doi: 10.1061/(ASCE)1090-0241(2003)129:4(307). (pages 5, 17).

Fleshman, M. and Rice, J. 2014. Laboratory modeling of the mechanisms of piping erosion initiation. Journal of Geotechnical and Geoenvironmental Engineering, **140**(6): 04014017. doi: 10.1061/(ASCE)GT.1943-5606.0001106. (page 18).

Fleshman, M. and Rice, J. 2013. Constant gradient piping test apparatus for evaluation of critical hydraulic conditions for the initiation of piping. Geotechnical Testing Journal, **36**(6): 20130066. doi: 10.1520/GTJ20130066. (page 37).

Foster, M. and Fell, R. 2001. Assessing embankment dam filters that do not satisfy design criteria. Journal of Geotechnical and Geoenvironmental Engineering, **127**(5): 398–407. doi: 10.1061/(ASCE)1090-0241(2001)127:5(398). (pages ix, 6, 33, 35).

Foster, M., Fell, R., and Spannagle, M. 2000. The statistics of embankment dam failures and accidents. Canadian Geotechnical Journal, **37**(5): 1000–1024. doi: 10.1139/t00-030. (pages 1, 5).

Frost, J. and Kuo, C. 1996. Automated determination of the distribution of local void ratio from digital images. Geotechnical Testing Journal, **19**(2): 107–117. doi: 10.1520/GTJ10334J. (page 42).

Hameiri, A. and Fannin, R. 2002. A cyclic gradient ratio test device. Geotechnical Testing Journal, **25**(3): 9921. doi: 10.1520/GTJ11097J. (page 37).

Heikkila, J. and Silven, O. 1993. A four-step camera calibration procedure with implicit image correlation. Journal of Geotechnical Engineering, **119**(1): 36–53. doi: 10.1061/(ASCE) 0733-9410(1993)119:1(36). (pages 45, 110).

Hicher, P. 2013. Modelling the impact of particle removal on granular material behaviour. Géotechnique, **63**(2): 118–128. doi: 10.1680/geot.11.P.020. (pages 6, 26).

Horikoshi, K. and Takahashi, A. 2015a. Effects of redeposition of fines on seepage-induced fines transport in embankments. Japanese Geotechnical Journal, **10**(4): 473–488. doi: 10.3208/jgs.10. 473. (page 83).

Horikoshi, K. and Takahashi, A. 2015b. Suffusion-induced change in spatial distribution of fine fractions in embankment subjected to seepage flow. Soils and Foundations, **55**(5): 1294–1305. doi: 01.1016/j.sandf.2015.09.027. (pages ix, 5, 20, 21, 95, 129, 131, 132).

Humes, A. A new approach to compute the void size distribution curves of protective filters. In Lafleur, J. and Rollin, A., editors, *Proceedings of Geofilters'96*, pages 57–66, Richmond, B.C., 1996. Bitech Publications. (page 187).

Indraratna, B. and Raut, A. 2006. Enhanced criterion for base soil retention in embankment dam filters. Journal of Geotechnical and Geoenvironmental Engineering, **132**(12): 1621–1627. doi: 10.1061/(ASCE)1090-0241(2006)132:12(1621). (page 10).

Indraratna, B. and Vafai, F. 1997. Analytical model for particle migration within base soil-filter system. Journal of Geotechnical and Geoenvironmental Engineering, **123**(2): 100–109. doi: 10.1061/(ASCE)1090-0241(1997)123:2(100). (page 10).

Indraratna, B., Raut, A., and Khabbaz, H. 2007. Constriction-based retention criterion for granular filter design. Journal of Geotechnical and Geoenvironmental Engineering, **133**(3): 266–276. doi: 10.1061/(ASCE)1090-0241(2007)133:3(266). (pages 6, 11, 187).

Indraratna, B., Trani, L., and Khabbaz, H. 2008. A critical review on granular dam filter behaviour from particle sizes to constriction-based design criteria. Geomechanics and Geoengineering, **3** (4): 279–290. doi: 10.1080/17486020802406632. (pages 11, 187).

Indraratna, B., Nguyen, V., and Rujikiatkamjorn, C. 2011. Assessing the potential of internal erosion and suffusion of granular soils. Journal of Geotechnical and Geoenvironmental Engineering, **137** (5): 550–554. doi: 10.1061/(ASCE)GT.1943-5606.0000447. (pages 11, 184, 186, 187).

Indraratna, B., Nguyen, V., and Rujikiatkamjorn, C. 2012. Hydraulic conductivity of saturated granular soils determined using a constriction-based technique. Canadian Geotechnical Journal, **49**(5): 607–613. doi: 10.1139/t2012-016. (page 11).

Indraratna, B., Israr, J., and Rujikiatkamjorn, C. 2015. Geometrical method for evaluating the internal instability of granular filters based on constriction size distribution. Journal of Geotechnical and Geoenvironmental Engineering, **141**(10): 04015045. doi: 10.1061/(ASCE)GT.1943-5606.0001343. (page 11).

Ishihara, K. 1993. Liquefaction and flow failure during earthquakes. Géotechnique, **43**(3): 351–451. doi: 10.1680/geot.1993.43.3.351. (pages 5, 49, 68, 70, 72).

Ishihara, K., Tatsuoka, F., and Yasuda, S. 1975. Undrained deformation and liquefaction of sand under cyclic stresses. Soils and Foundations, **15**(1): 29–44. doi: 10.3208/sandf1972.15.29. (pages 49, 76).

JGS. 2000. Method for k0 consolidated-undrained triaxial compression test on soils with pore water pressure measurement. JGS standard 0525-2000. *In* Standards of Japanese Geotechnical Society for laboratory shear tests. Japanese Geotechnical Society. pp. 28-34. (pages 58, 59).

Jiang, M., Konrad, J., and Leroueil, S. 2003. An efficient technique for generating homogeneous specimens for dem studies. Computers and Geotechnics, **30**(7): 579–597. doi: 10.1016/S0266-352X(03)00064-8. (pages 58, 123).

Ke, L. and Takahashi, A. 2012. Strength reduction of cohesionless soil due to internal erosion induced by one-dimensional upward seepage flow. Soils and Foundations, **52**(4): 698–711. doi: 10.1016/j.sandf.2012.07.010. (page 19).

Ke, L. and Takahashi, A. 2014a. Experimental investigations on suffusion characteristics and its mechanical consequences on saturated cohesionless soil. Soils and Foundations, **54**(4): 713–730. doi: 10.1016/j.sandf.2014.06.024. (pages 6, 20, 95).

Ke, L. and Takahashi, A. 2014b. Triaxial erosion test for evaluation of mechanical consequences of internal erosion. Geotechnical Testing Journal, **37**(2): 1–18. doi: 10.1520/GTJ20130049. (pages 5, 20, 39, 55, 59, 99, 100, 119, 120, 132).

Ke, L. and Takahashi, A. 2015. Drained monotonic responses of suffusional cohesionless soils. Journal of Geotechnical and Geoenvironmental Engineering, **141**(8): 04015033. doi: 10.1061/(ASCE)GT.1943-5606.0001327. (pages ix, 6, 14, 15).

Kenney, T. and Lau, D. 1985. Internal stability of granular filters. Canadian Geotechnical Journal, **22**(2): 215–225. doi: 10.1139/t85-029. (pages ix, 6, 8, 9, 26, 31, 32, 59, 92, 131, 184, 186, 187).

Kenney, T., Chahal, R., Chiu, E., Ofoegbu, G., Omange, G., and Ume, C. 1985. Controlling constriction sizes of granular filters. Canadian Geotechnical Journal, **22**(1): 32–43. doi: 10.1139/t85-005. (pages ix, 6, 7, 32, 34, 151, 187).

Kezdi, A. 1979. Soil physics: selected topics. Elsevier. (pages 9, 187).

Kovacs, G. 1981. Seepage hydraulics. Elservier. (pages 9, 61).

Kuo, C. and Frost, J. 1996. Uniformity evaluation of cohesionless specimens using digital image analysis. Journal of Geotechnical Engineering, **122**(5): 390–396. doi: 10.1061/(ASCE)0733-9410(1996)122:5(390). (page 42).

Kuo, C., Frost, J., and Chameau, J. 1998. Image analysis determination of stereology based fabric tensors. Géotechnique, **48**(4): 515–525. doi: 10.1680/geot.1998.48.4.515. (page 43).

Ladd, R. 1978. Preparing test specimens using undercompaction. Geotechnical Testing Journal, **1**(1): 16–23. doi: 10.1520/GTJ10364J. (page 58).

Lafleur, J., Mlynarek, J., and Rollin, A. 1989. Filtration of broadly graded cohesionless soils. Journal of Geotechnical Engineering, **115**(12): 1747–1768. doi: 10.1061/(ASCE)0733-9410(1989)115:12(1747). (page 6).

Lee, J., Salgado, R., and Carraro, J. 2004. Stiffness degradation and shear strength of silty sands. Canadian Geotechnical Journal, **41**(5): 831–843. doi: 10.1139/t04-034. (page 47).

Leong, W. and Chu, J. 2002. Effect of undrained creep on instability behaviour of loose sand. Canadian Geotechnical Journal, **39**(6): 1399–1405. doi: 10.1139/t02-076. (pages 50, 80).

Li, M. and Fannin, R. 2013. Capillary tube model for internal stability of cohesionless soil. Journal of Geotechnical and Geoenvironmental Engineering, **139**(5): 831–834. doi: 10.1061/(ASCE)GT.1943-5606.0000790. (page 9).

Li, M. and Fannin, R. 2008. Comparison of two criteria for internal stability of granular soil. Canadian Geotechnical Journal, **45**(9): 1303–1309. doi: 10.1139/T08-046. (page 8).

Li, M. and Fannin, R. 2012. A theoretical envelope for internal instability of cohesionless soil. Géotechnique, **62**(1): 77–80. doi: 10.1680/geot.10.T.019. (page 9).

Locke, M., Indraratna, B., and Adikari, G. 2001. Time-dependent particle transport through granular filters. Journal of Geotechnical and Geoenvironmental Engineering, **127**(6): 521–529. (page 187).

Lone, M., Hussain, B., and Asawa, G. 2005. Filter design criteria for graded cohesionless bases. Journal of Geotechnical and Geoenvironmental Engineering, **131**(2): 251–259. doi: 10.1061/(ASCE)1090-0241(2005)131:2(251). (page 12).

Marot, D., Bendahmane, F., and Konrad, J. 2011a. Multichannel optical sensor to quantify particle stability under seepage flow. Canadian Geotechnical Journal, **48**(12): 1772–1787. doi: 10.1139/t11-074. (page 23).

Marot, D., Regazzoni, P., and Wahl, T. 2011b. Energy-based method for providing soil surface erodibility rankings. Journal of Geotechnical and Geoenvironmental Engineering, **137**(12): 1290–1293. doi: 10.1061/(ASCE)GT.1943-5606.0000538. (page 23).

Mitechell, J. and Soga, K. 2005. Fundamentals of soil behavior. Wiley, New York. (page 83).

Moffat, R. and Fannin, R. 2006. A large permeameter for study of internal stability in cohesionless soils. Geotechnical Testing Journal, **29**(4): 100021. doi: 10.1520/GTJ100021. (pages 38, 99).

Moffat, R. and Fannin, R. 2011. A hydromechanical relation governing internal stability of cohesionless soil. Canadian Geotechnical Journal, **48**(3): 413–424. doi: 10.1139/T10-070. (pages ix, 21, 22).

Moffat, R. and Herrera, P. 2014. Hydromechanical model for internal erosion and its relationship with the stress transmitted by the finer soil fraction. Acta Geotechnica, **10**(5): 643–650. doi: 10.1007/s11440-014-0326-z. (page 9).

Moffat, R., Fannin, R., and Garner, S. 2011. Spatial and temporal progression of internal erosion in cohesionless soil. Canadian Geotechnical Journal, **48**(3): 399–412. doi: 10.1139/T10-071. (pages 6, 21, 95, 132).

Moraci, N., Mandaglio, M., and Ielo, D. 2012. A new theoretical method to evaluate the internal stability of granular soils. Canadian Geotechnical Journal, **49**(1): 45–58. doi: 10.1139/t11-083. (page 12).

Moraci, N., Mandaglio, M., and Ielo, D. 2014. Analysis of the internal stability of granular soils using different methods. Canadian Geotechnical Journal, **51**(9): 1063–1072. doi: 10.1139/cgj-2014-0006. (page 12).

Muir Wood, D. 1990. Soil behaviour and critical state soil mechanics. Cambridge University Press. (pages ix, 53, 54).

Muir Wood, D. 2007. The magic of sands – the 20th bjerrum lecture presented in oslo, 25 november 2005. Canadian Geotechnical Journal, **44**(11): 1329–1350. doi: 10.1139/T07-060. (pages 1, 77).

Muir Wood, D. and Maeda, K. 2008. Changing grading of soil: effect on critical state. Acta Geotechnica, **3**(1): 3–14. doi: 10.1007/s11440-007-0041-0. (pages 77, 78).

Muir Wood, D., Maeda, K., and Nukudani, E. 2010. Modelling mechanical consequences of erosion. Géotechnique, **60**(6): 447–457. doi: 10.1680/geot.2010.60.6.447. (pages 28, 77, 78).

Murthy, T., Loukidis, D., Carroro, J., Prezzi, M., and Salgoda, R. 2007. Undrained monotonic response of clean and silty sands. Géotechnique, **57**(3): 273–288. doi: 10.1680/geot.2007.57.3.273. (pages 5, 50, 51, 77, 78).

Najafi, E. K. and Eslami, A. 2015. Assessment of the likelihood of suffusion in alluvial soils: case history. Bulletin of Engineering Geology and the Environment, **74**(2): 611–620. doi: 10.1007/s10064-014-0681-x. (page 19).

Ni, Q., Tan, T., Dasari, G., and Hight, D. 2004. Contribution of fines to the compressive strength of mixed sands. Géotechnique, **54**(9): 561–569. doi: 10.1680/geot.2004.54.9.561. (pages 5, 50).

Oda, M. 1972. Initial fabrics and their relations to mechanical properties of granular material. Soils and Foundations, **12**(1): 17–36. doi: 10.3208/sandf1960.12.17. (page 42).

Ouyang, M. and Takahashi, A. 2015. Optical quantification of suffosion in plane strain physical models. Gèotechnique Letters, **5**(3): 118–122. doi: 10.1680/jgele.15.00038. (page 187).

Ouyang, M. and Takahashi, A. 2016a. Influence of initial fines content on fabric of soils subjected to internal erosion. Canadian Geotechnical Journal, **53**(2): 299–313. doi: 10.1139/cgj-2014-0344. (pages 183, 187).

Ouyang, M. and Takahashi, A. 2016b. Reply to the discussion by Ahmad ALsakran et al. on "Influence of initial fines content on fabric of soils subjected to internal erosion". Canadian Geotechnical Journal, **53**(8): 1360–1361. doi: 10.1139/cgj-2016-0131. (page 186).

Planés, T., Mooney, M., Rittgers, J., Parekh, M., Behm, M., and Snieder, R. 2016. Time-lapse monitoring of internal erosion in earthen dams and levees using ambient seismic noise. Géotechnique, **66**(4): 301–312. doi: 10.1680/jgeot.14.P.268. (page 6).

Rahman, M., Lo, S., and Gnanendran, C. 2008. On equivalent granular void ratio and steady state behaviour of loose sand with fines. Canadian Geotechnical Journal, **45**(10): 1439–1456. doi: 10.1139/T08-064. (pages 50, 51).

Rahman, M., Lo, S., and Baki, M. 2011. Equivalent granular state parameter and undrained behaviour of sand-fines mixtures. Acta Geotechnica, **6**(4): 183–194. doi: 10.1007/s11440-011-0145-4. (pages 50, 51).

Reboul, N., Vincens, E., and Cambou, B. 2010. A computational procedure to assess the distribution of constriction sizes for an assembly of spheres. Computers and Geotechnics, **37**(12): 195–206. doi: 10.1016/j.compgeo.2009.09.002. (page 12).

Reddi, L., Lee, I., and Bonala, M. 2000. Comparison of internal and surface erosion using flow pump tests on a sand-kaolinite mixture. Geotechnical Testing Journal, **23**(1): 116. doi: 10.1520/GTJ11129J. (pages 38, 99).

Reinson, J., Fredlund, D., and Wilson, G. 2005. Unsaturated flow in coarse porous media. Canadian Geotechnical Journal, **42**(1): 252–262. doi: 10.1139/t04-070. (page 44).

Richards, K. and Reddy, K. 2007. Critical appraisal of piping phenomena in earth dams. Bulletin of Engineering Geology and the Environment, **66**(4): 381–402. doi: 10.1007/s10064-007-0095-0. (pages 1, 24).

Richards, K. and Reddy, K. 2010. True triaxial piping test apparatus for evaluation of piping potential in earth structures. Geotechnical Testing Journal, **33**(1): 102246. doi: 10.1520/GTJ102246. (pages 38, 59, 99, 106, 129).

Richards, K. and Reddy, K. 2012. Experimental investigation of initiation of backward erosion piping in soils. Géotechnique, **62**(10): 933–942. doi: 10.1680/geot.11.P.058. (pages 6, 24).

Roscoe, K., Schofield, A., and Wroth, C. 1958. On the yielding of soils. Géotechnique, **8**(1): 22–53. doi: 10.1680/geot.1958.8.1.22. (page 77).

Rosenbrand, E. and Dijkstra, J. 2012. Application of image subtraction data to quantify suffusion. Géotechnique Letters, **2**(2): 37–41. doi: 10.1680/geolett.12.00006. (pages 5, 46, 83, 95, 132).

Salgado, R., Bandini, P., and Karim, A. 2000. Shear strength and stiffness of silty sand. Journal of Geotechnical and Geoenvironmental Engineering, **126**(5): 451–462. doi: 10.1061/(ASCE)1090-0241(2000)126:5(451). (pages 47, 143).

Scholtès, L., Hicher, P., and Sibille, L. 2010. Multiscale approaches to describe mechanical responses induced by particle removal in granular materials. Comptes Rendus Mécanique, **338**(1011): 627–638. doi: 10.1016/j.crme.2010.10.003. (page 28).

Seghir, A., Benamar, A., and Wang, H. 2014. Effects of fine particles on the suffusion of cohesionless soils. Experiments and modeling. Transport in Porous Media, **103**(2): 233–247. doi: 10.1007/s11242-014-0299-2. (page 19).

Sherard, J. and Dunnigan, L. 1989. Critical filters for impervious soils. Journal of Geotechnical Engineering, **115**(7): 927–947. doi: 10.1061/(ASCE)0733-9410(1989)115:7(927). (page 6).

Sherard, J., Dunnigan, L., and Talbot, J. 1984. Basic properties of sand and gravel filters. Journal of Geotechnical Engineering, **110**(6): 684–700. doi: 10.1061/(ASCE)0733-9410(1984)110:6(684). (page 6).

Shimizu, Y. 2011. Microscopic numerical model of fluid flow in granular material. Géotechnique, **61**(10): 887–896. doi: 10.1680/geot.8.P.102. (page 29).

Shire, T. and O'Sullivan, C. 2013. Micromechanical assessment of an internal stability criterion. Acta Geotechnica, **8**(1): 81–90. doi: 10.1007/s11440-012-0176-5. (pages 6, 8).

Sibille, L., Lominé, F., Poullain, P., Sail, Y., and Marot, D. 2015a. Internal erosion in granular media: direct numerical simulations and energy interpretation. Hydrological Processes, **29**(9): 2149–2163. doi: 10.1002/hyp.10351. (pages 6, 28).

Sibille, L., Marot, D., and Sail, Y. 2015b. A description of internal erosion by suffusion and induced settlements on cohesionless granular matter. Acta Geotechnica, **10**(6): 735–748. doi: 10.1007/s11440-015-0388-6. (pages 5, 22).

Silveira, A. An analysis of the problem of washing through in protective filters. In *Proceedings of the 6th International Conference on Soil Mechanics and Foundation Engineering*, pages 551–555, Montrèal, Que., 1965. (pages 185, 186, 187).

Silveira, A., de Lorena Peixoto, T., and Nogueira, J. On void size distribution of granular materials. In *Proceedings of the 5th Pan American Conference on Soil Mechanics and Foundation Engineering*, pages 161–171, Buenous Aires, 1975. (pages 185, 186, 187).

Skempton, A. and Brogan, J. 1994. Experiments on piping in sandy gravels. Géotechnique, **44**(3): 449–460. doi: 10.1680/geot.1994.44.3.449. (pages 5, 10, 18, 20, 30, 33, 93, 99, 140).

Sladen, J., D'Hollander, R., and Krahn, J. 1985. The liquefaction of sands, a collapse surface approach. Canadian Geotechnical Journal, **22**(4): 564–578. doi: 10.1139/t85-076. (pages 49, 72, 77, 145).

Sterpi, D. 2003. Effects of the erosion and transport of fine particles due to seepage flow. International Journal of Geomechanics, **3**(1): 111–122. doi: 10.1061/(ASCE)1532-3641(2003)3:1(111). (pages 6, 27).

Takahashi, A. 2016. Closure to Drained monotonic responses of suffusional cohesionless soils by Lin Ke and Akihiro Takahashi. Journal of Geotechnical and Geoenvironmental Engineering, **142** (5): 07016006. doi: 10.1061/(ASCE)GT.1943-5606.0001470. (pages 5, 83, 131, 145, 187).

Take, W. 2015. Thirty-sixth canadian geotechnical colloquium: Advances in visualization of geotechnical processes through digital image correlation. Canadian Geotechnical Journal, **52**(9): 1199–1220. doi: 10.1139/cgj-2014-0080. (pages 5, 44).

Taylor, H., OSullivan, C., and Sim, W. 2015. A new method to identify void constrictions in micro-CT images of sand. Computers and Geotechnics, **69**: 279–290. doi: 10.1016/j.compgeo.2015.05.012. (pages 6, 12).

Thevanayagam, S. and Mohan, S. 2000. Intergranular state variables and stress-strain behaviour of silty sands. Géotechnique, **50**(1): 1–23. doi: 10.1680/geot.2000.50.1.1. (pages 50, 51).

Thevanayagam, S., Shenthan, T., Mohan, S., and Liang, J. 2002. Undrained fragility of clean sands, silty sands, and sandy silts. Journal of Geotechnical and Geoenvironmental Engineering, **128** (10): 849–859. doi: 10.1061/(ASCE)1090-0241(2002)128:10(849). (pages 50, 51, 184, 187).

To, H., Scheuermann, A., and Calinda-Torres, S. 2016. Probability of transportation of loose particles in suffusion assessment by self-filtration criteria. Journal of Geotechnical and Geoenvironmental Engineering, **142**(2): 04015078. doi: 10.1061/(ASCE)GT.1943-566.0001403. (page 12).

Tomlinson, S. and Vaid, Y. 2000. Seepage forces and confining pressure effects on piping erosion. Canadian Geotechnical Journal, **37**(1): 1–13. doi: 10.1139/t99-116. (pages 36, 95, 99, 129, 131).

Tovey, N. and Dadey, K. 2002. Quantitative orientation and micro-porosity analysis of recent marine sediment microfabric. Quaternary International, **92**(1): 89–100. doi: 10.1016/S1040-6182(01)00117-3. (page 43).

Tovey, N., Krinsley, D., Dent, D., and Corbett, W. 1992. Techniques to quantitatively study the microfabric of soils. Geoderma, **53**(3): 217–235. doi: 10.1016/0016-7061(92)90056-D. (page 42).

Tsukamoto, Y., Ishihara, K., and Kamata, T. 2009. Undrained shear strength of soils under flow deformation. Géotechnique, **59**(5): 483–486. doi: 10.1680/geot.2007.00043. (pages ix, 49, 53, 54).

USDA. 1994. Gradation design of sand and gravel filters, *In* National engineering handbook, Part 33, Chapter 26. Soil Conservation Service, U.S. Department of Agriculture (USDA), Washington, D.C. (pages 58, 101).

Vaid, Y., Chung, E., and Kuerbis, R. 1990. Stress path and steady state. Canadian Geotechnical Journal, **21**(1): 1–7. doi: 10.1139/t90-001. (page 49).

Vardoulakis, I. 2004. Fluidisation in artesian flow conditions: Hydromechanically unstable granular media. Géotechnique, **54**(3): 165–177. doi: 10.1680/geot.2004.54.3.165. (page 29).

Vaughan, P. Criteria for the use of weak and weathered rock for embankment fill and its compaction control. In *Proceedings of 13th International Conference, Soil Mechanics and Foundation Engineering*, pages 195–206, New Delhi, India, 1994. (page 183).

Vincens, E., Witt, K., and Homberg, U. 2015. Approaches to determine the constriction size distribution for understanding filtration phenomena in granular materials. Acta Geotechnica, **10** (3): 291–303. doi: 10.1007/s11440-014-0308-1. (page 7).

Wan, C. and Fell, R. 2004a. Investigation of rate of erosion of soils in embankment dams. Journal of Geotechnical and Geoenvironmental Engineering, **130**(4): 373–380. doi: 10.1061/(ASCE) 1090-0241(2004)130:4(373). (page 25).

Wan, C. and Fell, R. 2004b. Laboratory tests on the rate of piping erosion of soils in embankment dams. Geotechnical Testing Journal, **27**(3): 1–9. doi: 10.1520/GTJ11903. (pages ix, 35, 36, 37, 99).

Wan, C. and Fell, R. 2008. Assessing the potential of internal instability and suffusion in embankment dams and their foundations. Journal of Geotechnical and Geoenvironmental Engineering, **134**(3): 401–407. doi: 10.1061/(ASCE)1090-0241(2008)134:3(401). (pages 6, 8).

Wanatowski, D. and Chu, J. 2006. Stress-strain behavior of a granular fill measured by a new plane-strain apparatus. Geotechnical Testing Journal, **29**(2): 1–9. doi: 10.1520/GTJ12621. (pages 40, 101, 119, 187).

Wang, Y. and Ng, C. 2005. Effects of stress paths on the small-strain stiffness of completely decomposed granite. Canadian Geotechnical Journal, **42**(4): 1200–1211. doi: 10.1139/t05-009. (page 47).

White, D., Take, W., and Bolton, M. 2003. Soil deformation measurement using particle image velocimetry (piv) and photogrammetry. Géotechnique, **53**(7): 619–631. doi: 10.1680/geot.2003.53.7.619. (pages 5, 45).

Xiao, M. and Shwiyhat, N. 2012. Experimental investigation of the effects of suffusion on physical and geomechanic characteristics of sandy soils. Geotechnical Testing Journal, **35**(6): 104594. doi: 10.1520/GTJ104594. (pages 23, 39, 99).

Xu, Y., Zhang, L., and Jia, J. 2011. Diagnosis of embankment dam distresses using Bayesian networks. Part II. Diagnosis of a specific distressed dam. Canadian Geotechnical Journal, **48**(11): 1645–1657. doi: 10.1139/t11-070. (page 25).

Yamamuro, J. and Covert, K. 2001. Monotonic and cyclic liquefaction of very loose sands with high silt content. Journal of Geotechnical and Geoenvironmental Engineering, **127**(4): 314–324. doi: 10.1061/(ASCE)1090-0241(2001)127:4(314). (pages 5, 50, 140).

Yamamuro, J. and Lade, P. 1998. Steady-state concepts and static liquefaction of silty sands. Journal of Geotechnical and Geoenvironmental Engineering, **124**(9): 868–877. doi: 10.1061/(ASCE)1090-0241(1998)124:9(868). (page 50).

Yang, J. and Liu, X. 2016. Shear wave velocity and stiffness of sand: the role of non-plastic fines. Gèotechnique, **66**(6): 500–514. doi: 10.1680/jgeot.15.P.205. (page 144).

Yang, J. and Wei, L. 2012. Collapse of loose sand with the addition of fines: the role of particle shape. Géotechnique, **62**(12): 1111–1125. doi: 10.1680/geot.11.P.062. (pages 50, 52).

Yang, J., Wei, L., and Dai, B. 2015. State variables for silty sands: Global void ratio or skeleton void ratio? Soils and Foundations, **55**(1): 99–111. doi: 10.1016/j.sandf.2014.12.008. (pages 50, 51).

Yang, S., Sandven, R., and Crande, L. 2006a. Instability of sand-silt mixtures. Soil Dynamics and Earthquake Engineering, **26**(2-4): 183–190. doi: 10.1016/j.soildyn.2004.11.027. (pages 50, 51, 80).

Yang, S., Sandven, R., and Grande, L. 2006b. Steady-state lines of sand-silt mixtures. Canadian Geotechnical Journal, **43**(11): 1213–1219. doi: 10.1139/t06-069. (pages 50, 51, 74).

Yang, Z., Li, X., and Yang, Y. 2008. Quantifying and modelling fabric anisotropy of granular soils. Géotechnique, **58**(4): 237–248. doi: 10.1680/geot.2008.58.4.237. (pages 43, 97, 145).

Yoshimine, M. and Ishihara, K. 1998. Flow potential of sand during liquefaction. Soils and Foundations, **38**(3): 189–198. doi: 10.3208/sandf.38.3_189. (pages 50, 68, 76).

Zhang, L. and Chen, Q. 2006. Seepage failure mechanism of the Gouhou rockfill dam during reservoir water infiltration. Soils and Foundations, **46**(5): 557–568. doi: 10.3208/sandf.46.557. (page 26).

Zhang, L., Xu, Y., and Jia, J. 2009. Analysis of earth dam failures: A database approach. Georisk: Assessment and Management of Risk for Engineered Systems and Geohazards, **3**(3): 184–189. doi: 10.1080/17499510902831759. (page 25).

Zhang, L., Xu, Y., Jia, J., and Zhao, C. 2011. Diagnosis of embankment dam distresses using Bayesian networks. Part I. Global-level characteristics based on a dam distress database. Canadian Geotechnical Journal, **48**(11): 1630–1644. doi: 10.1139/t11-069. (page 25).

Zlatovic, S. and Ishihara, K. 1997. Normalized behavior of very loose non-plastic soils: effects of fabric. Soils and Foundations, **37**(4): 47–56. doi: 10.3208/sandf.37.4_47. (pages 50, 78, 149).

Appendix A

Discussion on "Influence of initial fines content on fabric of soils subjected on internal erosion"

The discussion was written by ALsakran et al. (2016).

The authors have presented a good paper related to the internal stability investigation of gap-graded soils (Ouyang and Takahashi, 2016a). Coarse-grained silica (No. 3) and fine-grained silica (No. 8) were mixed to obtained mixtures with 15%, 25%, and 35% fine grains. The discussers present herein some simple notes related to the mixtures and calculating the skeleton void ratio presented in Table 2 (in the paper under discussion).

The authors stated that "it could be assumed that the effective stresses are mainly transferred by the coarse fractions." his inherently means that the soil mixtures have "bimodal soil structures," where the soil has a main soil skeleton composed of coarser particles (silica No. 3), which transfer most of the effective stresses, and among the voids of these particles there are fine loose particles (silica No. 8) under low or no effective stresses. Such a structure is termed a "clast-supported structure". If the fine grain content is increased beyond a certain level, the coarser particles would lose their contacts among each other, resulting in what is termed a "matrix-supported structure". In other words, in a clast-supported structure there is a shortage of fines, while in a matrix-supported structure there is an excess of fines (Vaughan, 1994). The soil has a clast-supported structure if the fines content, Fc, is less than the maximum value of fines content, FC_{max}.

$$FC_{max} = \frac{W_{l,max}}{W_{l,max} + W_c} \tag{A.1}$$

where W_c is the weigh of the primary skeleton grains and $W_{l,max}$ is the maximum weight of fine soil grains that fill the voids of the main soil skeleton (Indraratna et al., 2011).

$$W_{l,max} = \frac{e_x}{1+e_l} W_c \tag{A.2}$$

where e_x and e_l are the void ratios of the primary skeleton and loose finer particles, respectively.

From eqs. A.1 and A.2, we have found that FC_{max} = 27.4%. Accordingly, the mixtures with Fc = 15% and 25% ($<FC_{max}$) have clast-supported structures and have undergone suffusion, while soil samples with Fc = 35% ($>FC_{max}$) have matrix-supported structures and some portion of the effective stresses is transferred by the fine-grained soils, and this mixture has undergone piping. Suffusion is quite different from piping, so the internal erosion results of mixtures with Fc = 15% and 25% should not be compared with those of Fc = 35%.

Also, it should be pointed out that the method of Kenney and Lau (1985), used by the authors, is not applicable for matrix-supported structures such as the mixture with FC = 35%.

Soil mixtures with FC = 35%, which is larger than FC_{max}, bring rise to another discussion on the calculation of skeleton void ratio (see the relations in the footnote of Table 2 in the paper under discussion). Actually, those relations are applicable for cases where the value of FC is less than the threshold boundary, FC_{th} (Thevanayagam et al., 2002).

$$FC_{th} \leq \frac{100e_s}{1+e_s+e_{max,HF}}\% = \frac{100e}{e_{max,HF}}\% \tag{A.3}$$

where e_s is the skeleton void ratio, e is the global void ratio, and $e_{max,HF}$ is the maximum void ratio of fine grains. For the soils tested by the authors we have found that FC_{th} = 25.5%, which is close to the value obtained from eqs. A.1 and A.2. Accordingly, the skeleton void ratio, e_s , of a mixture with FC = 35% ($>FC_{th}$) should be calculated as (Thevanayagam et al., 2002).

$$e_s = \frac{e+(1-b)FC}{1-(1-b)FC} \tag{A.4}$$

where b is a factor between 0 and 1.

Another point of view is related to the paragraph below Fig. 6 (in the PDF version of the paper under discussion), where the authors stated that

> The median particle size of coarse and fine particle is 1.76 and 0.16 mm (Table 1), respectively. If both are assumed as spheres, the diameter of the inscribed sphere in the

> minimum void space formed by coarse particles is around 0.73 mm. It is approximately five times larger than the median diameter of fines...

In reality, in suffusion we are not as concerned about the size of the void space as we are about the constriction size, or the window size, that is formed among the soil particles. Based on the assumption made by the authors, for a median particle size of 1.76 mm and minimum void space, the constriction size is equal to $0.155d$,where d is the diameter of the soil particles. Accordingly, the constriction size is 0.27 mm, which is about two times larger than the median diameter of the fines. The constriction size can be computed accurately according to the Silveira model (Silveira, 1965; Silveira et al., 1975) or it can be computed according to Dallo et al. (2013).

Appendix B

Reply to the discussion by Ahmad ALsakran et al. on "Influence of initial fines content on fabric of soils subjected to internal erosion"

The response to the discussion was written by Ouyang and Takahashi (2016b).

The writers appreciate the discussers (ALsakran et al., 2016) for their interest in the paper and their contributions to the further interpretation of the vulnerability of soils to suffusion.

The discussers divided the soil structure into two categories: clast-supported structure, in which the coarse fraction would transfer most of the effective stresses; and matrix-supported structure, where the coarse particles would lose their contacts among each other due to the excess of fines. With reference to the work by Indraratna et al. (2011) the discussers stated that the specimen with 35% initial fines content was a matrix-supported structure. Thus, it underwent piping rather than suffusion and could not be assessed by the method of Kenney and Lau (1985) and its intergranular void ratio needed revision. Moreover, as per the median diameters of coarse and fine particles, the discussers mentioned that the constriction-size distributions (CSDs) could be obtained by Silveira (1965) and Silveira et al. (1975). Accordingly, the description of the fabric of soil mixtures and the interpretation of suffusion vulnerability based on the constriction size are presented in this response.

On the basis of eqs. A.1 and A.2 in the discussion, the maximum fines content (FC_{max}) is expressed as

$$FC_{max} = \frac{W_{l,max}}{W_{l,max} + W_c} = \frac{\frac{e_x}{1+e_l} W_c}{\frac{e_x}{1+e_l} W_c + W_c} = \frac{e_x}{e_x + e_l + 1} = 1 - \frac{e_l + 1}{e_x + e_l + 1} \tag{B.1}$$

where W_c is the weight of coarse fraction; $W_{l,max}$ is the maximum weight of the fine fraction; and e_l ($e_l \in [0.70, 1.33]$) and e_x ($e_x \in [0.65, 0.94]$) are the void ratio of the fine and coarse fraction, respectively. From the above equation, when e_l reaches the minimum value (0.70) and e_x reaches the maximum value (0.94), FC_{max} would have the maximum value (= 35.6%). This indicates that the maximum threshold fines content could be 35.6% for the mixtures of silica Nos. 3 and 8.

It is known that the soil fabric would be affected by the preparation approach (Kezdi, 1979; Takahashi, 2016). The moist tamping method was employed in this research. Due to the capillary suction among moist soil particles, it could produce specimens looser than the maximum void ratio measured by the standard method (Wanatowski and Chu, 2006). To examine the fabric of the soil mixtures, the microscopic images taken by a digital microscope were presented by Ouyang and Takahashi (2015, 2016a). Observation of the images reveals that there are still many contacts between coarse particles even though the specimen was prepared with 35% initial fines content. This indicates that the 35% mixtures would not be the matrix-supported structure. Therefore, the terminology "suffusion" and the method proposed by Kenney and Lau (1985) were employed in our paper. With reference to Thevanayagam et al. (2002), the first-order calculation of intergranular void ratio in Ouyang and Takahashi (2016a) could also be reasonable within the research scope.

According to Kenney et al. (1985), the constriction size is defined as the diameter of largest sphere that will pass through a particular constriction. That is to say, the constriction size equals the diameter of the inscribed sphere that can move through the minimum void space formed by coarse particles (Indraratna et al., 2007, 2011). Figure B.1 shows the particle-size distributions (PSDs) for silica Nos. 3 and 8, together with the CSDs of the coarse fraction. The CSDs for soils in the densest and loosest states are derived from the methods proposed by Silveira (1965) and Silveira et al. (1975). Based on Locke et al. (2001), the CSDs for the specimen prepared targeting 30% relative density are also obtained, and are indicated as the solid line in Fig. B.1.

Indraratna et al. (2007) suggested that the controlling constriction in a granular filter can be given by the specific constriction size D_{c35} (35% finer in the CSD). According to Humes (1996), the PSD by mass for the fines fraction is applicable to deal with the uniform filters. Therefore, d_{85} (85% finer in the PSD of the fines fraction) is proposed as the representative parameter for the fines fraction (Indraratna et al., 2007). To consider the fundamental parameters including the PSD, CSD, and relative density, Indraratna et al. (2008) noted that the D_{c35} model could be employed to evaluate the suffusion vulnerability, which is given by

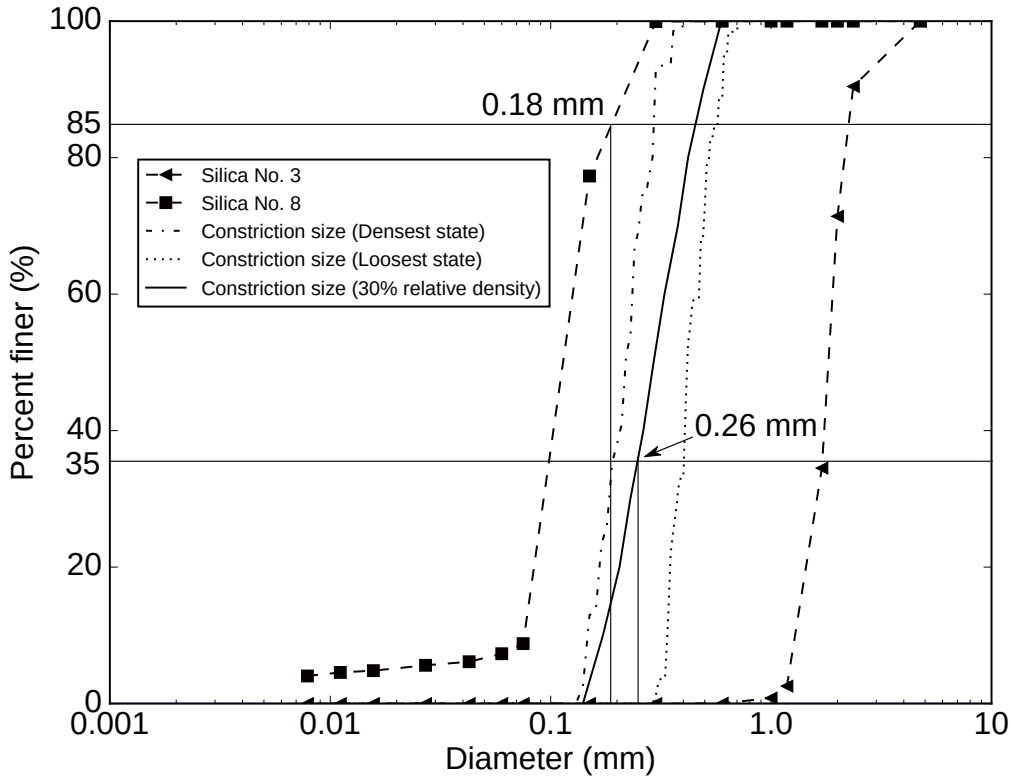

Figure B.1: Particle size distributions and constriction size distributions

$$\frac{D_{c35}}{d_{85}} > 1 \tag{B.2}$$

When D_{c35} is larger than d_{85}, the coarse fraction cannot form self-filtration, and soils will experience internal instability. For the materials tested in this research, D_{c35} = 0.26 mm, and d_{85} = 0.18 mm (as shown in Fig. B.1), thus D_{c35}/d_{85} = 1.44. This suggests that the self-filtration might be difficult to form, and fines could pass through the constriction.